d Collection

Ph.D. Dissertation of Seismology

Seismological Constraints on the Upper Mantle Structure in Northeast Asia and Implications for Mantle Dynamics and Intraplate Volcanism

지진학적 방법을 이용한
동북아시아 상부 맨틀 속도 구조 규명 및
맨틀 동역학과 판내 화산 활동에 대한 고찰

August 2021

Graduate School of
Earth and Environmental Sciences
Seoul National University

Jung-Hun Song

Seismological Constraints on the Upper Mantle Structure in Northeast Asia and Implications for Mantle Dynamics and Intraplate Volcanism

Junkee Rhie

Submitting a Ph.D. Dissertation of
Seismology

August 2021

Graduate School of Earth and Environmental Sciences
Seoul National University
Seismology Major

Jung-Hun Song

Confirming the Ph.D. Dissertation written by
Jung-Hun Song
August 2021

Chair	YoungHee Kim
Vice Chair	Junkee Rhie
Examiner	Haemyeong Jung
Examiner	Tae-Seob Kang
Examiner	Seongryong Kim

Abstract

Volcanism and plate subduction are manifestations of vigorous mantle convection, and are important research subjects for understanding the thermodynamic state of the Earth's interior. Seismic waves propagating through the mantle reflect the physical properties of the mantle, providing detailed information on its thermal and compositional structure. Here we use various seismic methods to investigate the detailed upper mantle structure in northeast Asia where there are active intraplate volcanoes and ongoing plate subduction. Based on our results, we discuss the evolution of the upper mantle and mechanism of intraplate volcanism. Specifically, we apply teleseismic body−wave traveltime tomography to image the volcanic structure beneath Jeju Volcanic Island (Chapter 1), lithosphere and asthenosphere structures beneath the Korean Peninsula (Chapter 2), the stagnant Pacific slab and mantle transition zone structures (Chapter 3), and shallow asthenosphere structures beneath Quaternary volcanoes (Chapter 4). We measure relative arrival time residuals of the teleseismic P and S waves in high precision based on waveform similarity, and invert the datasets for constructing three−dimensional velocity structures using an iterative nonlinear tomography inversion technique. In Chapter 1, we use a unique dataset collected from the deployment of temporary broadband stations in Jeju Island and find out magmatic structures associated with a complex volcanic system that show evidence of a strong interaction between the continental lithosphere and ascending magmas. In Chapter 2, we image the detailed upper mantle structures beneath the Archean−Proterozoic massifs in the Korean Peninsula, which suggest the possible presence of a long−lasting lithospheric root that has experienced heterogeneous modification and reactivation at a craton margin in northeast Asia. In chapter 3, we image high−resolution deeper upper mantle structures including the mantle transition zone in northeast Asia by using the datasets of dense seismic arrays in the Korean Peninsula and southwest Japan.

We find segmented stagnant Pacific slabs with a pronounced gap beneath the Korean Peninsula that was not revealed by previous studies due to limited resolution in this region. We detect and model wavefield variations of teleseismic body waves caused by the deeper upper mantle heterogeneities using 3−D waveform simulation. In the last chapter, we constrain thermal and compositional properties of the upper mantle based on quantitative assessment of high−resolution upper mantle seismic velocity models using thermodynamic calculations, mineralogical modeling, and seismic attenuation. We find evidence for shallow upper mantle melting zones focused beneath major Quaternary volcanoes and suggest an important role of shallow decompressional melting in developing and sustaining localized, long−lived intraplate volcanoes. Throughout all chapters, we have general implications for the origin, evolution, and relationships between the imaged upper mantle structures in the context of geology, tectonics, and geodynamics.

Keywords: Upper mantle, Teleseismic traveltime tomography, Intraplate volcanism, Mantle transition zone, Waveform modeling, Seismic attenuation

Student Number: 2016−20419

Table of Contents

List of Figures

List of Tables

Introduction

Seismic traveltime tomography is a useful technique to constrain the Earth's mantle heterogeneity (e.g., Fukao & Obayashi, 2013). Seismic body-waves travel through the Earth's interior, recording physical properties along their raypaths. Teleseismic relative traveltime tomography is one of novel approaches to constrain velocity heterogeneities beneath seismic arrays (Aki et al., 1977; Thurber, 2002). This method uses relative arrival time differences of distant earthquake's body-wave signals recorded by local seismic arrays. Since seismic stations are closely spaced compared to the event-station distance, waveforms from distant earthquakes among different stations are similar in shape, which allows to measure relative arrival time differences in high precision based on cross-correlation type methods (Van Decar & Crosson, 1990; Rawlinson & Kennett, 2004). Also, as teleseismic raypaths from the common event share similar trajectories outside of the local model space, data sensitivity is maximized on the heterogeneities beneath the local seismic arrays with minor influences or contaminations from source side heterogeneities or errors in source location and origin time. Precise measurements of seismic phase arrival time based on high-quality dataset with a robust technique are necessary to extract structural information of the upper mantle. Also, proper settings of model parameters with an appropriate inversion method to convert observations to model parameters are required. Assessment on the robustness of the imaged structures such as by synthetic checkerboard or structural tests are necessary to evaluate the robustness of the imaged features, which can largely affect our interpretation.

The evolution of the upper mantle is strongly controlled by dynamic interaction between the continental/oceanic lithosphere and asthenosphere at continental margins (e.g., Conrad et al., 2011; Davies et al., 2015; Levander et al., 2014). Intense and multiple episodes of plate margin tectonism result in distinct heterogeneities in the upper mantle, which are related to the past and current tectono−magmatic activities (Schmandt & Lin, 2014; Thomas, 2006). Illuminating fine details of the upper mantle structure is important to understand the intensity of the marginal tectonic processes and mantle dynamics (Holford et al., 2011; S. Kim et al., 2016). Northeast Asia, in the eastern margin of the Eurasian plate, is a natural laboratory that allows us to study the detailed tectonic and magmatic processes in the intra−continental settings.

Here, we constrain upper mantle structures in northeast Asia using teleseismic body−wave traveltime tomography. From records of densely deployed permanent and temporary stations, we image the detailed upper mantle structure in high resolution, finding out distinct anomalies that reflect various processes of continental margin tectonics and mantle dynamics. In Chapter 1, we describe the upper mantle structure beneath the Jeju Volcanic Island, which is a Cenozoic intraplate volcanic field. We deployed 20 temporary broadband stations operated for more than 2 years and together with 3 permanent stations, our dataset resolves detailed lithosphere and sublithospheric upper mantle structure at depths down to ~60 km. We discuss the formation of magmatic structures and the mechanism of the intraplate volcanism. In Chapter 2, using more than 5 years of records of dense permanent seismic arrays, we image the detailed upper mantle structure of the continental lithosphere beneath the Archean−Proterozoic massifs in the Korean Peninsula. We discuss

heterogeneous modification and reactivation of the craton margin lithosphere in relation to tectonic evolution in northeast Asia. In Chapter 3, we further expand our study area to the deeper upper mantle, which includes mantle transition zone, by combining seismic data from southwest Japan. We discuss the origin of deeper upper mantle heterogeneities based on interaction between the stagnant slab and mantle transition zone. In the last chapter, we constrain physical states of the shallow upper mantle in northeast Asia margin based on thermodynamic calculations and high−resolution 3−D upper mantle velocity models. We focus on the shallow upper mantle structure beneath major Quaternary volcanoes and discuss the mechanism of intraplate volcanism.

Chapter 1. Imaging of Lithospheric Structure Beneath Jeju Volcanic Island by Teleseismic Traveltime Tomography

1.1. Introduction

Small−scale magmatic systems are often displayed at the Earth' s surface as a monogenetic volcanic field (Smith & Németh, 2017) where individual volcanoes are active for a short duration, erupting small volumes of magma with a variety of eruptive styles and systematic changes of geochemical compositions (Brenna et al., 2010, 2011; Németh, 2010; Németh & Kereszturi, 2015). Though the volcanic system is widely found in intraplate regions (Connor & Conway, 2000; Le Corvec et al., 2013), the origin and evolution of the magmatism system are still enigmatic due to a lack of information about the behavior of melt in the lithosphere and sublithospheric upper mantle, and its complex interaction with tectonic structure (Brenna et al., 2015a; Cañón−Tapia & Walker, 2004; Hoernle et al., 2006; Smith & Németh, 2017).

Jeju Island (JI) is a Cenozoic volcanic field located off the south coast of the Korean Peninsula. Tectonically, JI is in an intraplate tectonic setting at the southeastern margin of the continental lithosphere in northeast Asia (Figure 1.1a). The major tectonic boundaries surrounding JI are the Ryukyu trench, about 650 km to the southeast, and the Japan Trench further to the east, which are formed by the subduction of the Philippine Sea plate (Nakamura et al., 1989) and Pacific plate (Sager et al., 1988) beneath the Eurasian plate. The volcanic eruption initiated by hydrovolcanic activity on a continental shelf of granitic basement from the Pleistocene (~1.8 Ma)

(Koh et al., 2013; Sohn et al., 2008; Sohn & Park, 2004). Subsequent large-volume lava effusion formed a composite shield with hundreds of individual eruptive centers above the sea surface since the Middle Pleistocene (~0.5 Ma). Several tuff rings and tuff cones were formed during the Late Pleistocene and Holocene (Figure 1.1b) (Brenna et al., 2015a; Koh et al., 2013). About 25 ka, lava flows with evolved magma formed the uppermost part of the island consisting of Mt. Halla trachyte (Brenna et al., 2012b), covered by subsequent basaltic eruptions, which shaped the current surface of the volcanic edifice (Ahn & Hong, 2017; Koh et al., 2003). The volcanic activity lasted until recently based on dating (~3.7 ka) and historical records (~1 ka; Ahn, 2016; Sohn et al., 2015) forming more than 300 small-scale volcanoes of different types, including scoria cones, tuff rings, tuff cones, and lava domes with a central basaltic shield in a confined area ($75 \times 32\ km^2$). It has also been suggested that more than 150 of pyroclastic cones could exist beneath the younger lava flows (Sohn & Park, 2004, 2005). A small number of studies have elucidated the lithospheric structure beneath JI. The basement of the island consists of Jurassic-Cretaceous granites with layers of overlying Cretaceous-Tertiary rhyolitic tuff (Choi et al., 2006; K. H. Kim et al., 2002; Park et al., 2005; Tatsumi et al., 2005). The crustal thickness beneath the island estimated by seismological studies varies from 24.8 to 35 km (Y. Kim et al., 2015; Yoo et al., 2007; Zheng et al., 2011). Gravity and magnetic anomaly data favor shallow Moho and mafic intrusions (Shin et al., 2012). The lithosphere is generally thin, not exceeding 60 km (Pasyanos et al., 2014).

JI and the Korean Peninsula have experienced a similar tectonic evolution during the Mesozoic and Cenozoic (Chough et al., 2000; K. H. Kim et al., 2002; Sager et al., 1988; Yang et al., 2010). In the

Cretaceous, the regions were part of the arc−back−arc system associated with the subduction of the proto−Pacific (Izanagi) plate beneath the continental lithosphere (Chough et al., 2000). Since the Late Cretaceous to early Tertiary, the rollback of the subducting plate led to a change to a back−arc extensional environment with the emplacement of calc−alkaline magmatism (Chough & Sohn, 2010; K. H. Kim et al., 2002; Woo et al., 2014). The opening of the Cenozoic back−arc basins, for example, East Sea and East China Sea, occurred between 27 and 15 Ma (Chough et al., 2000; Otofuji et al., 1985), and JI and the Korean Peninsula transitioned from a back−arc to intraplate tectonic system

Tomographic approaches using data on the relative traveltime of teleseismic body waves have been used to image upper mantle structures from continental scales (e.g., Argnani et al., 2016; Biryol et al., 2011; Schmandt & Lin, 2014) to regional scales (e.g., Bastow et al., 2008; Rawlinson & Kennett, 2008; Schlömer et al., 2017). This method has been successful in revealing detailed three−dimensional (3−D) velocity heterogeneities beneath seismic arrays by taking advantage of individual rays from a common event sharing the same path outside of the region of interest and sampling velocity variations inside the modeled space (Aki et al., 1977; Lévêque & Masson, 1999; Thurber, 2003). This method has provided useful information on unrevealed localized upper mantle structures, for example, in Northeast Asia (e.g., Chen et al., 2017; Lei & Zhao, 2005; Ma et al., 2018; Zhao et al., 2009). However, care must be taken when interpreting results from this method despite its ability to resolve horizontal velocity contrast. As the approach uses rays with subvertical trajectories, vertical velocity contrasts are not well constrained due to vertical smearing, effects by unresolved surface

structures in the model space, and potential influence by heterogenous velocity structures below the model region (Rawlinson et al., 2006b; Zhao et al., 2013). Therefore, a comprehensive analysis is necessary to ensure robust images by incorporating prior knowledge about the geology and tectonics of the region and meticulous recovery experiments to test the obtained features of velocity anomalies.

In this study, we applied the above method to image the lithospheric structure related to the intraplate volcanism in JI. To this end, we deployed 20 temporary broadband stations across the island for a period of over 2 years (October 2013 to December 2015). Relative arrival time differences between seismic stations were measured by the adaptive stacking procedure (Rawlinson & Kennett, 2004), using selected high-quality teleseismic waveforms from the recordings of the network. With resolution analysis using various synthetic models, it was possible to estimate reliable 3-D crust and upper mantle velocity structures beneath JI for the first time, which provided insights into the magmatic processes related to the intraplate volcanism in the island.

Several hypotheses have been suggested for its formation mechanism (e.g., Brenna et al., 2015a; Lee, 1982; Nakamura et al., 1990; Shin et al., 2012; Tatsumi et al., 2005) but consensus has not been reached yet. Nakamura et al. (1990) and Tatsumi et al. (2005) suggested a possible mantle plume origin. Decompressional melting by tectonic extension (Choi et al., 2006) or lithospheric folding (Shin et al., 2012) due to plate interactions have also been suggested. Localized asthenospheric upwelling induced by sublithospheric mantle convections (Guo et al. 2018; West et al., 2009) are proposed. However, due to a lack of geophysical studies, the proposed

7

mechanisms for the origin and magmatic processes of volcanism in JI have not been examined.
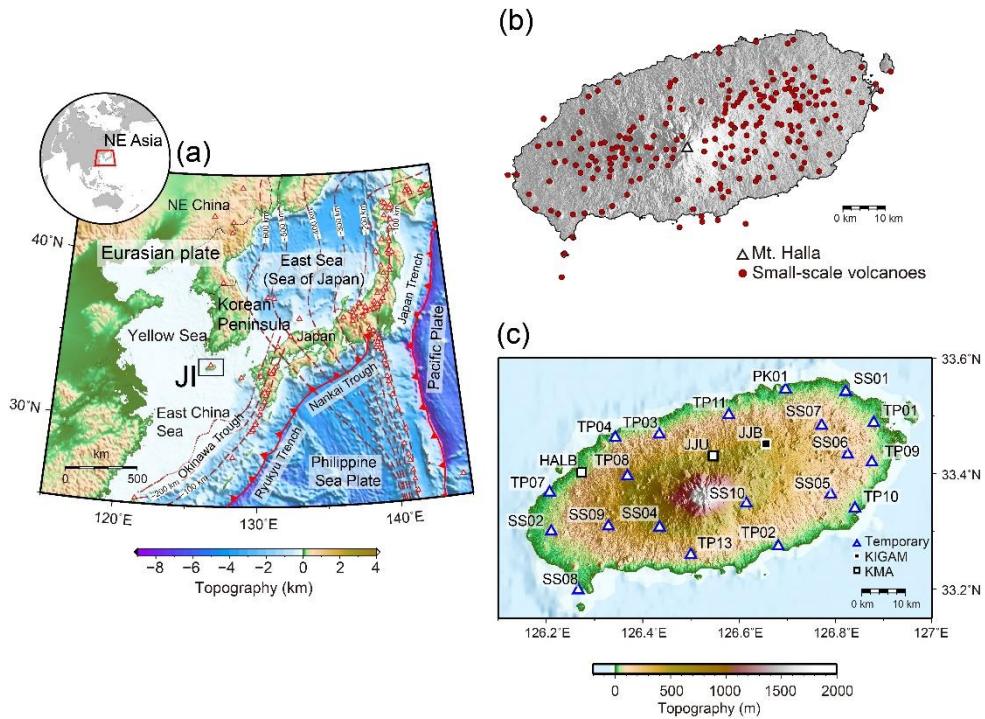
Figure 1.1 Maps of northeast Asia and Jeju Island (JI). (a) Tectonic map of northeast Asia. The location of JI is indicated by the black rectangular box. Slabs of oceanic plate are denoted by brown dashed contour lines at a 100-km depth interval (Iwasaki et al., 2015). Volcanoes in northeast Asia are indicated by triangles. Convergent plate boundaries are shown with red saw-toothed lines (Bird, 2003). (b) Map of seismic stations used in this study. The 20 temporary stations are shown as triangles, and the three permanent stations operated by the Korea Institute of Geoscience and Mineral Resources (KIGAM) and Korea Meteorological Administration (KMA) are shown as black and white squares, respectively. (c) Distribution of small-scale volcanoes (e.g., scoria cones, tuff rings, tuff cones, and lava domes) on JI indicated by red dots. Mt. Halla, the central shield volcano, is denoted by the white triangle. The figures were generated using Generic Mapping Tools (Wessel et al., 2013).

9

1.2. Methods

In this section, we first summarize theoretical background of teleseismic traveltime tomography. We then explain the data acquisition and processing, followed by tomographic inverse method.

1.2.1. Theoretical Background of Telesesimic Traveltime Tomography

We briefly introduce the principle of teleseismic body−wave traveltime tomography based on the derivation of Aki et al. (1977), emphasizing on what types of parameters are used, and how the dataset is connected with the model parameters. Also, we will notice some assumptions and limitations of this method.

The initial model consists of homogeneous layers with a constant thickness and a uniform averaged velocity as shown in Figure 1.2. The model space consists of NL layers, and at each layer, there are NB blocks. Total number of model parameters is M, which is $NL \times NB$. We define a volume of the earth under the array. The earth's structure is assumed to be defined by the standard earth velocity model, such as ak135 (Kennett et al., 1995). Inside the model space, the slowness fluctuation in each block is determined by traveltime data observed at local arrays from large set of teleseismic events.
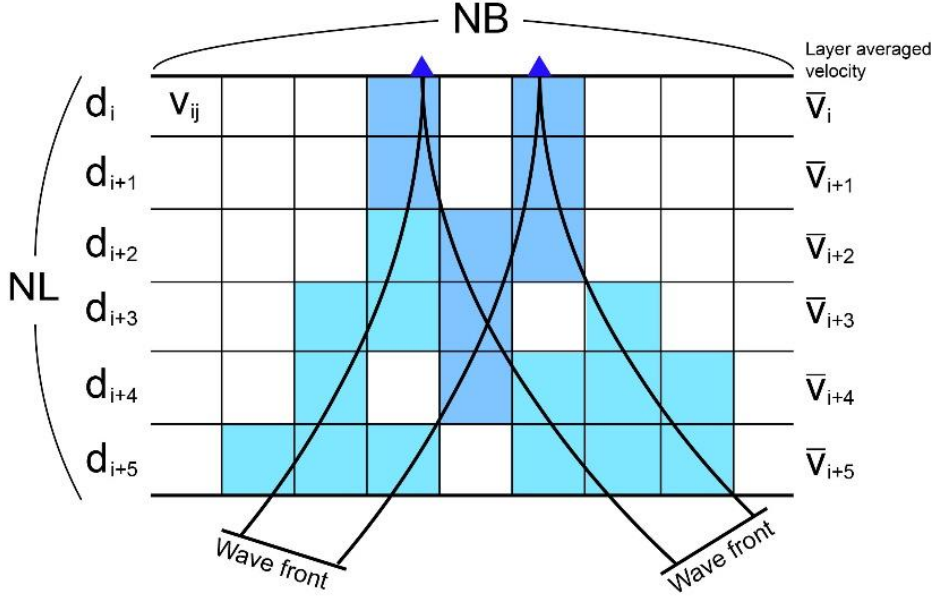
Figure 1.2 A diagram showing the layered model and parameters for teleseismic traveltime tomography. Layered model divided by *NL* layers in constant thickness (d_i) with averaged velocity ($\bar{v}_i$). Each layer consists of *NB* blocks with velocity v_{ij}. The velocity perturbations of individual blocks represent an average over all rays of which most of the path is in the layer within the block.

We apply ray theoretical approach for computing the traveltime, which assumes infinite frequency of rays. The traveltime of an arbitrary ray passing through the ith layer is t_i, which can be calculated by

$$d_i/v_i \tag{1}$$

where d_i is the actual distance traveled in the layer, and v_i indicates the actual velocity. With fractional slowness perturbation of s_i, which can be expressed by

$$1/v_i = 1/\bar{v}_i(1 + s_i) \tag{2}$$

where $\bar{v}_i$ indicates the average velocity in the layer, (1) can be expressed as

$$t_i = \frac{(\bar{d}_i + \Delta d_i)}{\bar{v}_i}/v_i \tag{3}$$

where $d_i = \bar{d}_i + \Delta d_i$.

The arrival time t at receivers that travels through the all layers within the model space can be expressed as

$$t = \sum_{i=1}^{NL} t_i + \tau + \varepsilon \tag{4}$$

where τ is the arrival time from the earthquake to the bottom of the model space, and ε is a residual term including measurement errors (uncertainties). Let $\bar{\tau}$ indicates the arrival time at the bottom for the unperturbed ray and consider $\Delta\tau = \tau - \bar{\tau}$, we get

$$t = \bar{\tau} + \sum_{i=1}^{NL} \frac{\bar{d}_i}{\bar{v}_i}(1 + s_i) + \Delta\tau + \sum_{i=1}^{NL} \frac{\Delta\bar{d}_i}{\bar{v}_i}(1 + s_i) + \varepsilon \tag{5}$$

According to Fermat's principle, the derivative of traveltime with respect to path perturbations around the geometrical ray path is stationary ($\frac{dt}{ds} \approx 0$), we can assume that

$$\Delta\tau + \sum_{i=1}^{NL} \frac{\Delta\bar{d}_i}{\bar{v}_i}(1 + s_i) \tag{6}$$

1 2

is of higher order than other terms in (5). Then, (5) can be rewritten as

$$t = \bar{\tau} + \sum_{i=1}^{NL} \frac{\bar{d}_i}{\bar{v}_i}(1 + s_i) + \varepsilon = \bar{\tau} + \sum_{i=1}^{NL} T_i (1 + s_i) + \varepsilon \tag{7}$$

where $T_i = \frac{\bar{d}_i}{\bar{v}_i}$.

Let assign to each ray only the block that contains most of the unperturbed ray path; only one block for each layer is considered having a dominant part of trajectories for each ray. For contributions from neighboring blocks when parts of the ray pass travel through them, the slowness perturbations within the jth block of the ith layer are formulated as

$$s_{ij} = \bar{s}_{ij} + \Delta s_{ij} \tag{8}$$

Where $\bar{m}_{sj}$ represents the slowness anomaly of the ith layer averaged over rays having most of the path within the jth block. Rewriting (7) using (8), we get

$$t = \bar{\tau} + \sum_{i=1}^{NL} T_i + \sum_{i=1}^{NL} T_i \sum_{j=1}^{NB} s_{ij} \times F_{ij} + \varepsilon^* \tag{9}$$

where F_{sj} indicates 1 if the unperturbed ray in the ith layer has most of the path in the jth block, otherwise 0. ε^* represents summation of ε^* and Δs_{ij}.

Followings are additional symbols to introduce the number of receivers and corresponding arrival time:

N : total number of stations;

$\underline{t}$: vector of arrival times at the surface = $(t_1, t_2, …, t_N)^T$;

$\underline{\bar{\tau}}$: vector of arrival time at the bottom of model space based on the standard earth model = $(\tau_1, \tau_2, …, \tau_N)^T$;

T_0: traveltime spent in the model for the unperturbed ray = $\sum_{i=1}^{NL} T_i$;

$\underline{l}$: vector of unity = $(1,1, …, 1)^T$;

1 3

$\underline{s}$: vector of slowness anomalies $=(\bar{s}_{11}, \bar{s}_{12}, \ldots, \bar{s}_{21}, \bar{s}_{22}, \ldots, \bar{s}_{NL*NB})^T$;

$\underline{\varepsilon}$: vector of high order and error terms $=(\varepsilon_1{}^*, \ldots, \varepsilon_N{}^*)^T$;

$G = \begin{bmatrix} T_{11} & \cdots & T_{1M} \\ \vdots & \ddots & \vdots \\ T_{N1} & \cdots & T_{NM} \end{bmatrix}$ where the $T_{pq} = T_i$ if the ray to p^{th} instrument

travels through the qth block in the ith layer, other wise 0 (this is the sensitivity matrix which connects ray's traveltime and contributions of each block).

Using the above parameters, (9) becomes

$$\underline{t} = \bar{\underline{\tau}} + T_0 \underline{l} + G\underline{s} + \underline{\varepsilon} \tag{10}$$

The first term represents the traveltimes through the standard earth from the earthquakes to the bottom of model space. The second term in (10) indicates the traveltime for rays traveling through the initially defined velocity model of model space, and the third term indicates traveltime anomalies due to perturbations of blocks. We can calculate the G, $\bar{\underline{\tau}}$, and T_0 from the initial model and source−receiver geometry. $\underline{s}$ is the unknown parameters to be estimated. By defining T_0 as unknown, errors from origin time, uniform anisotropy effect throughout the model space can be absolved.

If we consider small errors in the standard earth model, initial model, and source parameters, we can write

$$\hat{\underline{t}} = \bar{\underline{\tau}} - \Delta(\hat{\underline{t}}) \tag{11}$$

and

$$\hat{G} = G - \Delta(\hat{G}) \tag{12}$$

where $\Delta(\hat{\underline{t}})$ is due to errors in source location and origin time, standar earth model, $\Delta(\hat{G})$, which is by raypath perturbation within the model space, and errors in initial model of crust and mantle.

Using (11) and (12), we get from (10)

$$\underline{t} = \hat{\underline{t}} + \Delta(\hat{\underline{t}}) + T_0 \underline{l} + \hat{G}\underline{s} + \Delta(\hat{G})\underline{s} + \underline{\varepsilon} \tag{13}$$

The fifth term in (13) can be assumed to be a higher order term,

and can be neglected because each $\Delta(\hat{G})$ and $\underline{\bar{s}}$ is of first order. The second term is of the same order as errors in the standard model and errors in source location.

The effects of near-source structure are negligible considering the long transmission of teleseismic rays through the relatively homogeneous lower mantle, resulting in smoothed wave front right before reaching at the receivers. The dataset has a greater sensitivity for velocity heterogeneities closer to the local arrays. Therefore, the effects from heterogeneities outside of the model space are efficiently minimized, given that there are events with good and uniform azimuthal and distance coverage.

We further assume $\Delta(\hat{t})$ (outside box effect) in (13) to be of higher order term, which is negligible and common effect to all stations. We now construct the least squares solutions to estimate model parameters by rewriting (10) as

$$\underline{t} - \underline{\bar{\tau}} = (G - \bar{G})\underline{\bar{s}} + T_0\underline{l} + \bar{G}\underline{\bar{s}} + \underline{\varepsilon} \qquad (14)$$

Note that $\bar{G}\underline{\bar{s}}$ is deducted from the third term of (10) and included again, where

$$(G - \bar{G}) = t_s$$

$$= \begin{bmatrix} T_{11} - (\sum_{i=1}^{N} T_{i1})/N & \cdots & T_{1M} - (\sum_{i=1}^{N} T_{iM})/N \\ \vdots & \ddots & \vdots \\ T_{N1} - (\sum_{i=1}^{N} T_{i1})/N & \cdots & T_{NM} - (\sum_{i=1}^{N} T_{iM})/N \end{bmatrix} \qquad (15)$$

(15) allows us to eliminate the necessity of somewhat arbitrarily choosing one particular station for reference (we do not need reference station). This is to mitigate that the observational errors in reference station residuals to bias the final results.

$T_0\underline{l}$ and $\bar{G}\underline{\bar{s}}$ can be lumped together to be common station term as

$$cl = T_0 \underline{l} + \bar{G}\underline{\bar{s}} \tag{16}$$

For n events, (14) can be

$$\tilde{\underline{t}}_k = \underline{t} - \bar{\underline{t}} = (G_k - \bar{G}_k)\underline{\bar{s}} + c_k\underline{l} + \varepsilon_k \quad (k = 1, \dots, n) \tag{17}$$

For all events,

$$\tilde{\underline{t}} = \begin{bmatrix} \tilde{\underline{t}}_1 \\ \tilde{\underline{t}}_2 \\ \vdots \\ \tilde{\underline{t}}_n \end{bmatrix} = \begin{bmatrix} \underline{l} & 0 & \cdots & 0 & G_1 - \bar{G}_2 \\ 0 & \underline{l} & \cdots & 0 & G_2 - \bar{G}_2 \\ \vdots & \vdots & \ddots & \vdots & \vdots \\ 0 & 0 & \cdots & \underline{l} & G_n - \bar{G}_n \end{bmatrix} \begin{bmatrix} c_1 \\ c_2 \\ \vdots \\ c_n \\ \bar{s} \end{bmatrix} + \begin{bmatrix} \varepsilon_1 \\ \varepsilon_2 \\ \vdots \\ \varepsilon_n \end{bmatrix} \tag{18}$$

which is consistent with

$$\tilde{\underline{t}} = \left(\tilde{L}\tilde{G}\right)\left(\frac{c}{\bar{s}}\right) + \tilde{\underline{\varepsilon}} \tag{19}$$

Due to orthogonality of the columns of $\tilde{L}$ it self and with respect to the columns of $\tilde{G}$, we can divide $\underline{c}$ and $\underline{\bar{s}}$ individually in the least square solvation. We first get $\underline{c} = \tilde{L}^T\tilde{\underline{t}}$ and define $\underline{\hat{c}}$ as

$$\underline{\hat{c}} = \frac{1}{N}\tilde{L}^T\tilde{\underline{t}} \tag{20}$$

where $\underline{\hat{c}}$ is the average of traveltime residual $\tilde{\underline{t}}$ over all the stations. Now we subtract $\underline{\hat{c}}$ from each traveltime dataset in each event, we finally isolate $\underline{\tilde{s}}$ by solving

$$\underline{t}^*(relative\ traveltime\ residual) = \tilde{\underline{t}} - \tilde{L}\underline{\hat{c}} \tag{21}$$
$$= \tilde{G}\underline{\bar{s}} + \tilde{\underline{\varepsilon}} - \bar{\tilde{\underline{\varepsilon}}}$$

where $\bar{\tilde{\underline{\varepsilon}}}$ is the averaged error for average station term.

In order to solve $\underline{\tilde{s}}$, we subtract average traveltime from each events. However, we lose information on absolute average properties of each layer. The summation of the columns in $\tilde{G}$ for any one layer is identically zero because uniform slowness perturbation in a layer does not affect $\underline{t}^*$. The rank of $\tilde{G}$ is less than $\mathbf{M} - \mathbf{NL}$. The best possible resolution matrix can be $R_{ij} = 1 - \frac{1}{NB}$ (for $i = j$) where NB indicates number of blocks in the layer to which block j belongs. This means that resolution of each block is 1 for best case except their absolute property, which is averaged over NB; $R_{ij} = -\frac{1}{NB}$ (for $i \neq$

j) where blocks in the same layer as block j)　；　and　$R_{ij} = 0$　for otherwise. The last incidence indicates that there is no information on relationship between blocks of different layers; only perturbations within the same layer can be compared. The least squares estimate for $\underline{\tilde{s}}$ is obtained by

$$\tilde{G}^T \tilde{G} \underline{\tilde{s}} = \tilde{G}^T t_s \underline{t}^* \tag{22}$$

The solution of this equation is unique only if there are ideal numbers of earthquake data with good coverage in azimuth and distance. In practice, however, the number of rays sampling through different blocks; some of them are not sampled. Even after excluding non−sampled model parameters, there still remains model non− uniqueness due to the case of sampling of neighboring blocks by a single ray, etc. In order to overcome this problem, dense station coverage and large number of observations are necessary so that each individual block is sampled by several rays from different directions. Also, by using regularization parameters, such as damping and smoothing, we can find optimized solution to be interpreted. We will continue to explain how to solve inverse problem in the following section.

1.2.2. Data Acquisition: The 2013–2015 Jeju Seismic Array Network

From October 2013 to November 2015, we deployed 20 temporary broadband seismic stations to investigate the seismic activity and velocity structures beneath JI (Figure 1.1c). Twenty-three stations, including three permanent stations, namely, the JJU and HALB of the Korea Meteorological Administration (KMA) and the JJB of the Korea Institute of Geoscience and Mineral Resources (KIGAM), with an average spacing of 9 km across the island, provided the data during the study period. All temporary stations are equipped with Nanometrics Trillium compact broadband sensors with Taurus recorders and global positioning system clocks, continuously acquiring data at 200 samples per second for three individual components. We find 484 teleseismic events with magnitudes larger than mb 5.5 in an epicentral distance range of 30–95° during the recording periods of temporary array from the Data Management Center of Incorporated Research Institutions for Seismology. Before examining the waveforms, instrument responses are removed from all recorded data to obtain three-component (Z, N, and E) displacement signals. We use vertical component data to identify P waves and tangential component data to identify S waves. Two-pole Butterworth band-pass filters with corner frequencies of 0.1–5.0 and 0.05–0.2 Hz are applied for P and S waves, respectively. We visually inspect all the teleseismic waveforms and use only those with clear phase arrivals recorded at more than 13 stations measuring relative arrival time residuals. We analyze a total of 180 events for P waves and 161 for S waves, counting the direct P and S phases and the additional pP, sP, and sS phases (Figure 1.3).
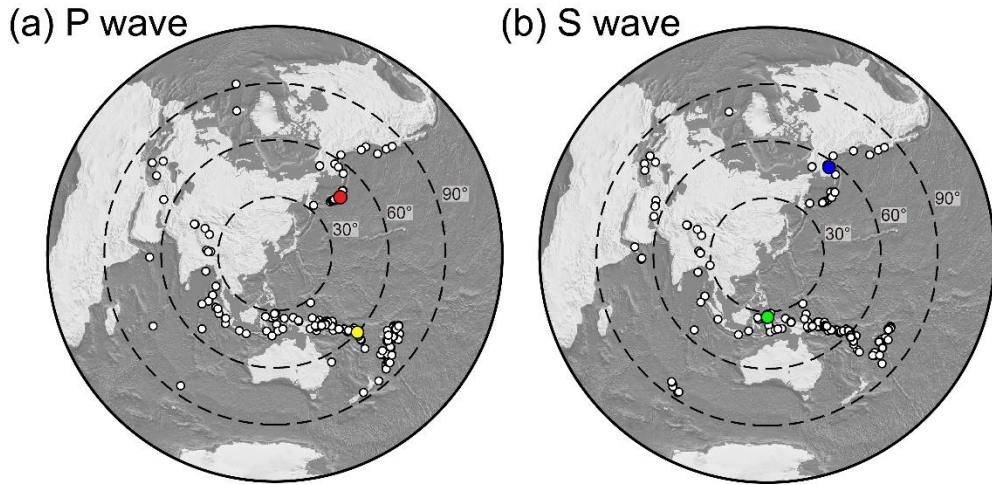
Figure 1.3 Distribution of teleseismic events used in tomographic inversion. All events are in distance range of 30–95° with mb > 5.5, recorded by the Jeju array from October 2013 to November 2015. (a) Events used in the P wave tomography (180 in total). Yellow and red circles indicate the event locations of the waveforms in Figure 1.4. (b) Events used in the S wave tomography (161 in total). Green and blue circles indicate event locations of waveforms in Figure 1.4. Black dashed circles indicate epicentral distances with 30° increments.

1.2.3. Measurement of Relative Traveltime Residuals and Uncertainties

Relative traveltimes of the arriving signal across the stations are defined as the time−shifts that optimally align the traces. Since seismic stations are closely distributed with respect to the distance to the sources, waveforms at each station are similar. Thus, precise measurement of relative traveltime residuals is available based on waveform similarity (Rawlinson & Kennett, 2004; Van Decar & Crosson, 1990). We apply the adaptive stacking method (Rawlinson & Kennett, 2004) to measure relative arrival time residuals. The principle of the adaptive stacking method is based on the minimization of misalignments between records of each stations based on misfits between each traces and the reference waveform, which is formed waveform stacking.

For N stations with records of $u_i(t)$, the line ($V_l(t)$) and quadratic stack ($V_q(t)$) are defined as (Rawlinson et al., 2006b)

$$V_l(t) = \frac{1}{N} \sum_{i=1}^{N} u_i(t - t_i^c) \tag{23}$$

and

$$V_q(t) = \frac{1}{N} \sum_{i=1}^{N} u_i (t - t_i^c)^2 \tag{24}$$

where t_i^c indicate moveout correction based on a standard earth model (e.g., ak135). The linear stack indicates linear summation of waveforms and the quadratic stack represents the spread in alignment between receivers. From (23), the optimum alignment with the stacked trace $V_l(t)$ can be obtained by a search over time−shift τ for each traces to minimize total misfit E_p which is defined by

$$E_p = \sum_{j=1}^{M} \left| V_l(t_j) - u_i(t_j - t_i^c - \tau) \right|^p \tag{25}$$

where M is the number of samples, and τ is a specified time intervals to find the time−shift with minimum misfit. Once the time−shift τ_i are estimated for all traces, time corrections of $t_i^c + \tau$ are applied to each trace and form wavetrain with improved alignment. Then, the linear and quadratic stacks are calculated again with the aligned traces and calculate misfit again, estimating further alignment to improve remaining misalignment. In summary, the procedure includes (1) teleseismic waveforms are first aligned by predictions from a given one−dimensional propagation model (e.g., ak135 (Kennett et al., 1995)), (2) the traces are stacked to form a reference trace, (3) the waveform similarity is measured between each trace and the reference trace, measuring a proper time shift to minimize waveform discrepancy, (4) apply the measured time shift to each trace and stack the traces to generate new reference waveform. Steps from 3 to 4 are conducted iteratively to improve the alignment, which makes total waveform misfits to be minimized. Misfits are powered by designated coefficient p in (25). Since the waveforms are varied by seismic events, a proper choice of the value is needed to correctly extract relative residuals while minimizing total misfit. We choose the coefficient changing the value from 1.0 to 4.0 with an interval of 0.1. For the most cases, minimum misfit is achieved with values around 3.0, which are consistent to that suggested by Rawlinson and Kennett (2004). Examples of waveforms from the four teleseismic sources are shown in Figure 1.4 that are aligned by the adaptive stacking procedure, and corresponding residual maps are shown in Figure 1.5. It is observed that later arrivals are at stations located at greater distances whose raypaths had to pass through the central region of

JI. This suggests that relatively slow velocity structures likely exist beneath the central part of the island, thereby delaying wave propagation. There are changes in amplitudes and patterns in residual patterns depending on source back-azimuths, which implies a certain degree of complexity in velocity structures in the lithosphere beneath JI.

An accuracy of the measured traveltime residual depends on waveform similarity of each trace. The estimated uncertainties can be used as data weights in the tomographic inversion. The adaptive stacking method quantifies the relative uncertainty of residuals based on waveform misfits. When the waveform of a trace and the reference trace are very similar (e.g., high signal-to-noise ratio or cross-correlation), then the minimum misfit at the optimum time-shift is pronounced, but if not, the minimum misfit is broader, i.e. for the same amount of arbitrary time-shift, the misfit increases much steeply for the trace in higher similarity with the reference trace. This behavior can be used to characterize residual uncertainty. Let $E_p(\tau_n)$ represent the minimum misfit for a particular trace n. The uncertainty in the estimated residuals is defined as the smallest difference $|T_n - \tau_n|$, which results in $E_p(T_n) \geq aE_p(\tau_n)$ where a is a calibration factor that is to be chosen *a priori*. This factor quantifies how much a minimum time-shift is required to produce an error that corresponds to the minimum misfit value multiplied by a calibration factor. In order to choose a calibration factor, which determines absolute residual uncertainty for each relative traveltime measurement, we perform following procedures: (1) the estimation of an average root-mean-square (RMS) value of the uncertainty for each event dataset and (2) the calculation of absolute residual uncertainties for individual rays in the same event dataset based on

relative uncertainty estimations with respect to the determined average RMS value. In the first step, we perform the recovery test suggested in the adaptive stacking method (Rawlinson & Kennett, 2004). We apply random time perturbations using a Gaussian distribution with a standard deviation of 0.2 s for P waves and 0.75 s for S waves to the aligned traces, measuring RMS differences between the input time shifts and their recoveries. We repeat this test 100 times to obtain the average RMS uncertainty value for each event dataset. In the second step, the absolute uncertainties for each individual ray are obtained from the relative uncertainties, which are estimated by the adaptive stacking method based on the waveform coherence between the individual waveforms and stacked reference waveform (Rawlinson & Kennett, 2004). Different values of random time perturbation would result in different RMS of uncertainties; however, we find that relative distribution of uncertainties between residuals is consistent. Proper value of random time distribution can be determined based on data RMS. We find that random time perturbation equivalent to the data RMS results in too narrow distribution of uncertainties by this approach. Therefore, we choose twice or third times of data RMS as RMS of random time shifts. Further test is needed comparing inversion results with uncertainties calculated with different amount of perturbations (we will show that this is not significant on tomographic results). We adjust the calculation limits of the absolute error level, which corresponds to a in $E_p(T_n) \geq aE_p(\tau_n)$) such that the RMS value of the relative residual uncertainties is equal to the predetermined average RMS uncertainty. We set the minimum individual residual uncertainty values to no less than 35 ms, which is equivalent to 70% of the sampling interval, to account for imperfect coherence in the records and data noise

(Rawlinson et al., 2006b). Examples of the uncertainties measured for the traces shown in Figure 1.6. Generally, higher uncertainties are found in S wave than in P wave residual data because of the longer−period waveforms. Higher uncertainties obtained at some stations (e.g., stations TP02 and SS08) are likely due be to relatively noisy conditions or incoherent waveforms resulting from local structural heterogeneities (Rawlinson & Kennett, 2004). The RMS of the uncertainties for all observed P and S wave data are 31 and 71 ms, respectively.
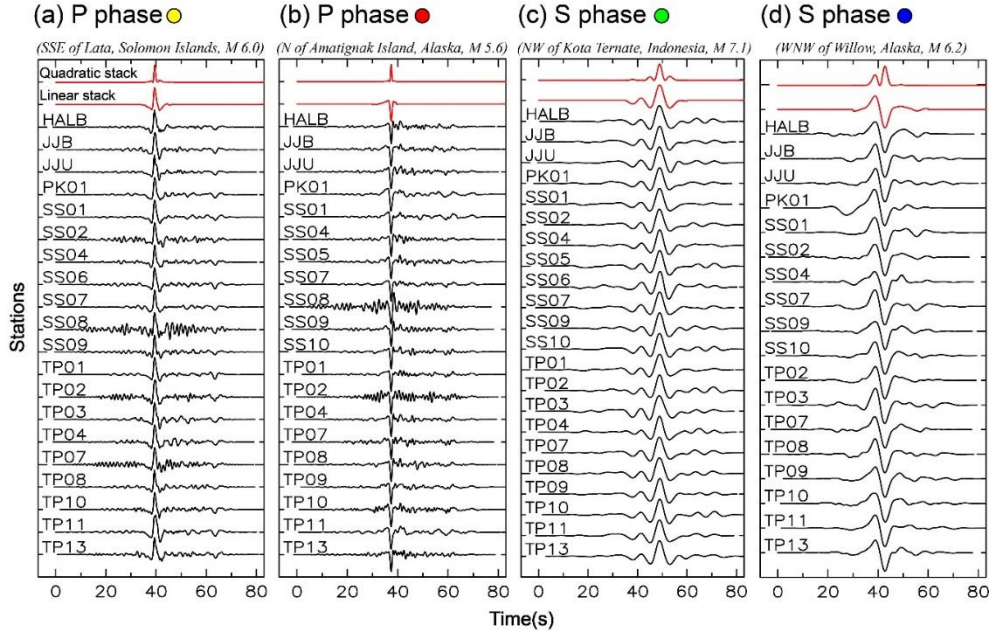
Figure 1.4 Examples of teleseismic waveforms. (a,b) P waveforms and (c,d) S waveforms recorded by the stations on Jeju Island (JI). Waveforms in each panels are aligned by the adaptive stacking technique (Rawlinson & Kennett, 2004). The two topmost waveforms in red correspond to the quadratic and linear stacks, respectively, followed by the waveforms in black corresponding to the signals recorded at given stations (e.g., station HALB). Circles next to the panel titles are coded in the same color as the circles in Figure 1.3 to indicate the sources.
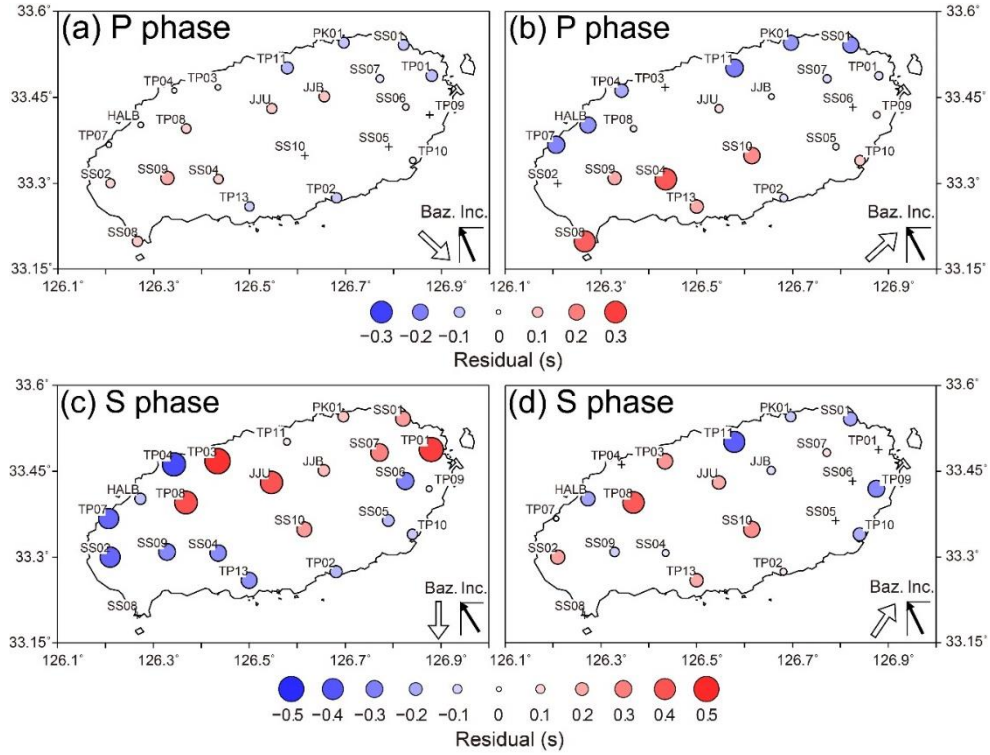
Figure 1.5 Examples of relative arrival time residuals. The event locations are shown in Figure 1.3, and corresponding waveforms aligned by adaptive stacking shown in Figure 1.4. Maps of P wave residuals for the traces in (a) Figure 1.4a and (b) Figure 1.4b. Maps of S wave residuals for the traces in (c) Figure 1.4c and (d) Figure 1.4d. The back azimuth (Baz.) and event incidence angles (Inc.) are denoted by the arrows in the bottom right corner of each map. Stations without arrival time measurements are indicated with a cross.
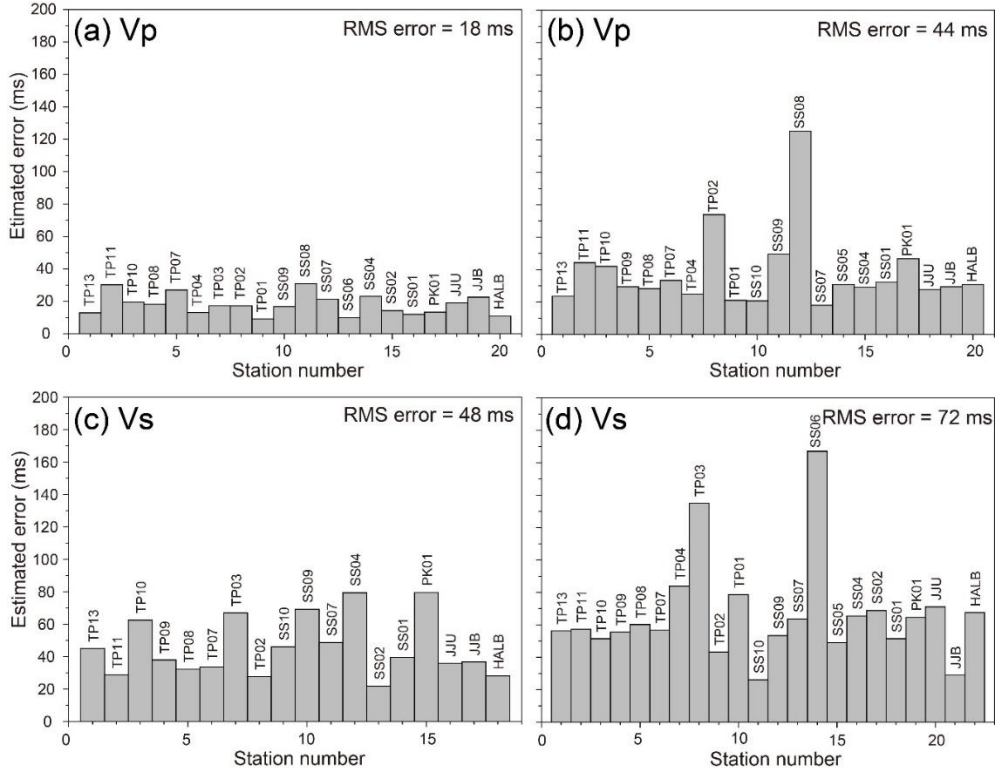
Figure 1.6 Uncertainty estimates of relative arrival time residual. (a,b) Uncertainties of estimated residuals for P phase using the traces shown in Figure 1.4a and 1.4b. (c,d) Uncertainties of estimated residuals for S phase using the traces shown in Figure 1.4c and 1.4d.

1.2.4. Tomographic Inversion

1.2.4.1. Forward Traveltime Calculation Using Fast Marching Method (FMM)

We apply the teleseismic tomography method of Rawlinson et al. (2006b) to calculate the $3-$D velocity perturbations of P and S waves. The method sets the $3-$D model volume beneath the seismic array consisting of regular grids in the spherical coordinate. Forward traveltime calculation is conducted by Fast Marching Method (FMM) (Sethian & Popovici, 1999), which is a grid-based eikonal solver. Nonlinear tomographic inversion process is conducted using a subspace inversion scheme (Kennett et al., 1988). The forward and inverse processes are iteratively applied while adjusting the values of the velocity nodes to satisfy the observed data. Ray paths are also updated at each iteration.

FMM computes the evolution of monotonically advancing wavefronts. It has been used in the migration of reflection data (Sethian & Popovici, 1999) and computation of reflection and refraction phases in layered and complex media (Rawlinson & Sambridge, 2004). It solves the eikonal equation using upwind entropy satisfying operators to track the first-arrival wave front along and evolving narrow band of grid points (Figure 1.7). The entropy satisfying upwind scheme to solve the eikonal equation $|\nabla_x T| = s(x)$, where T is traveltime and s is slowness at the spatial coordinate x, is defined by (Rawlinson et al., 2006a)

$$\left[\begin{array}{l} \max(D_a^{-r}T, -D_b^{+r}, 0)^2 \\ +\max(D_c^{-\theta}T, -D_d^{+\theta}, 0)^2 \\ +\max(D_e^{-\varphi}T, -D_f^{+\varphi}, 0)^2 \end{array}\right]_{i,j,k}^{\frac{1}{2}} = s_{i,j,k} \qquad (26)$$

where i, j, k are spherical grid increment variables in r, θ, φ, and integers a to f are the order of accuracy of the upwind finite difference operator, e.g., the first two upwind operators for $D_e^{-\varphi} T_{i,j,k}$ are calculated by

$$D_1^{-\varphi} T_{i,j,k} = \frac{T_{i,j,k} - T_{i,j,k-1}}{r_i sin\theta_j \delta\varphi}$$

$$D_2^{-\varphi} T_{i,j,k} = \frac{3T_{i,j,k} - 4T_{i,j,k-1} + T_{i,j,k-2}}{2r_i sin\theta_j \delta\varphi}$$

(27)

where $\delta\varphi$ is the grid spacing in φ. If the two equations in (27) are applied, it is a mixed-order scheme where it uses preferentially D_2 operators while reverting to D_1 if the second upwind traveltime is inaccessible. In order to make the order where node traveltimes are updated consistent with the direction of flow from smaller to larger values of T, a narrow band approach is applied. This approach labels all grid points as either "alive," "close," or "far.", which are the state that indicates whether the grid points are passed or not during the wavefront evolution. The alive state indicates upwind of the narrow band with correct traveltime. The close state indicates within the narrow band and trial values are computed from (1) based on the alive points only. The far point indicates downwind of the narrow band with no traveltime information. The narrow band moves toward the far points identifying the close point with minimum traveltime using a heap sort algorithm. After the close points are selected, new narrow band is defined with the prior close points are tagged as the new alive points. The application of a heap sort algorithm makes this approach both fast and stable (Rawlinson et al., 2006a). For teleseismic wave, the initial narrow band can be defined from the bottom surface of the local model beneath the array with initial traveltimes provided by the reference earth model (e.g., ak135). After the (1) is solved for all grids, ray paths are computed

based on the traveltime gradient from the receiver to the base of the model. The Fréchet derivatives, which define sensitivities of grid points on each rays, are also calculated during this process. The velocity grid required by FMM is defined by the cubic B spline velocity field.
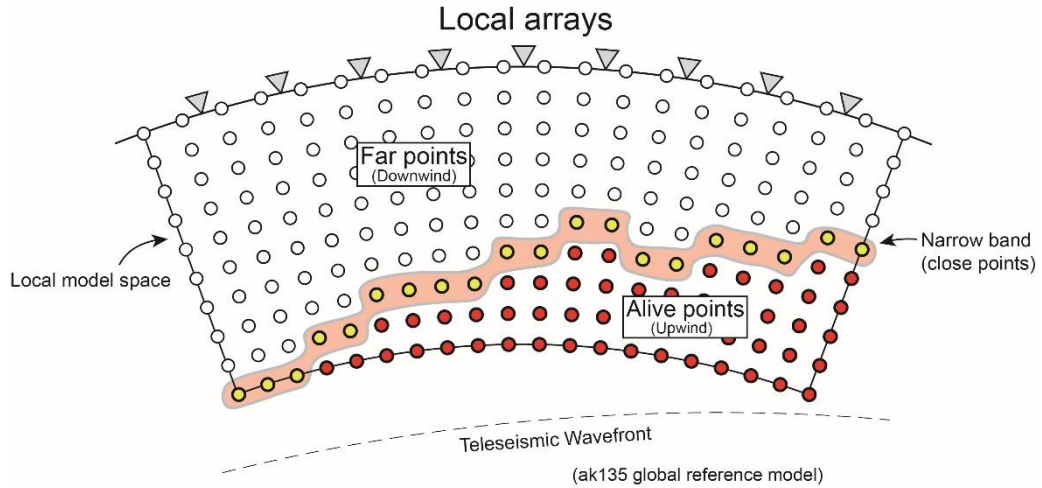
Figure 1.7 A schematic diagram showing the method used to calculate traveltimes. The Earth is assumed to be spherically symmetric with a standard earth model (ak135) outside the local model volume. FMM calculates the wavefront propagation with the starting narrow band including all points on the bottom surface of the model. The narrow band is evolved from the bottom through the grid until all points become alive with traveltimes computed. Close points have trial traveltimes, while far points are yet to have traveltimes computed (The figure is modified from Rawlinson et al. (2006b)).

1.2.4.2. Data Inversion and Model Parameterization

The inverse problem is solved to estimate the adjustment of model parameters. The basic inverse problem equation can be constructed by specifying an objective function $S(m)$ to be minimized, where m are the model parameters, by

$$S(m) = (g(m) - d_{obs})^T C_d^{-1}(g(m) - d_{obs}) \qquad (28)$$
$$+\epsilon(m - m_0)^T C_m^{-1}(m - m_0) + \eta m^T D^T Dm)$$

where $g(m)$ are the predicted traveltime, d_{obs} are the observed residuals, C_d is the a priori data covariance matrix, which is defined by residual uncertainties to be used for data weighting, m_0 is the starting velocity model, C_m is the a priori model covariance matrix, and D is a second derivative smoothing operator. ϵ and η are the damping and smoothing parameters, which regulates the degree of departures of model parameters with respect to the initial model and smoothness of resulting model, respectively. These parameters govern the trade−off between data variance, and the model variance (or smoothness).

Subspace inversion method solves (28) by projecting the quadratic approximation of $S(m)$ onto an n−dimensional subspace of model space (Kennett et al., 1998). The perturbation δm is calculated by (Rawlinson and Sambridge, 2003)

$$\delta m = -A(A^T(G^T C_d^{-1} G + \epsilon C_m^{-1} + \eta D^T D)A)^{-1}A^T \hat{\gamma} \qquad (29)$$

where $A = [a^j]$ is the $M \times n$ projection matrix with M unknowns, G is the sparse matrix comprised by Fréchet derivatives, and $\hat{\gamma}$ is the gradient vector ($\partial S/\partial m$). The basis vectors of n−dimensional subspace are based on the gradient vector in model space $\gamma = C_m \hat{\gamma}$ and the model space Hessian $H = C_m \hat{H}$ where $\hat{H} = \partial^2 S/\partial m^2$. The first search direction of model can be given by $a^1 = \gamma$, which is the

direction of steepest ascent. Based on the rate of change of a^j, all subsequent search directions are given by $a^{j+1} = Ha^j$ $(for\ j = 2, ...)$. Singular value decomposition (SVD) is used to avoid linear dependence between a^j to calculate an orthonormal basis vector. The number of subspace dimension is dynamically adjusted by identifying and removing the unnecessary basis vectors at each iteration. The subspace inversion technique shows efficient and stable convergence in comparison to other technique (e.g., least−square inversion) as it can deal with individual gradients of each model parameters on data variance (Kennett et al., 1998).

For both P and S wave tomographic inversions, we define the local model as spanning $1.94°$ in longitude, $1.13°$ in latitude, and 65 km in depth. A total of 14,560 nodes with grid spacing of 4.5 km in the horizontal direction (40×28 nodes) and 5.5 km in the vertical direction (13 nodes) is used to invert relative arrival time residuals. The spacing of grids and the maximum depth of the model space are determined based on resolution tests with synthetic data and inversion results using real data. We use the ak135 global reference velocity model (Kennett et al., 1995) for the initial velocities of each grid node. The inversion procedure minimizes the misfit between observations and predictions by iteratively updating model parameters and ray geometries. Regularization factors such as damping and smoothing are applied during the inversion procedure to find optimized solution for interpretation. We perform only 10 iterations with a subspace dimension of 10 for an inversion, noting that additional iterations or larger subspace dimensions merely improve the data variance and model features. Based on trade−off curve analyses, we determine the optimum values of damping (10.0 for P wave and 50.0 for S wave tomography) and smoothing (5.0 for

P wave and 10.0 for S wave tomography) (Figure 1.8). Station elevations are corrected during the inversion process and station correction terms are included in the tomographic inversion so that the results are less affected by the local shallow crustal structures beneath the stations.
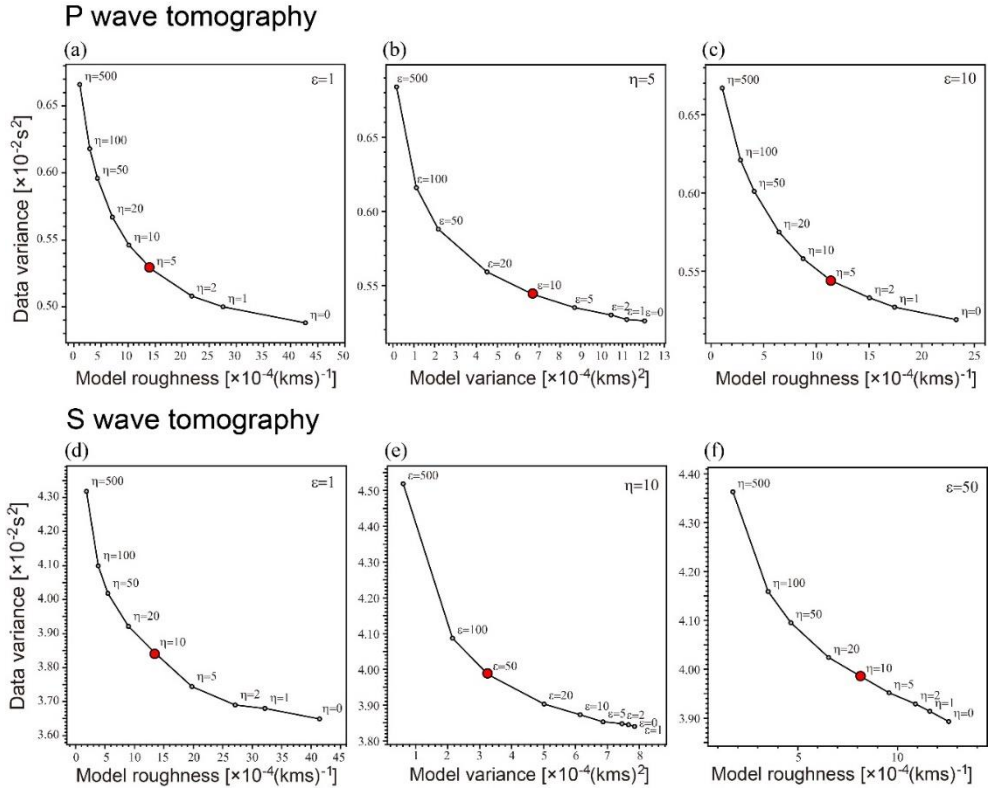
Figure 1.8 Determination of regularization factors, damping (ε) and smoothing (η), of P and S wave tomography by the trade-off curve analysis (Rawlinson et al., 2006b). (a,d) Trade-off between model roughness and data variance when η is varied while ε is held equal to 1. (b,e) The relationship between the model variance and data variance when ε is varied while η is held equal to a value determined from the previous step. (c,f) The relationship between the model roughness and data variance when η is varied while ε is held equal to a value determined from the previous step. Final ε and η are chosen as 10 and 5 for P wave tomography, and 50 and 10 for S wave tomography, respectively. The selected ε and η at each step are indicated by the red circles.

1.2.4.3. Joint Inversion of *P* and *S* Wave Dataset for Vp/Vs Model

In Chapter 3 and Chapter 4, we perform joint inversion of *P* and *S* wave teleseismic dataset to construct the 3−D Vp/Vs model. We follow a similar procedure of Schmandt and Humphreys (2010a) in which simultaneous inversion of the two datasets is performed with an additional regularization on the smoothness of Vp/Vs. To reduce artefacts from different ray density of each individual dataset on results, data with common source−receiver pairs are used. We determine the smoothing parameter for Vp/Vs based on the trade−off between the total data misfit and model smoothness while maintaining regularization factors for individual datasets determined in individual inversions. For this process, we first determine optimum solutions for Vp and Vs individually, and using the determined regularization factors of each model, we conduct the joint inversion with an additional smoothing parameter that controls Vp/Vs smoothness. The smoothness of the Vp/Vs model is obtained by calculating first− and second−derivative smoothness of Vp/Vs, which were then added to the smoothness of Vp and Vs models. The total data misfit is calculated as the sum of the *P* and *S* wave residuals weighted by their respective data norms and uncertainties, so that the both datasets contribute equally in determining the final model. We calculate Vp/Vs variations based on the ak135 reference model, taking into account that differences in the 1−D reference model have little effect on the pattern of d(Vp/Vs) (e.g., Giacomuzzi et al., 2012; Papaleo et al., 2018).

1.2.5. Resolution Tests

The resolution of solution model and reliability of the imaged features are tested by multiple synthetic tests using models with checkerboard and specific patterns. All processes are conducted with the same settings, i.e., model parameters, regularization factors, and source−receiver geometries, that are used in the inversion of the real data. For checkerboard test, we apply checkers with a peak amplitude of ± 0.3 km/s and size of $15 \times 15 \times 15$ km (north−south $\times$ east−west $\times$ vertical), which is similar to the dimension of the smallest−velocity anomaly obtained in the solution model. Gaussian noise equivalent to the RMS of estimated residual uncertainties are added to synthetic P wave (31 ms) and S wave (71 ms) traveltime data, which are equal to the RMS of traveltime uncertainties of the real dataset. We also conduct different checkerboard tests using the same checker size but with different levels of Gaussian noise (twice the RMS error) and with different checker sizes ($10 \times 10 \times 10$ and $30 \times 30 \times 30$ km) but the same level of Gaussian noise. For recovery tests with specific patterns, spatially separated spike anomalies and several cases of synthetic velocity structures are used to assess the reliability of the observed velocity structures. In addition, we test the tomographic inversion under different conditions, namely, inversion without station terms and inversion with some portions of the original data to assess the consistency of the observed results.

1.3. Results and Discussions

1.3.1. Resolution of Solution Model

The inverted models from synthetic P and S wave data for checkerboard resolution tests with checker sizes of 15 × 15 × 15 km (Figures 1.9a–1.9j) and 30 × 30 × 30 km (Figures 1.9k–1.9r) show generally good horizontal and vertical resolution beneath the island. Smears appear at the side edges in the vertical slices (e.g., Figures 1.9g and 1.9h). The inversion results using a higher level of noise also preserve the input patterns, though the velocity contrasts are slightly degraded (Figure 1.10). The test using the smaller checker size shows a good resolution at shallower depths (7.5–30 km; Figure 1.11), which indicates that structures as small as 10 km in horizontal scale are resolvable at depths above 30 km. In order to verify the effects due to smearing (Rawlinson et al., 2006b), we conduct synthetic test with six spatially distributed spikes (peak amplitude of ±0.4 km/s). The solution model (Figure 1.12) successfully recover all the input anomalies, though vertical smearing appears particularly at greater depths.

　For resolution tests with specific structural patterns, we first assume a low−velocity structure located at the center of the island at a depth of 55 km, with a size of 30 × 30 km in the horizontal dimension and height of 15 km (Figure 1.13a). The input pattern is well constrained without significant horizontal offset or smearing, and with minor positive velocities (not exceeding 0.05 km/s) around the low−velocity anomaly as inversion artifacts compensating for the input low−velocity anomaly. For comparison, we create a model with the same low−velocity anomaly (Figure 1.13a) with neighboring higher−velocity structures to the north, east, and west of the island

(Figure 1.13b). Although the size and amplitude of the input anomalies are underestimated, the locations of the positive and negative input structures are effectively resolved. We additionally perform a synthetic test using a conduit shape model. The model consists of a single column at a depth range of 45–60 km and three separate columns on top that extend from a depth of 45 km to the surface (Figure 1.13c). The input P wave velocity perturbation is constant at 0.3 km/s. The inverted model successfully recovers the three separated narrow conduits at shallower depths as well as the single column at greater depths. Figure 1.14 shows a model resulting from a recovery test using patterns that combined all the structures. The results confirmed that the resolved individual features (Figure 1.13) are equally robust in the combined tomography, without underestimating any of the structures or smearing of the dominant features. We further interpret the resulting velocity anomalies for the areas showing robust and reliable results in the resolution tests.

Additionally, we test the P and S wave tomography results under different conditions: (1) inversion without station terms and (2) inversion using a randomly chosen half and quarter of the data. In the second test, we chose only 20% of the rays from the southeast (back azimuth from 120 to 160°, which account for nearly 50% of the original data) to balance the input data. Although we omit static corrections and some of the original data, the observed structures at depths below 10 km are consistently resolved (Figure 1.15).
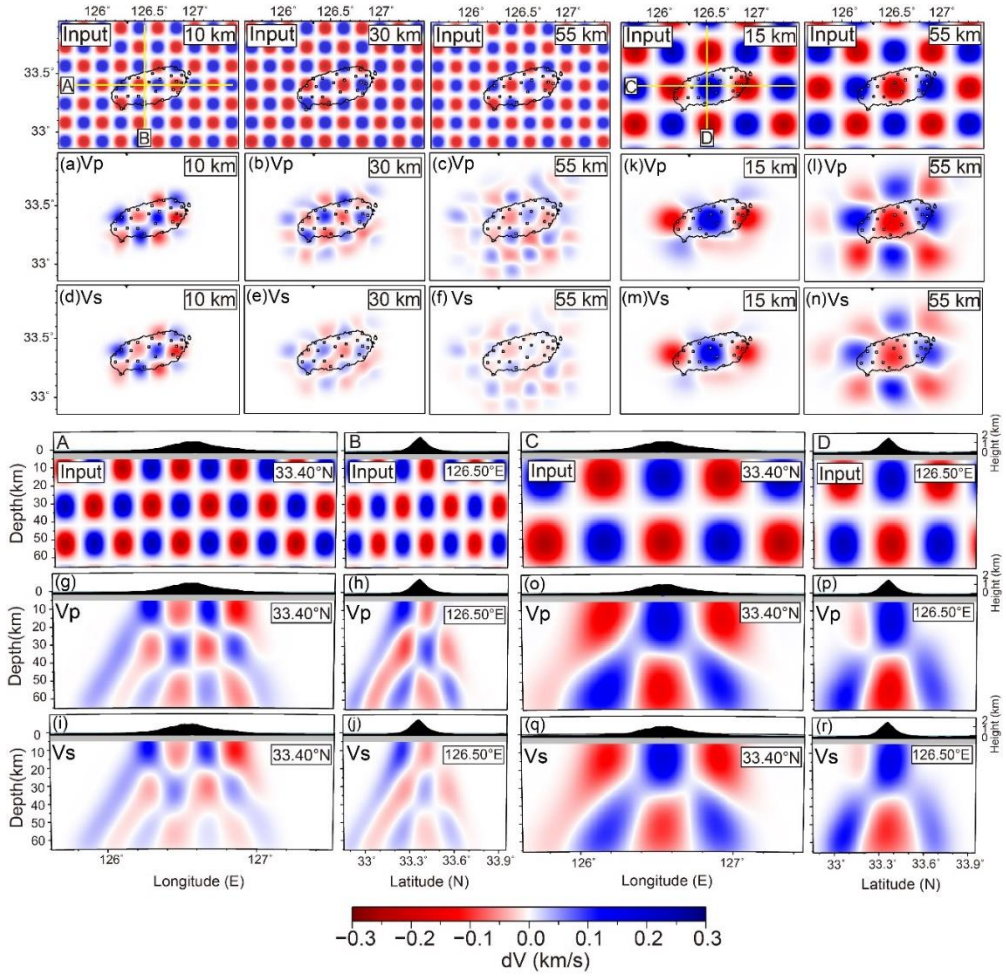
Figure 1.9 Checkerboard test results for P and S wave tomography. (a–j) Output models with checker size of 15 × 15 × 15 km. (k–r) Output models with checker size of 30 × 30 × 30 km. (a–c) Output models at depths of 10, 30, and 55 km for Vp. (d–f) Output models at depths of 10, 30, and 55 km for Vs. (g,h) Output models at latitude 33.40° N and longitude 126.50° E for Vp. (i,j) Output models at latitude 33.40° N and longitude 126.50° E for Vs. (k,l) Output models at depths of 15 and 55 km for Vp. (m,n) Output models at depths of 15 and 55 km for Vs. (o,p) Output models at latitude 33.40° N and longitude 126.50° E for Vp. (q,r) Output models at latitude 33.40° N and longitude 126.50° E for Vs. Gaussian random

noise equivalent to estimated residual error is added to the synthetic dataset.
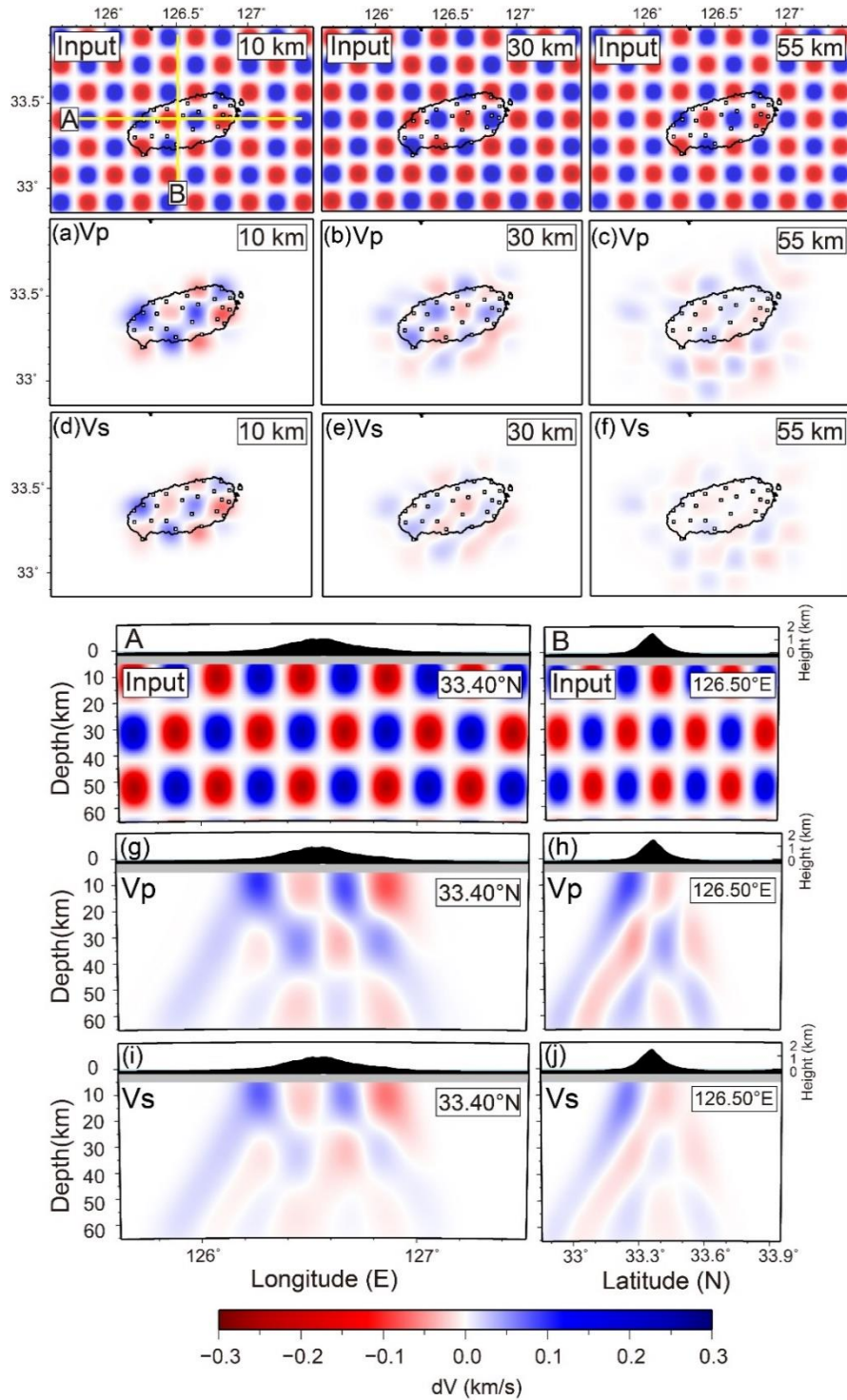
Figure 1.10 Checkerboard test results for P and S wave tomography with different levels of Gaussian random noise (twice the root mean square error of the estimated data residuals). (a–c) Output models at

depths of 10, 30, and 55 km for Vp. (d–f) Output models at depths of 10, 30, and 55 km for Vs. (g,h) Output models at latitude 33.40° N and longitude 126.50° E for Vp. (i,j) Output models at latitude 33.40° N and longitude 126.50° E for Vs.
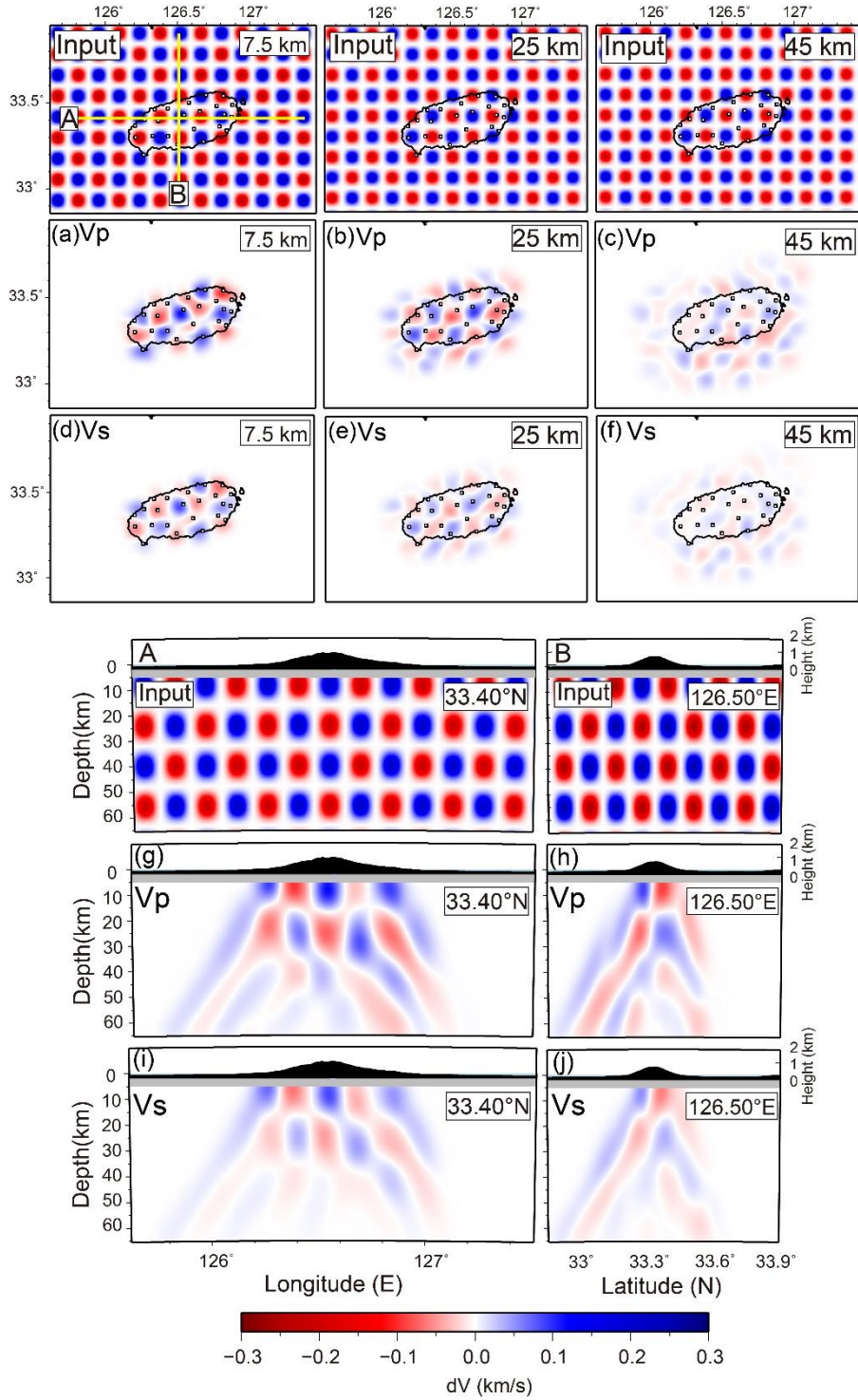
Figure 1.11 Checkerboard test results for P and S wave tomography with different checkerboard size ($10 \times 10 \times 10$ km). (a–c) Output model at depths of 7.5, 25, and 45 km for Vp. (d–f) Output models at

depths of 7.5, 25, and 45 km for Vs. (g,h) Output models at latitude 33.40° N and longitude 126.50° E for Vp. (i,j) Output models at latitude 33.40° N and longitude 126.50° E for Vs. Gaussian random noise equivalent to the estimated residual error has been imposed on synthetic dataset.
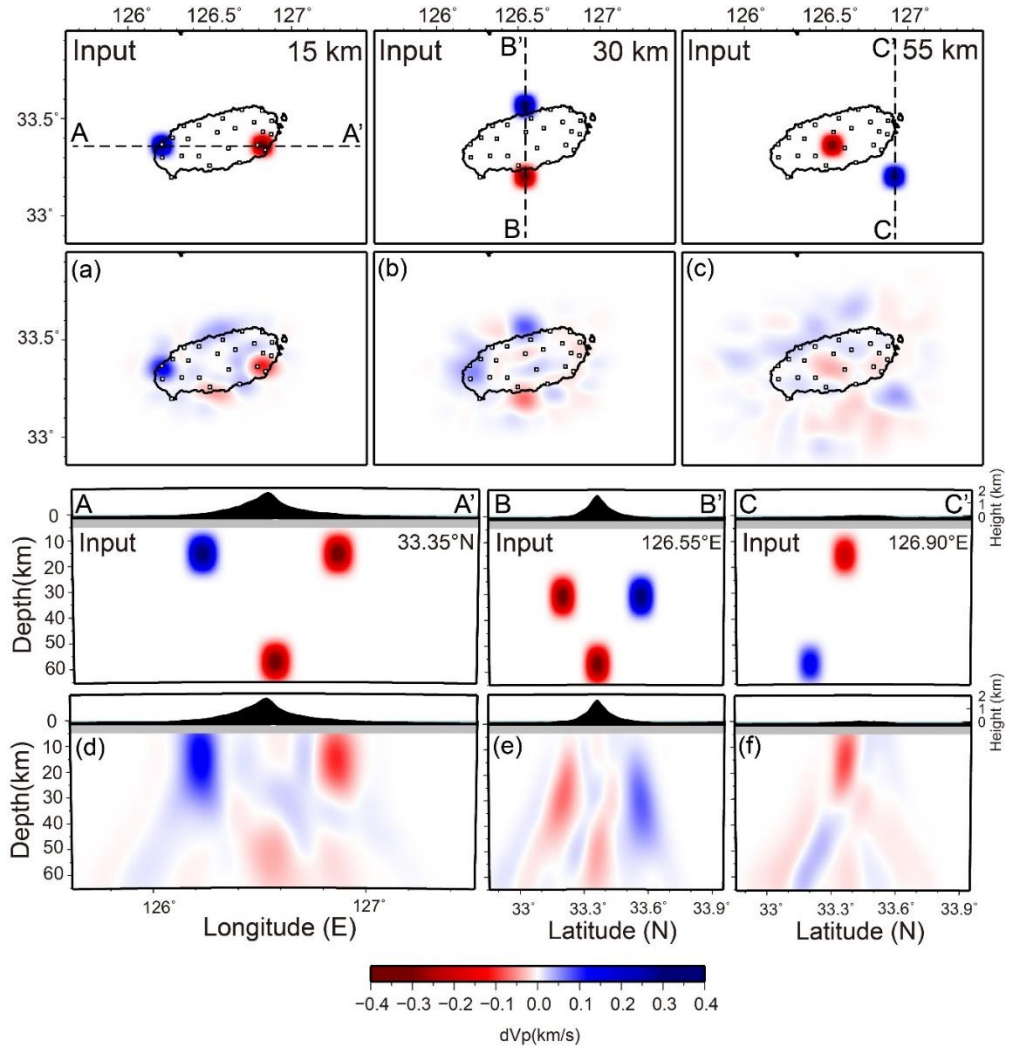
Figure 1.12 Spike resolution test results for P wave tomography with sparsely separated six anomalies (peak amplitude of ± 0.4 km/s). (a–c) Depth slices at 15, 30, and 55 km. (d) Vertical slice at 33.35° N. (e,f) Vertical slices at 126.55° E and 126.90° E.
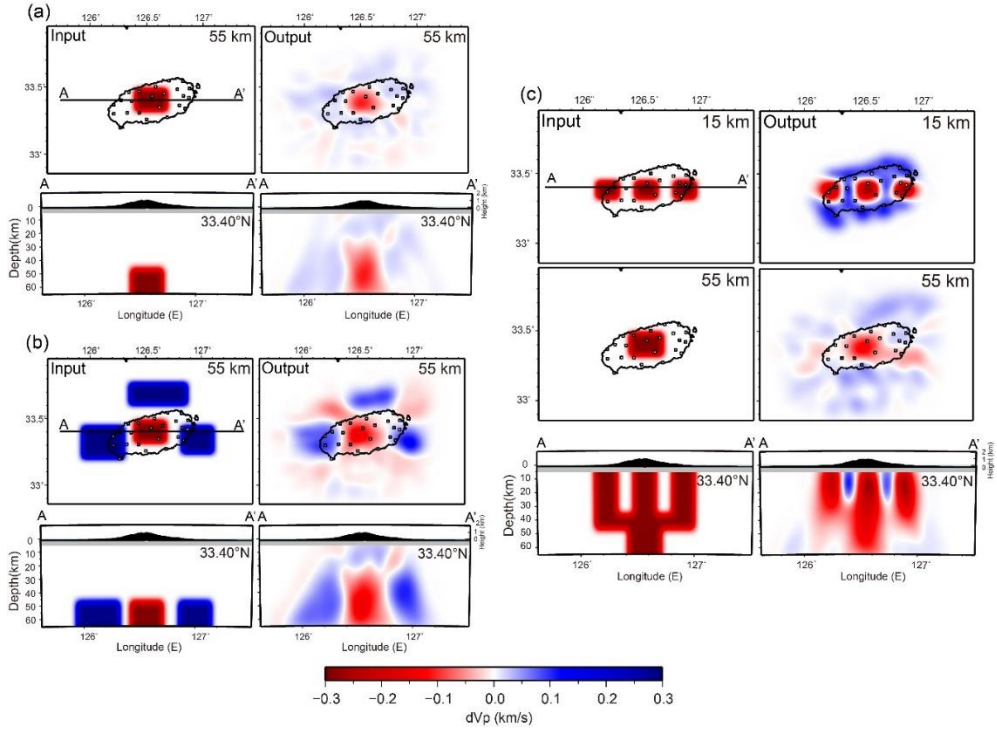
Figure 1.13 Structural resolution test results for P wave tomography.
(a) A low−velocity structure (−0.3 km/s) at the center of the island.
The anomaly has a scale length of 30 × 30 km horizontally and 15
km vertically, located at a depth of 55 km. (b) Higher velocity
structures (+0.3 km/s) located to the north, east, and west of the
island. The central part of the island has lower velocity perturbation
(−0.3 km/s), with anomaly size identical to that in (a). (c) Conduit
model test with −0.3 km/s perturbation. Initial and output models are
shown in the left and right columns, respectively. Initial and output
models are shown in the left and right column, respectively.

4 7
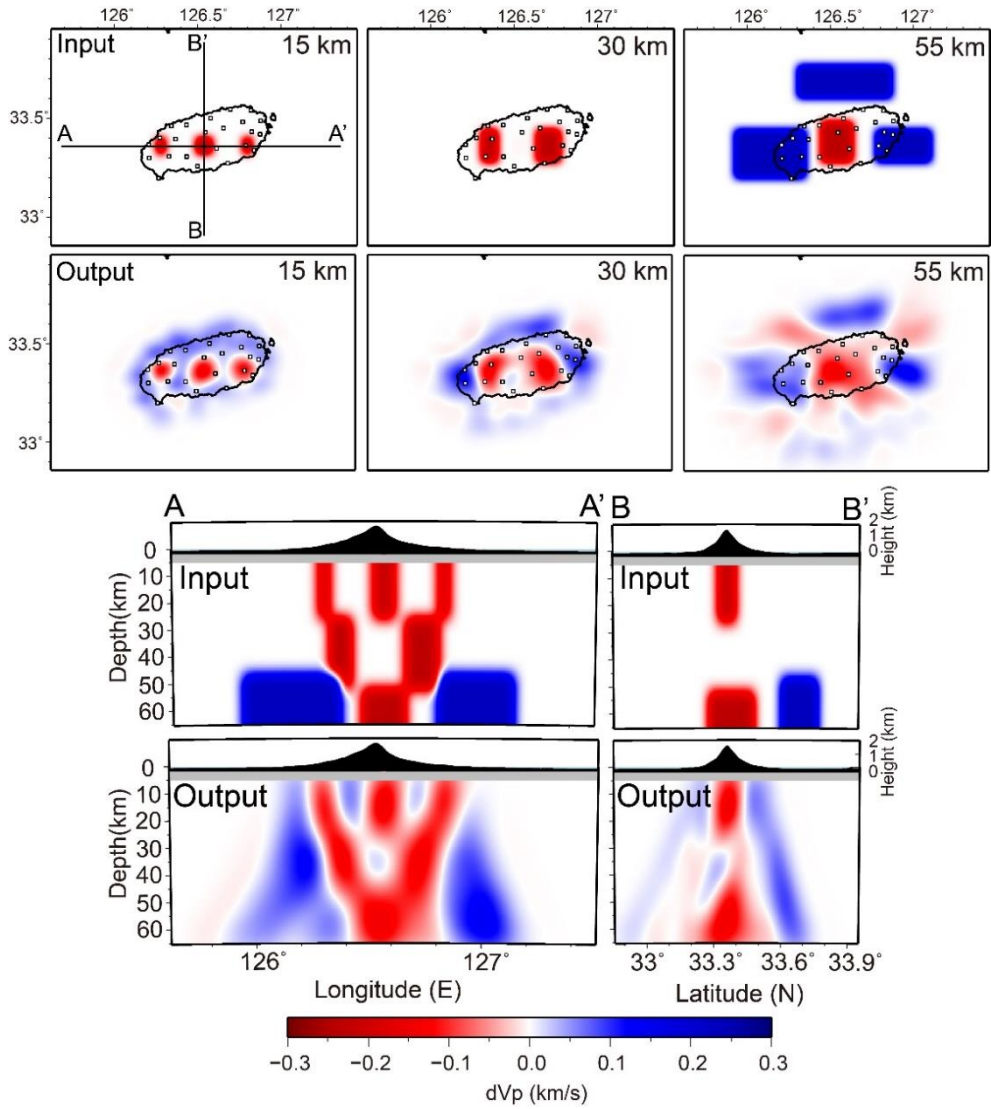
Figure 1.14 Resolution test results of P wave tomography with synthetic velocity structures consisting of the main features in observed results.
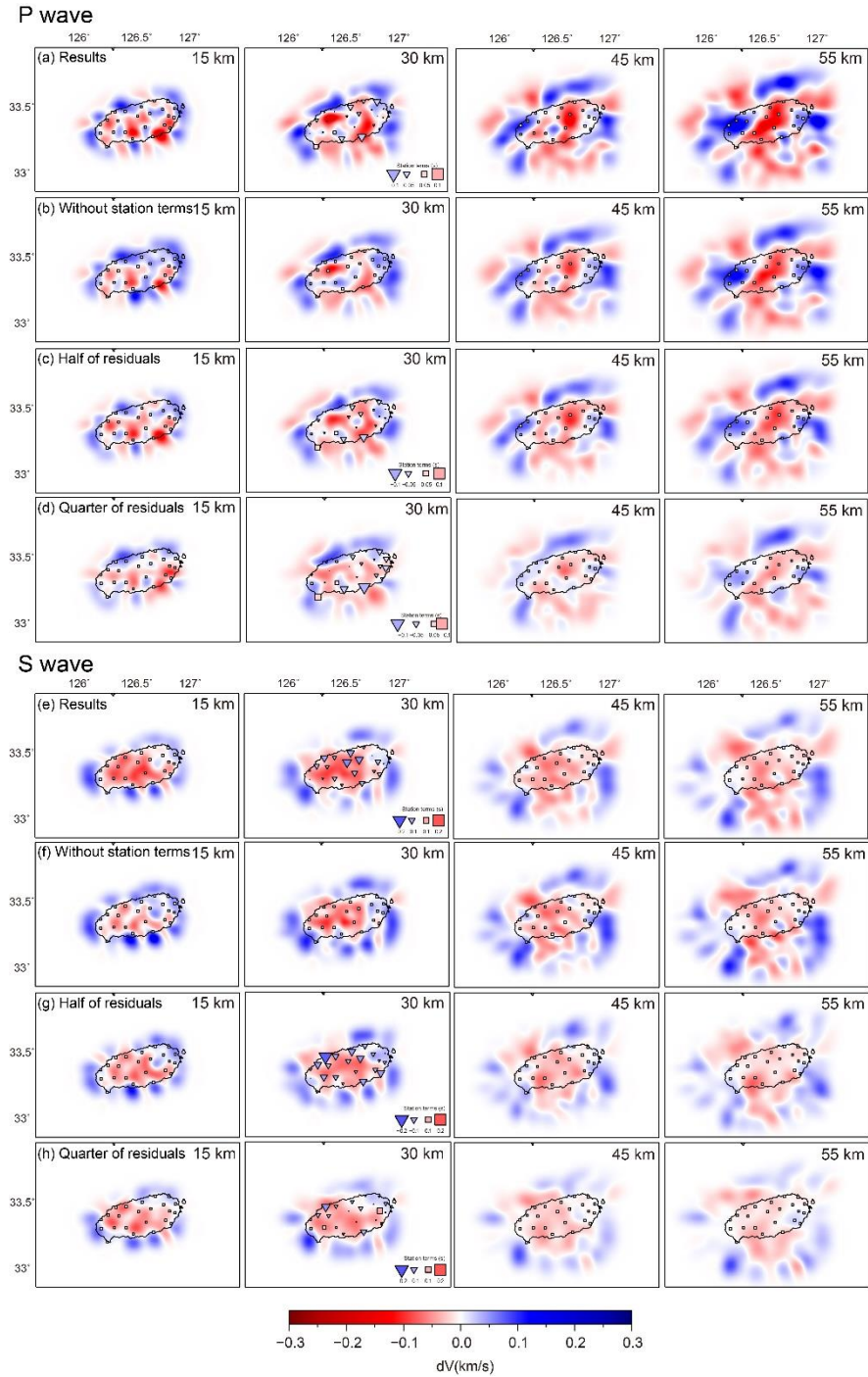
Figure 1.15 Tomography results under different conditions. (a–d) Results for Vp. (a) Original results. (b) Results without station. (c) Results calculated with half of residuals. (d) Results calculated with quarter of residuals. (e–h) Identical to (a–d) but for Vs.

1.3.2. Solution Models

The final models obtained by the tomographic inversion result in a reduction of data variance by 34% from 0.0082 to 0.0054 s^2 (from 90.5 to 73.8 ms in RMS) for P wave tomography (Figure 1.16a) and by 33% from 0.0572 to 0.0385 s^2 (from 239.2 to 196.1 ms in RMS) for S wave tomography (Figure 1.16b). There are clear improvements in the variance reduction, though the values are not substantial. This could be due to relatively small traveltime variances in the modeled region compared to the noise level, but also by unaccounted factors, such as unresolvable small−scale or shallow structures, anisotropy, heterogeneous velocity structures beneath the model space (Rawlinson et al., 2006b).

Depth slices of the 3−D P wave tomography model from 15 to 55 km (Figure 1.17) reveal a characteristic pattern of relatively low velocity anomalies beneath the island that varies in their shapes and patterns at different depths. At depths of 45 and 55 km (Figures 1.17c and 1.17d), a strong low−velocity anomaly (<0.2 km/s) is clearly observed beneath the central part of the island (Anomaly 1). At a depth of 30 km (Figure 1.17b), the deeper anomaly divides into narrower low−velocity zones (Anomaly 2). The pattern of low−velocity anomalies becomes more complex at a depth of 15 km (Figure 1.17a).

We observe relatively high velocities (>0.1 km/s) to the north, east, and west of the island at greater depths (Figure 1.17d), where a strong contrast exists between the central low−velocity and high−velocity areas. In the vertical profile at 126.50° E (Figure 1.17f), the high−velocity structure occurs at around 33.6° N, whereas the low−velocity zones are located beneath and to the south of JI. In the east−

west vertical profile at 33.35° N (Figure 1.17e), the high-velocity regions are visible to the east and west of the island.

The results of S wave tomography are shown in Figure 1.18. The overall patterns of velocity anomalies are similar to the P wave structure, showing a low-velocity anomaly at the center of the island while relatively high velocities to the north, east, and west. However, the relatively small scale pattern of the low-velocity anomaly revealed by P wave tomography is not identified. This loss in resolution may be attributed to one or a combination of factors, such as the longer wavelengths of S wave signals, higher uncertainties in estimated residuals, and the relatively small number of residual data (Bastow et al., 2008).
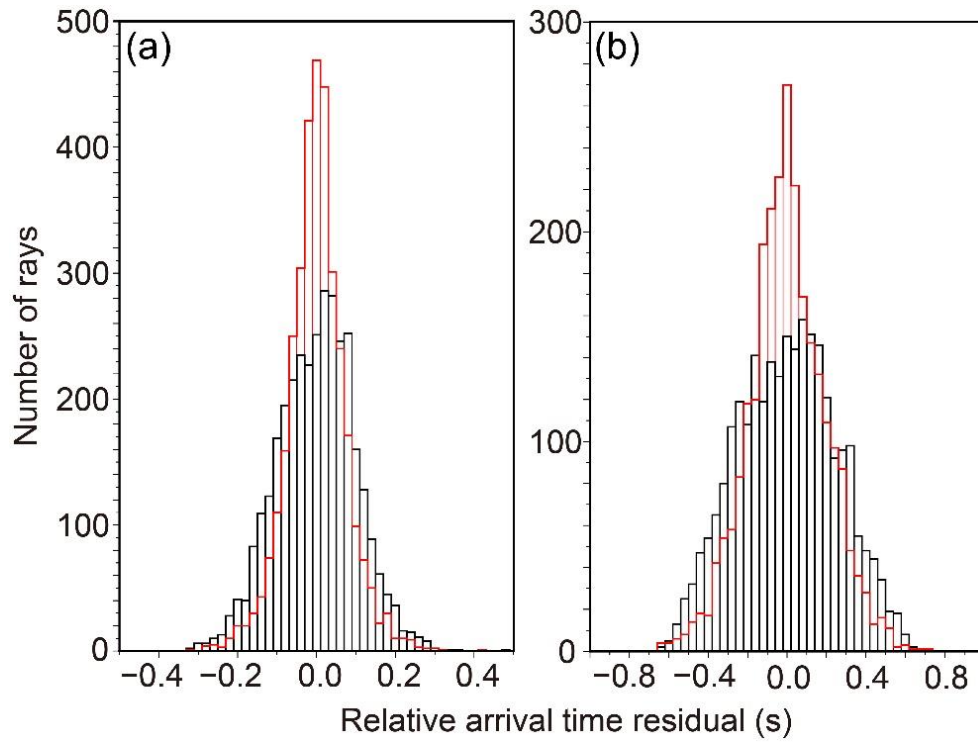
Figure 1.16 Histograms of relative arrival time misfit obtained from initial models (black) and solution models (red) of (a) P wave and (b) S wave tomography.
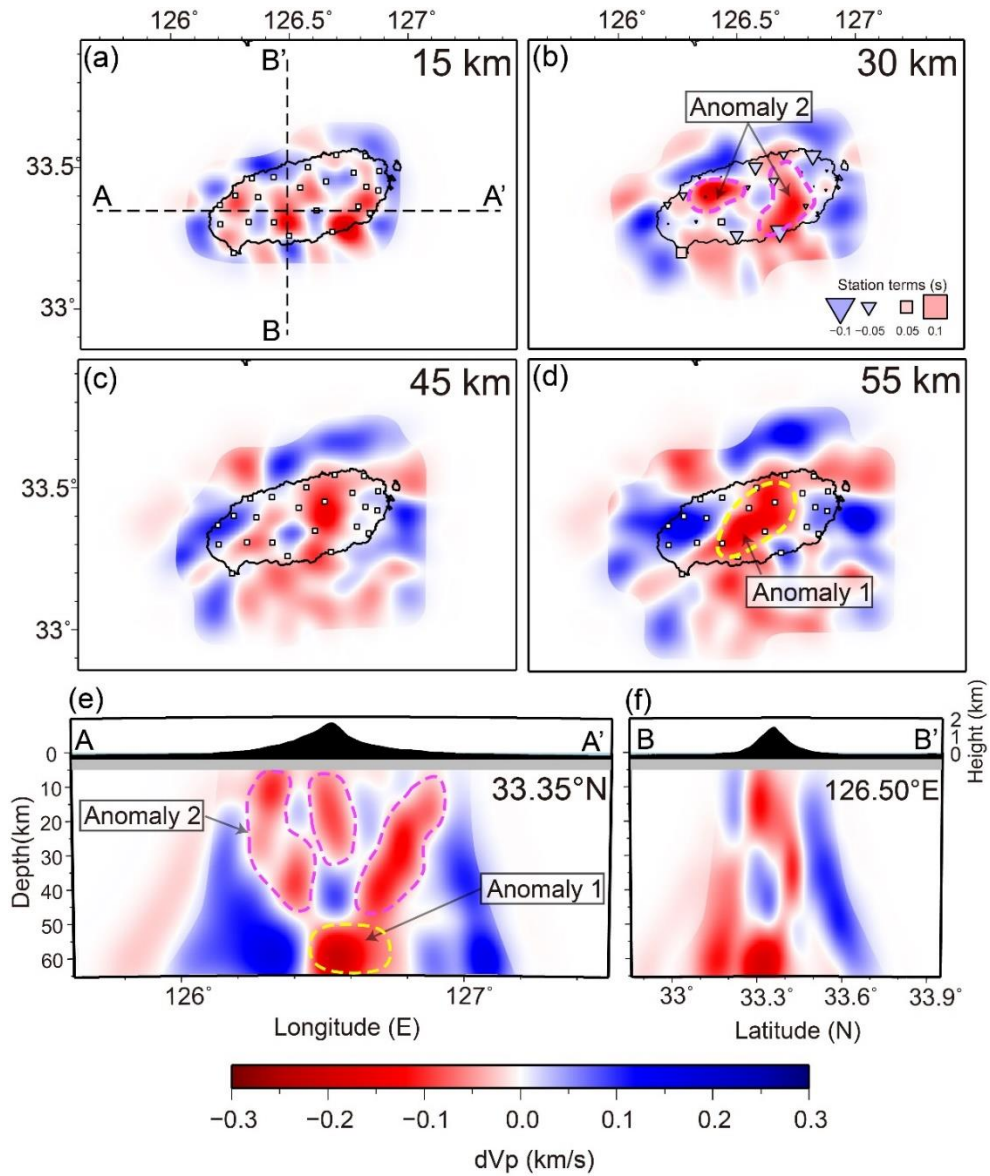
Figure 1.17 *P* wave tomography results. (a–d) Depth slices at 15, 30, 45, and 55 km. Seismic stations are indicated by white squares. Station terms calculated by tomographic inversion are shown in (b). (e,f) Vertical profiles at latitude 33.35° N and longitude 126.50° E. Contour lines show major features observable in the model (Anomalies 1 and 2).
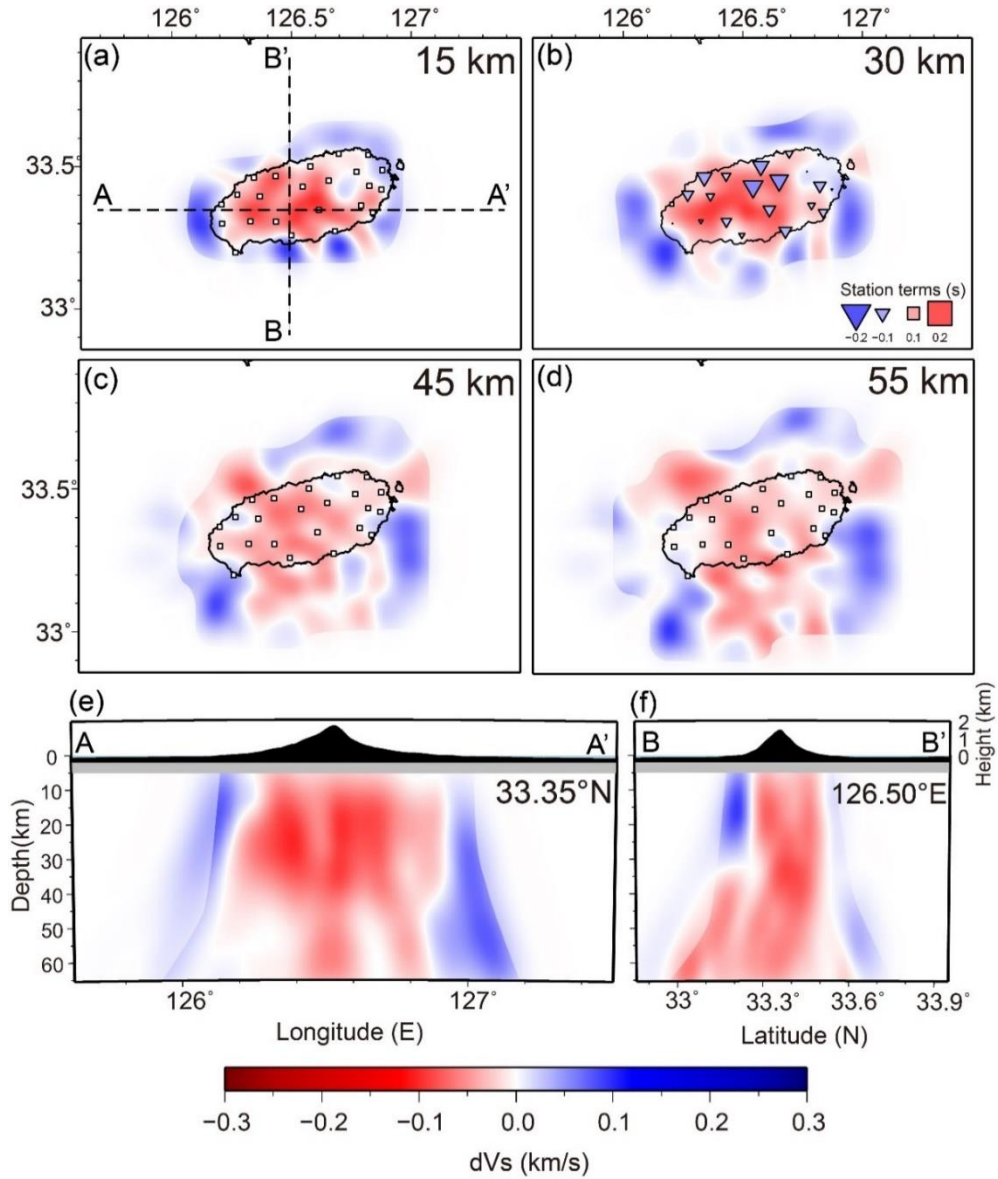
Figure 1.18 *S* wave tomography results. (a–d) Depth slices at 15, 30, 45, and 55 km. Seismic stations are indicated by white squares. Station terms calculated by tomographic inversion are shown in (b). (e,f) Vertical profiles at latitude 33.35° N and longitude 126.50° E.

1.3.3. Interpretations

In relative traveltime tomography, care should be taken when interpreting images with velocity perturba− tions because this method only provides relative velocity; absolute velocities are unknown (Aki et al., 1977; Lévêque & Masson, 1999; Rawlinson et al., 2006). Therefore, it is useful to compare previous results that constrain either the velocity structure at larger scales (e.g., global or regional tomography) or the absolute velocity structures, such as when surface wave dispersion data were used (Bastow, 2012).

In global tomography models (Mégnin & Romanowicz, 2000; Ritsema et al., 2011), northeast Asia has a relatively slow upper mantle S wave velocity (<1% at a depth of ~100 km). Studies of regional P wave tomography that cover East Asia upper mantle (Li & Van Der Hilst, 2010; Wei et al., 2012) also show relatively low velocity anomalies (<1%) at depths of 50−150 km under JI and the nearest regions. Studies using multimode surface waveform tomography (e.g., Legendre et al., 2015; Pandey et al., 2014; Priestley et al., 2006) have revealed prominent slow S wave speeds (<2.5%) at the back−arc basins of the western Pacific subduction zones comprising the East Sea and extending to the East China Sea. These results point to slower upper mantle velocities beneath JI and nearby regions (dVp = 1% and dVs = 1% in lower bounds) compared with the normal mantle velocity. Therefore, we suggest that the low velocity (P wave velocity < 0.15 km/s) beneath the center of JI observed in our study is potentially slower than the regionally slow upper mantle.

The high velocity structures at greater depths correspond to the high−velocity anomalies imaged in previous tomographic studies.

Global models observed relatively thick lithospheric structures (>60 km) in the central and western parts of the Korean Peninsula (e.g., Pasyanos et al., 2014). In regional studies, relatively high velocity anomalies were commonly observed at locations similar to the regions with relatively thick lithosphere (e.g., Chen et al., 2017; S. Kim et al., 2016; Ma et al., 2018; Wei et al., 2012; Zheng et al., 2011). S. Kim et al. (2016) suggested that sharp boundaries of high-to-low-velocity transition exist near JI, which they interpreted to be the lateral boundary at a shallow upper mantle depth (<60 km) between the relatively thick continental lithosphere beneath the Korean Peninsula and East China and the asthenospheric upper mantle beneath regions with a thinner lithosphere.

The peak-to-peak variation between Anomaly 1 and surrounding high-velocity regions is approximately 0.4 km/s, which corresponds to a 5% velocity perturbation. Considering the globally slow upper mantle in our study area, the velocity reduction of Anomaly 1 could reach 6% in comparison with the normal mantle. However, such large variation is unlikely to form within the sublithospheric mantle beneath the island, compared with active magmatic rift zones or hot spots where a similar magnitude of velocity reduction has been reported in the upper mantle (e.g., Bastow et al., 2008; Huang et al., 2015). Considering previously suggested lithospheric structures and the velocity pattern obtained in our study, we suggest that the high-velocity structures represent the southern margin of the lithospheric structures that extended from the Korean Peninsula and East China.

The source depth of the magma of JI volcanism has been suggested to be greater than lithospheric depths to form such a large-volume central shield volcano (Brenna et al., 2012a) and to

explain the geochemical evidence (Baek et al., 2014; Choi et al., 2006). Our image (Figure 1.17d) shows at least a 0.3-km/s perturbation of P wave velocity between the central low-velocity structure (Anomaly 1) and the surrounding high-velocity regions, which is about a 3.7% velocity perturbation with respect to the reference model. Such an observed velocity change corresponds to a temperature variation range of 185-740 ° C (Bastow et al., 2005; Goes et al., 2000), assuming that there is only the thermal effect on seismic velocity perturbation. It is unlikely for such a large temperature variation to occur within the small area (~100 × 100 km) without localized melt focusing (e.g., Lee & Lim, 2014; Tang et al., 2014). Because the imaged low-velocity features are not localized around JI but cover the entire region of the East China Sea (e.g., Wei et al., 2012; Zheng et al., 2011) or extend along the expected margins of the continental lithosphere (e.g., S. Kim et al., 2016), other factors are needed to explain the focused large velocity contrast. A small fraction (~1-2%) of partial melting (Hammond & Humphreys, 2000; Mavko, 1980; Sobolev et al., 1996) can result in a large velocity contrast in a confined area. Anisotropy can also play a role in the variation of seismic velocity (W. Gao et al., 2004). However, only a weak (<1.5%) azimuthal anisotropy is suggested beneath JI without abrupt changes in the fast direction and amount of anisotropy (Huang et al., 2004; Kang & Shin, 2009; Wei et al., 2016). Chemical compositions and grain sizes of materials in the lithospheric upper mantle may affect seismic velocity (Cammarano et al., 2003; Faul & Jackson, 2005), but they are second-order effects compared to temperature in the upper mantle (Goes et al., 2000), and it is unfeasible to explain the amount of velocity perturbation solely by these factors. Therefore, it can be argued that Anomaly 1 in our

result is a high—temperature upper mantle structure potentially with partial melts (Figure 1.17).

Small—scale low—velocity perturbations at shallow depths (Anomaly 2) indicate the existence of more complex magmatic structures at lithospheric depths. JI comprises more than 300 small volcanoes (Figure 1.1b) characterized by geochemical features that favor monogenetic eruptions fed by dispersed and independent plumbing systems (Brenna et al., 2011; Koh et al., 2013; Sohn et al., 2012). The pattern with narrower low—velocity anomalies depicts magmatic paths in the lithosphere that connect the locally ponded melts at sublithospheric depth (Anomaly 1) to the dispersed volcanoes at the surface (~100 km in horizontal scale). The low—velocity structures mainly extend to the east and west of the center of JI. Small—scale volcanoes characterized by more recent basaltic eruptions populate the surface above these low—velocity zones. In addition, the shallow anomalies spatially overlap with central volcanism with a later (~25 ka) large volume of trachyte magma (Brenna et al., 2012b; Ko & Yun, 2016). Thus, it can be inferred that these anomalies represent a shallow magma plumbing structure related to volcanism with primitive basaltic and evolved magma. Reactivation of individual vents after longer time breaks (>200 ka) has been reported (Brenna et al., 2015b). The low—velocity pattern at shallow depths (<45 km in Figure 1.17) might be due to more complex magmatic structures overlapping with multiple volcanic eruptions. More scattered low—velocity features can be found at a depth of 15 km (Figure 1.17a), focused at the center, eastern, and western margins of JI. The central low—velocity portion is located beneath the shield volcano, which erupted basaltic lava and formed a trachytic dome. However, the other narrow low—velocity zones are

not directly connected to the region with clustered scoria cones (Figure 1.1b). These discrepancies are probably due to the smearing of the heterogeneous upper crustal (<10 km) magmatic structures (e.g., narrow sills and dykes) even though the effect of local near-surface structures is taken into account by the station term in inversions. Further investigations are needed to confirm the shallow magmatic structures beneath JI. Compared to a magma evolution model based on geochemical data (Brenna et al., 2012b), our results show similarities in the dispersed magma plumbing system at shallower depths (~15 km) beneath the island, but the seismic images (Figure 1.17) suggest a more focused origin of the sublithospheric magma.

Our findings of dispersed and complex magmatic structures beneath JI (Figure 1.17) are suggestive of intensive interaction between the ascending magma and the lithospheric environment (Li et al., 2018; Martí et al., 2017; Németh, 2010). Complex magmatic structures within the lithosphere are generally formed by the movement and emplacement of magmas in the lithosphere (e.g., Benz et al., 1996; Huang et al., 2015; Martí et al., 2017; Miller & Smith, 1999; Thybo & Artemieva, 2013). Such magma emplacement and movement are controlled by various factors, including local or regional stress fields and preexisting structural (e.g., fault or fracture) or rheological discontinuities (Maccaferri et al., 2010; Martí et al., 2016; Németh, 2010; Takada, 1989; Valentine & Perry, 2007). A previous petrological study on JI revealed that peridotite xenoliths metasomatized by evolved alkali basalt (Yang et al., 2012), which could promote the intensive interaction between the host magma and the lithospheric environment.

Several hypotheses have been proposed to explain the mechanism of intraplate volcanism in JI. Nakamura et al. (1990) and Tatsumi et al. (2005) suggested a possible mantle plume origin. However, the absence of mantle plume signatures, such as hot spot tracks, volcanic age progressions, topographic swells, and deep−seated thermal anomalies (Chen et al., 2017; Choi et al., 2006; Y. Kim et al., 2015; Ma et al., 2018), together with the observed nonplume trace element characteristics and relatively low geothermal gradient (Brenna et al., 2012a), makes this suggestion implausible. Decompressional melting by tectonic extension (Choi et al., 2006) or lithospheric folding (Shin et al., 2012) due to plate interactions have likewise been suggested. However, these large−scale mechanisms cannot account for the focused and isolated volcanism in JI, where neighboring volcanoes aligned to the corresponding stress regime are absent. Localized asthenospheric upwelling can be induced by sublithospheric mantle convections (West et al., 2009). Guo et al. (2018) argued that convective downwelling in the upper mantle beneath the Songliao basin triggered by upwelling beneath the Mt. Baekdu (Changbai) volcano in northeast China may have induced localized asthenospheric upwellings in regions surrounding the basin, forming localized and isolated intraplate volcanism. However, no such convective flow has been reported beneath the Korean Peninsula and Yellow Sea, which is coeval with the volcanism in JI despite the proposed tectonic proximity between northeast China and the Korean Peninsula, both being part of Sino−Korean old basement with a relatively thick lithosphere (Chough et al., 2000).

Convective mantle flows can be developed by edge−driven convection processes (Conrad et al., 2010; King & Anderson, 1998). Decompressional melting is able to be generated at locations with

lithosphere thickness gradients induced by thermal differences or dynamic processes between the relatively thick and thin lithospheres. This mechanism has been used to explain intraplate volcanism without mantle plumes in some regions (Ballmer et al., 2015a; Davies & Rawlinson, 2014; S. Kim et al., 2017; King & Ritsema, 2000; Van Wijk et al., 2010, 2008). Based on our results (Figures 1.17 and 1.19) and recently improved seismological images of the lithosphere in northeast Asia, JI is located at a transitional region of lithospheric thickness at the southern margin of the continental lithosphere beneath the Korean Peninsula and Yellow Sea. The amount of the velocity heterogeneities and the distribution of high-velocity structures (Figures 1.17 and 1.19) may indicate inherent rheological weaknesses or geometrically non-uniform structures along the margin of the thicker lithosphere, which may have been formed during previous extensional events (Chough et al., 2000; Chough & Sohn, 2010). It has been reported that the preexisting structural complexity in the lithosphere controls melt focusing (Davies & Rawlinson, 2014; Davies et al., 2015; Hoke & Lamb, 2007). Hence, it can be inferred that decompressional melting induced by convective flows at the lithosphere thickness transition could be a possible mechanism of volcanism in JI. To confirm this, further investigation (e.g., geodynamic simulation) is required to demonstrate whether the lithospheric thickness gradient at the continental margin of the Korean Peninsula is sufficient for thermal instability (e.g., Kaislaniemi & Van Hunen, 2014; Missenard & Cadoux, 2012) in the region with low asthenospheric shear (Conrad et al., 2011; King, 2011). Horizontally and vertically driven mantle flows by a subducting slab could play a role in promoting such decompressional melting at the edge of the continental lithosphere. A subducting slab

can trigger 3-D upper mantle flows (Motoki & Ballmer, 2015; Piromallo et al., 2006; Schellart, 2004) and focused upwelling away from the slab (Faccenna et al., 2010). In addition, it has been suggested that the stagnant Pacific slab beneath East Asia induces large-scale convective flows due to deep dehydration (Kameyama & Nishioka, 2012; Richard & Iwamori, 2010; Zhang et al., 2014), which may result in intraplate volcanism (Sakuyama et al., 2013; Wang et al., 2015; Zhao et al., 2009). Furthermore, horizontally induced shear or transported melts are possible based on the extension of the back-arc low-velocity bodies in the Okinawa trough and the Sea of Japan (East Sea) to the continental margin around the Korean Peninsula (S. Kim et al., 2016; Zheng et al., 2011). Such a mechanism has been proposed in back-arc settings (e.g., Brenna et al., 2015a; Currie et al., 2008; Wei et al., 2015).
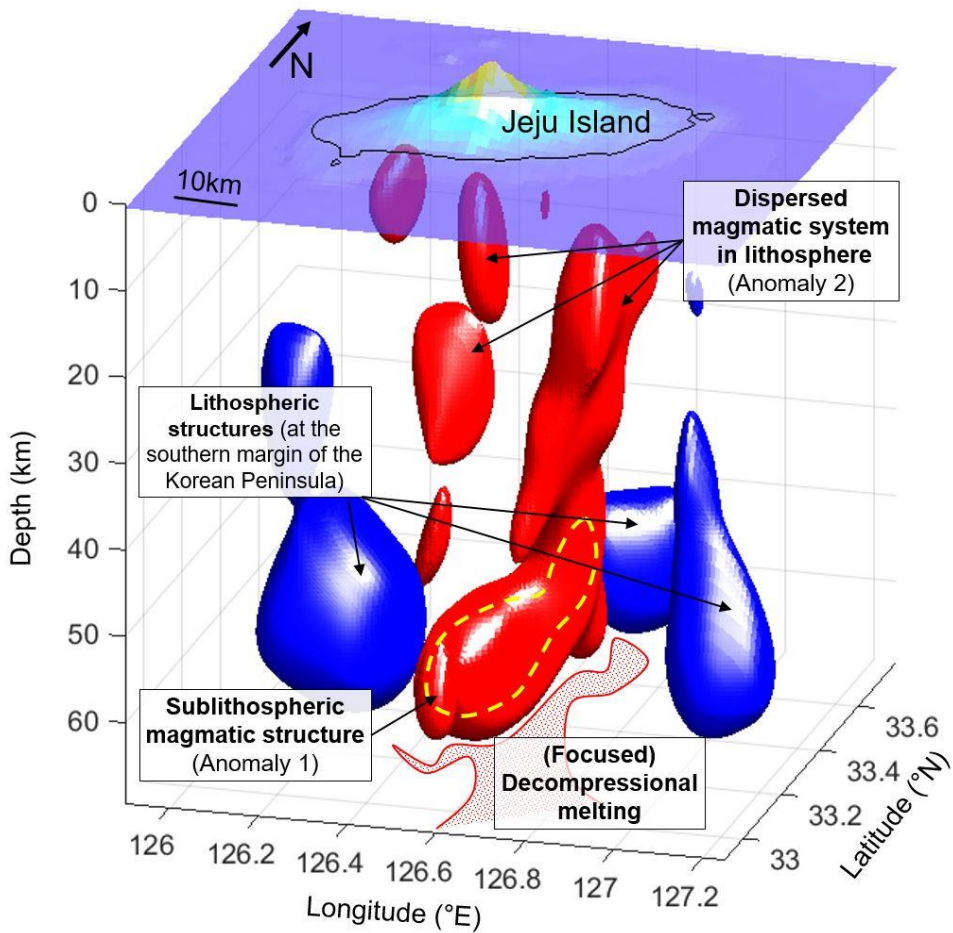
Figure 1.19 A three-dimensional image of P wave tomography results with the interpreted main features. Structures in red and blue denote -1 and $+0.5\%$ velocity isosurfaces, respectively. Yellow dashed line marks the -1.5% velocity isosurface at greater depths (50–60 km). Surface topography is vertically exaggerated by five times.

1.4. Conclusions

We constrain 3-D seismic velocity structure lithosphere beneath JI. We deployed a dense seismic array consisting of 20 temporary stations and three permanent stations for over 2 years, recording high-quality continuous seismic waveforms. Based on these data, we apply teleseismic traveltime tomography. The adaptive stacking technique is used to precisely measure the relative arrival time residuals of P and S waves. For data inversion and retrieval of velocity structures, we use the fast marching tomography method. The model identifies a prominent low-velocity anomaly under the summit of the island at greater depths (50–60 km), which separates into narrower low-velocity zones at shallower depths (10–45 km). Moreover, we observe velocity changes from lower velocities beneath the center of the island and southern part of the model space to higher velocities to the north, east, and west at a greater depth (~55 km). Through a series of synthetic recovery tests with checkerboard and specific anomaly patterns, we confirm that the observed velocity anomalies and patterns are robust and reliable. Based on previous geological observations, we interpret the significant low-velocity anomaly (>3.7% reduction in P wave velocity compared to surrounding high-velocity structures) beneath the central part of JI at a depth of ~55 km as a sublithospheric high-temperature upper mantle structure potentially with partial melts. The low-velocity anomalies become separated and extend toward the east and west of the island as depth decreases. The structure represents a dispersed magmatic system corresponding to the surface features of volcanism. On the other hand, the high-velocity structures to the north, east, and west of the island are interpreted

as relatively thick lithospheric structures extending from the southern margin of the lithosphere beneath the Korean Peninsula structure, considering its consistency with a previously observed velocity transition around the island and the magnitude of velocity contrasts in previous tomographic studies. In summary, we suggest that focused decompressional melting at sublithospheric depths formed at the transition of lithospheric thickness beneath the island, and the intensive interaction between the ascending magma and lithosphere resulted in complex and dispersed intraplate volcanic system in JI.

Chapter 2. Heterogeneous Modification and Reactivation of a Craton Margin Beneath the Korean Peninsula by Teleseismic Traveltime Tomography

2.1. Introduction

Craton lithosphere, which comprises the core of continents, is composed of a strong resistance against thermo−chemical erosion since its formation (>2.5 Ga). The longevity of it arises from its thick and iron−depleted mantle keel, and strong crust (Lee et al., 2011). However, persistent and multiple episodes of tectonic events at continental margins make craton margin prone to ongoing modification processes. Constraints on the properties of the continental lithosphere indicate that marginal tectonic processes play an important role in altering entire cratonic structures (Artemieva, 2006; Boyce et al., 2019; Thomas, 2006). Previous studies have suggested interactions with slab subduction, collision, mantle dynamics, and effects due to deeper structures to explain tectonic processes at margins (e.g., Hu et al., 2018; Levander et al., 2014; Moresi et al., 2014; Schmandt & Lin, 2014). Modification of the cratonic lithosphere is a salient process by which we can understand the evolution and destruction of old continents (Artemieva & Mooney, 2002; Foley, 2008). However, unraveling the detailed modification process of their margins is often difficult (e.g., Rawlinson et al., 2014; Savage et al., 2017) since multiple episodes of tectonic events overlap each other and blur the resulting features.

The continental lithosphere in the eastern Eurasian plate margin comprises several cratonic blocks (e.g., the North China Craton (NCC), South China Craton (SCC), and Siberian Craton). The region

has experienced multiple tectonic events, including continental collisions and accretions, the subduction of various oceanic plates (e.g., Paleo−Asian, Paleo−Tethys, Mongol−Okhotsk, Izanagi, and Pacific slab), and subsequent back−arc extension and rifting (e.g., East Sea or Sea of Japan, Yellow Sea, and East and South China Sea) (Kusky et al., 2014; Otofuji et al., 1985; Tang et al., 2018). Extensive reworking and destruction of the cratonic lithosphere mainly occurred in eastern China (S. Gao et al., 2004; Menzies et al., 1993) based on the detection of lossing significant portion of its deep root (from >180 km to <100 km) during the Mesozoic and Cenozoic (e.g., Chen, 2010; Huang et al., 2009). Widespread Mesozoic to Cenozoic magmatism indicates entirely non−cratonic geochemical and geophysical signatures (Choi et al., 2006; Kimura et al., 2018), accompanied by ubiquitous extensional basins (Figure 2.1) (Chough et al., 2018; Liu et al., 2017; Ren et al., 2002). Due to the complex structure, previous studies have suggested numerous different modes of lithosphere modification for the cratons in China (e.g., Griffin et al., 1998; Guo et al., 2016a; Wu et al., 2019; Zhang, 2005).

The Korean Peninsula composes the Archean–Proterozoic continental lithosphere located in the eastern Eurasian plate margin (Chough et al., 2000). Previous studies have suggested the presence of tectonic affinities in the cratonic lithosphere modification process between China and the Korean Peninsula (Cho et al., 2017; Choi, 2019; Oh et al., 2019). The basement of the Korean Peninsula consists of late Archean to early Proterozoic massifs: from north to south, the Nangrim (NM), Gyeonggi (GM), and Yeongnam (YM) (Figure 2.2a) (Chough et al., 2000; Cho et al., 2008). As in China, each of the massifs in the Korean Peninsula were subject to different tectonic processes during amalgamations and breakups of

supercontinents (Columbia, Rodinia, Gondwana, and Pangea) before the formation of the current setting since the late Paleozoic to early Triassic (S.W. Kim et al., 2014, 2018, 2019; Lee et al., 2019; Oh et al., 2019). Two fold−and−thrust belts, i.e., the Paleozoic Imjingang belt (IB) and late Precambrian−Paleozoic Okcheon belt (OB), separate the GM from the NM and YM, indicating collisional and accretional processes during their formation. Extensive Mesozoic− to−early Cenozoic plutonic emplacements followed in a post− collisional and subduction tectonic setting (S.W. Kim et al., 2011, 2017). Subsequent oblique subduction and rollback of the oceanic plates affected the Precambrian lithosphere from eastern China to the YM, forming the Gyeongsang arc−back−arc basin (GB) at the south− eastern margin of the YM and rifted structures in the East Sea to the east of the Korean Peninsula, respectively (Chough & Sohn, 2010; Ren et al., 2002). Spatially non−uniform and complex tectonic structures indicate that the cratonic lithosphere in the Korean Peninsula has been exposed to intense, complicated modification processes at the forefront of the continental margin during the Phanerozoic period (Chough et al., 2000). However, due to lack of information on the detailed structure of the continental margins owing to reduced sampling in the region, effects by current dynamics in the upper mantle and nearby subducting slabs on the craton margin lithosphere have not been examined in detail.

The Korean Peninsula has been an intensive research area providing important geological evidence on the marginal tectonism of the eastern Eurasian plate. Similarities between the Archean and Paleoproterozoic geological features of the Korean Peninsula and that of China suggest possible connection between the North or South China Blocks and the Precambrian basement of the Korean Peninsula.

However, consensus has not been reached yet on the geological affinities between different tectonic units in the Korean Peninsula and those of eastern China. Debates were on the detailed process of the assembly of the Korean Peninsula and whether the collisional boundary between the two cratons in China formed in Late Paleozoic to early Triassic extends to the Korean Peninsula. Several tectonic models have been proposed: Indented wedge model (Choi et al., 2019; Chough et al., 2000) (Figure 2.3a), collisional belt model (Oh et al., 2019) (Figure 2.3b), Korean collisional orogen model (Kwon et al., 2009; S.W. Kim et al., 2011) (Figure 2.3c), Gyeonggi marginal belt model (Cho et al., 2017) (Figure 2.3d), and crustal detachment model (Chang & Zhao, 2012; Zhai et al., 2007) (Figure 2.3e).

We conduct high-resolution seismic tomography of the upper mantle beneath the southern Korean Peninsula (SKP) to understand the detailed structure and tectonic evolution of a craton margin. Detailed 3-D upper mantle P and S wave velocity variations are estimated for the first time using data from dense seismic arrays throughout the SKP with a recording time of more than 5 years. Unlike previous large-scale tomography studies in East Asia (e.g., Chen et al., 2017; Ma et al., 2018), we report velocity models based entirely on teleseismic relative arrival time data from the local seismic arrays (Aki et al., 1977; Thurber, 2003) to estimate local velocity heterogeneities in greater detail by measuring small traveltime differences caused by an area of interest. Together with a set of resolution tests, we suggest that marginal tectonic processes played a significant role in breaking up the continental lithosphere.
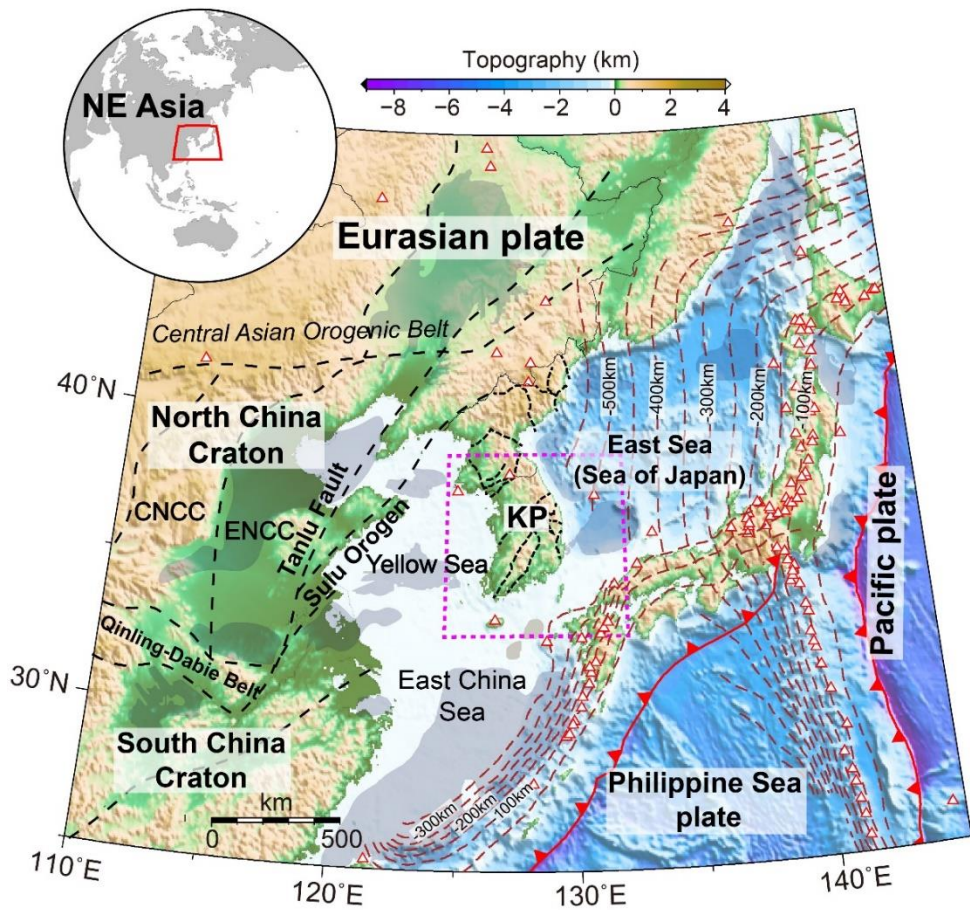
Figure 2.1 Regional tectonic map of northeast Asia. Major tectonic provinces are indicated by black dashed lines. Convergent plate boundaries are shown with red saw-toothed lines (Bird, 2003). Depths of the subducting oceanic slabs are indicated by brown dashed contours at 100-km intervals based on the Slab2 model (Hayes et al., 2018). Cretaceous and Cenozoic extensional basins are shaded in gray (Ren et al., 2002). Volcanoes are indicated by red triangles. A pink dashed rectangular box shows the map boundary of Fig. 2.2. CNCC: central North China Craton; ENCC: eastern North China Craton; KP: Korean Peninsula.
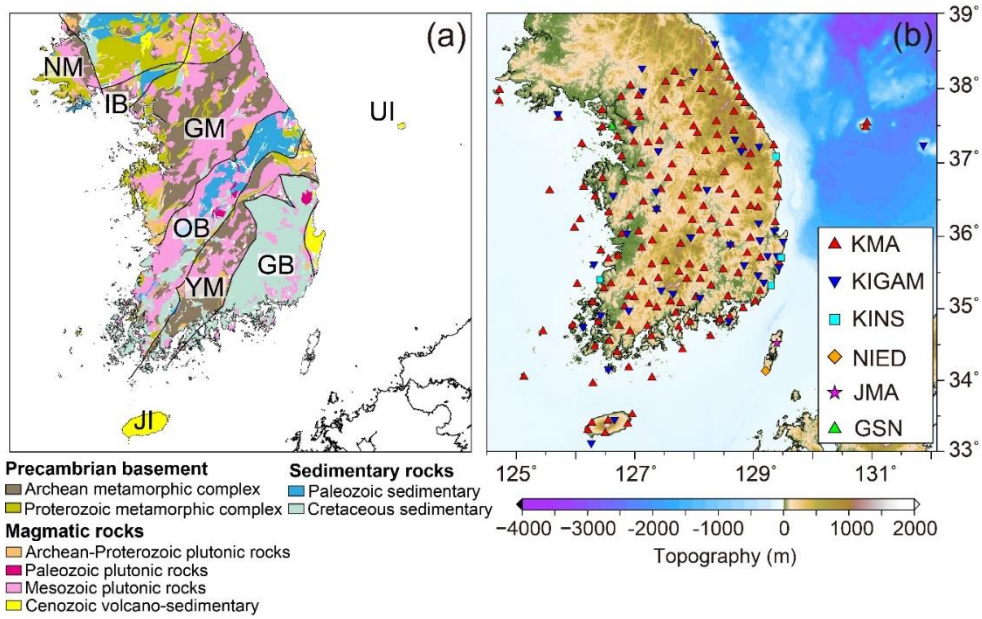
Figure 2.2 (a) Map showing the geology of the Korean Peninsula (Chwae et al., 1995). Black solid lines indicate the boundaries of the different geologic provinces. GB: Gyeongsang Basin; GM: Gyeonggi Massif; IB: Imjingang Belt; JI: Jeju volcanic Island; NM: NangrimMassif; OB: Okcheon Belt; UI: Ulleung volcanic Island; YM: Yeongnam Massif. (b) Seismic stations used in this study. Stations from different networks are shown by different colors and symbols. KMA: Korea Meteorological Administration; KIGAM: Korea Institute of Geoscience and Mineral Resources; KINS: Korea Institute of Nuclear Safety; JMA: Japan Meteorological Agency; NIED: National Research Institute for Earth Science and Disaster Resilience; GSN: Global Seismic Network.
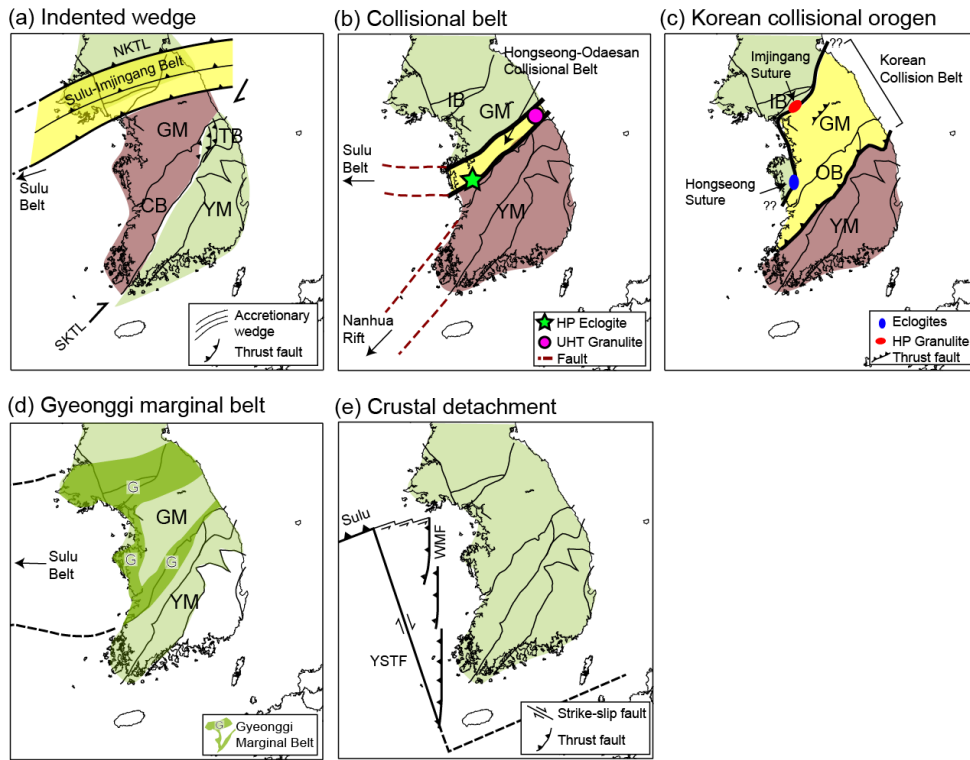
Figure 2.3 Tectonic models proposed for the formation of the Korean Peninsula during the Late Permian–Early Triassic. (a) Indented wedge model (Choi et al., 2019; Chough et al., 2000). (b) Collisional belt model (Oh et al., 2019). (c) Korean collisional orogen model (Kwon et al., 2009; S.W. Kim et al., 2011). (d) Gyeonggi marginal belt model (Cho et al., 2017). (e) Crustal detachment model (Chang & Zhao, 2012; Zhai et al., 2007). Green and brown regions in tectonic models are the areas suggested to be part of North and South China Blocks (NCB and SCB), respectively. Yellow regions indicate areas that are suggested to be extended from the collisional boundary between the NCB and SCB. GM: Gyeonggi massif, IB: Imjingang belt, OB: Okcheon belt, YM: Yeongnam massif.

2.2. Methods

2.2.1. Data Acquisition and Processing

We collect seismic data recorded by permanent seismic stations deployed in and around the SKP (Figure 2.2b), consisting of a total of 254 broadband, short-period, and accelerometer sensors. We select 1388 events between 2013 and 2018 with magnitudes greater than mb 5.4 at epicentral distances from 30 to 95° from the International Seismological Catalogue, identifying P and S waves from the vertical and tangential component data, respectively. The waveform data are corrected for corresponding instrument responses and filtered with frequency bands from 0.1–5.0 Hz for P waves and 0.1–1.0 Hz for S waves. Interstation coherency in the P and S wave waveforms is used to measure the high-quality relative arrival time residuals (Rawlinson & Kennett, 2004). To incorporate waveform data from different instrumental settings and obtain more detailed results, we scrutinize the ranges of frequency bands for P and S waves by testing different passbands. With these frequency ranges, the highest degree of waveform coherence is achieved while maintaining similar levels of signal-to-noise ratios among different types of instruments (Figure 2.4). All teleseismic waveforms are visually inspected and noisy or incoherent data are eliminated to obtain more reliable measurements. Figure 2.5 shows examples of P and S phases recorded by the local arrays. The waveforms of the processed data are similar in shape, which allowed us to measure the relative residuals with high precision. For the example data, the measured relative traveltime residuals generally show positive (delayed) values at stations in the north and eastern margins of the SKP, and negative (preceded) values in the southwest (Figure 2.6).

Our final dataset comprises 96,273 rays from 684 events for P waves and 35,418 rays from 274 events for S waves (Figure 2.7). The average cross−correlation coefficient of our dataset is 0.92 for P waves and 0.83 for S waves.

We determine the uncertainty in the traveltime residuals based on waveform similarity (Rawlinson & Kennett, 2004; see section 1.2.3 for the detailed description). The estimated uncertainties are used as data weights in the tomographic inversion. The absolute uncertainties of each residual are measured by synthetic recovery test, which applies random time perturbations for the aligned traces using a Gaussian distribution with a standard deviation of 0.9 s for P waves and 1.7 s for S waves, measuring RMS differences between the imposed shifts and their recoveries based on the same stacking process. We repeat the test for 50 times to obtain the average RMS uncertainty value for each event dataset. The average uncertainties in the total residual traveltime observations (Rawlinson et al., 2006b; Song et al., 2018) are 78 ms for P waves and 149 ms for S waves. We also test different random time perturbations to measure the residual uncertainty but the comparison of the uncertainties among the different event datasets are consistent.
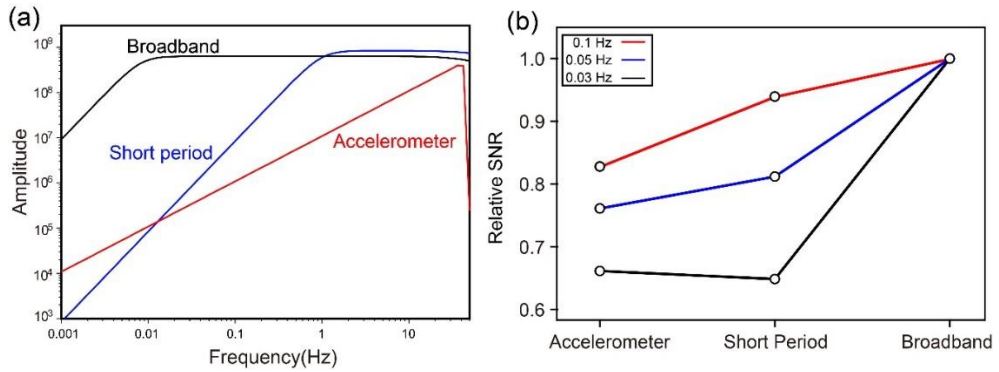
Figure 2.4 (a) Instrument response plots for the broadband (black), short period (SS−1) (blue), and accelerometer (ES−T) (red) sensors. (b) The relative signal−to−noise ratio between different instruments with different long−period cut−off frequency limits that are applied to the teleseismic S wave data (0.03, 0.05, and 0.1 Hz).
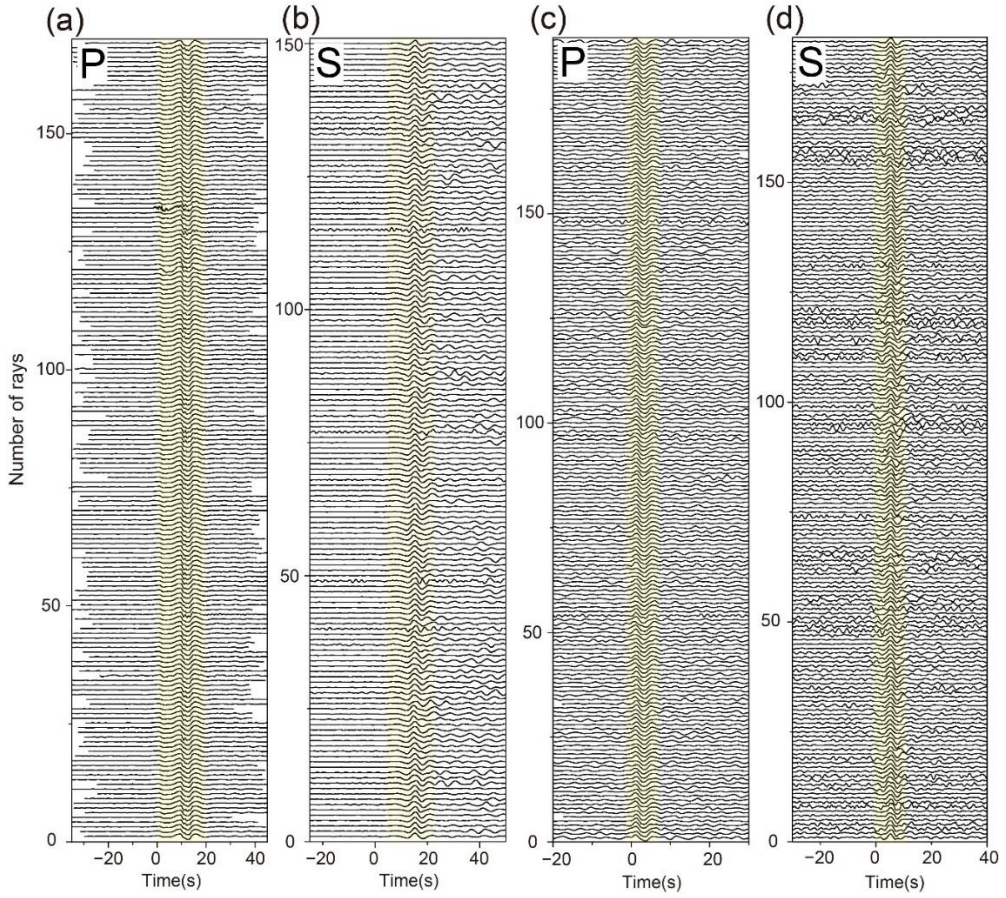
Figure 2.5 Examples of stacked *P* and *S* wave waveforms analyzed in this study. (a,b) Waveforms of the event that occurred S of Ndoi Island, Fiji (Mw = 6.9). (c,d) Waveforms of the event that occurred NNE of Kerman, Iran (Mw = 6.0). The time windows applied for waveform stacking are indicated with yellow shading. The locations of the events are indicated in Figure 2.7.
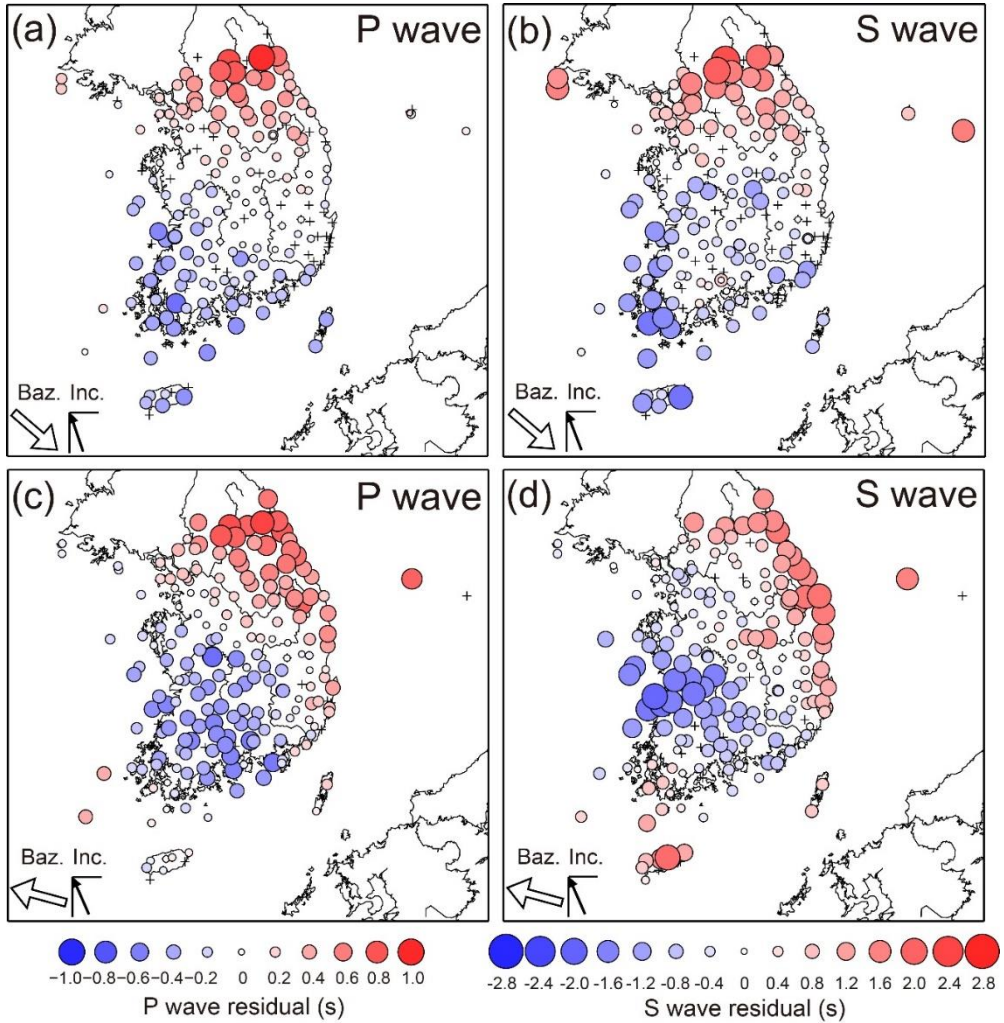
Figure 2.6 Relative arrival time residuals for P and S waves estimated using the waveforms shown in Figure 2.5. The event back－azimuth (Baz.) and incidence angle of the incoming rays (Inc.) are shown by the white and black arrows on the bottom left of each panel, respectively. Stations without arrival time measurements are indicated with a cross.
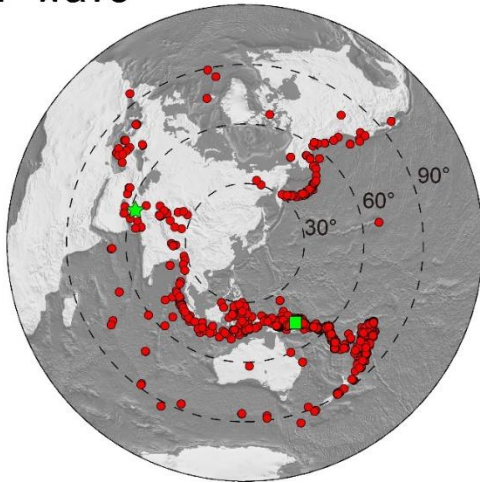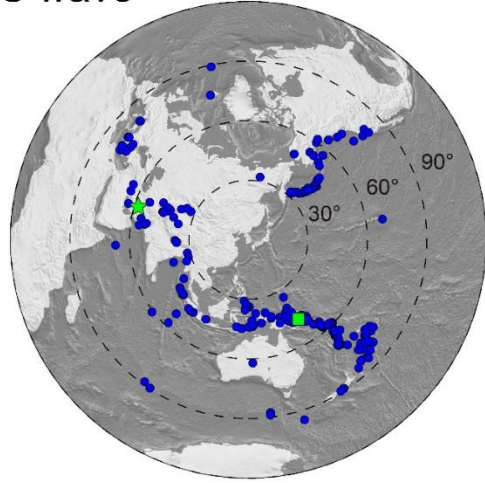
Figure 2.7 Distribution of teleseismic events used for P (red dots on the left diagram) and S (blue dots on the right diagram) wave tomography. Dashed black circles are plotted at 30° increments from the center of the SKP. Green stars and squares in each panel represent event locations of the example data from Figures 2.5a,b and Figures 2.5c,d respectively.

2.2.2. Tomographic Methods

2.2.2.1. Model Parameterization and Regularization

Fast marching ray-tracing (Rawlinson et al., 2006a) and the subspace inversion scheme (Kennett et al., 1988) are iteratively applied to perform tomography. We define a model space spanning a depth of ~800 km with a uniform grid spacing of ~10 km in the crust and ~20 km in the mantle. Regularization factors (damping (ε) and smoothing (η)) for the model are systematically determined by evaluating the trade-offs between the data misfit, model smoothness, and model variance (Rawlinson et al., 2006b) (Figure 2.8). Data misfit for the inversion is determined based on the difference between the observed and predicted traveltimes starting from an initial model, which consisted of a 3-D crustal model over the mantle portion with the ak135 reference model (Kennett et al., 1995). We simultaneously invert the model for crustal and upper mantle structures with fixed Moho depths to account for crustal effects. Instead of using local crustal models in the SKP, a global crustal model (Crust1.0; Laske et al., 2013) is adopted to cover regions beneath not only the SKP but also its margins and off-coasts. Further tests are conducted for different configurations of the crustal structure using a 1-D initial model (S. Kim et al., 2011) and a 3-D local crustal structure (Rhie et al., 2016) with Moho interfaces (Chang & Baag, 2007; Y. Kim et al., 2015) (Figures 2.9). We find that patterns and amplitudes of upper mantle structures deeper than 60 km are consistent and robust for different crustal settings (Figures 2.10 and 2.11), such that determining those depths is the primary focus of our interpretations.
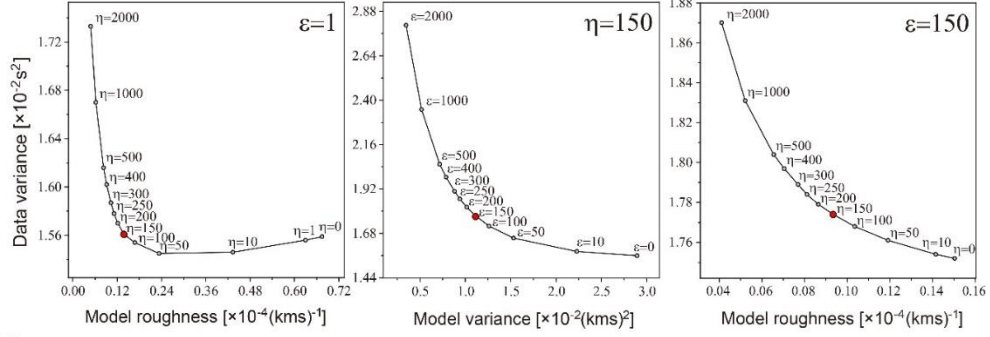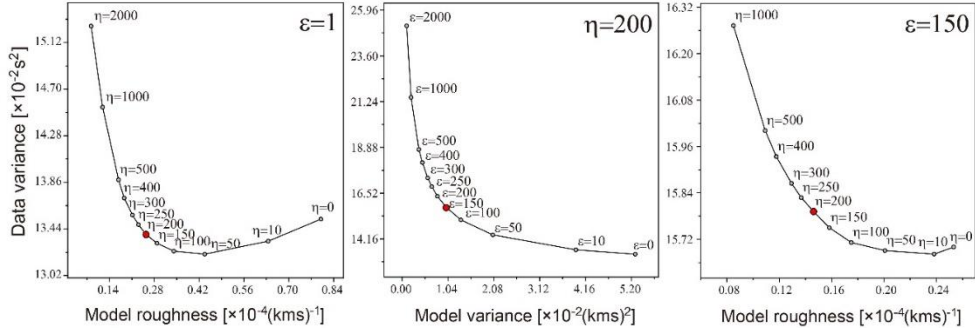
Figure 2.8 Determination of regularization factors (damping (ε) and smoothing (η)) for P (top) and S (bottom) wave tomography based on trade-off analyses (Rawlinson et al., 2006b). (Panels on the left) The optimum value of η is determined based on the trade-off between model roughness and data variance measured by changing the η while holding ε at 1. (Panels in the middle) The optimum value of ε is subsequently determined in a similar manner to the first step, changing ε and holding η at the value determined in the previous stage. (Panels on the right) The final values of η are determined based on the relationship between model roughness and data variance, changing η while holding ε at the value determined in the previous step. Selected ε and η values in each step are indicated by red circles in each panel.
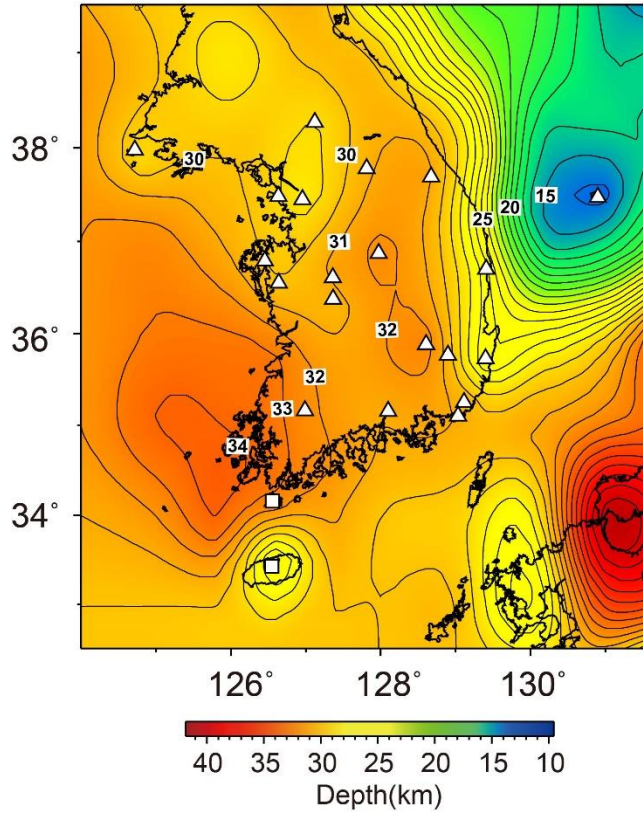
Figure 2.9 Moho depths of the SKP used for tomography. Black solid curves indicate the Moho depth contours in km below sea level at 1−km intervals. White triangles and squares are the sampled sites of Chang and Baag (2007) and Y. Kim et al. (2015), respectively.
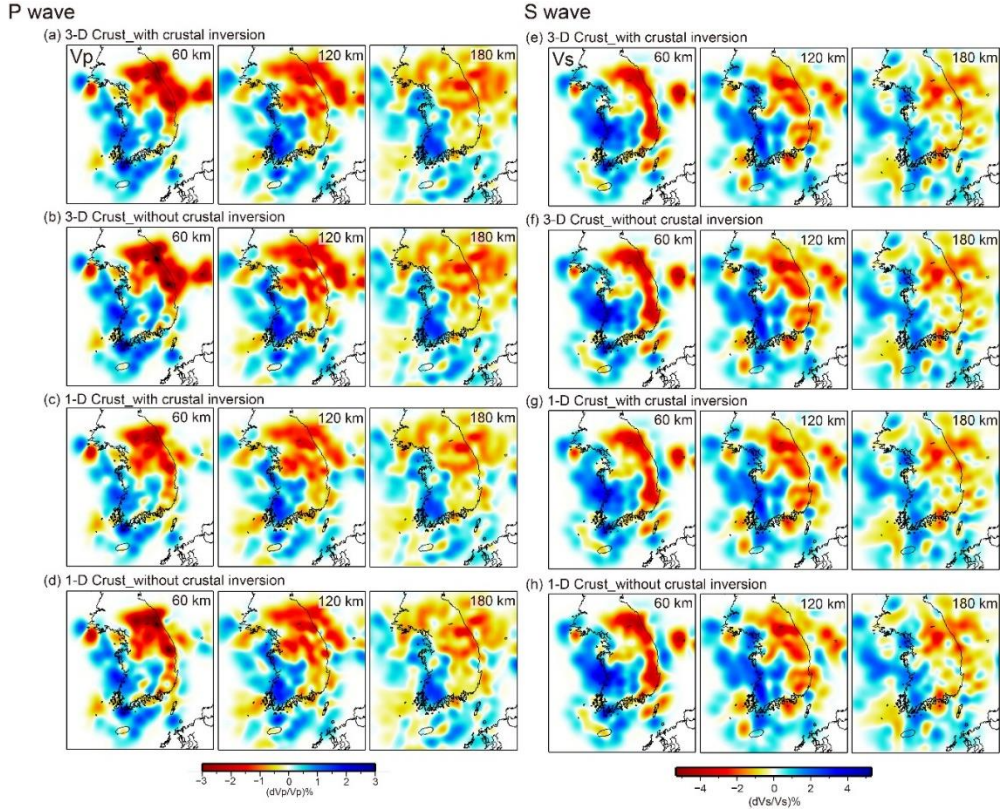
Figure 2.10 Comparisons of the tomographic results with different crustal structure settings. (a–d) The results for *P* wave tomography. Inversion results with (a,b) 3–D crust (Crust1.0; Laske et al., 2013) and (c,d) 1–D crust (S. Kim et al., 2011) are shown. For each crustal model, we compare the results by inverting both the crustal and mantle domain (a,c) and inverting only the mantle domain while fixing the crust (b,d). (e–f) Identical to (a–d) but for *S* wave tomography.
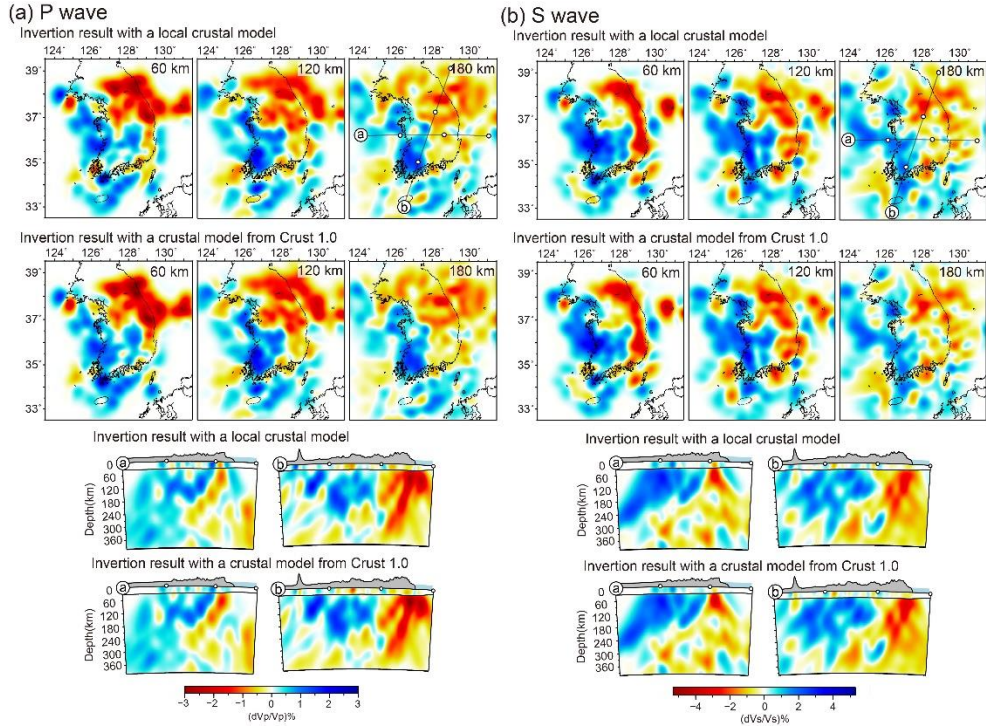
Figure 2.11 (a) A comparison of the inversion results with different initial crustal models (a local crustal model and Crust1.0) for P wave tomography. (b) A comparison of the inversion results with different initial crustal models (a local crustal model and Crust1.0) for S wave tomography.

2.2.2.2. Assessment and Minimization of Effects from Deeper Upper Mantle Heterogeneity

Our tomographic method assumes that velocity heterogeneities outside the model space is less significant owing to similar ray trajectories of teleseismic signals recorded at local arrays (Aki et al., 1977). However, in the case of strong velocity perturbations at relatively less-constrained bottom depths, amplitudes and patterns of the estimated residuals are contaminated, which leads to biases in shallow anomalies (e.g., Zhao et al., 2013). In our study area, regional tomography at depths of 400-800 km suggested velocity perturbations of up to 5% in the Vp and 7% in the Vs, mainly due to the stagnant Pacific slab in the mantle transition zone (Li & Van Der Hilst, 2010; Tao et al., 2018). We test and minimize the impacts that the deeper anomalies had on our results. We first calculate synthetic residuals from a recent 3-D upper mantle velocity model for deeper depths (Tao et al., 2018) (Figures 2.12a and 2.12b) and compare them with our observations. As a result, a long-period pattern of similarity is observed as a function of the back-azimuth between the observed and synthetic residuals (Figures 2.12c and 2.12d), confirming that this pattern originates from deeper upper mantle structures. However, this effect cause only a small decrease in amplitude (dlnVp < 0.3% and dlnVs < 0.5%) in our images for shallower areas (< 300 km) based on an additional inversion with a corrected dataset generated by subtracting the synthetic data from the observations (Figure 2.13). As a conservative choice, we determine the results by inversion with the corrected dataset as our final model.
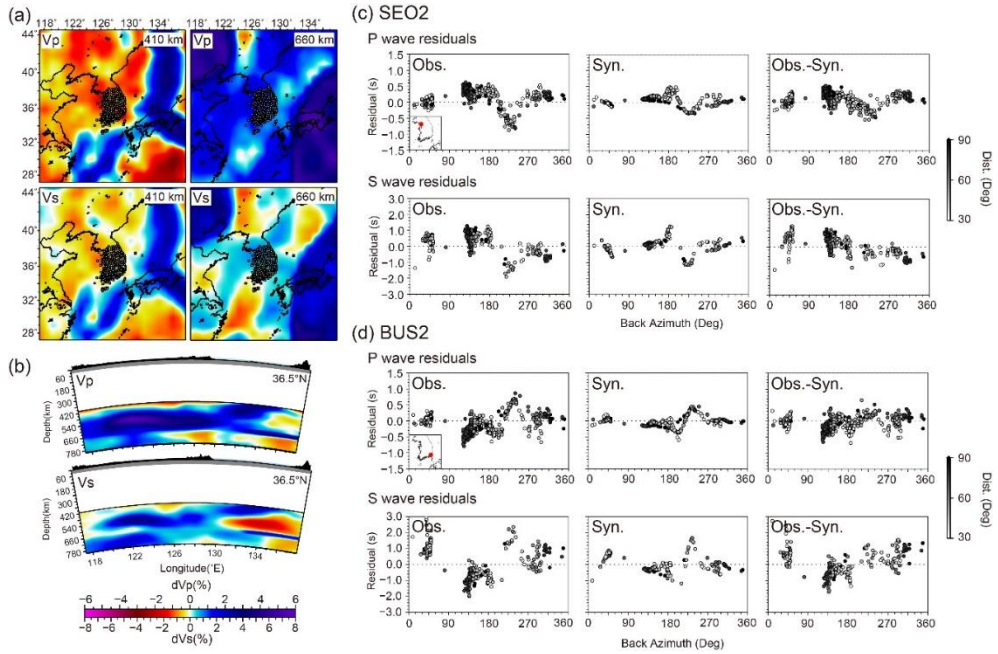
Figure 2.12 (a,b) 3−D mantle velocity model (Tao et al., 2018) used to calculate the synthetic residuals. The velocity perturbations are shown with respect to the reference velocity model (ak135; Kennett et al., 1995). (a) Horizontal profiles of *P* (Vp) and *S* (Vs) wave velocities at depths of 410 and 660 km. (b) Vertical profiles at a latitude of 36.5°N. (c,d) Examples of the *P* and *S* wave residual plots for stations (c) SEO2 and (d) BUS2 as a function of the back−azimuth. The locations of each station are indicated in the insetmaps of the panels, i.e., the observed *P* wave residuals. The residuals are shown in grayscale on the right based on their epicentral distances. Obs.: observed residual; Syn.: synthetic residual; Obs.−Syn.: observed residuals subtracted by the synthetic residuals.

8 5

(a) P wave

Result 1. Model inverted with the original data
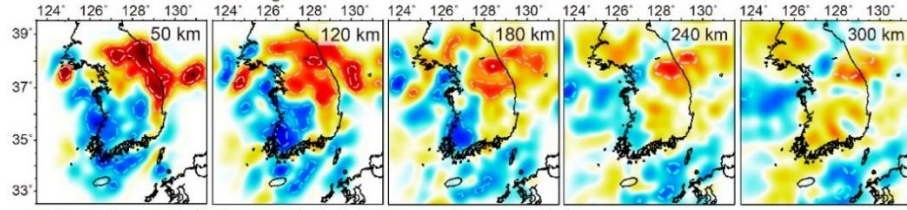
Result 2. Model inverted with the corrected data (observation - synthetic)
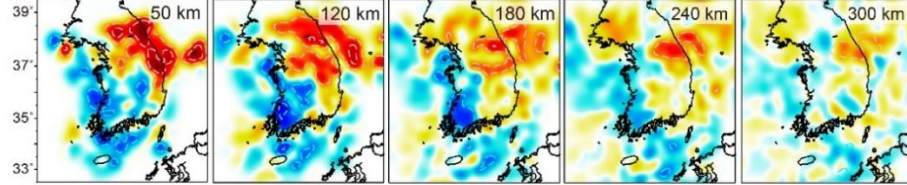
Difference (Result 2 - Result 1)

(b) S wave

Result 1. Model inverted with the original data
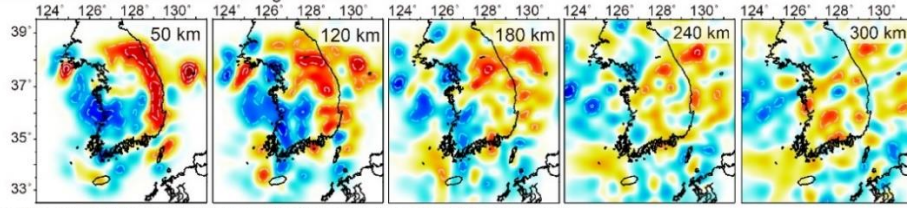
Result 2. Model inverted with the corrected data (observation - synthetic)

Difference (Result 2-Result 1)

(dVp/Vp)%
−4 −3 −2 −1 0 1 2 3 4
−6 −4 −2 0 2 4 6
(dVs/Vs)%
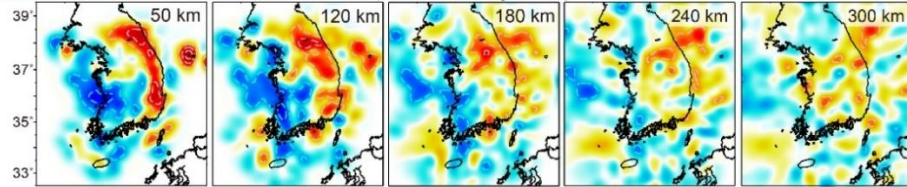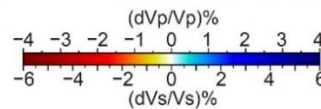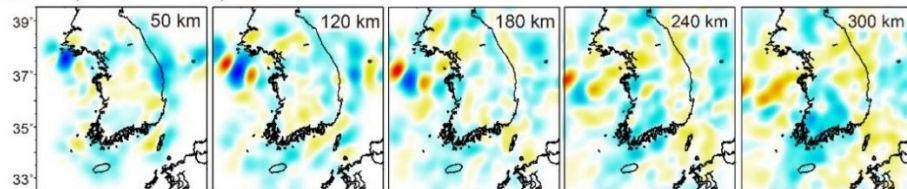
Figure 2.13 A comparison of the results inverted with the original data and data corrected by the synthetic residuals (Figure 2.12). (a) Depth profiles of P wave tomography. The model inverted with the

original dataset is shown in the first row (Result 1), the model inverted with the corrected dataset is shown in the second row (Result 2), and the difference between Results 1 and 2 are shown at the bottom. (b) A comparison of the results for the S wave tomography.

2.2.2.3. Resolution Tests

The resolution of the velocity model is meticulously assessed by performing multiple synthetic recovery tests. All synthetic data are generated using an identical source−receiver combination as the actual data with Gaussian random noise, whose standard deviation is equivalent to the estimated residual uncertainties. We first conduct conventional checkerboard tests using various scales (with diameters of 45, 60, 90, and 120 km) of high− and low−velocity anomalies: ±4% for Vp and ± 7% for Vs. The output models show good resolution, particularly beneath the SKP, and are able to resolve structures at 60 and 120 km checkers down to depths of 200 and 360 km, respectively (Figures 2.14 and 2.15). Second, a spike test is performed using discrete short−wavelength anomalies to better verify the effects due to smearing (Rawlinson et al., 2006b). We use spikes with a diameter of 60 km and maximum amplitudes of ±5% for Vp and ±8% for Vs (Figures 2.16a and 2.16c) distributed in discrete positions with different polarities. Input anomalies are generally well−identified, preserving their original polarities and locations without significant merging. Last, we test the resolution with realistic structural input models, which applied simplified block anomalies to evaluate the vertical resolutions of the interfaces (e.g., Youssof et al., 2015). The input models consisted of a positive anomaly (dlnVp of +1.5% and dlnVs of +2.0%) in the southwest and a negative anomaly (dlnVp of −2.5% and dlnVs of −3.5%) in the north and along the eastern areas of the SKP (Figures 2.16b and 2.16d) for two different thicknesses of 90 and 150 km. The original shape of the input structures is well−recovered with a velocity contrast of up to 65%. We interpret the resulting velocity anomalies

in the following section for the areas showing robust and reliable recovery in the resolution tests.
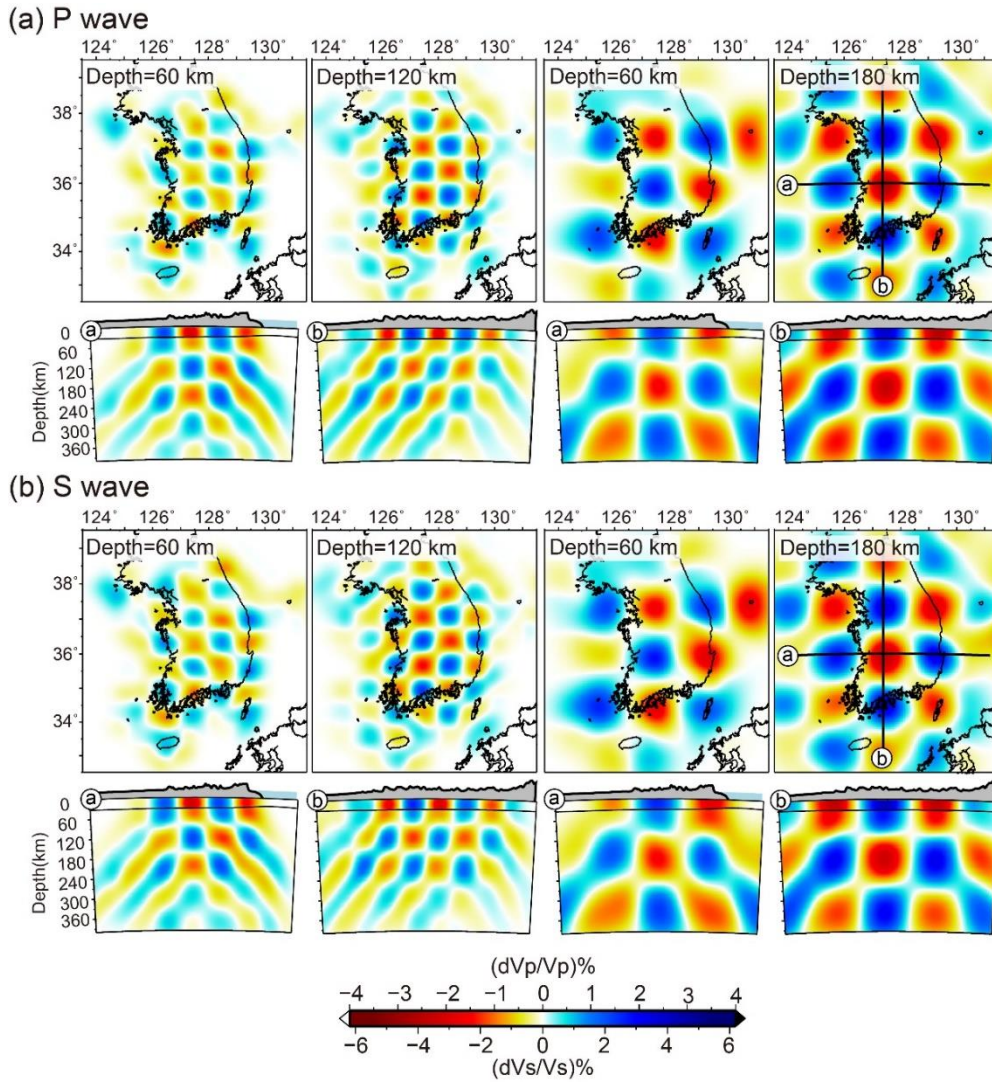
Figure 2.14 Checkerboard test results for (a) *P* and (b) *S* wave tomography. Checkers with diameters of 60 and 120 km and amplitudes of ±4% for Vp and ±7% for Vs are shown.

9 1
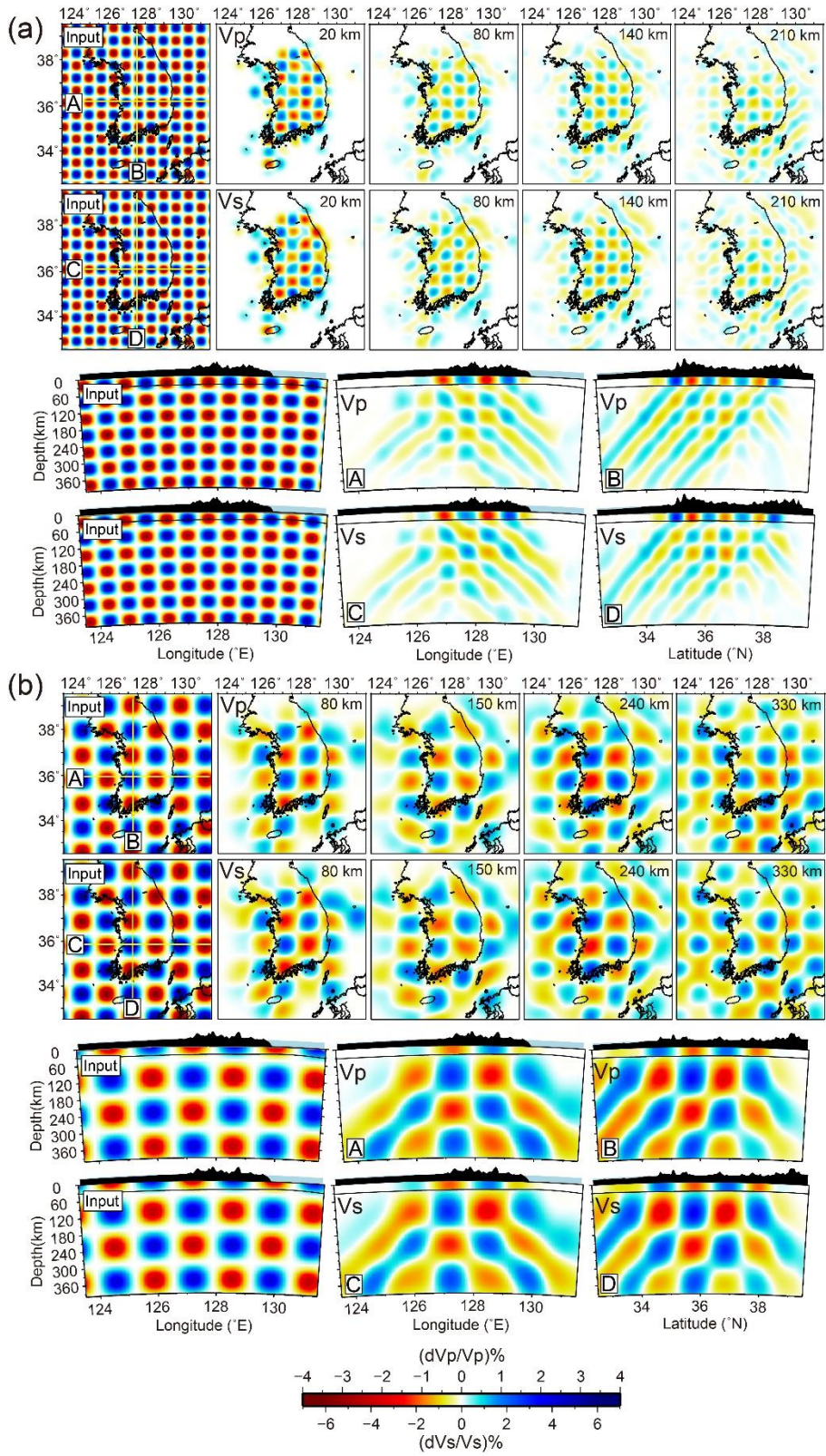
Figure 2.15 Checkerboard test results with diameters of (a) 45 km and (b) 90 km for P (Vp) and S (Vs) wave tomography. Input anomalies have velocity perturbations of $\pm 4\%$ for Vp and $\pm 7\%$ for Vs.

9 3
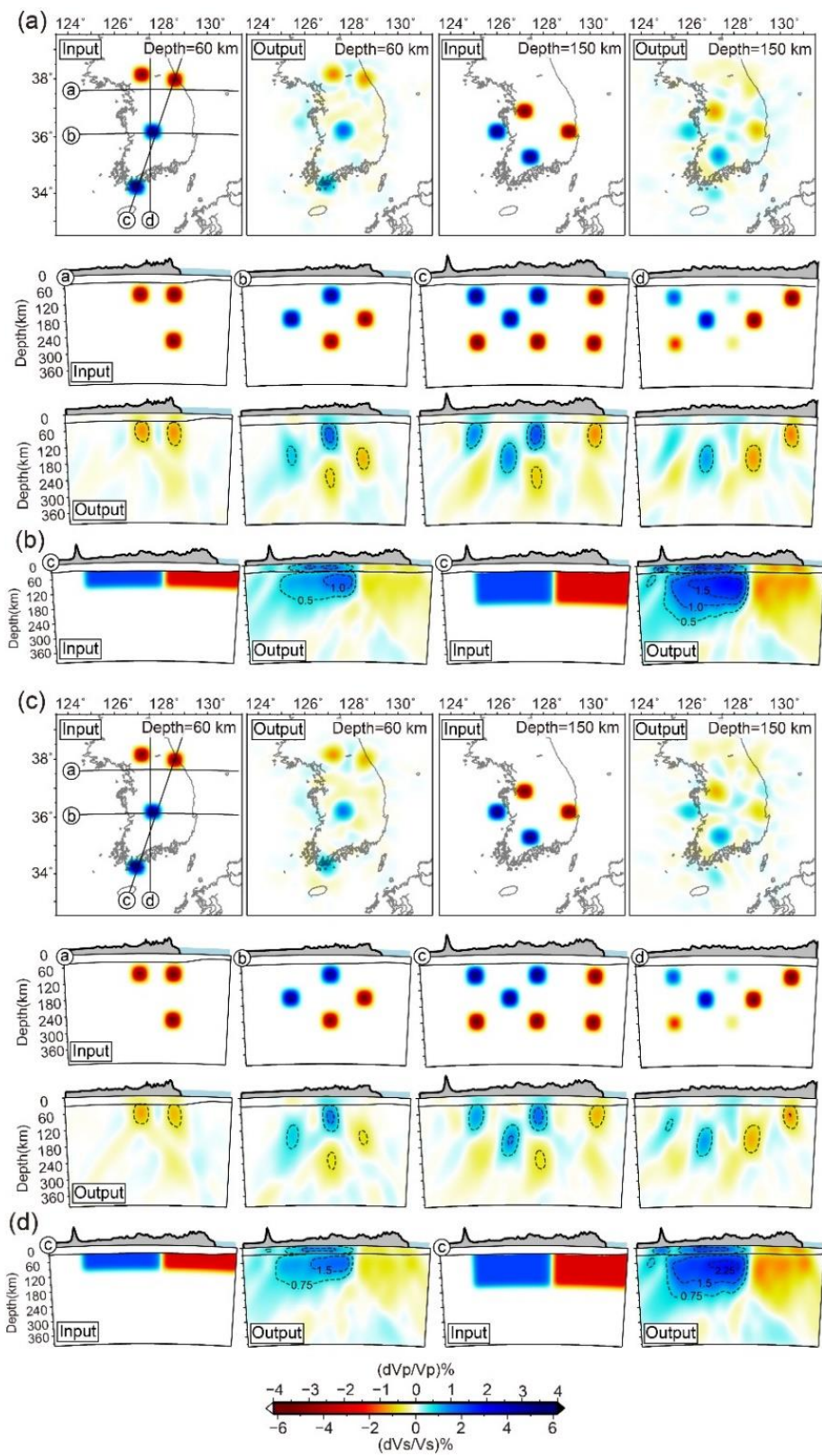
Figure 2.16 Resolution test results using spikes and structural anomalies. (a) Spike test for P wave tomography using anomalies with a diameter of 60 km and amplitudes of $\pm 5\%$. (b) Structural tests for P wave tomography using high- and low-velocity blocks with amplitudes of $+1.5\%$ and -2.0%, respectively, with thicknesses of 90 and 150 km. (c,d) Identical to (a,b) but for S wave tomography. Black dashed lines in (a,c) represent $\pm 0.5\%$ and $\pm 0.75\%$ velocity contours for P and S wave tomography, respectively. Black dashed lines in (b,d) represent $+0.5\%$ and $+0.75\%$ velocity contours for P and S wave tomography, respectively.

2.3. Results and Discussions

2.3.1. Solution Models

2.3.1.1. Upper Mantle

Figure 2.17 shows the results of the P and S wave tomographic models for the horizontal cross-sections while Figure 2.18 shows the same results for the vertical cross-sections. Our models result in a reduction of data variance by 80.8% from 0.0841 to 0.0162 s^2 (from 290.0 to 127.1 ms in RMS) for P wave tomography and 74.9% from 0.651 to 0.164 s^2 (from 806.9 to 404.4 ms in RMS) for S wave tomography. We observe an overall pattern of relatively high velocities in the west and southwest and relatively low velocities beneath the north and east in the upper mantle of the SKP (Figure 2.17). A distinct high-velocity structure (dlnVp of ~1.5% and dlnVs of ~3.0%) extends ~150 km laterally and ~220 km vertically mainly beneath the YM at the southwestern part of the Korean Peninsula (Figures 2.18b and 2.18d). Low-velocity anomalies are located beneath the GM, GB, and along the eastern margin (Figure 2.18) showing a sharp contrast (dlnVp ≈ 4.0%, dlnVs ≈ 6.0%) with the observed high-velocity anomaly. Distinct areas of slower anomalies, with dlnVp < −2% and dlnVs < −3%, appear at shallow depths (60 km in Figure 2.17) within the generally low-velocity upper mantle in the north and eastern margin of the SKP.

2.3.1.2. Crust

More details are resolved in the crustal depths, though we mainly focus on upper mantle structures in this study. Figure 2.19 shows comparisons between the initial and the results of the crustal velocity structures from the inversion, where the velocity perturbations are superimposed on the initial crustal model. In the upper part of the crust (~10 km). Relatively low velocities are found mainly beneath the Cretaceous－Cenozoic volcano sedimentary deposits in the southern part of the SKP (e.g., GB and JI), which are consistent with a previous study (Kang & Shin, 2006). In the lower part of the crust (~20 km), we find relatively low velocities beneath the GM (Cho et al., 2006).
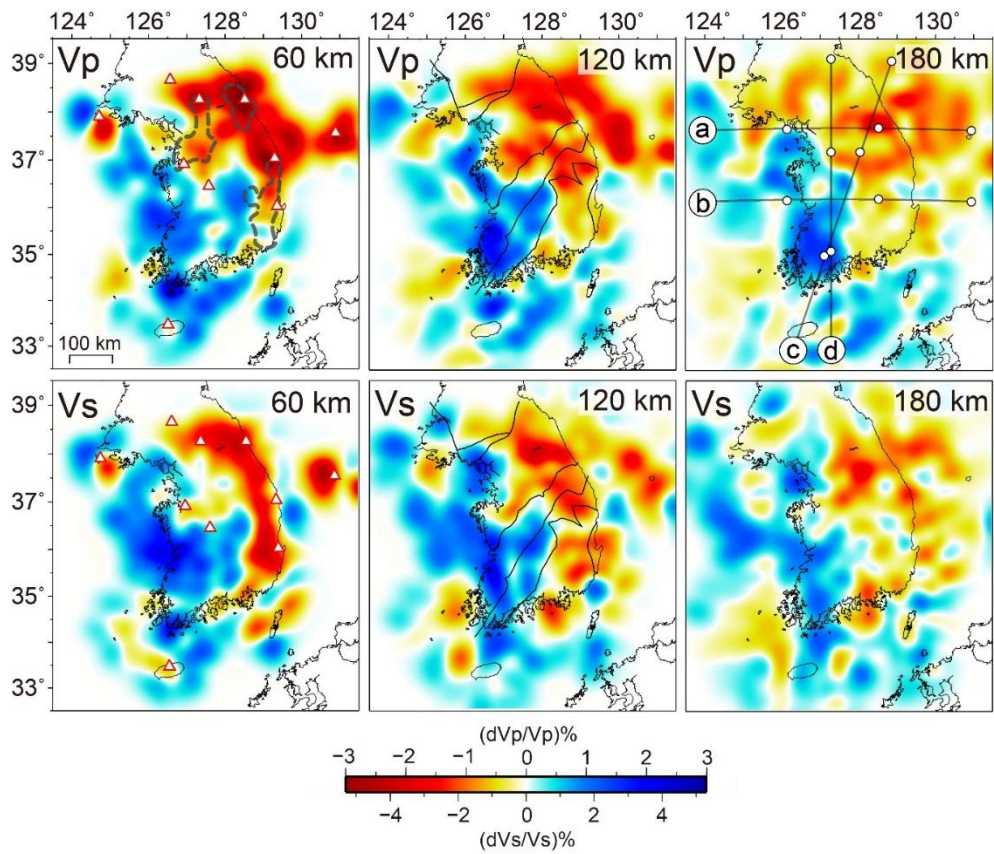
Figure 2.17 Horizontal cross‑sections through P (Vp; top) and S (Vs; bottom) wave tomography at depths of 60, 120, and 180 km. The depths of each section are indicated in the upper right corner. The black solid lines at a depth of 120 km denote the tectonic divisions shown in Figure 2.2a. Regions with surface heat flow rates >70 mW/m^2 are shown by gray dashed contours at a depth of 60 km of the Vp. Cenozoic volcanism is indicated by red triangles.
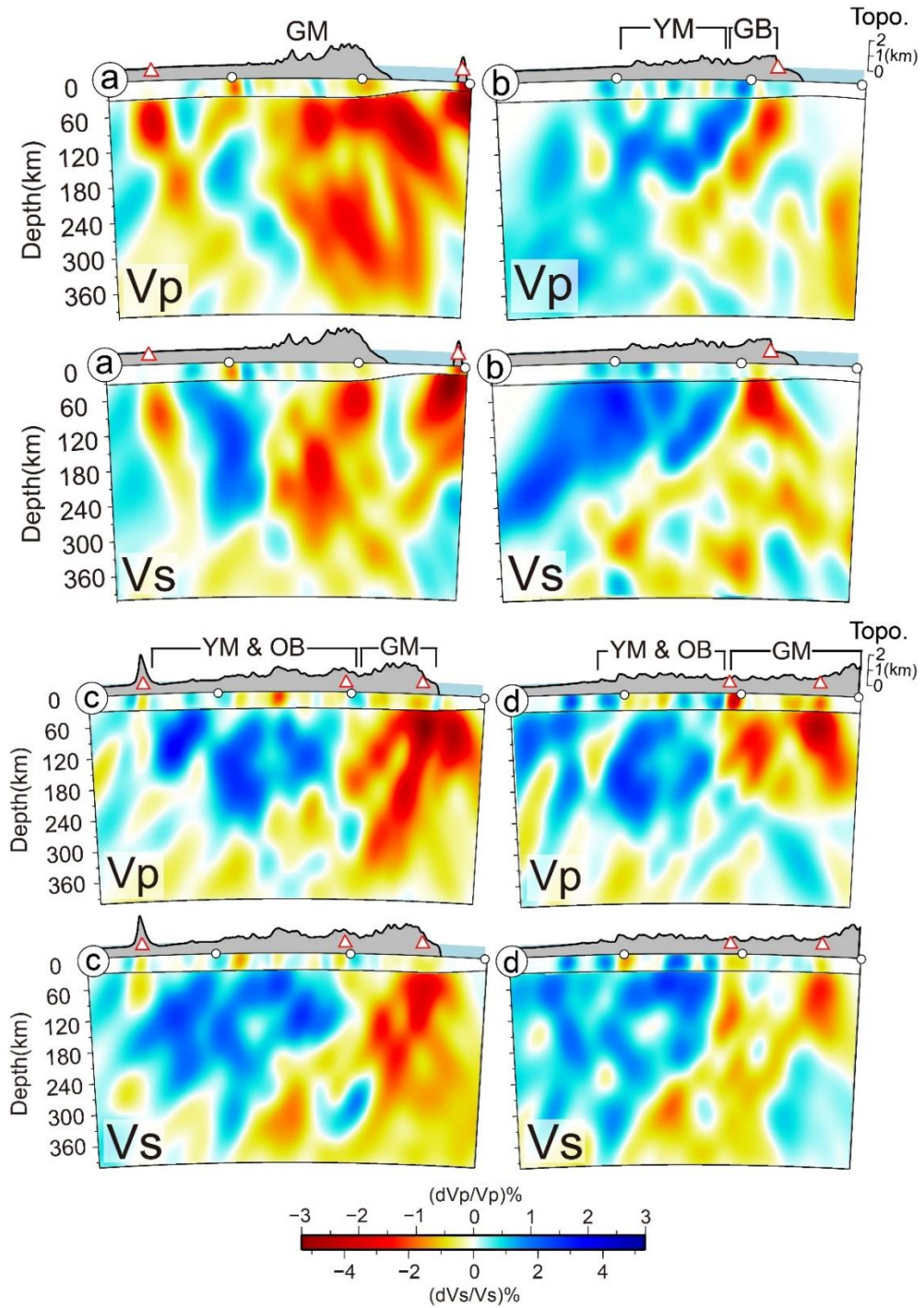
Figure 2.18 Vertical cross−sections through P (Vp) and S (Vs) wave tomography. The locations of each section (a–d) are indicated in Figure 2.17. Cenozoic volcanism is indicated by red triangles. Black horizontal lines in the cross−sections indicate Moho interfaces. GB:

Gyeongsang Basin; GM: Gyeonggi Massif; YM & OB: Yeongnam Massif and Okcheon Belt.
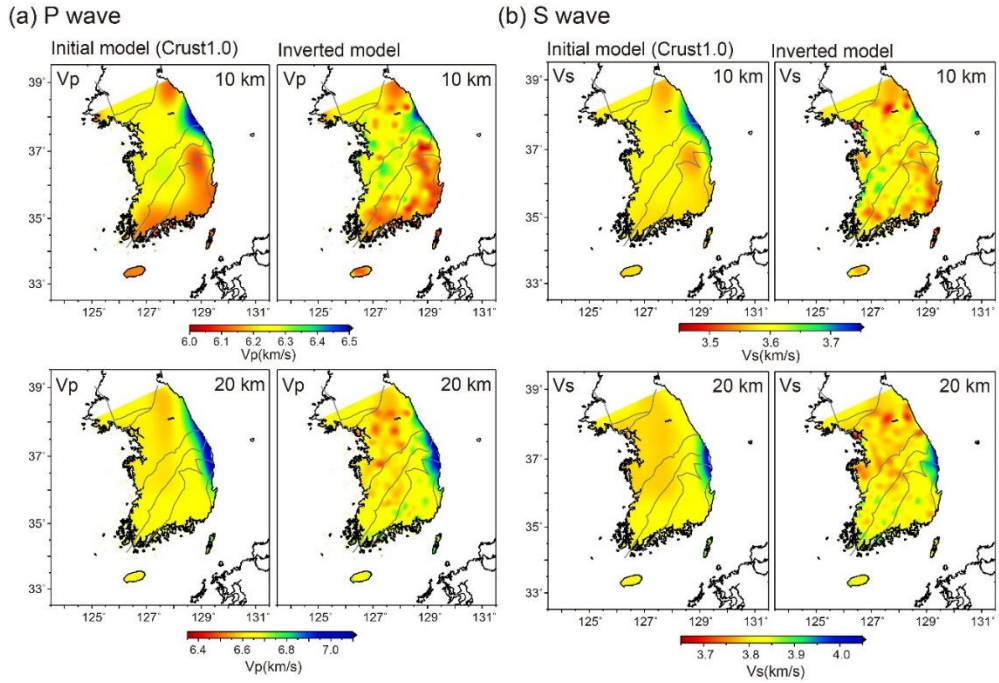
Figure 2.19 Comparisons of initial and final crustal velocity structures. (a) Crustal *P* wave velocity structure of (left column) the initial model (Crust 1.0) and inverted model at depths of 10 (top) and 20 km (bottom). Major tectonic divisions are indicated by black solid lines. (b)

2.3.2. Interpretations

The velocity patterns observed in our results agree with previous results from tomography studies (e.g., Ma et al., 2018; Tao et al., 2018) that have shown a high−velocity block located beneath the SKP within a relatively slow upper mantle. Specifically, previous studies have suggested the existence of broad slower upper mantle velocities (<−1%) at shallow depths (<300 km) beneath northeast Asia (e.g., Chang et al., 2015; Debayle et al., 2016; Legendre et al., 2015), which indicates the presence of a more thermally enhanced upper mantle (Li & Van Der Hilst, 2010). This suggests that the mean velocities in our models are possibly slower than the normal mantle. Recent regional studies have shown that upper mantle structures are likely complex in nature, suggesting the possibility of sharp contrasts in lateral velocities at the margins around the Korean Peninsula in the shallow upper mantle (Huang & Zhao, 2006; S. Kim et al., 2016). Our results provide greater details with respect to the distribution of relatively high− and low−velocity anomalies beneath the Korean Peninsula, consistent with previous observations.

Synthetic tests using structural models (Figures 2.16) show that the vertical extent (~220 km) and amplitude of the high−velocity anomaly in the southwest SKP is well constrained. Together with an estimated low heat flow of <50 mW/m^2 (Lee et al., 2010), the Archean−Proterozoic surface geology (Figure 2.2a), and the possible affinity of the southwestern SKP to cratonic lithosphere in China, we note that the imaged high−velocity structure possibly reflects relatively thick continental lithosphere preserved in the cratonic margin beneath the Korean Peninsula. Recent tomographic studies found similar small−scale positive velocity anomalies beneath

the central and eastern margin of the NCC, which were interpreted as fragments of thick lithosphere (e.g., He & Zheng, 2018; Jiang et al., 2013; Xu et al., 2018). Paleoproterozoic subcontinental lithosphere signatures from distributed mantle xenoliths within reactivated regions of eastern China and the SKP also reflect the persistent but spatially heterogeneous feature of the continental lithosphere (Lee & Walker, 2006; Wang et al., 2003; Zheng et al., 2001). The observed complexity of the cratonic lithosphere beneath the SKP, based on our results, and northeast Asia, from previous studies, suggests a non-uniform modification process for the craton margin, which corresponds to episodic magma intrusions (Li et al., 2019; Wang et al., 2018) and extension (Ren et al., 2002) due to the subduction and rollback of multiple slabs since the Mesozoic.

Our results show a striking localization of lithosphere modification among the different Precambrian massifs in the SKP. We note that the GM is missing its deeper part, resulting in a clear velocity contrast at the boundary with the thicker lithosphere beneath the YM (Figures 2.18a, c, and 2.20). Differences in the physical and chemical properties, including thickness, thermal state, and composition, can affect the relative instability of the continental lithosphere (Foley, 2008; Zheng et al., 2015). Therefore, the loci of modification can be localized at an initial zone of lithospheric weakness due to collision, rifting, mobile belts, or lithospheric interlayers (Chen et al., 2014; Lu et al., 2011; Liu et al., 2018b). Recently, several studies have reported that the GM experienced multiple episodes of accretionary i.e., arc-related, and extensional, rift-related tectonic events through a series of pre- and post-collisional stages (e.g., Hyndman, 2019) since the Paleoproterozoic (Cho et al., 2017; S.W. Kim et al., 2013; Oh et al., 2019), which are

likely linked to the subsequent late Permian–Triassic collision between the NCC and SCC (S.W. Kim et al., 2011; Oh & Kusky, 2007). Re–Os isotopic data from the late Triassic kimberlite in the NM and O–Hf isotopic composition from the Triassic plutons in the GM indicate magmatic origins of metasomatized lithospheric mantle sources and the emplacement of asthenospheric mantle, supporting lithospheric modification as a coeval process with Mesozoic orogenies (Cheong et al., 2018; Yang et al., 2010). Inherent weaknesses beneath the GM during this period can be a possible mechanism to explain the removal of thick lithosphere focused at this location, whereas there is less of an effect on the YM due to a long–lasting lithospheric core. However, a recent and transient event (e.g., Bao et al., 2014; Levander et al., 2011) is more favorable due to less of a distinction in the geological expression across the tectonic regions (Figure 2.2a) compared with the large lateral variation in our image (Figure 2.17). Previous studies have suggested that the localization of tectonic activities, including magmatism, extension, and uplift, can be attributed to mantle dynamic processes at the undulating bottom of the lithosphere (e.g., Artemieva, 2019; Rawlinson et al., 2017; Steinberger et al., 2019). In this case, it is possible that the weak properties have maintained deeper regions of the GM and been removed during a short period due to effects from a more recent tectonic event, such as the opening of the East Sea (Sea of Japan) (e.g., Evanzia et al., 2014; Shen et al., 2018) or the initiation of Philippine Sea plate subduction during the Cenozoic.

A similar large variation defines the eastern margin of the thicker lithosphere characterized by a different level of lithospheric modification between the YM and GB. The continental arc and back–arc system at the GB developed during the Early Cretaceous to early

Tertiary due to the northward oblique subduction of the paleo‑Pacific plate (Chough & Sohn, 2010). Subsequent rollback of the subducting slab yielded extensional stress and an injection of hot asthenosphere toward the mantle wedge, which resulted in the thinning of the lithosphere via thermal erosion or hydrous weakening (S.W. Kim et al., 2016; Kusky et al., 2014). In our image, a significant coincidence in the tectonic boundary between the YM and GB (at a depth of 120 km in Figure 2.17), as well as a rapid variation in the velocity, captures the resulting difference in lithospheric thickness, proving that subduction processes are the possible cause of lithospheric‑scale modification in the southeastern SKP (Chough & Sohn, 2010).

Distinct areas of slower anomalies at shallow depths (60 km in Figure 2.17) along the eastern margin of the SKP are recognized as sublithospheric upper mantle due to significant velocity contrasts (dlnVp of ~4.0% and dlnVs of ~6.0%) with the continental lithosphere in the YM. The magnitude of the decrease in velocity is a minimum estimate based on synthetic tests using structural models (Figures 2.16b and 2.16d), where the low‑velocity anomalies are resolved up to 35% of the input velocity perturbation compared with 65% for the high‑velocity anomalies. Considering the generally slower upper mantle in northeast Asia compared with the global average (~−1% in Vp and ~−2% in Vs), the observed reductions in velocity correspond to temperature increments of 300–350 K (Goes et al., 2000; Karato, 1993), with anelastic attenuation in the corresponding depth range (Adenis et al., 2017). Variations in the composition and grain size (velocity perturbation ~−1%) (Cammarano et al., 2003; Faul & Jackson, 2005) cannot account for such variations even when incorporating relatively weak upper mantle anisotropy (b1%) in this

region (Kang & Shin, 2009; Wei et al., 2016). The presence of a small fraction of partial melt (1–2%) can explain the large drop in velocity (Hammond & Humphreys, 2000; Mavko, 1980), which has also been suggested in previous tomography studies (Adenis et al., 2017; Simutė et al., 2016). The protracted subduction history of the current Pacific and former oceanic plates likely has accommodated a hot and wet sub-lithospheric upper mantle in back-arc and adjacent continental margins (S. Kim et al., 2016; Tauzin et al., 2017). Subsequent continental rifting, accompanied by upper mantle dynamics, have yielded partial melting at shallow depths, resulting in weakening and thinning along the eastern margin of the continental lithosphere.

We observe a clear correlation between the upper mantle low-velocity anomalies and areas characterized by Cenozoic basaltic eruptions (Choi et al., 2006; Choi et al., 2013; Won et al., 1994) and relatively high heat flow rates (>70 mW/m^2) (Figure 2.17). The topography of the lithosphere-asthenosphere boundary can derive accumulation of the ascending mantle flow beneath the thin lithosphere (e.g., Duggen et al., 2009; Steinberger et al., 2019). It has been suggested that a steep gradient in lithospheric thickness can induce and maintain localized mantle upwelling and decompressional melting along the margins of the relatively thick lithosphere (King & Anderson, 1998; Conrad et al., 2010). The hotter and buoyant upper mantle located beneath the thinner lithosphere can disturb the surface of the continental lithosphere (e.g., Karlstrom et al., 2012; Yang & Gao, 2018). This mechanism corresponds to the positive residual topography associated with the negative mantle gravity anomaly (Kaban et al., 2016) and high elevation with geomorphic disequilibrium in the late Pleistocene (~125 ka) (D.E.

Kim et al., 2016) observed in the eastern mountain ranges (Figures 2.17 and 2.20). Small-scale sub-lithospheric upper mantle convection can play a role in the reworking and modification of thicker lithosphere in a similar manner as asthenospheric swell or convective mantle infiltration through marginal heterogeneities (e.g., Liu et al., 2018a, 2018b; Wang & Kusky, 2019). The observed sharp contrast in mantle velocity and a spatial correspondence in recent surface magmatic activities potentially exhibit a destabilization process that characterizes the cratonic lithosphere margin due to intense interactions between the convective upper mantle and lithospheric heterogeneity.

Previous studies have found heterogeneous lithospheric structures in the NCC. An extensive but non-uniform modification process of craton lithosphere has been suggested in the central and eastern NCC. A series of seismic evidences, such as seismic tomography, anisotropy (e.g., Cheng et al., 2013; Jiang et al., 2013) and S wave receiver function analysis (e.g., Chen et al., 2009) indicate complex lithospheric structure due to deformation. An integrated thermomechanical model based on heat flow data, surface wave dispersion curves, geoid height, and absolute elevation (Guo et al., 2016a), demonstrated the highly heterogeneous physical state of the NCC developed by the uneven destruction of craton lithosphere due to sublithospheric mantle convection. Spatial distribution and temporal variation in geochemical characteristics of the Mesozoic ore deposits (e.g., gold metallogeny) (e.g., Li & Santosh, 2014, 2017) are interpreted to have resulted from inhomogeneous decratonization. Therefore, the heterogeneous destruction and reactivation of the craton lithosphere occurred extensively throughout the Sino-Korean craton margin, which includes the Korean Peninsula and NCC. The

structural heterogeneity of the craton lithosphere could be sharper in scale and thickness within a confined area than previous observations, as observed at the current continental margin of the Korean Peninsula. A distinct spatial correlation between active surface tectono－magmatic processes and modified regions indicates that upper mantle dynamics played an important role in deforming the craton lithosphere, which is likely facilitated by multiple subduction－collision events of oceanic/continental plates at the continental margin (e.g., Cai et al., 2018; Santosh, 2010).
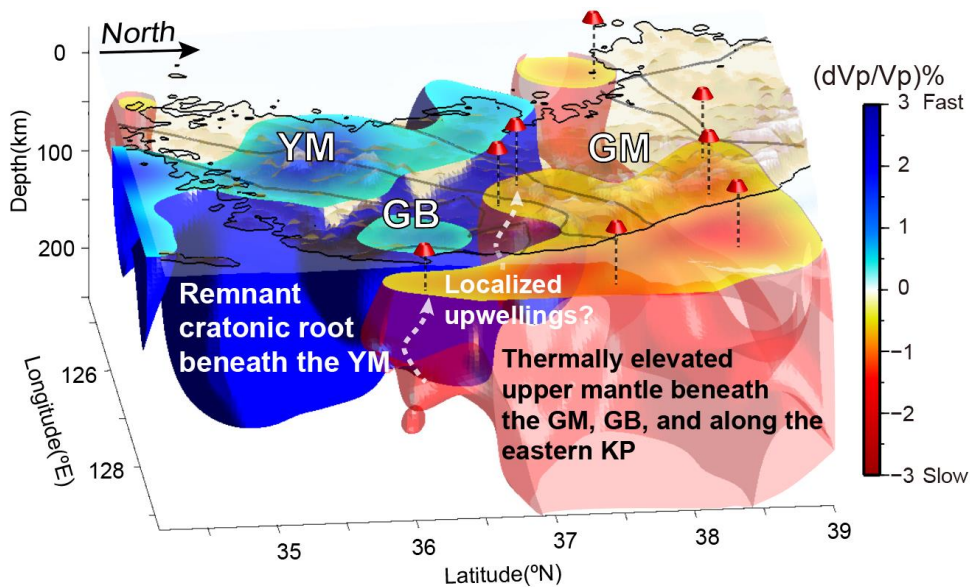
Figure 2.20 A three-dimensional plot of P wave tomography with interpretations of the main features. Structures in blue and red show +0.5 and −0.5% velocity isosurfaces, respectively, which are cut at the top by a horizontal velocity cross-section at a depth of 60 km with a color scale on the right. On the surface, red truncated cones indicate Cenozoic volcanism and gray and black lines delineate tectonic boundaries and coastlines, respectively. Vertical black dashed lines connect the Cenozoic volcanism and locations vertically projected onto the horizontal velocity cross-section. Surface relief is shown as a transparent layer. GB: Gyeongsang Basin; GM: Gyeonggi Massif; KP: Korean Peninsula; YM: Yeongnam Massif.

2.4. Conclusions

Craton lithosphere is generally composed of cold and thick lithospheric root, which is evidenced by thick, high velocity seismic upper mantle anomalies. However, the detailed processes of its formation, evolution, and deformation remain enigmatic due to its complex structure evolved during the long geological history. Craton lithosphere in northeast Asia represents a dramatic case of a significantly modified and currently deforming craton lithosphere. The Korean Peninsula, as part of craton lithosphere at the eastern forefront of the Eurasian plate, experienced intense tectonic modification process during the Phanerozoic period. In order to understand the structure and evolution of craton lithosphere beneath the Korean Peninsula, we constrain high-resolution upper mantle seismic velocity structure by teleseismic relative-time tomography. Our model clearly shows heterogeneous craton margin lithosphere structure. In particular, distinct upper mantle features beneath different Archean-Proterozoic massifs indicate different responses of each lithosphere to recent marginal tectonic processes. An anomalously thick high-velocity structure beneath the YM suggests the presence of a cold and resistant cratonic lithosphere fragment at the eastern margin of the Eurasian plate. In contrast, the absence of deeper lithosphere mostly occupied by high-temperature, buoyant upper mantle beneath the GM, continental arc and back-arc system of the GB in the southeast, and along the eastern margin indicate highly modified regions. A clear spatial coincidence between low velocities and recent tectono-magmatic activities suggests continuous reactivation of a cratonic margin by intense interaction

between the prominent lithospheric structures and convective upper mantle.

Our result suggests that craton lithosphere can be significantly modified when exposed to marginal tectonic activities. However, the existence of thick lithosphere beneath the southwestern Korean Peninsula seems to contradict the previous notion that the eastern continental margins of northeast Asia are widely deformed and thinned. Simple geodynamic models accompanying large−scale mantle convections cannot reconcile with current lithospheric structure. Instead, alternative mechanisms such as inherited structural weakness within lithosphere, small−scale mantle dynamics induced by structural heterogeneities could play important role for shaping the lithospheric structures at northeast Asia margin.

Chapter 3. Segmented Stagnant Pacific Slab and Its Interaction with the Mantle Transition Zone Beneath Northeast Asia Continental Margin by Teleseismic Traveltime Tomography

3.1. Introduction

As diving into the deep mantle, subducting plate leaves distinct geophysical and geochemical signatures in the upper mantle (Chang et al., 2016; Chen et al., 2019; Kimura et al., 2018; Schmandt & Lin, 2014; Wu et al., 2019). Evidence of interaction between the subduction and the surrounding upper mantle can be found from the mantle transition zone (MTZ), where mineralogical phase changes of the upper mantle take place (Bina & Helffrich, 1994). Seismic observations found correspondences between subducting slabs and heterogeneities within and around the MTZ (e.g., Tauzin et al., 2017), indicating a close linkage between the slab and upper mantle. Variations in temperature, chemical composition, volatile contents have been suggested to be caused by subducting plates, which can significantly affect mantle properties, control melt generation and convection (Hier−Majumder & Tauzin., 2017; Schmandt et al., 2011), and deep cycling of Earth's materials (J. Liu et al., 2016; Thomson et al., 2016; Walter et al., 2011).

Previous studies have suggested that the northwestern Pacific plate is extensively subducting beneath the Eurasian plate, influencing upper mantle dynamics and tectonics in east Asia (Yang et al., 2019) (Figure 3.1). Global and regional tomographic models have found distinct fast anomalies that are stagnated in the MTZ of the northwestern Pacific, which extends more than 1000 km from

trench to inland of northeast Asia (Fukao & Obayashi, 2013; Huang & D. Zhao, 2006; Zhao et al., 2012). Distinct upper mantle heterogeneities within and around the MTZ were observed and attributed to the stagnant Pacific plate (e.g., Lai et al., 2019; Li & Van Der Hilst, 2010; Z. Liu et al., 2016; Tauzin et al., 2017). Complex mantle processes enhanced by configuration of the slab with a localized gap or tear have been suggested (Obayashi et al., 2009; Tang et al., 2014; Tao et al., 2018). However, the detailed geometries of the stagnant slab at the continental margin of northeast Asia remain unclear, where the interactions between the subducting slab, upper mantle, and MTZ become intense as the slab is deflected and stagnated (Richard & Iwamori, 2010). This is due to lack of high−resolution imaging of deeper upper mantle structure limited by less sampling at northeast Asia margin.

By using datasets from dense seismic arrays in the Korean Peninsula, we resolve finer details of the upper mantle structures beneath the northeast Asia margin that were previously not well constrained. We also use a part of seismic arrays in Japan near the Korean Peninsula to improve depth resolution. Our results revealed distinct lateral variations in Vp, Vs, and Vp/Vs within and around the MTZ (300~660 km). We identify a horizontal corridor−like low−velocity structure beneath the northeast Asia margin that extends from the East Sea (Sea of Japan) to the East China Sea across the Korean Peninsula. This structure is surrounded by high−velocity anomalies with sharp velocity changes at its boundaries, and we interpret the velocity pattern as a pronounced gap in the stagnant Pacific plate. A clear correspondence between the imaged velocity pattern and upper mantle heterogeneities observed by previous receiver function studies (e.g., Z. Liu et al., 2016; Tauzin et al., 2017)

suggests that the velocity anomalies originates in composition (e.g., partial melt) as well as the temperature around the MTZ. We suggest that a slab tearing of Pacific plate could enhance dynamic interaction between MTZ and the upper mantle along the northeast Asia continental margins.
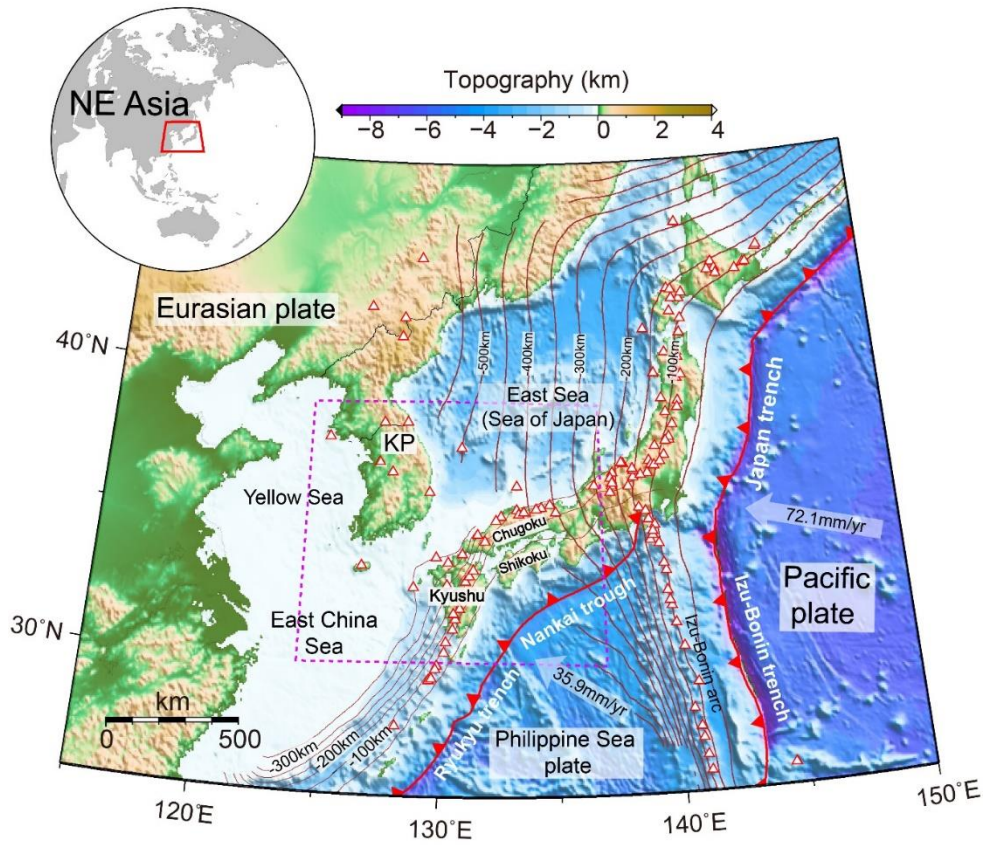
Figure 3.1 Regional tectonic map of northeast Asia. Convergent plate boundaries are shown with red saw-toothed lines (Bird, 2003). Depths of the subducting oceanic slabs are indicated by brown solid (Pacific slab) and dashed (Philippine Sea slab) contours at 50-km intervals based on the Slab2 model (Hayes et al., 2018). Volcanoes are indicated by red triangles. A pink dashed rectangular box shows the map boundary of Figure 3.2. KP: Korean Peninsula.

3.2. Methods

3.2.1. Data Acquisition and Processing

We collect seismic data recorded by permanent seismic stations deployed in the southern Korean Peninsula and southwestern Japan, consisting of a total of 565 broadband, short−period, and accelerometer sensors. Seismic networks include Korea Meteorological Administration, Korea Institute of Geoscience and Mineral Resources, Korea Nuclear and Hydro Power, and Korea Institute of Nuclear Safety for the southern Korean Peninsula, and Hi−net and F−net of National Research Institute for Earth Science and Disaster Resilience, and Japan Meteorological Agency for southwestern Japan (Figure 3.2). We select 1175 events between 2013 and 2018 with magnitudes greater than mb 5.4 at epicentral distances from 30 to 95° from the International Seismological Catalogue, identifying P and S waves from the vertical and tangential component data, respectively. The waveforms are first aligned by traveltime predictions from the ak135 reference earth model (Kennett et al, 1995). We calculate relative traveltime residuals by using interstation coherency in the P and S wave waveforms (Rawlinson & Kennett, 2004). The waveform data are first corrected for corresponding instrument responses to incorporate waveform data from different instrumental settings. The waveforms are filtered with frequency bands from 0.1−5.0 Hz for P waves and 0.1−1.0 Hz for S waves. All teleseismic waveforms are visually inspected and noisy or incoherent data are discarded to obtain more reliable measurement of relative residuals. Our final dataset consists of 281,920 rays from 725 events for P waves and 92,838 rays from 258 events for S waves (Figure 3.3). The uncertainties of relative

residuals are measured based on waveform similarity (Rawlinson & Kennett, 2004) (see section 1.2.3 for the detailed descriptions).
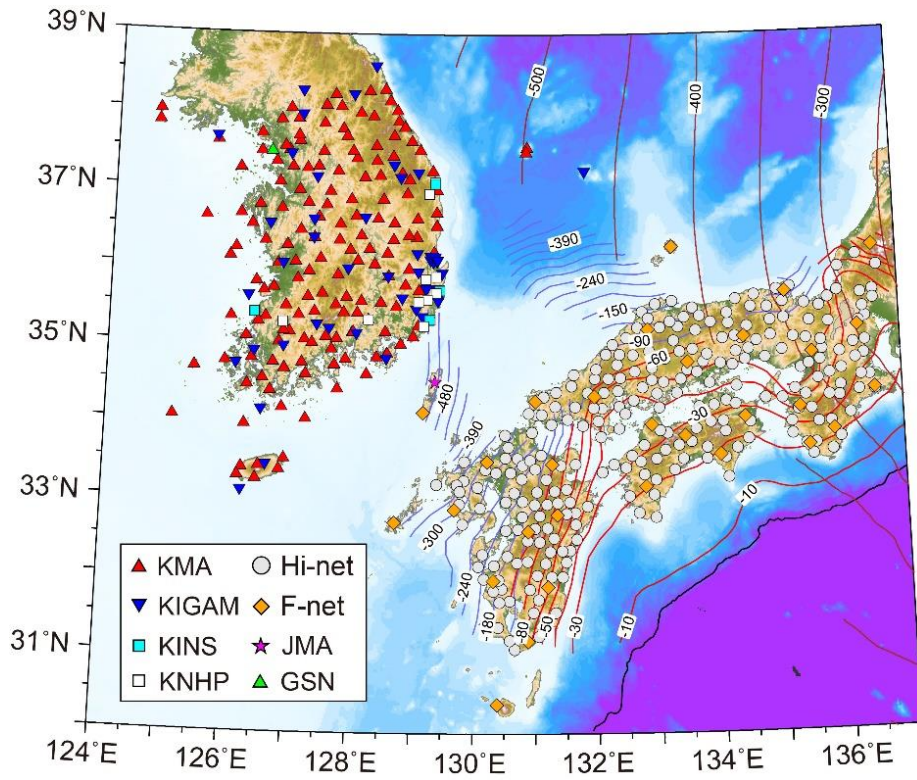
Figure 3.2 Seismic stations used in this study. Stations from different networks are shown by different colors and symbols. KMA: Korea Meteorological Administration; KIGAM: Korea Institute of Geoscience and Mineral Resources; KINS: Korea Institute of Nuclear Safety; KNHP: Korea Hydro and Nuclear Power; F- and Hi-net: networks of National Research Institute for Earth Science and Disaster Resilience; JMA: Japan Meteorological Agency; GSN: Global Seismic Network. The brown solid contours indicate subducting Pacific slab at 50-km intervals (Hayes et al., 2018). The red and blue contours indicate subducting Philippine Sea slab at 10-km and 30-km intervals, respectively (Asamori & Zhao, 2015; Nakajima et al., 2009)
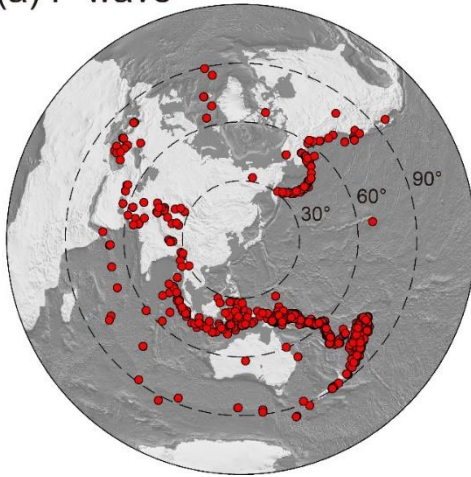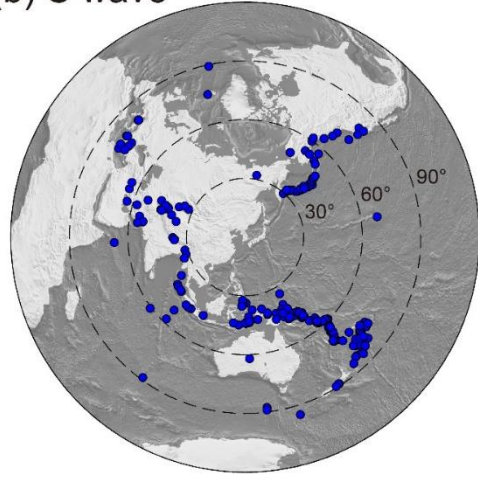
Figure 3.3 Distribution of teleseismic events used for (a) P and (b) S wave tomography. Dashed black circles are plotted at 30° increments.

3.2.2. Tomographic Methods

3.2.2.1 Model Parameterization and Regularization

Fast marching ray-tracing (Rawlinson et al., 2006b) and the subspace inversion scheme (Kennett et al., 1988) are iteratively applied to perform tomography. We define a model space spanning a depth of ~800 km with a uniform grid spacing of ~10 km in the crust and ~30 km in the mantle. Regularization factors (damping (ε) and smoothing (η)) for the model are determined based on an evaluation of the trade-offs between the data misfit, model smoothness, and model variance (Rawlinson et al., 2006b) Data misfit for the inversion are determined based on the difference between the observed and predicted traveltimes starting from the initial model, which consisted of a 3-D crustal model with Moho interface (Crust1.0, Laske et al., 2013) over the mantle portion with the ak135 reference model (Kennett et al., 1995). We simultaneously invert the model for crustal and upper mantle structures with fixed Moho depths to account for crustal effects.

3.2.2.2. Joint Inversion of *P* and *S* Waves

We perform joint inversion of *P* and *S* wave dataset to construct the 3−D Vp/Vs structure following the similar approach of Schmandt & Humphreys (2010a). This method simultaneously inverts the two dataset with an additional regularization on the smoothness of Vp/Vs while minimizing total data variance. To reduce artefacts from different ray density of each individual dataset on results, data with common source−receiver pairs are only used, which consists of 86,918 rays for 516 sources. We determine the smoothing parameter for Vp/Vs based on the trade−off between the total data misfit and model smoothness while maintaining regularization factors for individual datasets determined in individual inversions (Figure 3.4). To balance the contribution of different datasets to the overall data, each data is weighted in inverse proportion to the size of each data vector. We calculate Vp/Vs variations based on the ak135 reference model, taking into account that different settings of the 1−D reference model have a small effect on the resulting perturbation (e.g., Giacomuzzi et al., 2012; Papaleo et al., 2018).
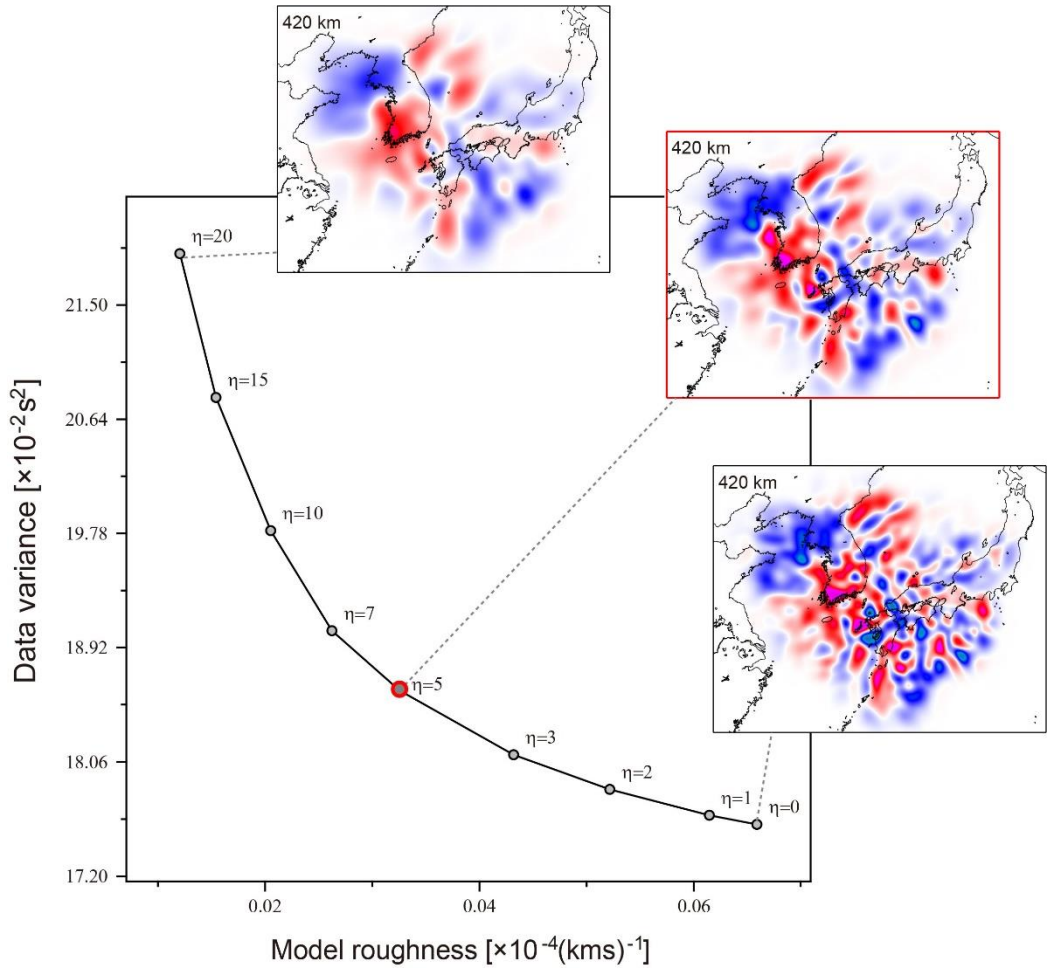
Figure 3.4 Determination of the regularization factor for the Vp/Vs model. A relationship between data variance and model roughness is shown for different smoothing parameters (η). As examples, horizontal cross−sections at a depth of 420 km for resulting Vp/Vs for $\eta=0$, 5, and 20 are shown. The final model is chosen for $\eta=5$, indicated by red outlines.

3.2.2.3. Resolution Tests

We test the resolution of the velocity model by performing recovery tests with checkerboard pattern and structural anomalies in specific geometry. All synthetic data are generated by using the identical source−receiver combination as the actual data with Gaussian random noise whose standard deviation is equivalent to the estimated residual uncertainties (58 ms for P wave, and 137 ms for S wave). We apply checkerboard anomalies with sizes of 90 and 150 km and amplitudes of ±4% for Vp and ±7% for Vs (Figures 3.5 and 3.6). For Vp/Vs, we apply checkerboard sizes of 120 and 150 km with an amplitude of ±3% (Figure 3.7). The output models of individual dataset show good resolution between the southern Korean Peninsula and southwestern Japan, where a checkerboard structure with a size of 90 km can be resolved to a depth of ∼ 600 km, and a checkerboard structure with a size of 150 km can be recovered to a depth of ∼ 800 km. The output model of Vp/Vs shows generally good resolution for a checkerboard size of 120 km to a depth of ∼400 km and for 150 km to a depth of ∼600 km. We also test a model that combines checkerboard patterns of different sizes consisting of small−size (∼150 km) checkerboard anomalies to ∼400 km depth and large−size (∼450 km) checkerboard anomalies below the 400 km depth to evaluate whether our dataset can resolve heterogeneity of different wavelengths at different depths at the same time (Figure 3.8). Our model successfully resolves the original structure without significant distortion in shapes of anomalies in different depths. We additionally perform a structural test for a small plate high−velocity anomaly with a scale of ∼400 km in horizontal and ∼80 km in vertical at a depth of ∼590 km to test the resolution at the deeper MTZ (Figure 3.9a). The

structure is clearly recovered without significant changes in shape and location with vertical smears of the upper boundary less than 80 km. We also test with a structure consisting of the high−velocity structure added with the addition of low−velocity layers above the MTZ (Figure 3.9b). The result confirms that our model can clearly resolve small−scale anomalies in different polarities and scales across the MTZ.
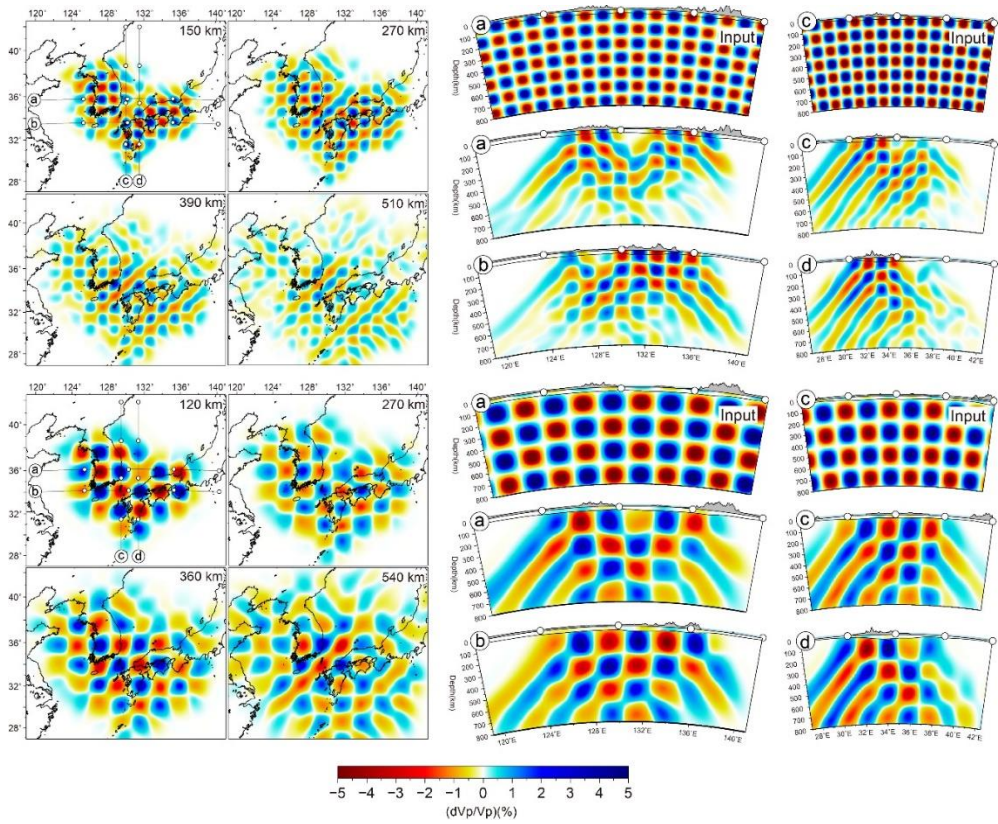
Figure 3.5 Checkerboard resolution test results for P wave tomography. Checkers with sizes of 90 and 150 km and amplitudes of $\pm 4\%$ for Vp are shown.
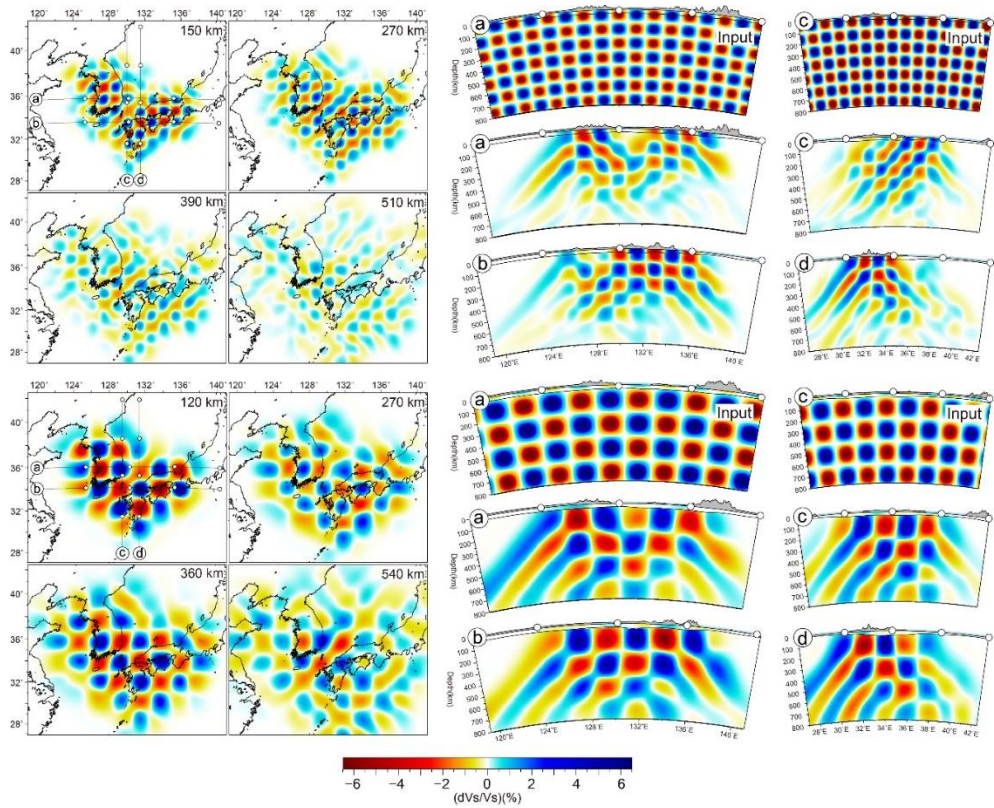
Figure 3.6 Checkerboard resolution test results for the S wave tomography. Checkers with sizes of 90 and 150 km and amplitudes of $\pm7\%$ for Vs are shown.
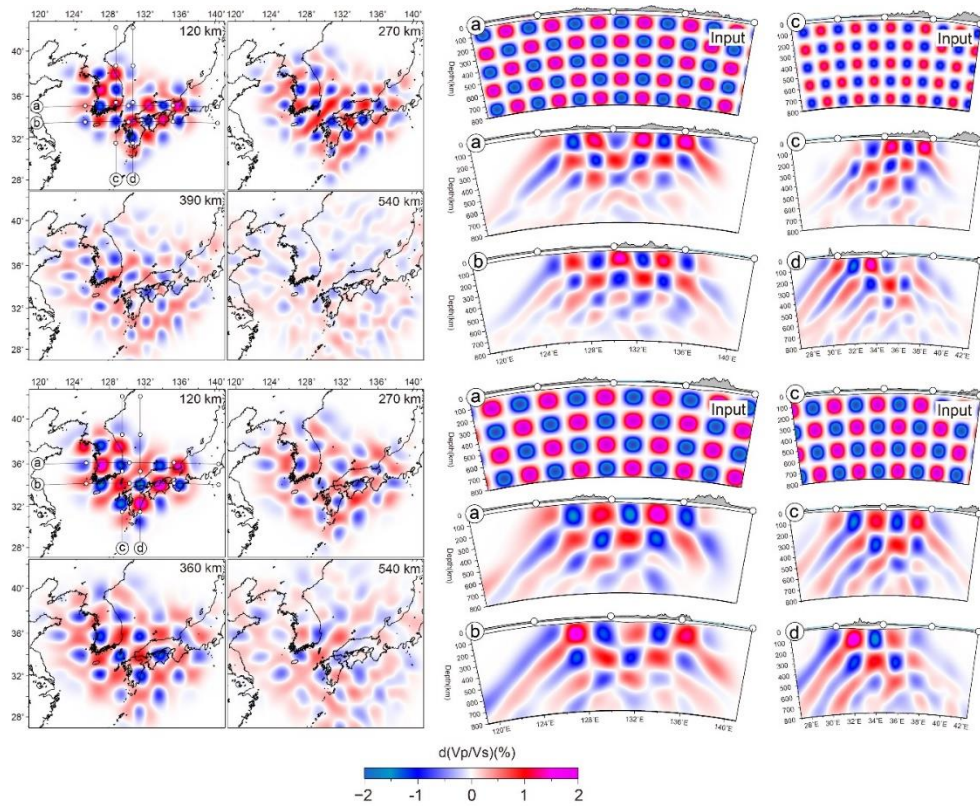
Figure 3.7 Checkerboard resolution test results for the Vp/Vs. Checkers with sizes of 120 and 150 km and amplitudes of $\pm 3\%$ for Vp/Vs are shown.
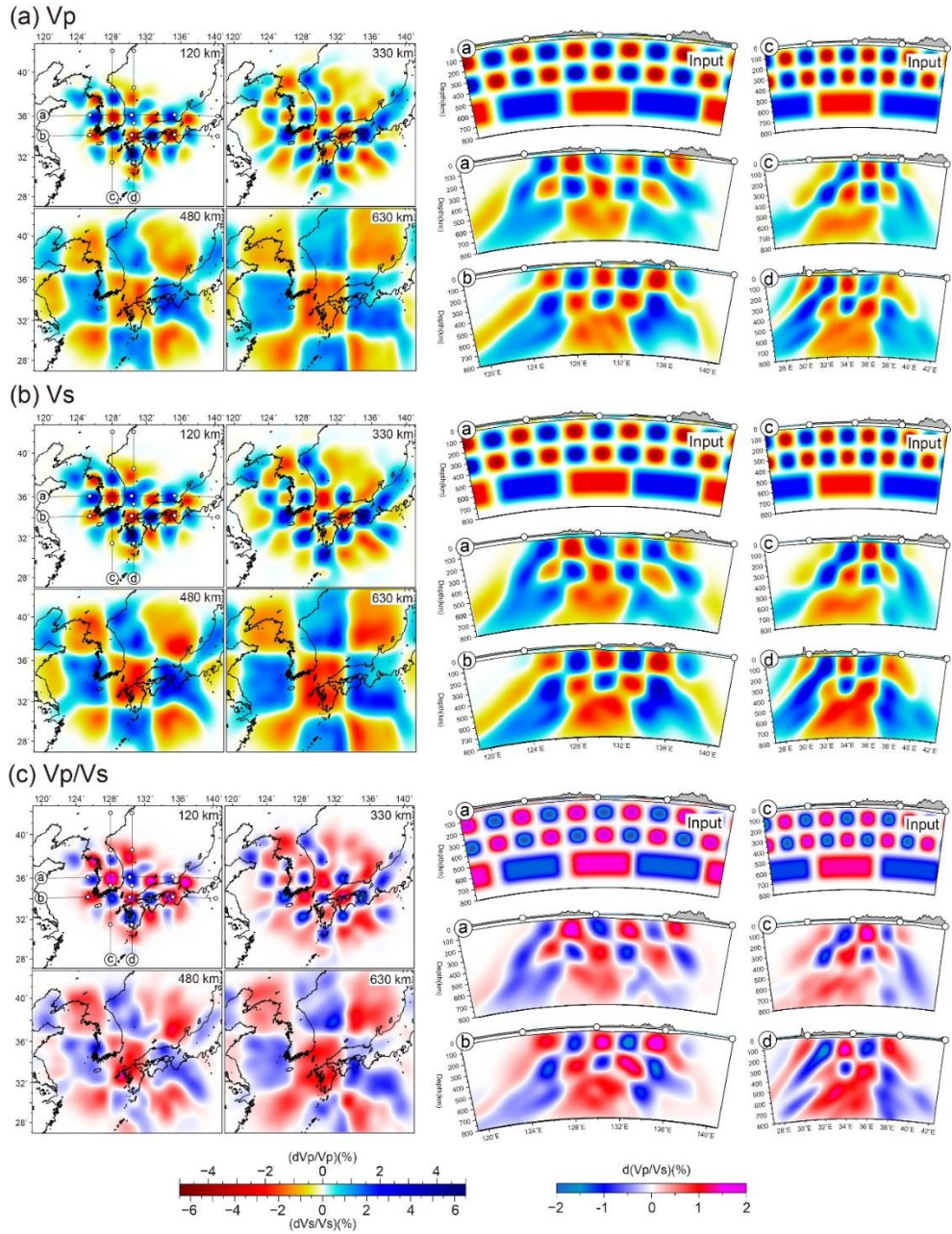
Figure 3.8 Resolution test results for (a) Vp, (b) Vs, and (c) Vp/Vs tomography with checkerboard patterns of different sizes at different depths. Checkers with sizes of 150 km and 450 km are applied at depths above and below the 400 km. Velocity amplitudes of Vp, Vs, and Vp/Vs are ±4%, ±7%, and ±3%, respectively for the

structures above the 400 km and ±3%, ±4.5%, and ±1.5%, respectively for the structures below the 400 km.
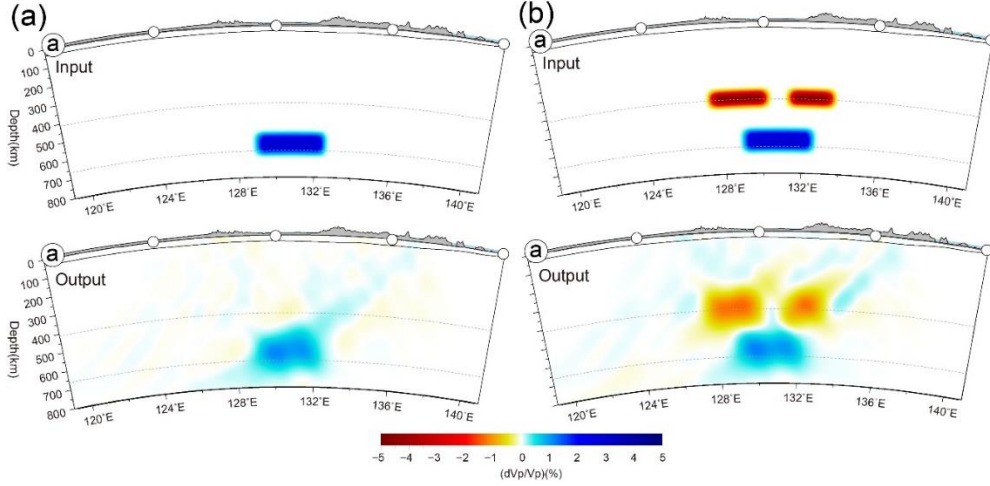
Figure 3.9 Structural resolution test results of P wave tomography. The location of the profile is indicated in the Figure 3.9. (a) The synthetic model consists of a plate-like high-velocity anomaly with a size of ~300 km in horizontal and ~80 km in vertical with an amplitude of ~3% of dVp at the bottom of the MTZ. (b) The synthetic model consists of the same high-velocity anomaly used in (a) added with low-velocity layers with a thickness of ~50 km and an amplitude of −5% of dVp right above the MTZ. The inputs and their corresponding outputs are shown in the first and second rows, respectively.

3.2.3. Waveform Simulation

We use the spectral-element method (SPECFEM3D_GLOBE)
(Komatitsch & Tromp, 1999) to conduct 3-D waveform simulation
of S wave from one deep focus earthquake beneath the Java Sea,
Indonesia (PDE: 2016-10-19 00:26:01.090, -4.8626°,
108.1627°, 614.0 km, 6.6 Mw) and one intermediate-depth
earthquake occurring in the Sumatra, Indonesia (PDE: 2015-05-15,
20:26:56.870, -2.542°, 102.2191°, 151.0 km, 6.0 Mw). We apply
3-D P and S wave velocity models obtained by teleseismic traveltime
tomography superimposed on the 1-D reference velocity from the
regional model (Tao et al., 2018) in the model space of latitude,
longitude, and depth ranges of 24.5–45° N, 117.5–144° E, and 0–800
km, and 1-D PREM (Dziewonski & Anderson, 1981) in the outside
of the model space. We apply a Butterworth band pass filter to the
SH displacement waveforms with corner frequencies of 0.02–0.1 Hz.
The 3-D mantle model is combined with the crustal model of
CRUST1.0 (Laske et al., 2013) and the topography of ETOPO1
(Amante & Eakins, 2009). The focal mechanism of the event is
obtained from the Global CMT (Ekström et al., 2012). The average
grid spacing in the upper mantle is ~5.20 km, which corresponds to
a dominant period of ~5.78 s (~0.173 Hz) for the S wave. We analyze
amplitude variations for transverse component S waves, which is
defined by the amplitude difference at each station compared to the
average amplitude in a logarithmic scale. Synthetic waveforms are
calculated for grid nodes with 0.2° spacing. We compare the results
with synthetic wave amplitude variations with the upper mantle model
that only includes 3-D velocity variations at depths less than 350 km.

3.3. Results and Discussions

Our model images fine details of upper mantle structures, showing general consistency with previous regional tomographic studies in depths to ~300 km. We observe a high-velocity anomaly beneath the southwestern Japan (Figure 3.10). The extent of the high-velocity anomaly is consistent with slab contours of the subducting Philippine Sea plate (Figure 3.1) (Asamori & Zhao, 2015; Hayes et al., 2018; Nakajima et al., 2009) and a spatial distribution of seismicity. In addition, there is a separation of the high-velocity anomaly into two individual anomalies beneath the northern Kyushu at a depth of ~120 km, which has been suggested to be a slab window of the Philippine Sea plate (Asamori & Zhao, 2015; Huang et al., 2013). Beneath the Korean Peninsula, a sharp and strong contrast between the high-velocity anomaly in the southwest and the low-velocity anomalies in northeast and eastern margins at a depth of ~120 km is consistent with previous results (e.g., S. Kim et al., 2016; Song et al., 2020; Zheng et al., 2012).

We find distinct lateral velocity variations above (~390 km) and within the MTZ (~535 km) (Figures 3.11 and 3.12), where previous studies only have detected long-wavelength (>1000 km) structures with weak velocity contrasts (dlnVp < 1% and dlnVs < 2%) (e.g., Chen et al., 2017; Huang & Zhao, 2006: Obayashi et al., 2009). Considering the vertical resolution of the dataset assessed by the checkerboard resolution test (Figures 3.5 to 3.7), and the persistency of the imaged patterns for different depths, we interpret each of the two slices as a representative image for velocity variations above (350~410 km) and within the MTZ (410~660 km), respectively.

Within the MTZ, continuous low−velocity anomalies are found beneath the continental margin with sharp and large velocity contrasts (~2.5% of dlnVp and ~4% of dlnVs) to the surrounding high−velocity structures. Given the seismologically constrained temperature contrast between the stagnant slab and the surrounding upper mantle of ~350 to ~400 K (Fukao et al., 2013; Wang et al., 2020), the observed anomalies are difficult to be explained by temperature variations within the slab (Karato, 1993). Variations in chemical composition (e.g., Fe and Mg) can change the seismic velocity (Sinogeikin et al., 1998). However, the magnitude of velocity contrasts cannot be entirely accounted for by reasonable compositional changes of the mantle materials (Irifune et al., 2008; Jacobsen et al., 2004; Jacobsen & Smyth, 2006; Nishiyama et al., 2009). The presence of small amounts of water can reduce the seismic velocity. However, laboratory experiments showed weak sensitivity of seismic velocities on water contents within the MTZ (Buchen et al., 2018; Mao et al., 2008; Schulze et al., 2018; Zhang et al., 2021). Therefore, it is possible that the imaged velocity variations correspond to the thermal variations due to uneven distribution stagnant slab.

We observe sharp changes in travel time residual over specific ranges of back azimuth (Figure 3.13). A sharp increase (decrease) in travel time residual of seismic stations in the southeast (northwest) as back−azimuth increases from ~180° to ~240°. Synthetic residual patterns calculated with the structures in the MTZ show that similar variations can be reproduced (Figure 3.13b). The fluctuations in residual only in certain back−azimuthal ranges are difficult to be reconciled with shallow upper mantle structures, as the structures close to the stations are more likely to form a constant residual over

the entire angular ranges. It is also confirmed that the amplitude of the teleseismic waveform varies up to about a factor of two across the corresponding back−azimuthal ranges (Figures 3.14c and g). We show that the observed variations can be explained by the elastic focusing/defocusing effect from the deeper upper mantle structures. The focusing effect is significant when there is a concentrated relatively low−velocity anomaly through which wave propagates (e.g., Tang et al., 2014; Hung et al., 2000). We observe relatively higher amplitudes for stations where rays propagate the low− velocity anomaly reach, while relatively lower amplitudes for stations where rays propagate boundaries of the low−velocity anomaly or surrounding high−velocity anomalies (Figures 3.14c and g). 3−D waveform simulation results show that waveforms calculated with the 3−D velocity model at depths 0~400 km show inconsistency in magnitudes and patterns of amplitude variation with the observation, while the 3−D velocity model at whole depths (0~800 km) predict comparable patterns with the observation. Also, depending on the direction of event, there is a variation in the location of the area where the wave amplitudes are amplified or reduced (Figures 3.14c and g). This can be understood as a change in the direction of wave incidence for the low−velocity anomaly in the deeper upper mantle: since the wavefront generated by event 1 comes farther south than event 2, the waves penetrating the low velocity anomaly in the MTZ reaches further north, northeastern part of the Korean Peninsula, where the amplitude is relatively amplified. These observations indicate that the velocity anomalies within the MTZ are reliable. Previous regional and global tomographic studies imaged velocity variations with long structural wavelength at similar locations (Figures 3.15 and 3.16). Our model image sharp velocity variations

in the MTZ, which possibly related to the non−uniform distribution of the stagnant Pacific slab beneath the northeast Asia margin.

Segmentation of a subducting slab is observed in various regions (e.g., Govers & Fichtner, 2016; Hawley et al., 2019; Li & Song, 2018; Liu et al., 2018; Portner et al., 2018; Sigloch et al., 2008; Sigloch & Mihalynuk, 2013; Zhou, 2018; Zhu et al., 2012). Convergence of plates with different resistance (Li & Song, 2018), inherited lithospheric weak structures within the subducting oceanic slabs (Hawley et al., 2019), and rapid plate reorganization at plate boundaries (Ma et al., 2019) can lead to detachment and internal segmentation of a slab. An ongoing slab tear at a cusplike junction between the Japan and the Izu−Bonin slabs due to stress concentration as the Pacific slab bends to flatten over the 660−km discontinuity has been observed (Obayashi et al., 2009). However, it is unlikely that the imaged gap in our study formed in the same or later period as a part of the ongoing tear given that the position of the subducted plates inferred from tomography (Tao et al., 2018) and plate reconstruction model (Ma et al., 2019) during the Cenozoic indicating that the age of the formation of the slab gap precedes the slab tear. A recent numerical model has shown that the slab tear formed and propagated through the subducted Pacific slab as a triple−junction between the Eurasian plate, Pacific plate, and Philippine Sea plate migrated northeastward along the East Asia margin due to the clockwise rotation of the Philippine Sea plate during the Miocene (Ma et al., 2019). The triple−junction reached at the southwest of the Japan arc ~20 Ma, and as the opening of the East Sea (Sea of Japan) initiated with a clockwise rotation of the SW Japan arc and the trench retreat of the Pacific plate, the migration direction changes and heads toward the current junction of Japan arc and Izu−

Bonin arc (Wu et al., 2016). The geometry of the slab gap beneath the Korean Peninsula, which is bent from the NE-SW in the southwest to the E-W in the east, coincides with the abrupt change in the propagation direction of the triple junction (Figure 3.17). Also, we observe that the gap is narrowing from the southwest of Korean Peninsula to the northeast. This likely reflects the northeastward slab segmentation as the distance between the Ryukyu trench and Izu-Bonin trench gradually increased. Subsequent movement of the Eurasian plate to the southeast with respect to the Philippine Sea plate and the Pacific plate likely explains the current position of the gap beneath the Korean Peninsula (Müller et al., 2018).

We compare our results with previous receiver function studies (Z. Liu et al., 2016; Tauzin et al., 2017) to correlate the imaged anomalies with the mantle heterogeneities. Tauzin et al. (2017) observed negative reflectivity zones at the base of the MTZ (560-660 km) beneath northeast Asia, which are geographically correlated with the high-velocity slab structures (Debayle & Ricard, 2012). The anomalies were interpreted to be the signature of a change in bulk chemistry near the 660-km boundary (Nakagawa et al., 2010; Ringwood & Irifune, 1988) due to chemical layering of constituents from subducted plates (Ballmer et al., 2015b; Shen & Blum, 2003). The distribution of the strong negative amplitudes matches well with high-velocity anomalies in our images, whereas the signals are weak or absent at the low-velocity anomalies (Figure 3.18a). In addition, Z. Liu et al. (2016) detected negative reflectivity zones below the depressed 660-km discontinuities. The anomalies were interpreted as water-induced partial meltings caused by downwelling of hydrous transition zone material by depression of the flat slab beneath the 660-km phase transition (Z. Liu et al., 2016; Schmandt et al., 2014).

These regions correlate with the high-velocity anomalies (Figure 3.18a). The distribution deep earthquake seismicity is also correlated with the high-velocity anomalies in the east of the Korean Peninsula (Figure 3.18a), showing high seismicity in the north of 37° where prominent high-velocity anomaly is observed, while there are few earthquakes in the south. Although the mechanism of deep earthquakes is currently debated (e.g., J. Li et al., 2018; Ye et al., 2016), previous studies suggested a possible relationship between the subducting cold slab and deep earthquakes. The series of coincidences and the imaged velocity contrasts support that the observed segmented high-velocity structures imaged by our results possibly reflect the non-uniform distribution of the Pacific slab within the MTZ.

We find spatial correlations between the negative reflectivity zones above the MTZ (Z. Liu et al., 2016; Tauzin et al., 2017) and the low-velocity anomalies within the MTZ (Figure 3.18b). The low-velocity anomaly above the MTZ can be differentiated from anomalies within the MTZ by our datasets based on the resolution tests (e.g., Figures 3.5 to 3.9). A small-scale low-velocity anomaly (dVp~−0.84, dVs~−2.78) with a high Vp/Vs ratio (dln(Vp/Vs) ~ 1.94%) is observed at the negative reflectivity beneath the Korean Peninsula (Figure 3.18b). Assuming that the observed the velocity perturbations are entirely produced by a thermal anomaly, temperature increase of 260–295K for a dry mantle condition, and 120–130 K for a wet mantle condition (C_{OH} = 1000 wt ppm) is required (Jackson & Faul, 2010; McCarthy et al., 2011). The anomaly with locally increased temperature possibly leads to depression of the 410-km discontinuity by 10.8–26.5 km assuming a Clapeyron slope for olivine to wadsleyite of ~3 Mpa/K (Ito & Takahashi, 1989).

However, the predicted depression is inconsistent with previous receiver function analyses (Lee et al., 2014; Sun et al., 2020; Tauzin et al., 2018) that show no obvious depression compared to the surrounding areas. Therefore, purely thermal origin cannot explain the observed anomaly. The lattice preferred orientation of olivine can cause seismic anisotropy, which can generate apparently slow/fast Vp or Vs and high/low Vp/Vs anomalies (Jacobsen et al., 2008). For radial anisotropy in which vertically incident waves propagate faster than horizontally incident waves, faster Vp while slower Vs are expected, resulting in higher Vp/Vs. For radial anisotropy in which horizontally incident waves propagate faster than vertically incident waves, slower Vp while faster Vs are expected, which results in lower Vp/Vs. The predicted perturbations are inconsistent with our observation where Vp and Vs are both slower. Although azimuthal anisotropy can cause seismic velocity variations, the distribution of seismic events over a wide range of azimuths (Figure 3.3) likely minimizes biases resulting from preferential incidence in a particular back−azimuthal direction. Therefore, the effect from anisotropy is unlikely to generate the observed velocity anomalies. Locally depressed 410−km discontinuity can generate a relatively low velocity anomaly at the depressed zone because the velocity of olivine above the discontinuity is slower than wadsleyite. However, the Vp/Vs variation across the seismic discontinuity is significantly less (~0.61%) than the observed variation. Compositional heterogeneities in the upper mantle can drive seismic velocity changes (Xu et al., 2008). Changing the composition from pyrolite to harzburgite results in decrease in Vs (−0.34%) while decrease in Vp/Vs (−0.69%), which cannot simultaneously explain the observed pattern of slower Vs and higher Vp/Vs. Also, changing the

composition from pyrolite to pyroxenite increases both Vs (3.96%) and Vp/Vs (0.4%), which are also inconsistent with the patterns. Increasing of water content in wadsleyite cause decreases in Vp and Vs, while there is an only weak increase in Vp/Vs (<0.3%/C_{OH}=1%) (Karato, 2011). The presence of melt effectively reduces Vp, Vs, while increases Vp/Vs (e.g., Takei, 2002). Assuming pyrolite composition with mantle potential temperature of ~1300° C, ~0.2–0.7% of melt can simultaneously explain the observed Vs reduction and Vp/Vs increase (1.93~1.96%). Previous studies observed slower Vp (−0.5–2.0%), Vs (−2–−4%), and higher Vp/Vs (~0.1–2.6%) above the 410−km discontinuity (Han et al., 2021; Tauzin et al., 2017), which correspond to our results. The imaged velocity reductions have been interpreted as an effect from a melt layer above the MTZ with variable thickness (10~110 km) (e.g., Han et al., 2021; Tauzin et al., 2010). A relatively thick low−velocity layer (80~100 km) has been imaged by receiver function analysis (Tauzin et al., 2017) beneath the Korean Peninsula. Together with previously observed low−velocity anomalies atop the MTZ, the imaged structure above the 410−km discontinuity in our result possibly reflects the effect from the thick melt layer above the MTZ (e.g., Schmandt et al., 2011).

The melt layer above the 410−km discontinuity has been suggested to generate by the water−induced partial melting due to upward flow from the MTZ (Bercovici & Karato, 2003; Han et al., 2021; Z. Liu et al., 2016; Tauzin et al., 2017). The complex morphology of the slab such as slab gap or tear can generate localized mantle upwelling (James et al., 2011; Liu & Stegman, 2012; Portner et al., 2017). Numerical models suggested that the subducting slab can generate upward flow at the slab−edge (Faccenna et al., 2010;

Yang & Faccenda, 2020), leading to deep dehydration melting by vertical flow at the nearby wet MTZ (Li et al., 2013; Z. Liu et al., 2018). A spatial coincidence between the imaged slab gap and the low-velocity anomaly and high Vp/Vs above the MTZ potentially reflects dynamic interaction between the subducting slab and the MTZ mantle.
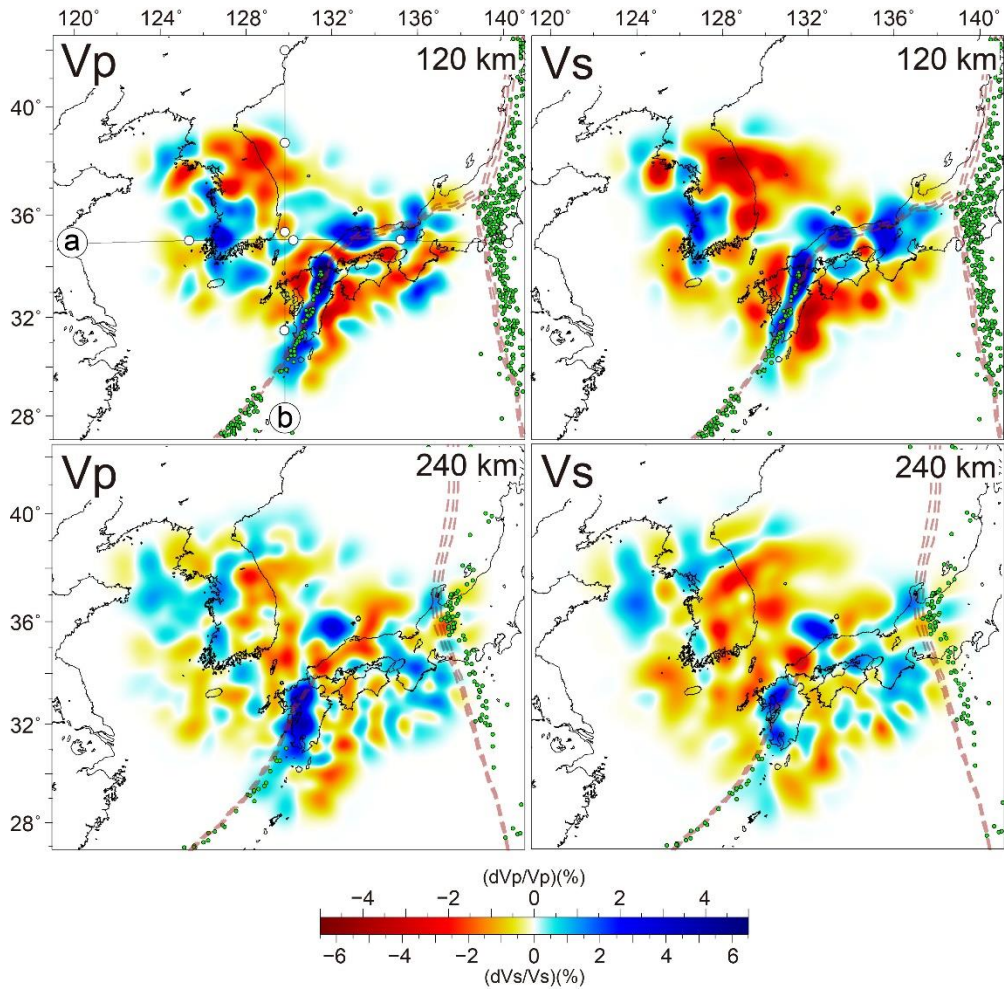
Figure 3.10 Horizontal cross-sections through the P (Vp; left) and S (Vs; right) wave tomography at depths of 120 and 240 km. The green dots indicate earthquakes that occurred within a depth range of ± 15 km for the sliced depths. The brown dashed contours indicate slab depths at 10-km intervals within a depth range of ± 15 km for the sliced depths.
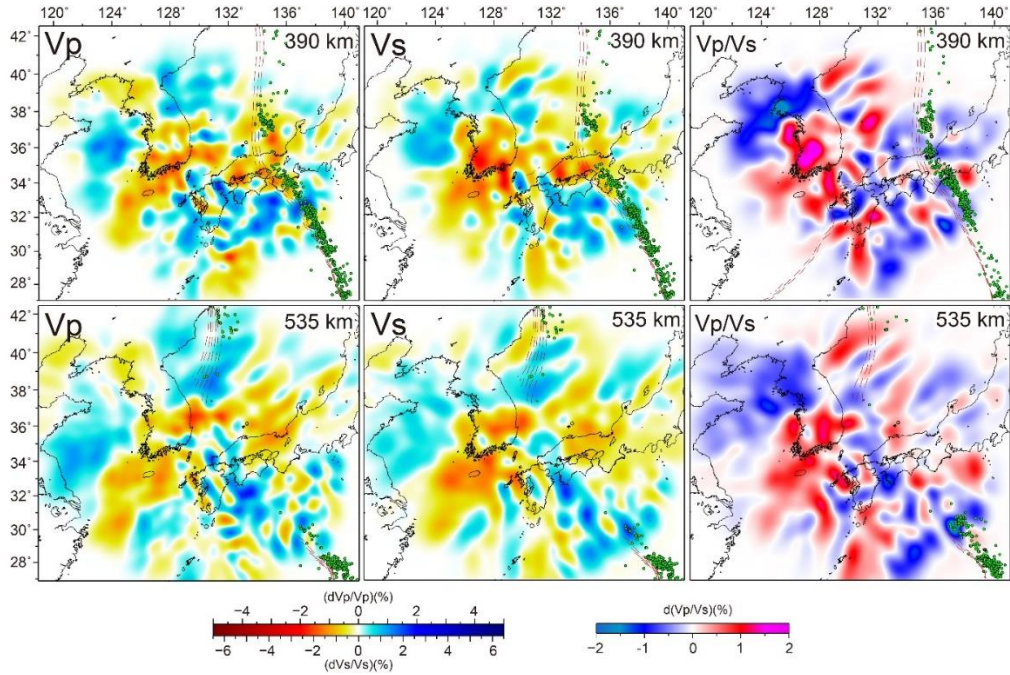
Figure 3.11 Horizontal cross−sections through P (Vp; left) and S (Vs; middle) wave tomography, and the Vp/Vs (right) at depths of 390 and 535 km. Slab depths and earthquakes are indicated by brown dashed contours and green dots, respectively, within a depth range of ±15 for the 390 km and ±30 km for the 535 km depth profiles.
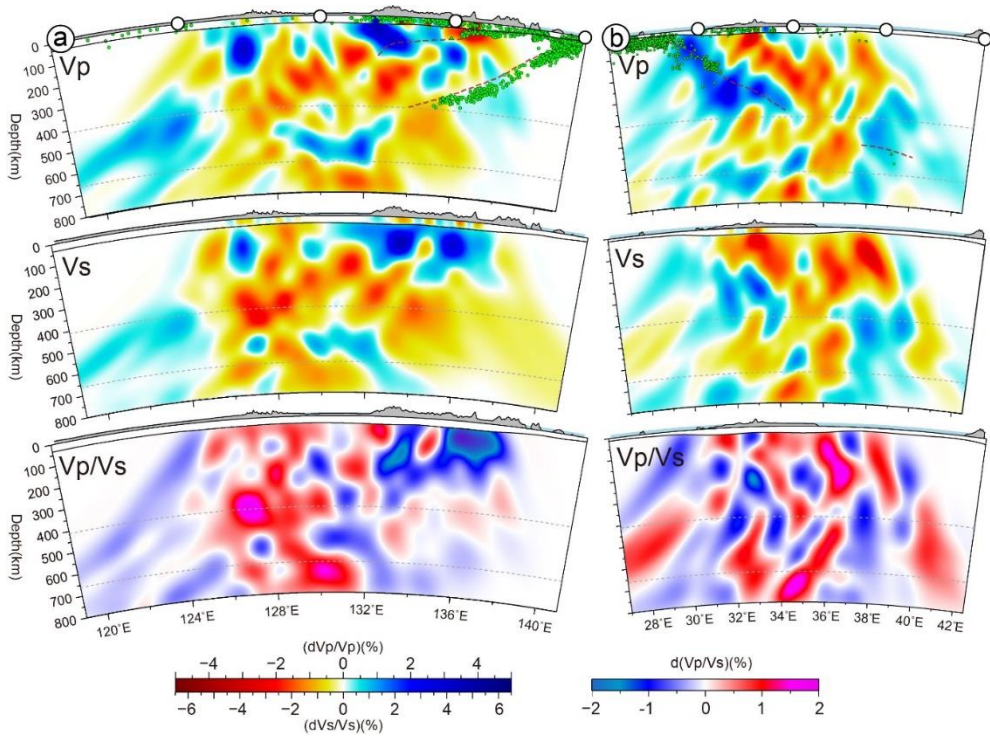
Figure 3.12 Vertical cross-sections of P (Vp; top) and S (Vs; middle) wave tomography, and the Vp/Vs (bottom). The locations of the cross-sections are shown in the 390 km depth profile of Vp in Figure 3.10. Green-dots represent earthquakes within an orthogonal distance range of ± 0.5 degree from each cross sections.
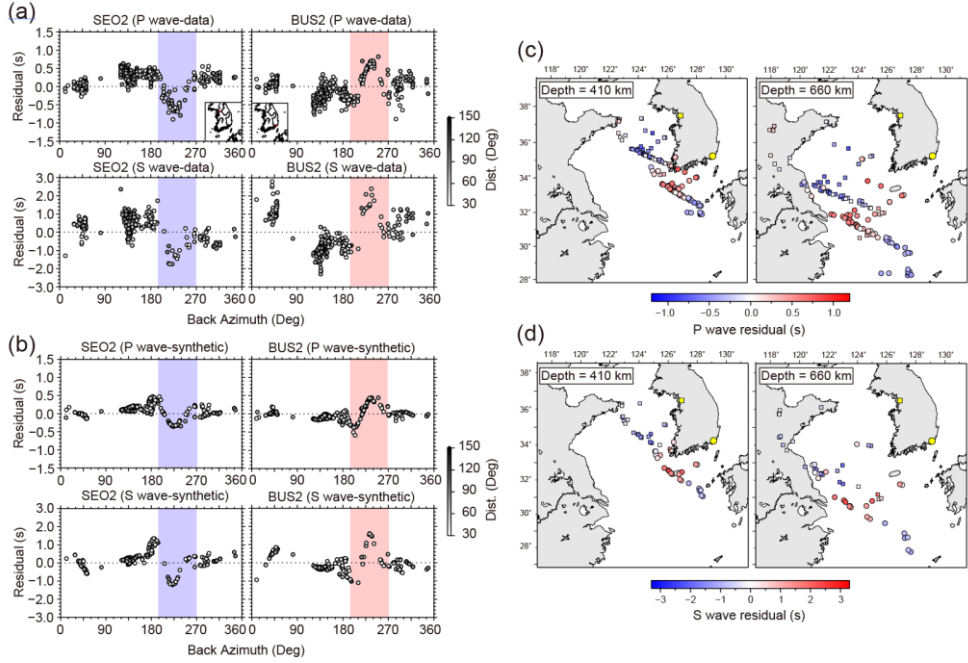
Figure 3.13 Back−azimuthal variation in P and S wave travel time residuals. (a) Observed residual plots for stations SEO2 (left) and BUS2 (right). The locations of stations are indicated by the red dot in the inset maps. The blue and red shades indicate degree ranges of sharp residual variations. (b) Synthetic residual plots for stations SEO2 (left) and BUS2 (right) using regional 3−D P and S wave velocity models of Tao et al., 2018 at depths from 400 to 800 km. (c) P wave residuals of the two stations projected onto the 410 (left) and 660 (right) km. The yellow squares indicate station locations. (d) Same as (c) but for S wave residuals.
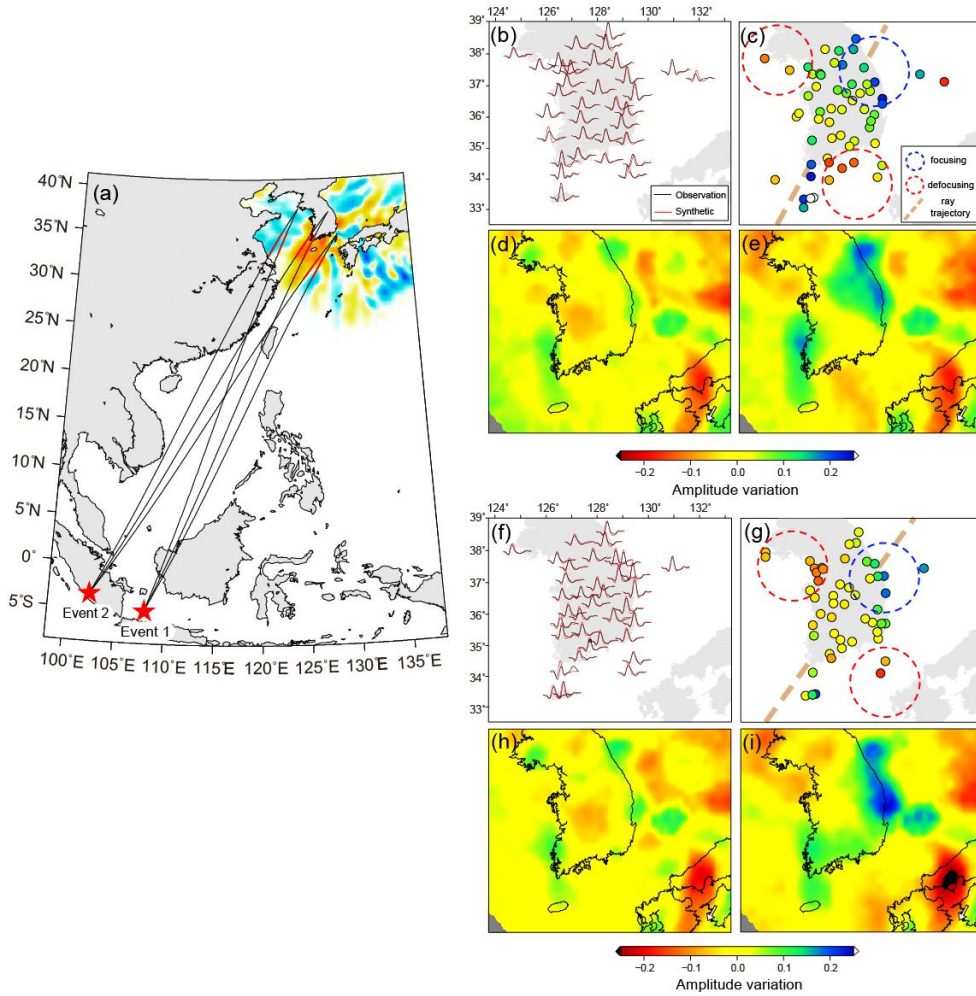
Figure 3.14 Synthetic waveform simulation results of S wave. (a) Map showing the events, ray trajectories, and the velocity model (Vs at a depth of ~560 km). Black solid lines represent the ray trajectories from the events with parts of rays crossing the depth between 660 and 410 km on the receiver side indicated by the red lines. (b) Comparison of observed (black) and synthetic (red) transverse component S waves for Event 1. (c) Amplitude variation of the observed waveform. The amplitude variation is calculated as the difference between the amplitude of the waveform at each receiver and the average amplitude of all receivers on a logarithmic scale. The area where the wave amplitude is amplified (reduced) by

wave focusing (defocusing) is indicated by blue (red) dashed circle. (d) Synthetic amplitude variation with a 3-D model using only the upper mantle at depths less than 350 km. (e) Synthetic amplitude variation with a 3-D model with the deeper upper mantle (350 to 800 km) included. (f–i) Same as (b–e) but for the results of event 2.
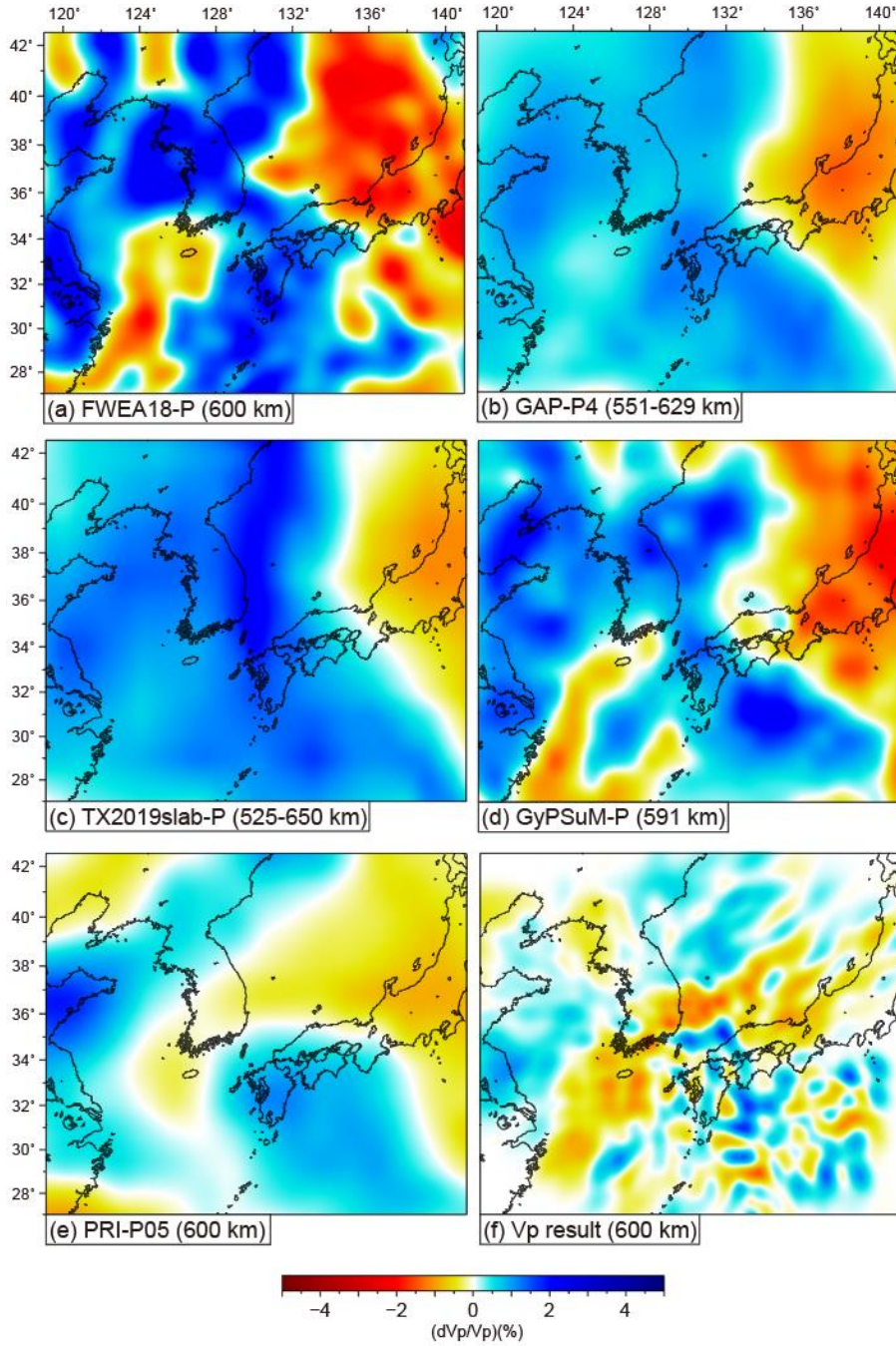
Figure 3.15 Comparisons of P wave velocity of different models within the mantle transition zone (MTZ). The models in comparisons are (a) P wave velocity perturbations at 600 km depth from FWEA18 (Tao et al., 2018), (b) P wave velocity perturbations at 551−629 km depths from GAP−P4 (Fukao & Obayashi, 2013), (c) P wave velocity

1 4 6

perturbations at 525–650 km depths from TX2019slab–P (Lu et al., 2019), (d) P wave velocity perturbations at 591 km depth from GyPSuM–P (Simmons et al., 2010), (e) P wave velocity perturbations at 600 km depth from PRI–P05 (Montelli et al., 2004), and (f) P wave velocity perturbations at 600 km depth from this study.
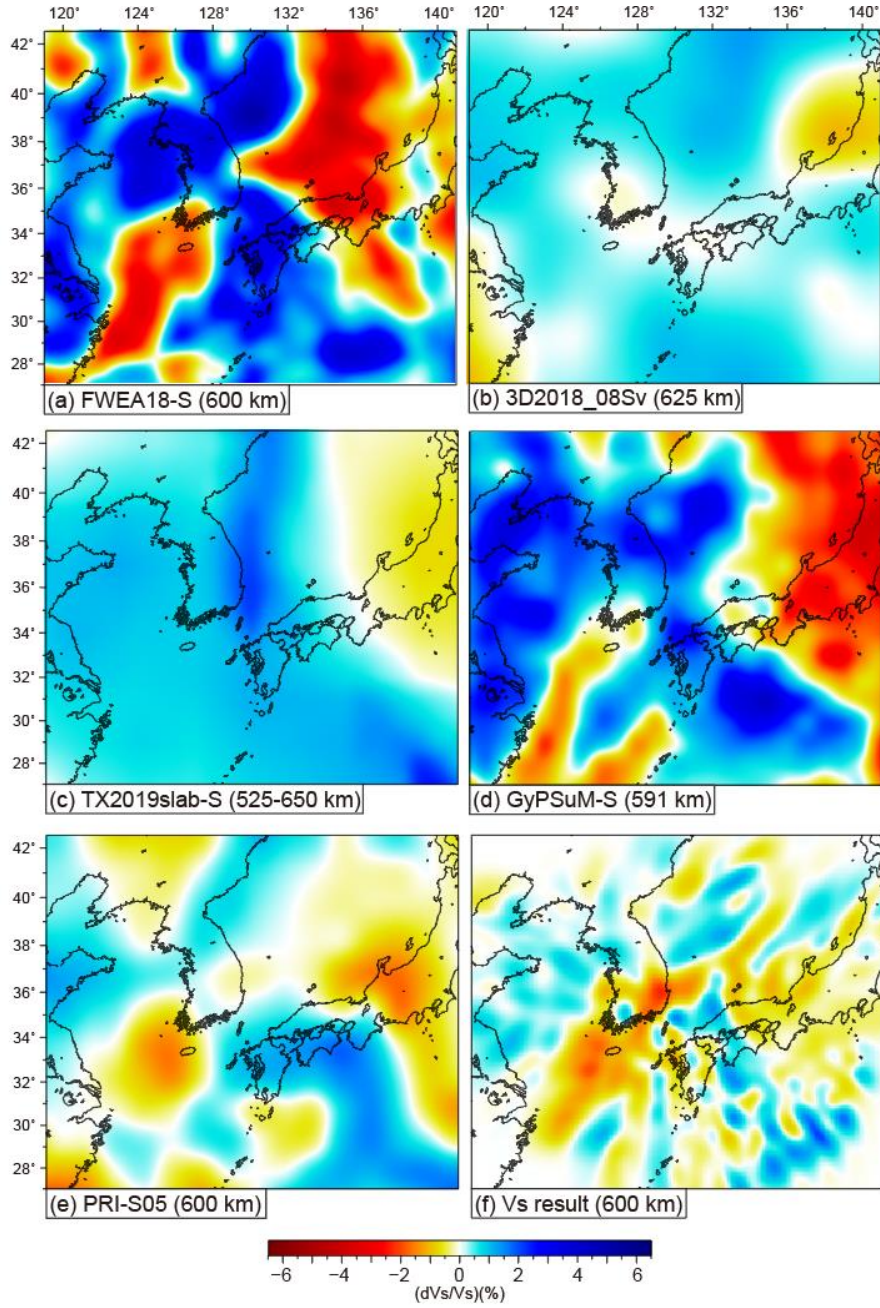
Figure 3.16 Comparisons of *S* wave velocity of different models within the MTZ. The models in comparisons are (a) *S* wave velocity perturbations at 600 km depth from FWEA18 (Tao et al., 2018), (b) *S* wave velocity perturbations at 625 km depth from 3D2018_08Sv (Debayle et al., 2016), (c) *S* wave velocity perturbations at 525–650 km depths from TX2019slab−S (Lu et al., 2019), (d) *S* wave velocity

perturbations at 591 km depth from GyPSuM—S (Simmons et al., 2010), (e) *S* wave velocity perturbations at 600 km depth from PRI—S05 (Montelli et al., 2004), and (f) *S* wave velocity perturbations at 600 km depth from this study.
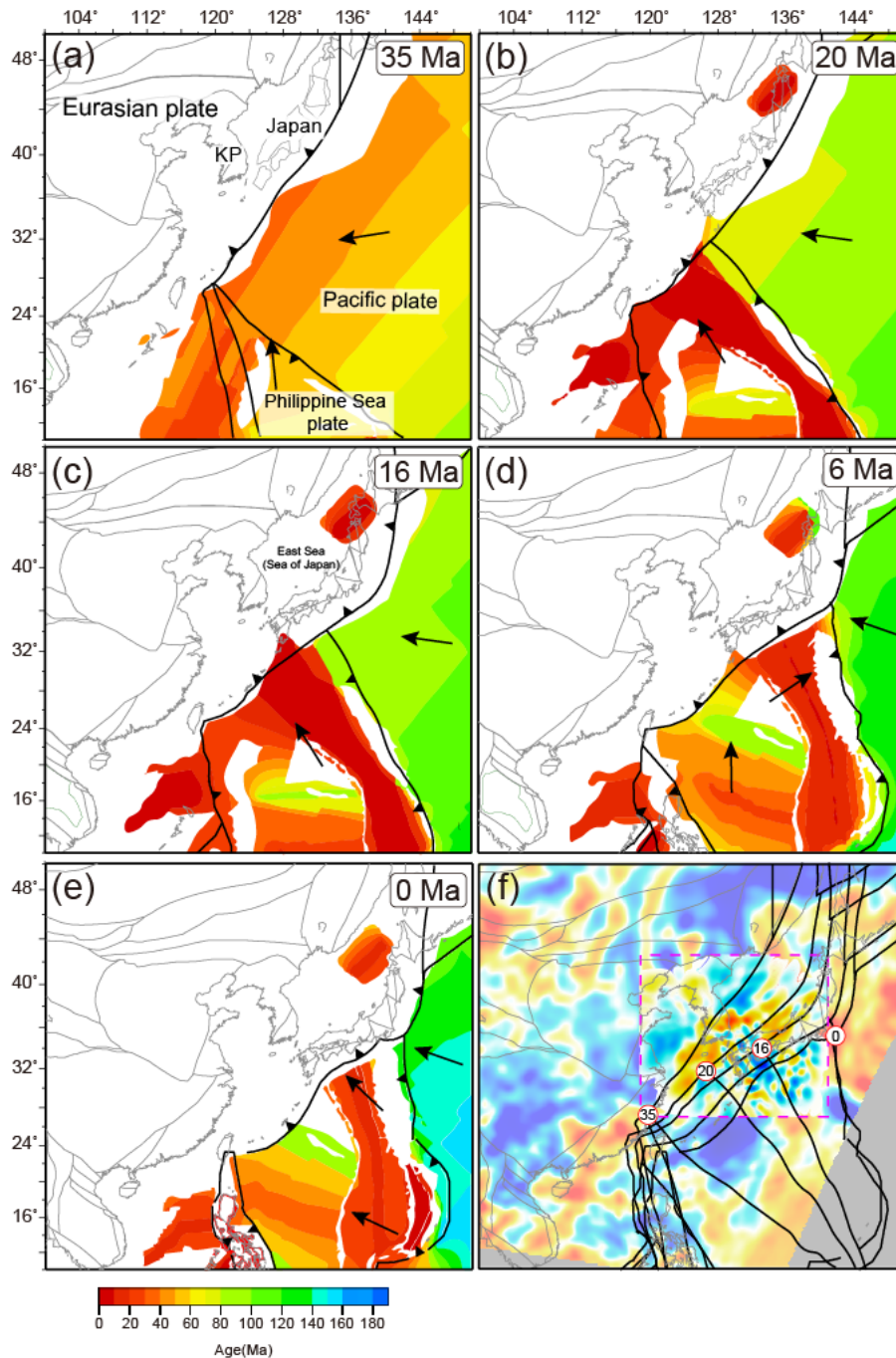
Figure 3.17 Plate reconstruction model in northeast Asia margin during the Cenozoic. The locations of plate boundaries are reconstructed from GPlates (Boyden et al., 2011) with colored seafloor ages from Müller et al. (2008). (a–e) Plate reconstructions at ages from 35 to 0 Ma. The black arrows indicate the direction of

plate motion of the Pacific plate and Philippine Sea plate with respect to the Eurasian plate. Convergent plate boundaries are shown with black saw-toothed lines. (f) S wave velocity image at a depth of 600 km superimposed by the plate boundaries at ages of 35, 20, 16, and 0 Ma. The velocity models inside and outside of the pink square are from this study and FWEA18 (Tao et al., 2018), respectively.
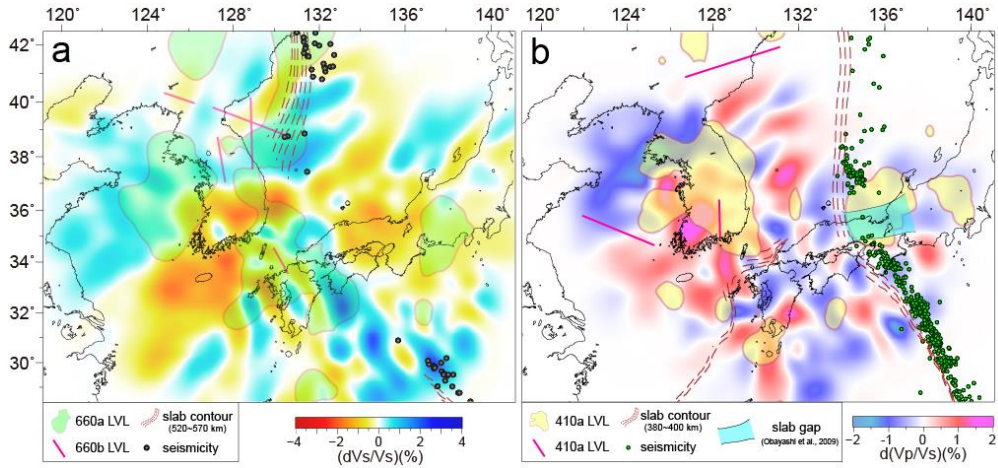
Figure 3.18 Tomographic results with main interpreted features. (a) A horizontal cross-section of Vs at a depth of 535 km. (b) A horizontal cross-section of the Vp/Vs at a depth of 390 km. Brown dashed lines indicate the depths of 410-km and 660-km discontinuities (Lee et al., 2014). Gray dotted lines indicate 410 and 660 km depths. 660a LVL: low-velocity layer above the 660-km discontinuity (Tauzin et al., 2017); 660b LVL: low-velocity layer below the 660-km discontinuity (Z. Liu et al., 2016); 410a LVL: low-velocity layer above the 410-km discontinuity (yellow shaded areas are from Tauzin et al. (2017) and pink profiles are from Z. Liu et al. (2016)).

3.4. Conclusions

Using the dense seismic arrays deployed in the Korean Peninsula and southwestern Japan, we construct high resolution 3-D upper mantle velocity models to deeper depths (~800 km) at the continental margin of northeast Asia by teleseismic body-wave traveltime tomography. We find a distinct velocity variation within the MTZ that has a spatial correlation with the upper mantle heterogeneities revealed by previous receiver function studies. We suggest that the velocity pattern reflects a wide and pronounced gap within the stagnant Pacific slab along the current continental margin. In addition, there are geographic correlations between the inferred slab gap, a fragmented slab structure at the bottom of the MTZ, small-scale (<200 km) low-velocity anomalies with high Vp/Vs, and the negative reflectivity above the 410-km discontinuity. This coincidence potentially indicates the melt generation process by an upward flow of wet MTZ materials induced by the subducting slab. The dynamic interaction between the non-uniformly distributed Pacific slab and the MTZ is suggested to play a major role in controlling the mantle dynamics during the Late-Cenozoic periods at the northeast Asia margin.

Chapter 4. Seismic Evidence of Persistent Intraplate Volcanism by Shallow Mantle Melting in Northeast Asia

4.1. Introduction

Unraveling the mechanism of intraplate volcanism, which is an effusive volcanic activity away from plate boundaries, is essential to understand the extent of mantle convection and evolution of thermochemical properties of the Earth's mantle. While some intraplate volcanic activities can be explained by mantle plume theory (Morgan, 1971), there are several non-hotspot intraplate volcanoes whose mechanisms are poorly understood. Several models have been proposed to explain localized melt generation and volcanic eruptions based on upper mantle processes, such as mantle upwelling caused by asthenospheric shear (Conrad et al., 2010), gradients in lithospheric thickness (King & Anderson, 1998), lithospheric cracking by tectonic stresses (Sandwell et al., 1995), buoyant melting instability (Hernlund et al., 2008), sublithospheric convective instability (Ballmer et al., 2007), and kinematic or thermochemical influences by subducting slab (Faccenna et al., 2010; Liu & Stegman, 2012; Richard & Iwamori, 2010; Yang & Faccenda, 2020). However, the characteristics of intraplate volcanism showing episodic and multiple eruptions without a clear trend of spatiotemporal evolution that accords with plate tectonics inhibited a simple and unified explanation of mantle dynamics for mantle upwelling and melt focusing, and the mechanism of intraplate volcanism often remains enigmatic.

There are widespread Cenozoic intraplate volcanoes in the continental part of northeast Asia. Previous studies suggested several modes of upper mantle dynamics, such as large scale hot and wet upper mantle convection above the stagnant Pacific slab (Kuritani et al., 2011; Zhao et al., 2009), high temperature narrow mantle upwellings from the MTZ (Tang et al., 2014; Tao et al., 2018), and upwellings of hydrous MTZ materials and dehydration melting instigated by subducting slab (Yang & Faccenda, 2020). However, none of the proposed models have been evaluated based on the detailed information on physical conditions of the upper mantle, and debates persisted over the relative contributions of different portions of the mantle (e.g., lithosphere, asthenosphere, subducting slab) in deriving melt focusing beneath intraplate volcanism.

In this study, we constrained the physical properties of the upper mantle in the northeast Asia margin based on high−resolution seismic tomography (Vs and Vp/Vs), seismic attenuation, and thermodynamic calculations, to better understand the mechanism of Cenozoic intraplate volcanism in this area. Along the northeast Asia margin, which includes the Korean Peninsula and the East Sea (Sea of Japan) (Figure 4.1a), there are several Quaternary intraplate volcanic events: Hantangang River Volcanic Field (~0.52 Ma to ~0.12 Ma) (A in Figure 4.1a), Baekdusan (Changbaishan) (~22.6 Ma to ~1.0 ka) (B in Figure 4.1a), Ulleung Island (~1.3 Ma to ~2.7 ka) (C in Figure 4.1a), and Jeju Volcanic Island (~1.8 Ma to ~1.0 ka) (D in Figure 4.1a). Neogene volcanic eruptions are sporadically distributed adjacent to the Quaternary volcanism in the Korean Peninsula (~9−4 Ma) and the East Sea (~12−2 Ma), indicating that there were multiple episodes of volcanic activities over an extended period of time within confined areas. Major tectonic events in the Cenozoic occurred during

the late Oligocene to middle Miocene (~14 Ma), when back−arc extension and continental rifting formed the East Sea (Chough et al., 2018), placing our study area into a stable tectonic environment. The study area offers a unique opportunity for assessing the mechanism of intraplate volcanism in northeast Asia because 1) there are active volcanoes (e.g., Baekdusan, Ulleung Island) (Mclean et al., 2020), which were intensively studied with various modes of upper mantle dynamics suggested (e.g., Wang et al., 2015; Tang et al., 2014; Yang & Faccenda, 2020), 2) high resolution seismic tomography models constructed based on dense seismic arrays exist (e.g., Simutė et al., 2016; Song et al., 2020; Tao et al., 2018), which enables detailed examination on upper mantle structure. We present the evidence of the presence of shallow mantle melting at common depths of ~65− 130 km focused beneath the Quaternary intraplate volcanoes, and propose that shallow upper mantle melting focusing played an important role in deriving intraplate volcanism in northeast Asia.
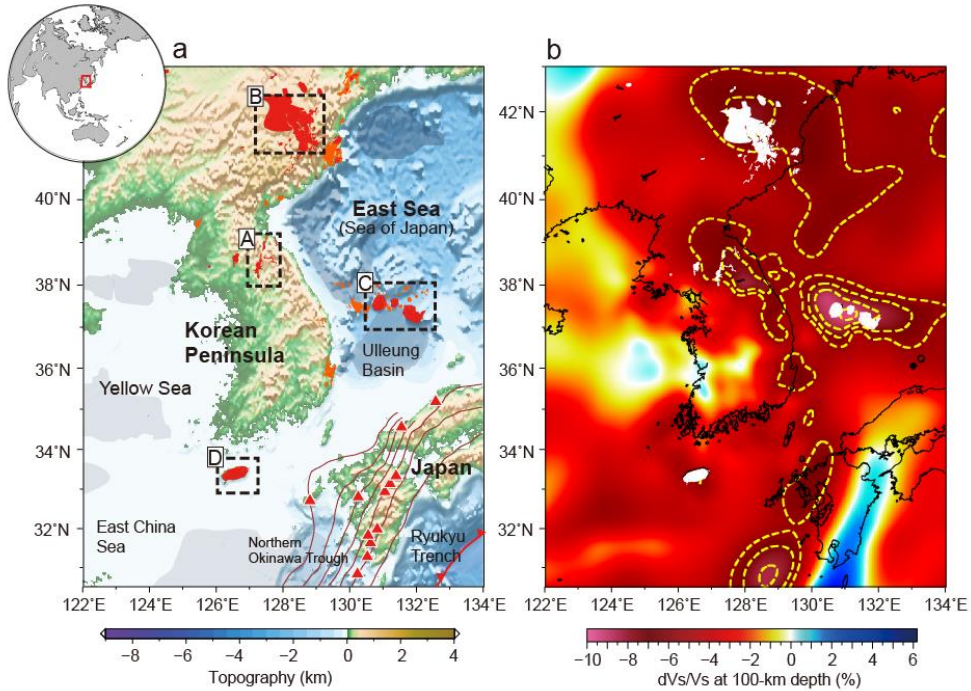
Figure 4.1 Map of Cenozoic volcanism in northeast Asia margin and the upper mantle seismic velocity. (a) Tertiary and Quaternary volcanic activities are shaded in orange and red, respectively. The dashed rectangular boxes show major Quaternary volcanic areas (A: Hantangang River Volcanic Field, B: Baekdusan (Changbaishan), C: Ulleung Island, D: Jeju Volcanic Island). Arc volcanoes are plotted as red triangles. The red saw-toothed line indicates the convergent plate boundary between the Eurasian plate and the Philippine Sea plate (Bird, 2003). Cretaceous to Cenozoic extensional basins are shaded in gray (Ren et al., 2002). Depths of the subducting oceanic slab are indicated by brown dashed contours at 50-km intervals (Slab2.0; Hayes et al., 2018). (b) Shear wave velocity map at the upper mantle depth of 100-km in the study area. Yellow dashed lines indicate velocity contours of dlnVs ≤ −6% at 1% intervals with respect to the ak135 global reference model (Kennett et al., 1995). Quaternary volcanic regions are shaded in white.

4.2. Methods

Constraints on the distribution and content of partial melt can provide direct evidence for thermodynamic properties of the upper mantle, which are key to understanding the evolution of intraplate volcanism (Davies & Rawlinson, 2014; Havlin et al., 2021; Sigurdsson et al., 2015). High resolution seismic tomography can provide detailed information on the thermal and compositional properties of the upper mantle (e.g., An et al., 2015; Schmandt & Humphreys, 2010b; Wei et al., 2015). However, inferring thermodynamic states of the upper mantle from tomographic models is often challenging because of difficulties by 1) nonlinear responses of mantle materials to seismic wave propagation, 2) nonlinear relationships among physical parameters (e.g., temperature, pressure, grain size) that define mantle rheology (e.g., Abers et al., 2014), and 3) frequency and wave type (e.g., P or S wave) dependent sensitivity of seismic waves on the mantle properties (e.g., Fichtner et al., 2014; Hung et al., 2000). Therefore, a comprehensive analysis of seismic data, such as seismic wave speed and anelastic attenuation, along with quantitative descriptions of mantle rheology that potentially affects seismic wave propagation are necessary to constrain the physical state of the upper mantle.

4.2.1. Seismic Velocity Models

We use voigt−average P and S wave velocities from the full waveform tomography models in northeast Asia (CSEM, Simutė et al., 2016; FWEA18, Tao et al., 2018) for the thermodynamic interpretation of the upper mantle in our study area. Using a full waveform tomography model facilitates a quantitative analysis of thermodynamic states of the upper mantle as it provides absolute velocity information that allows the observed wave speed to be directly compared to the velocity predicted by thermodynamic parameters (e.g., temperature, pressure) and chemical compositions (e.g., Cobden et al., 2018).

The original models are further refined by teleseismic travel time datasets measured from P and S wave waveforms in the period range of 0.5−10 s recorded by dense seismic arrays around the Korean Peninsula (Figure 4.2) (Song et al., 2020). This is done by inverting both teleseismic P and S wave travel time datasets using the full waveform tomography models as a starting model. For the teleseismic data, we used datasets of source−receiver pairs that record both P and S wave arrivals, which add up to 64074 rays from 278 events between 2013 and 2018. The use of common source−receiver pairs of the different wave types minimizes biases in an inverted Vp/Vs model resulting from different data coverages. Traveltime residuals are measured by interstation coherency in the P and S wave waveforms (Rawlinson & Kennett, 2004). The uncertainties of travel time residuals are determined based on waveform similarity (Rawlinson & Kennett, 2004) and used as data weight during the inversion.

Fast marching ray-tracing (Rawlinson et al., 2006b) and the subspace inversion scheme (Kennett et al., 1988) are used iteratively to perform tomography. We define a model space spanning a depth of ~800 km with a uniform grid spacing of ~10 km in the crust and ~20 km in the mantle. 3-D local crustal structure (Rhie et al., 2016) with Moho interfaces (Chang & Baag, 2007; Y. Kim et al., 2015) are used for crustal structures, and both crust and upper mantle are simultaneously inverted with fixed Moho depths. By this way, we reduce artifacts that arise by smearing of crustal heterogeneity in the upper mantle due to limited resolution of our dataset at crustal depths. The objective function used for the inversion consists of data residuals, model misfit and roughness with respect to the starting model (Rawlinson et al., 2003). Regularization factors, i.e., damping and smoothing, are systematically determined by evaluating the trade-offs between the data misfit, model smoothness, and model variance (Rawlinson et al., 2006b). We additionally apply spatial smoothing for the Vp/Vs model by calculating first- and second-derivative smoothness of Vp/Vs, which were added to the smoothness of Vp and Vs models. We first determine optimum solutions for Vp and Vs individually, and using the determined regularization factors of each model, we conduct the joint inversion with an additional smoothing parameter that controls Vp/Vs smoothness constrained by a trade-off curve analysis (Figure 4.3). The total data misfit is calculated as a sum of P and S wave residuals weighted by their respective data norms and uncertainties, so that both data sets contribute equally to determining the final model (Table 4.1). Differences in reference models only have minor changes in amplitudes and patterns of Vp/Vs (e.g., Giacomuzzi et al., 2012; Liang et al., 2011; Papaleo et al., 2018). The resulting model

depicts sharper structural variations with enhanced amplitudes of up to ~−2% in dVs and ~+1% in dVp/Vs compared to the original model around the Korean Peninsula (Figures 4.4 and 4.5).

The resolution of the full waveform model of FWEA18, evaluated by the degree of structural distortion based on the preconditioned Hessian−vector product, shows that an average resolution length to be 50–80 km throughout the upper mantle in northeast Asia (Tao et al., 2018). The resolution of the full waveform model of CSEM (Simutė et al., 2016) is analyzed by random probing (Fichtner & Leeuwen, 2015), showing that scale lengths of ~150 km and ~30 km can be recovered in the horizontal and vertical directions, respectively. For the resolution for the teleseismic traveltime dataset, we conduct checkerboard tests. Checkers with diameters of 40 and 80 km at a half amplitude and amplitudes of ±3 for Vp, ±7 for Vs, and ±4% of Vp/Vs are applied. The results show that the initial structures are recovered to a depth of ~200 km beneath the mainly interpreted regions (Figures 4.6 and 4.7). Based on the resolution test results of teleseismic datasets and full waveform inversion models, we conclude that the seismic model combining FWEA18 and the teleseismic dataset, which is mainly interpreted in our study, has a resolution on both horizontal and vertical directions with scale lengths of ~40 to ~80 km in the upper mantle, and the model combining CSEM and the teleseismic dataset has a resolution ~40 to ~150 km in horizontal, and ~40 km in vertical direction.
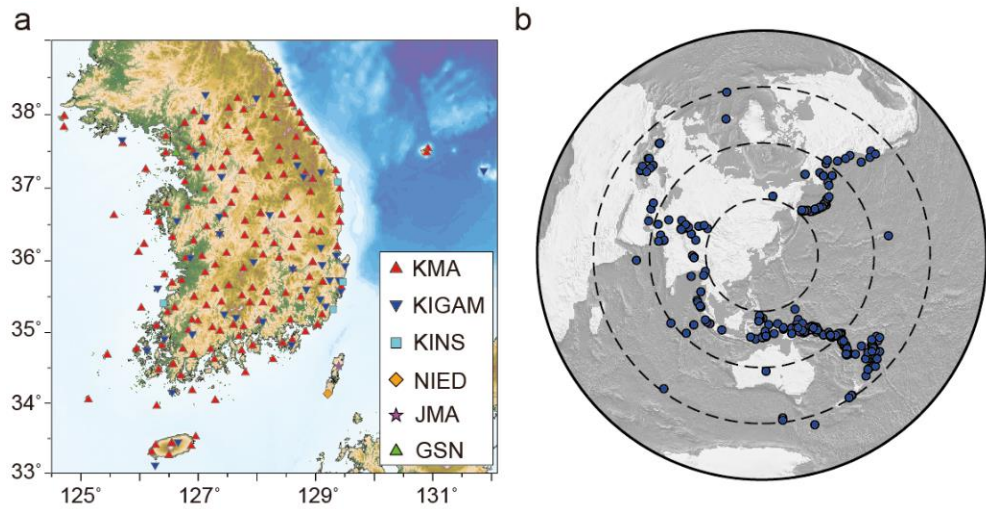
Figure 4.2 (a) Seismic stations and (b) events of teleseismic P and S wave traveltime datasets. Dashed concentric circles in (b) indicate great circle distances at a 30-degree interval. KMA: Korea Meteorological Administration; KIGAM: Korea Institute of Geoscience and Mineral Resources; KINS: Korea Institute of Nuclear Safety; JMA: Japan Meteorological Agency; NIED: National Research Institute for Earth Science and Disaster Resilience; GSN: Global Seismic Network.
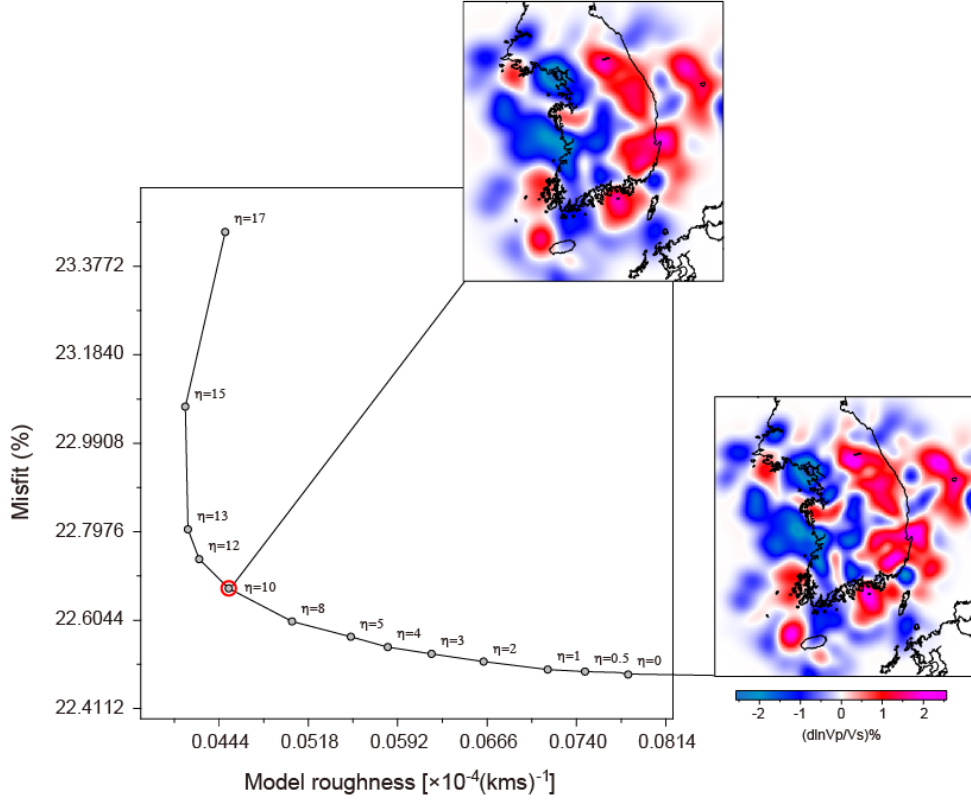
Figure 4.3 Determination of a smoothing parameter for the Vp/Vs model. The red circle indicates the final model. Examples of Vp/Vs at 120 km depth are shown.

	P wave	S wave	Joint model
Individual	82.64%	76.26%	-
Joint	82.73%	75.93%	77.29%
Joint with 3D model	81.92%	76.78%	77.81%

Table 4.1. Variance reductions of P, S wave tomography, and the joint inversion model. The individual and joint model use ak135 global reference model (Kennett et al., 1995), and joint with 3−D model use FWEA18 (Tao et al., 2018) as a starting velocity model in the tomographic inversion.
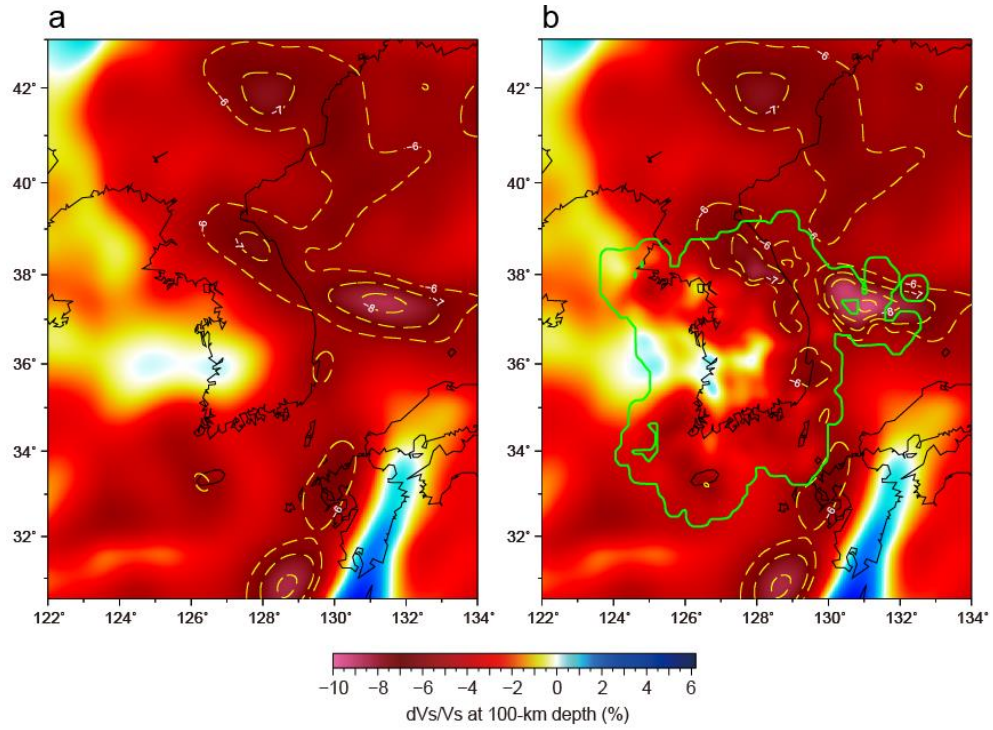
Figure 4.4 Comparison between (a) original full waveform tomography model of FWEA18 (Tao et al., 2018) and (b) the model refined by teleseismic travel time dataset (Song et al., 2020). The green line indicates the refined area.
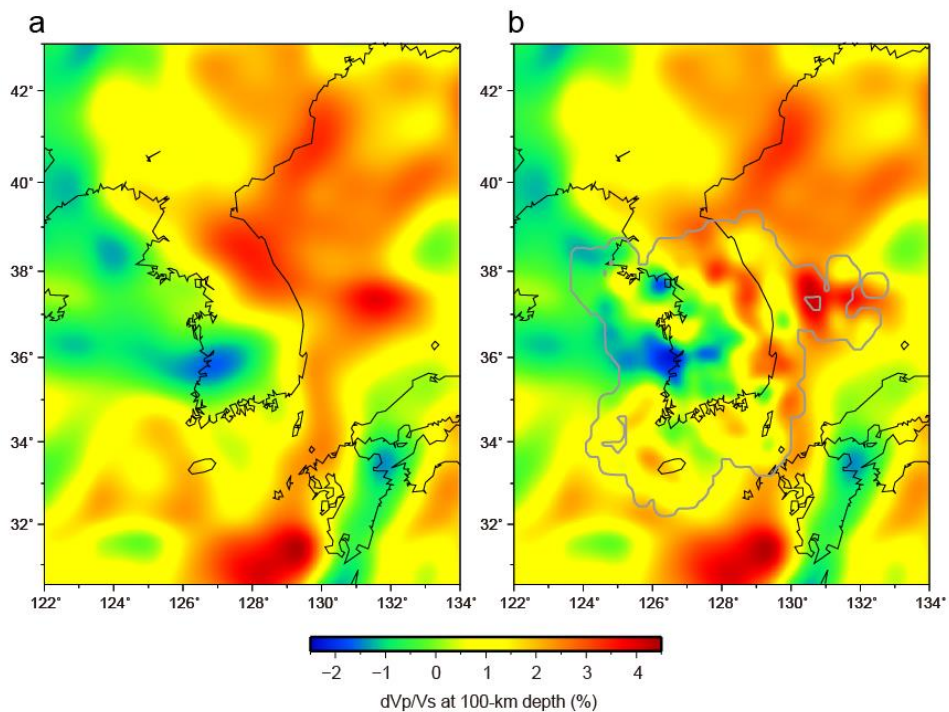
Figure 4.5. Comparison between d(Vp/Vs) of (a) FWEA18 (Tao et al., 2018) and (b) a model refined by teleseismic travel time dataset (Song et al., 2020). The gray line in (b) indicates the refined area.
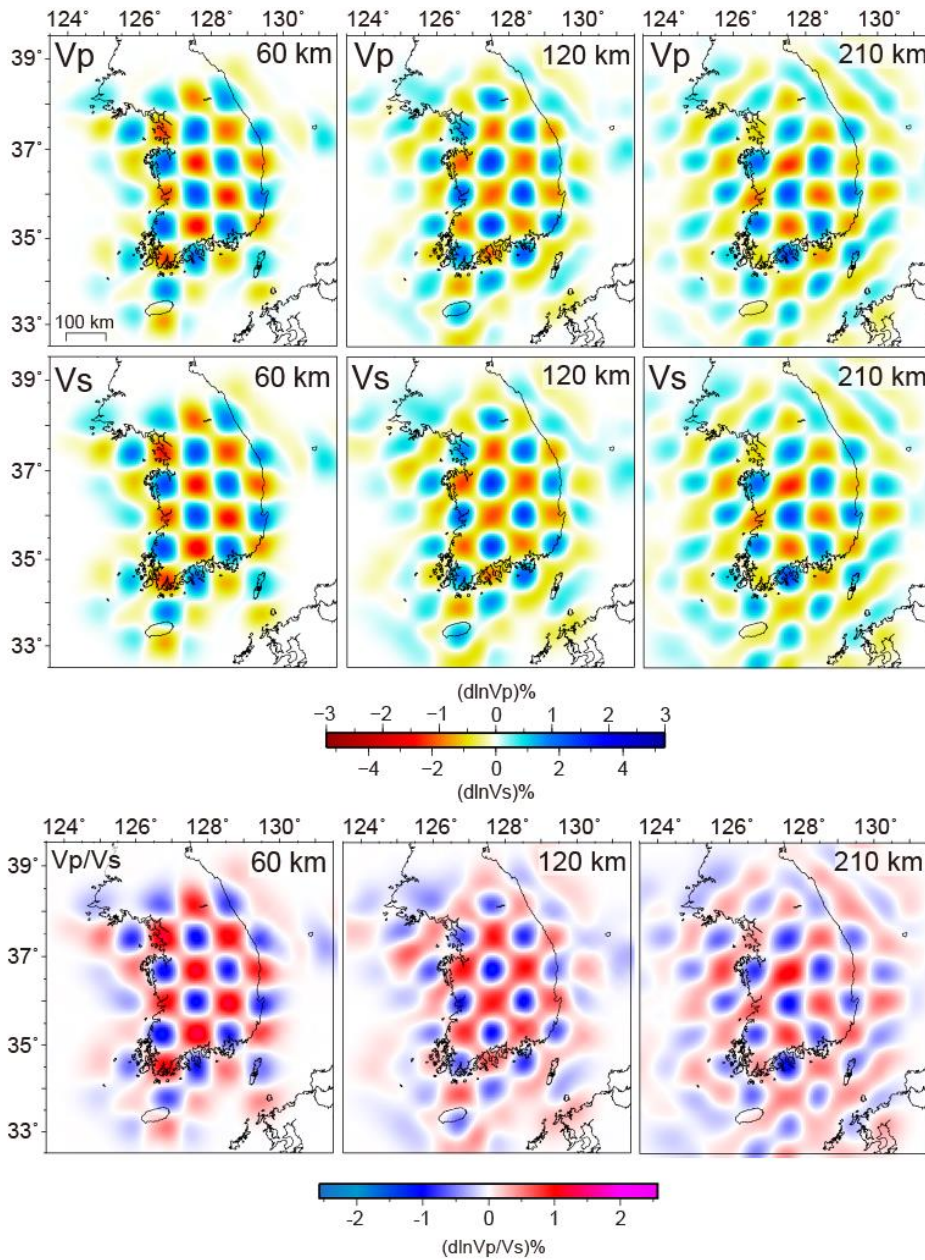
Figure 4.6. Checkerboard resolution tests for Vp, Vs, and Vp/Vs. The initial checkerboard models consist of checkers with amplitudes of ±4% in dVp, ±7% in dVs, and ±3% in dVp/Vs, and sizes of ∼40 km at a half amplitude. The depths of each section are indicated in the upper right corner.
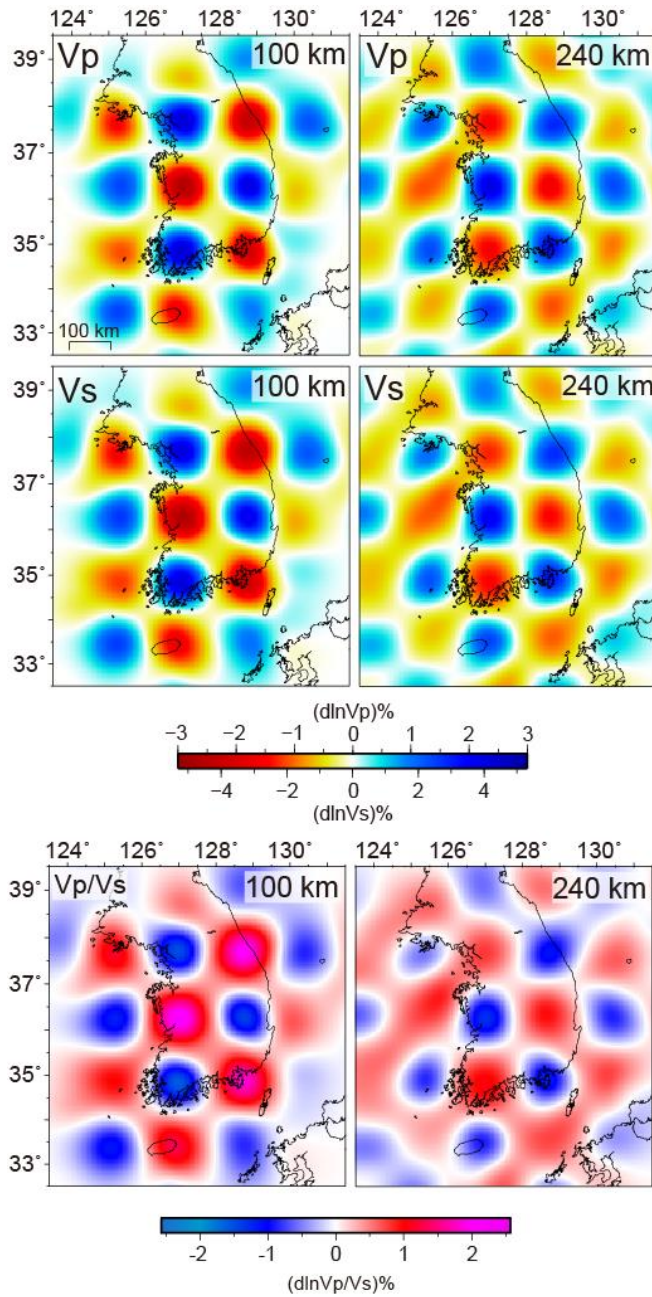
Figure 4.7. Checkerboard resolution tests for Vp, Vs, and Vp/Vs. The initial checkerboard models consist of checkers with amplitudes of ±4% in dVp, ±7% in dVs, and ±3% in dVp/Vs, and sizes of ~80 km at a half amplitude. The depths of each section are indicated in the upper right corner.

4.2.2 Thermodynamic Calculations

The upper mantle seismic velocity is primarily sensitive to rheological properties of the mantle, which depend on temperature, pressure, and composition (e.g., melt) (Cammarano & Romanowicz, 2007; Goes et al., 2000). At high temperatures (>900 ゜C), anelastic effects are significant and a linear relationship between the increased temperature and decreases in elastic moduli at lower temperature is no longer maintained (Karato, 1993). Therefore, it is necessary to consider anelastic effects to infer thermodynamic properties of the upper mantle from seismic velocity models.

There are several anelastic models proposed based on laboratory experiments using mantle minerals (e.g., olivine) or rock analogues (e.g., organic polycrystal) at a variable temperature, pressure, grain size, and frequency range (Faul & Jackson, 2005; Jackson & Faul, 2010; McCarthy et al., 2011; Yamauchi & Takei, 2016). The anelastic effect is associated with a process of energy loss, which depends on the frequency of an elastic wave and the characteristic frequency of relaxation (Takei, 2017). We calculate the anelastic effect from previously published anelastic models (Faul & Jackson, 2005; Jackson & Faul, 2010; McCarthy et al., 2011; Yamauchi & Takei, 2016). Each model is constructed based on laboratory experiments using different formulations and experimental conditions. We use scaling relationships parameterized by an extended Burgers model for the Faul and Jackson (2005) and Jackson and Faul (2010). Using melt－free polycrystalline aggregates of Fo90 olivine, Faul and Jackson (2005) fitted forced－oscillation data at temperatures of 1000–1200 ゜C and oscillation periods of 1–1000s based on high－temperature background dissipation with a fractional adjustment to

shear modulus at viscoelastic regime. Jackson and Faul (2010), using olivine polycrystal, accounted for high-temperature background dissipation at larger temperature ranges (800–1200 °C) with a constrainment on a semi-empirical high-frequency absorption peak. McCarthy et al. (2011) measured the viscoelastic properties of polycrystalline organic borneol, as an analogue to mantle rock, suggesting the universal scaling (Maxwell frequency scaling) over a broad frequency range (1e-4–2.15 Hz) at homologous temperatures of T/T_m = 0.61–0.67, where T_m indicating melting temperature. Yamauchi and Takei (2016), based on Maxwell frequency scaling, constrained elasticity, anelasticity, and viscosity of organic borneol at near solidus homologous temperature (0.92–1), formulating the effects of premelting (e.g., Cantwell et al., 2014) on the dynamical properties of the grain boundary, grain boundary sliding, and grain boundary diffusion creep by introducing a temperature dependent high-frequency peak.

We calculate the anelastic effect for a frequency range 0.02–1.0 Hz, which are within the frequency range used in the seismic velocity models. We constrain a grain size based on dynamic recrystallization and grain growth (e.g., Behn et al., 2009; Podolefsky et al., 2003) for a range of strain rates from 1e-14 to 5e-14/s, which are within the ranges derived from the regional geodynamic model (e.g., Yang et al., 2019). The temperature-velocity relationships predicted with different anelastic models at seismic frequencies and mantle grain sizes show large variability depending on anelastic models (Figure 4.8). Although the anelastic effect of water on seismic velocity is debated (e.g., Aizawa et al., 2008; Cline et al., 2018; Hirth & Kohlstedt, 1996; Karato & Jung, 1998), we consider the possible effects of water on anelasticity in two ways: First, water promotes

viscous and viscoelastic relaxation (Aizawa et al., 2008; Hirth & Kohlstedt, 1996), which enhances anelasticity, and second, the presence of water leads to larger grain size by increasing grain growth rate, which results in a decrease in anelasticity. The competing effects between these two mechanisms result in a mild decrease in anelasticity with increasing water content (e.g., Abers et al., 2014). We calculate for water contents of $C_{OH} = 3$ (dry) and 200 (wet) wt ppm, the latter is found to be incorporated in nominally anhydrous minerals at the upper mantle (~100 km) (Hirschmann et al., 2009). Anharmonic shear and bulk moduli as functions of temperature and pressure are obtained by calculating phase equilibria with linearized free energy minimization (Perple_X, Connolly et al., 2005) for a pyrolite composition (Xu et al., 2008). Using the calculated anelasticity at a specific frequency, water content, and strain rate, we convert shear wave velocities to temperature, and assign unity to the regions above the solidus, or zero otherwise. The results predicted with different anelastic models and strain rates are then added and normalized to create a consistency map that exhibits the degree of consistency between different anelastic conditions to predict supra－solidus temperatures (Figures 4.9 and 4.10).
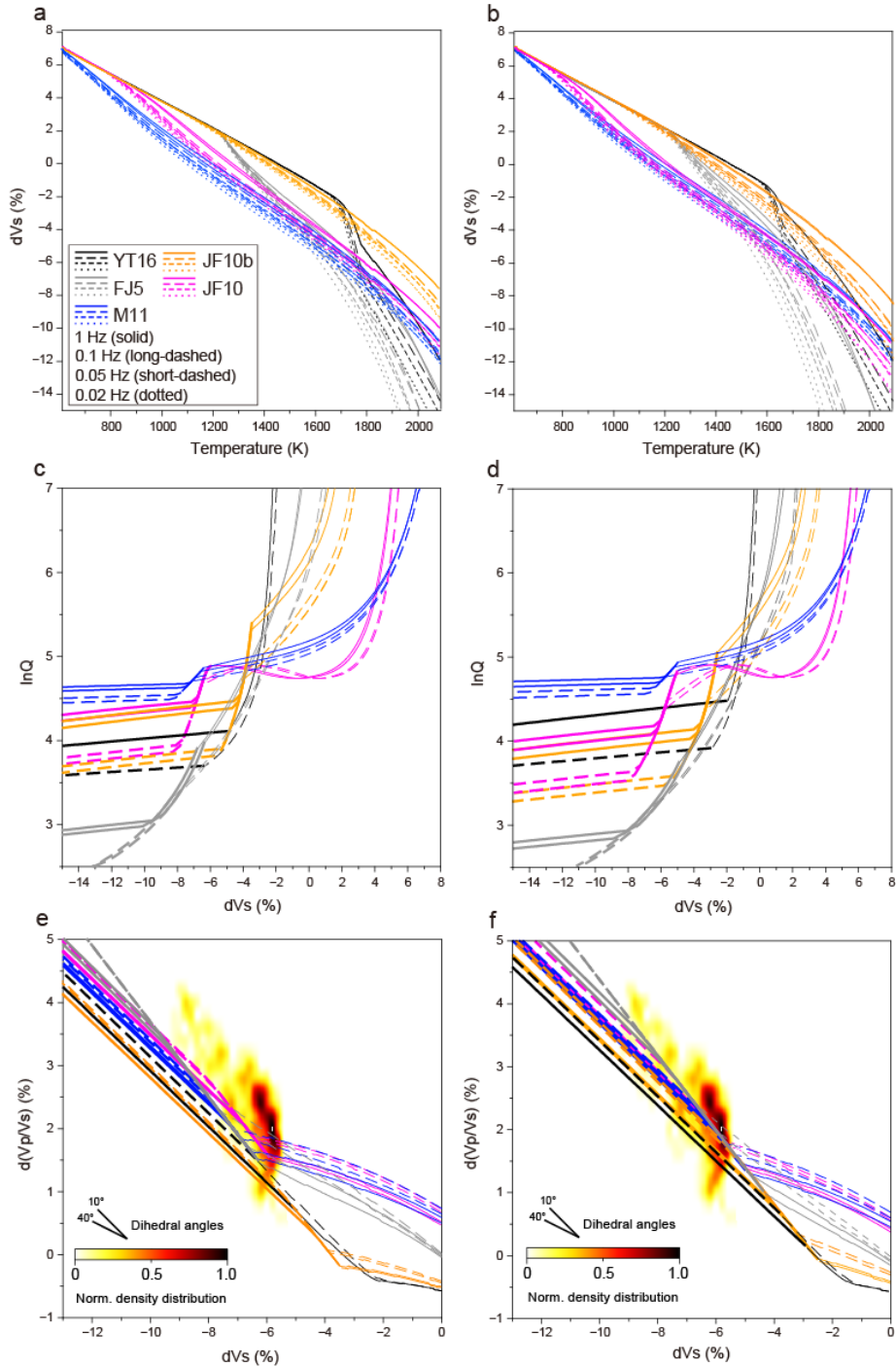
Figure 4.8 Diagrams showing the relationships between dVs, temperature, attenuation, and d(Vp/Vs) predicted from various anelastic models at different frequencies, strain rates, and water contents for a pyrolite composition at 100 km depth. In all panels,

lines in different colors indicate different attenuation models, and the solid, long–dashed, short–dashed, and dotted lines indicate frequencies of 1, 0.1, 0.05, and 0.02 Hz, respectively, each of which consist of two lines representing different strain rate conditions (1e–14/s and 5e–14/s). (a, b) Relationships between dVs and temperature for (a) dry and (b) damp (C_{OH} = 200 wt ppm) conditions. Attenuation models include Yamauchi and Takei, 2016 (YT16), Faul and Jackson, 2005 (FJ5); Jackson and Faul, 2010 (JF10b (only high–temperature dissipation), and JF10 (high–temperature dissipation with peak)); McCarthy et al. (2011) (M11). (c, d) Relationship between dVs and attenuation for (c) dry and (d) damp (C_{OH} = 200 wt ppm) conditions. Thick dashed lines represent the subsolidus temperature range, which are replaced by thin dashed lines above the solidus temperature. (e. f) Relationships between dVs and d(Vp/Vs) for (e) dry and (f) damp (C_{OH} = 200 wt ppm) conditions. Thick dashed lines represent the subsolidus temperature range, which are replaced by thin dashed lines above the solidus temperature. Background colors indicate the density distribution of the seismic velocity models (dVs and d(Vp/Vs)) for areas where temperatures are expected to be above the solidus at the corresponding depth.
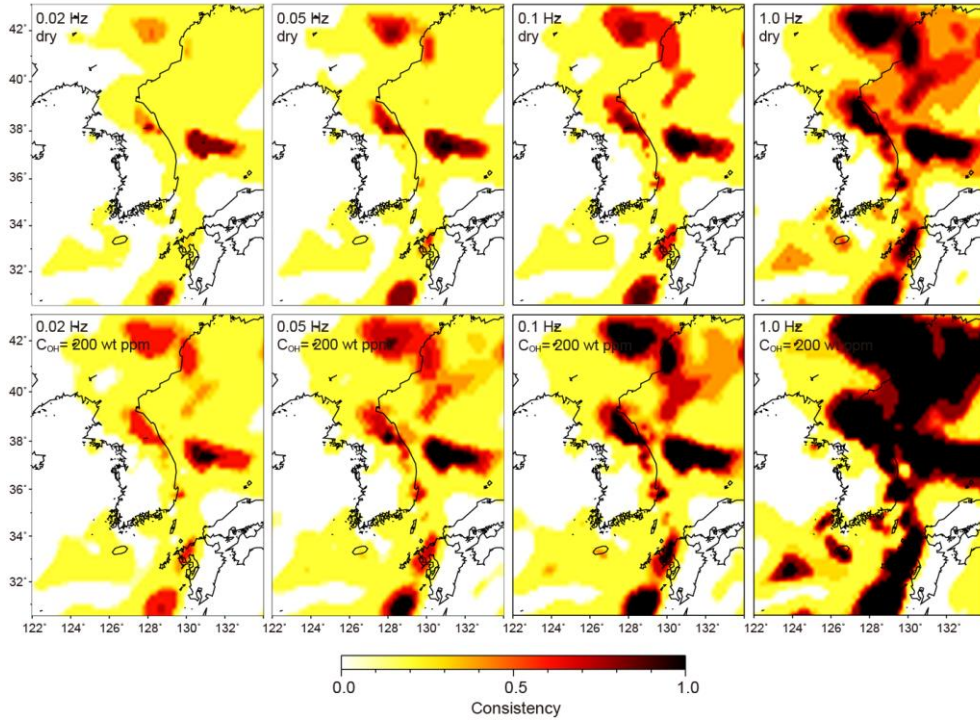
Figure 4.9 Maps showing the degree of consistency that depicts the mantle temperatures predicted to be above the mantle solidus with different anelastic models, different frequencies (0.02–1 Hz), and different water concentrations at 100–km depth based on the shear wave velocity model constructed by FWEA18 (Tao et al., 2018) and teleseismic travel time dataset (Song et al., 2020). The upper and lower rows correspond to the results of dry and damp ($C_{OH} = 200$ wt ppm) conditions, respectively. Each panel reflects ten different cases of predictions, which are derived from five different attenuation models with two different strain rate conditions. The closer the values are 1.0, the greater the number of anelastic conditions that predict the mantle temperature above the mantle solidus are.
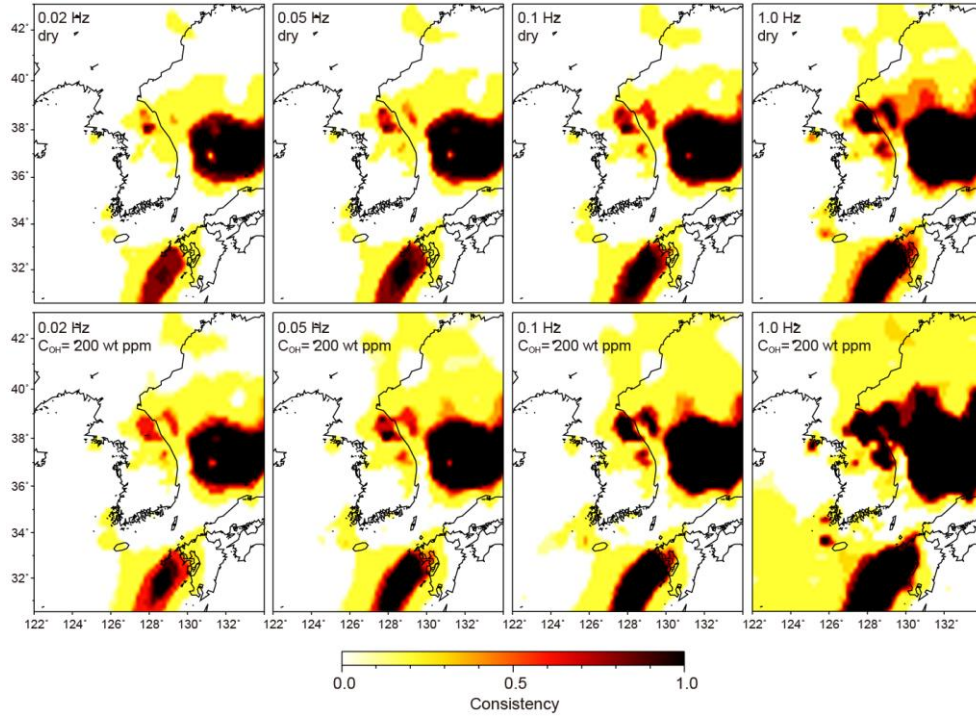
Figure 4.10. Same as Figure 4.09 but for the results from shear wave velocity model constructed by CSEM (Simutė et al., 2016) and teleseismic travel time dataset (Song et al., 2020).

4.2.3. Melt Content Estimation

We consider melt effects on seismic velocity if the estimated temperatures are predicted above the mantle peridotite solidus. Excess velocity reductions that cannot be accounted for by the temperature effects up to the mantle solidus (Hirschmann, 2000, Hirschmann et al., 2009) are converted to the amount of melt based on the calculated velocity−melt relationship (Figures 4.8c and d). The proposed mechanisms describing melt effects on seismic velocity and anelasticity include intergranular fluid flow (Hammond & Humphreys, 2000) and enhanced grain boundary diffusion (Holtzman, 2016). We calculate the anelastic effect of melt by accounting for its influence on diffusion creep viscosity (e.g., Eilon & Abers, 2017; Holtzman, 2016). For anelastic models of Faul and Jackson (2005), Jackson and Faul (2010), and McCarthy et al. (2011), we parameterize the effects of melt by scaling relaxation time scales for all processes of anelasticity calculation (e.g., Abers et al., 2014; Olugboji et al., 2013):

$$\tau = x_\varphi \left(\frac{C_{OH}}{C_{OH-R}} \right)^r d^m \tau_0(P,T) \tag{30}$$

where $r = 1.0$ (Hirth & Koholstedt, 2003), $\tau_0(P,T)$ is a timescale according to Arrhenius−type behavior, C_{OH} is water content, C_{OH-R} is reference water content (50 ppm H/Si), and x_φ is viscosity reduction pre−factor describing the melt effect. d is a grain size with a grain size exponent m. x_φ is represented by

$$e^{\left(-\alpha\varphi + \ln\left(x_{\varphi_c}\right)\,\mathrm{erf}\left(\frac{\varphi}{\varphi_c}\right)\right)} \tag{31}$$

(Holtzman, 2016), where φ is melt fraction, α is the empirically determined constant, ~26 for diffusion creep in olivine−basalt systems (Mei et al., 2002), x_{φ_c} is the viscosity reduction factor at φ_c, which is the critical melt fraction of ~1e−6 (Holtzman, 2016). We

choose x_{φ_c} to be 0.025, which is based on McCarthy and Takei, (2011). For anelastic model of Yamauchi and Takei (2016), we follow the same formulation and preferred values of melt parameters indicated in this model where the effect of partial melting on polycrystal anelasticity is constrained.

Anharmonic velocity perturbations caused by poroelastic effects are considered for a range of melt geometries represented by the equilibrium geometry model (Takei, 2002) with dihedral angles of 10° −40° (Garapić et al., 2013; Mei et al., 2002). At specific frequency and water content, the melt distributions are determined by the root− mean−square of the melt contents predicted with different anelastic models and strain rate conditions, which are then multiplied by the predetermined consistency maps (Figures 4.9 and 4.10) to reflect the variability in the predicted anelasticity.

4.2.4. Local Deep Earthquake Attenuation

We use local deep earthquake waveforms to constrain the upper mantle attenuation. We apply a path−averaged method to obtain attenuation parameters (t_P^* and t_S^*) (e.g., Pozgay et al., 2009). For a ray path between an earthquake j and a station i, the displacement spectrum can be parameterized as:

$$A_{ij}(f) = \frac{C_{ij}M_j e^{-\pi f^{1-\alpha} f_0^\alpha t_{ij}^*}}{1 + (f + f_{cj})^2} \tag{32}$$

where C_{ij} indicates frequency−independent effects, f is the frequency, f_0 is the reference frequency, M_j is the seismic moment, f_{cj} is the corner frequency, and α is the frequency−dependent exponent. t_{ij}^* describes a path−integrated attenuation defined as:

$$t_{ij}^* = \int \frac{1}{V(r)Q(r)} ds \tag{33}$$

where $V(r)$ and $Q(r)$ are the seismic velocity and the quality factor (Knopoff, 1964), which characterizes anelastic attenuation, at position r, respectively. For all waveforms, we remove the instrument response and apply corrections for geometric spreading (Kanamori & Steward, 1976), free surface effects (Kennett, 1991), and the spherically averaged radiation pattern (Boore & Boatwright, 1984). We calculate P wave spectra on the vertical component and S wave spectra on the transverse component using the multitaper spectral analysis method (Prieto et al., 2009) at frequency bands of 0.1−10 Hz. We set a common window length for both the signal and noise. We follow a spectra−fitting procedure of Eberhart−phillips and Chadwick (2002). Only parts of signal spectra with signal−to−noise ratios greater than three are used for the fitting. We apply a grid search to determine optimum choices of α and f_{cj} for each event (Figures 4.11−4.14). For all events, we find optimum values of α

between 0 and 0.2. The uncertainties of attenuation parameters are determined based on the variability in α and f_{cj}: for α, we consider possible ranges from 0 (frequency independent) to 0.27, the latter of which is preferred by experimental estimates (e.g., Jackson & Faul, 2010; McCarthy et al., 2011), and for f_{cj}, the uncertainty is determined based on variability of a spectral misfit at the optimum corner frequency estimated by the bootstrap resampling. We consider a range of corner frequencies whose spectral misfits are within the one standard deviation of the spectral misfit of the optimum corner frequency as possible values for f_{cj}. The obtained attenuation parameters are converted to relative variations (t_P^* and t_S^*) by:

$$\Delta t_{P,S}^* = t_{P,S}^* - \frac{t_{P,S}}{(\sum_{i=1}^{n} t_{i_{P,S}}/t_{i_{P,S}}^*)/n} \tag{34}$$

where $t_{P,S}$ are P (or S) wave travel time, and n is the number of stations.
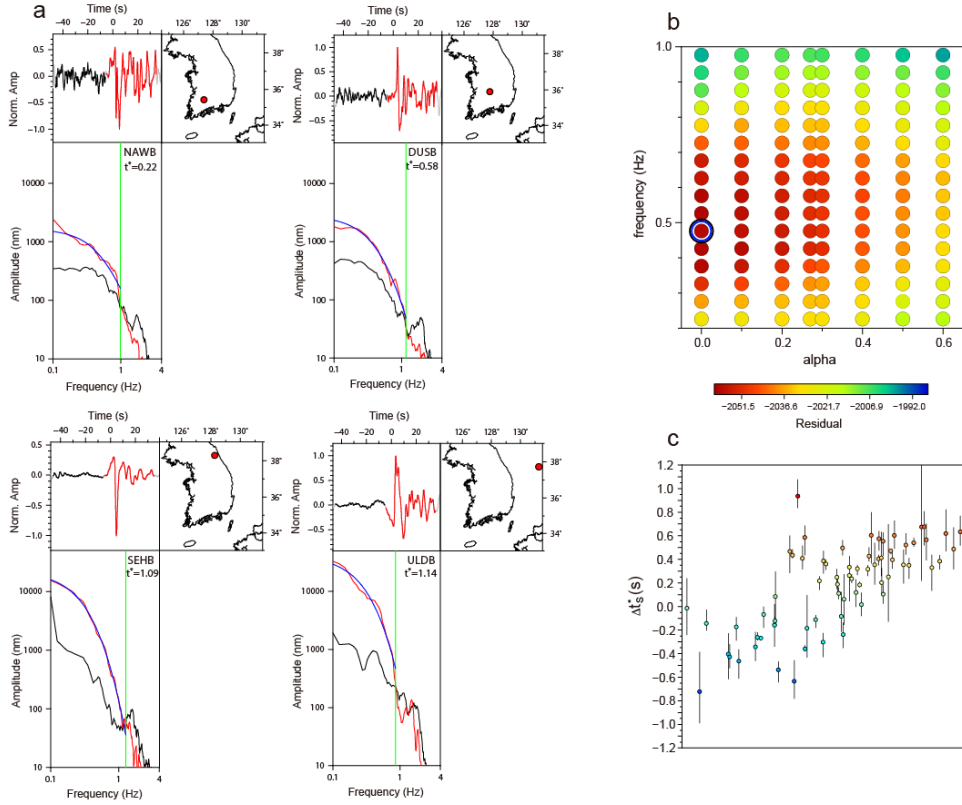
Figure 4.11 Analysis of S wave seismic attenuation for Event 1. (a) Examples of waveforms, spectra, and the estimated attenuation parameters. In each panel, the station location is indicated by the red dot in the inset map in the top right, the waveforms in red and black indicating the signal and noise, respectively, are shown in the upper left, and the calculated spectra are shown in the bottom left with the blue curves and green lines showing the fit ($\alpha = 0$) to the data and the spectral limit, respectively. The average upper frequency limit for data fittings is 1.22 Hz. (b) Results of a grid search for an optimum choice of the corner frequency (f_{cj}) and the frequency-dependent exponent (α). The blue and black circles represent the global minimum and the minimum with $\alpha = 0$, respectively. Residuals are calculated by $\sum_{i=1}^{n} \log[A(f) - D(f)]^2$, where n is the number of stations, $A(f)$ is predicted, and $D(f)$ is observed. (c) Results of relative attenuation parameters (t_S^*) with $\alpha = 0$ for all stations

aligned along the profile shown in Figure 4.18. Vertical black lines indicate the ranges for different choices of corner frequency.
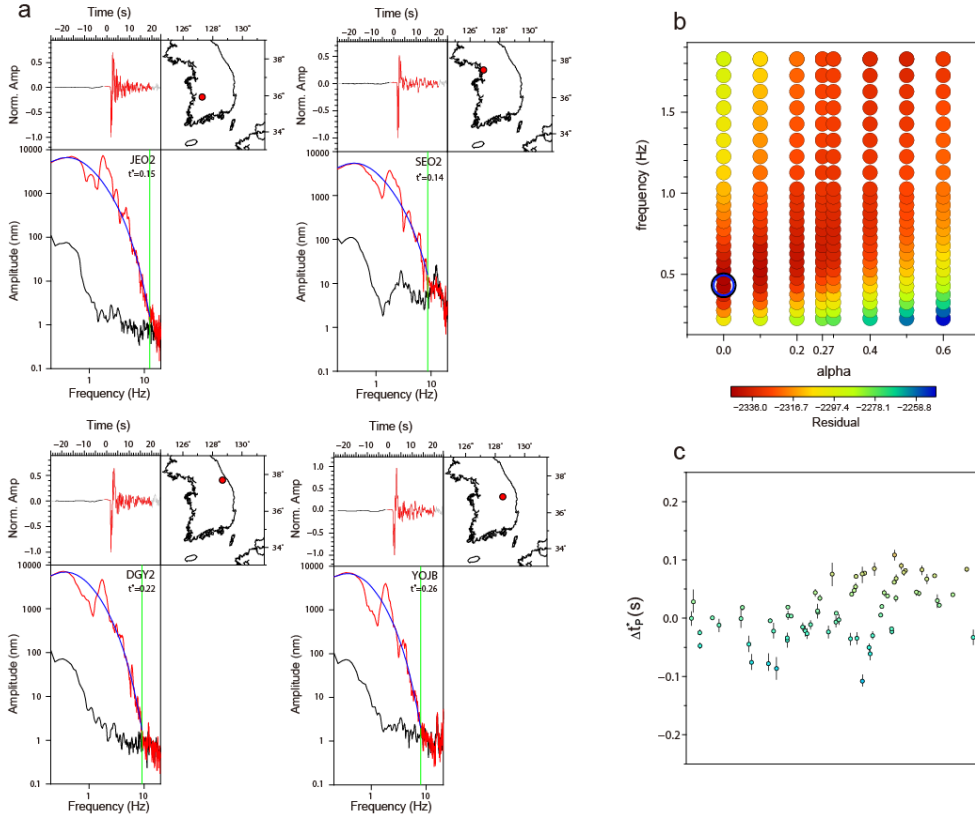
Figure 4.12 Analysis of P wave attenuation for Event 1. (a) Examples of waveforms, spectra, and the calculated attenuation parameters. In each panel, the station location is indicated by the red dot in the inset map in the top right, the waveforms in red and black indicating the signal and noise, respectively, are shown in the upper left, and the calculated spectra are shown in the bottom left with the blue curves and green lines showing the fit ($\alpha = 0$) to the data and the spectral limit, respectively. The average of maximum frequency used for a data fitting is 9.67 Hz. (b) Results of a grid search for finding the optimum choice of the corner frequency (f_{cj}) and the frequency-dependent exponent (α). The blue and black circles represent the global minimum and the minimum case of $\alpha = 0$, respectively. Residuals are calculated by $\sum_{i=1}^{n} \log[A(f) - D(f)]^2$, where n is the number of stations, $A(f)$ is predicted, and $D(f)$ is observed. (c)

Results of relative attenuation parameters (t_P^*) with $\alpha = 0$ for all stations aligned along the profile shown in Figure 4.18. Vertical black lines indicate the ranges for different choices of corner frequency.
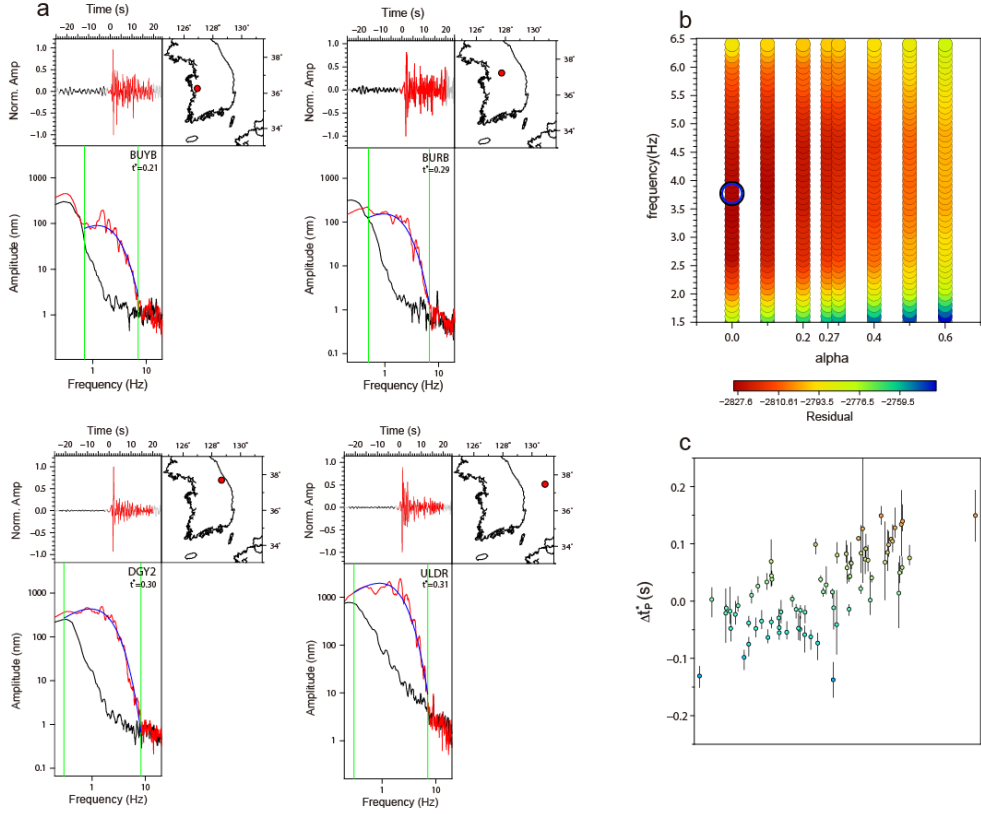
Figure 4.13 Same as Figure 4.12 but for Event 2. The average of maximum frequency used for a data fitting is 9.59 Hz
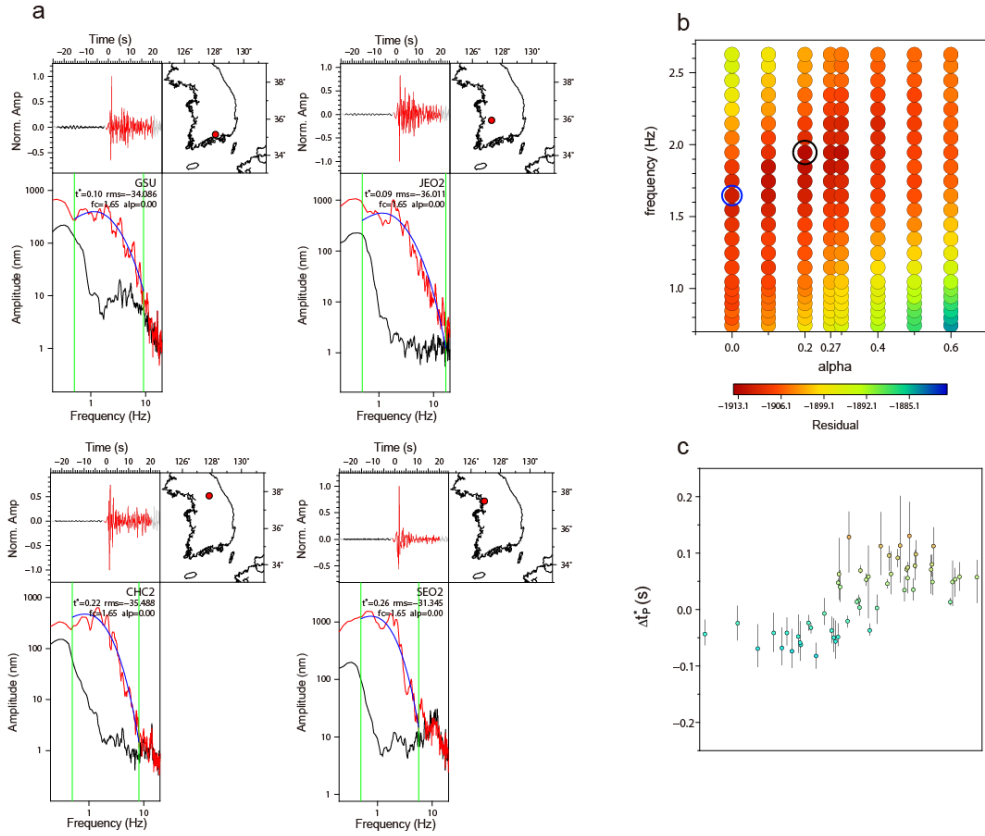
Figure 4.14 Same as Figure 4.12 but for Event 3. The average of maximum frequency used for a data fitting is 6.55 Hz.

4.2.5. Attenuation Modeling

We calculate synthetic t_P^* and t_S^* for the source−receiver pairs of the deep earthquakes using 3−D Qp and Qs and seismic velocity (V_P and V_S) models. For the Qs model, we use predictions from the tomography model combining FWEA18 and teleseismic datasets using the anelastic model of Faul and Jackson (2005), which is applied for teleseismic body−wave anelastic attenuation modeling (Eilon & Abers, 2017). We define a model space spanning a depth of ~800 km with a lateral and depth grid spacing of 10 km and 2 km, respectively. We construct the Qp grids from the predicted Qs assuming negligible bulk attenuation (Durek & Ekström, 1996). We apply our predicted Qs at depths <200 km and the global attenuation model (Adenis et al., 2017) for deeper depths. Tests with different Qs (e.g., 1−D PREM) at the deeper depths show minor changes in our results. The synthetic t_P^* and t_S^* are calculated by integrating the path−average Qp and Qs at a finite length over the entire ray path (Eq. 33) calculated by the fast marching method (Rawlinson et al., 2006a) with 3−D velocity structures, and converted to Δt_P^* and Δt_S^* following equation 34 in order to be compared with the observations.

4.2.6. Synthetic Wavefield Calculation

We use the spectral−element method (SPECFEM3D_GLOBE) (Komatitsch & Tromp, 1999) for a deep earthquake (Event 1) wavefield modeling to test if frequency dependent elastic focusing/defocusing effects affect our attenuation results. We apply 3−D P and S wave velocity models used in our study in latitude, longitude, and depth ranges of 24.5−45° N, 117.5−144° E, and 0−800 km, respectively. We use Crust1.0 (Laske et al., 2013) for the crust and Moho structure, and ETOPO1 (Amante & Eakins, 2009) for the surface topography. The focal mechanism of the event is obtained from the Global CMT (Ekström et al., 2012). The average grid spacing in the upper mantle is ~2.54 km, which corresponds to a dominant period of ~2.82 s (~0.35 Hz) for the S wave. We analyze amplitude variations for transverse component S waves for three different frequency ranges (0.05−0.1 Hz, 0.1−0.2 Hz, and 0.2−0.35 Hz), which correspond to the longer periods within our measurement frequency range. The waveforms are calculated for grid nodes with 0.2° spacing. The results of frequency dependent amplitude variations are shown in Figure 4.22.

4.3. Results

We observe several regions of high potentials to have mantle temperatures above the peridotite solidus for all frequencies and water contents (Figures 4.9 and 4.10). Although the presence of water is expected to increase anelasticity (Abers et al., 2014), its effect of reducing peridotite solidus leads to an increased possibility of temperature predicted to be above the solidus. Particularly high consistencies (>0.9) are estimated beneath the Quaternary volcanoes.

The estimated melt contents (Figures 4.15 and 4.16) calculated with the shear wave velocity model based on FWEA18 (Tao et al., 2018) and teleseismic travel time dataset (Song et al., 2020) shows a depth dependent distribution: the highest concentration is observed at the upper mantle depth of ~100 km, which gradually decreases with increasing or decreasing depth and diminishes at ~70 and ~140 km. Relatively high melt contents are estimated beneath the major Quaternary volcanoes: the results calculated with a damp upper mantle condition with a frequency range of 0.05–0.1 Hz, which is from the mean of the average period bands used in the full waveform model and the teleseismic travel time dataset to a common frequency of these two models, show melt contents of 0.6–0.8% beneath the Ulleung Island, 0.3–0.5% beneath Hantangang River Volcanic Field and Baekdusan, and ~0.05% focused beneath the Jeju Volcanic Island. Relatively low melt fractions (~0.05–0.2%) are sporadically distributed beneath the Neogene volcanism around the Korean Peninsula and the northern part of the East Sea. Pronounced meltings are found beneath the northern Okinawa Trough and northwestern Kyushu, which is consistent with a previously imaged strong low velocity in the depth from 40–100 km (Sadeghi et al., 2000) that

suggests the partially melted upper mantle. The result for a dry mantle condition show a similar melt distribution with slightly reduced (~0.1%) melt contents (Figure 4.16). For all frequency ranges, we obtain consistent results of requiring higher amounts of melt beneath the Quaternary volcanoes (Figure 4.17). Different choices of melt geometry (e.g., a dihedral angle of 40°) caused only minor changes (<0.05%) for the estimated melt content at small melt fractions (<1%).

We observe strong correlations between the distribution of melt, seismic attenuation, and Vp/Vs (Figure 4.18). The existence of melt can account for enhanced seismic attenuation and high Vp/Vs (>2%) (Figures 4.18e and 4.18f) compared to the temperature effect only (e.g., Chantel et al., 2016). Apparently high seismic attenuations are observed for rays penetrating the inferred upper mantle melting areas (Figure 4.18c, 4.18h, and 4.18m). Sharp increases in seismic attenuations (~0.15 of t_P^* and ~0.75 of t_S^*) and Vp/Vs ratio (~2–4%) within a lateral distance of ~200 km are geographically correlated with the presence of melt (Figures 4.18e–4.18g, 4.18j–4.18l, and 4.18o–4.18q). The synthetic attenuation calculated with an anelastic model (Figure 4.18e, 4.18j, and 4.18o) shows that the predictions considering only temperature effect have systematically lower amplitudes than the observations, while the presence of melt with relatively wet mantle condition (C_{OH} = 200 wt ppm) estimated variations closer to the observed attenuation (Figure 4.19). Similarly, the observed Vp/Vs variations show relatively higher values (~1%) than the predictions with only temperature effect or dry melt (Figure 4.18e), while the condition of damp mantle melting closely matches the observed Vp/Vs (Figure 4.19). Linear fitting of t_P^* versus t_S^* for Event 1 shows an estimated Qp/Qs of ~ 2.33 ± 0.43 (Figure 4.20),

which is consistent with the theoretical value for a Poisson solid (Anderson et al., 1965) and the assumption of negligible bulk attenuation (Dziewonski & Anderson, 1981; Durek & Ekström, 1996).
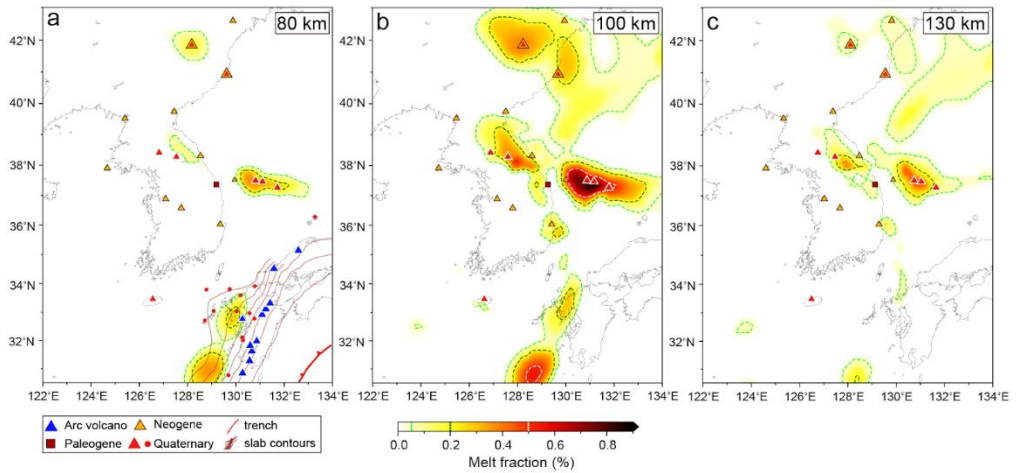
Figure 4.15 Melt distributions at the upper mantle depths of (a) 80 km, (b) 100 km, and (c) 130 km calculated with the frequency of 0.1 Hz and C_{OH} = 200 wt ppm. The green, black, and white dashed contours indicate melt contents at 0.05, 0.2, and 0.5%, respectively.
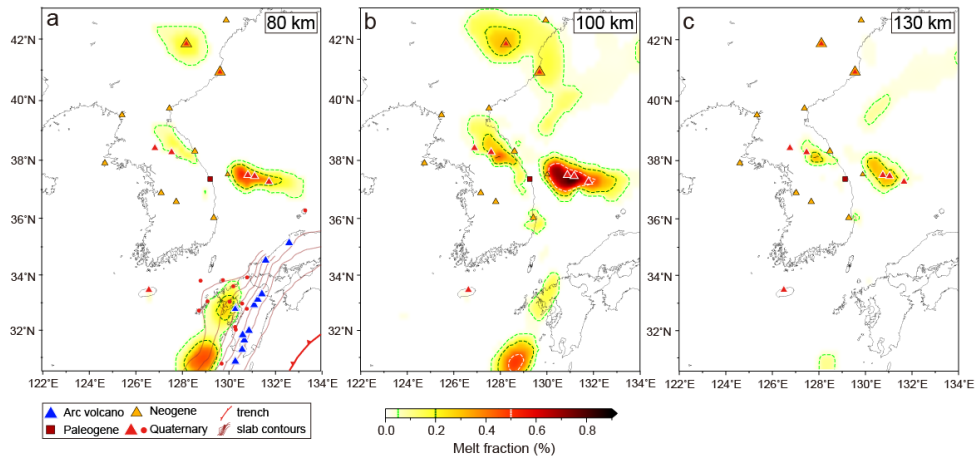
Figure 4.16 Calculated melt distribution at the upper mantle depths of (a) 80 km, (b) 100 km, and (c) 130 km calculated with the frequency of 0.1 Hz and a dry condition. The green, black, and white dashed contours indicate melt contents at 0.05, 0.2, and 0.5%, respectively.
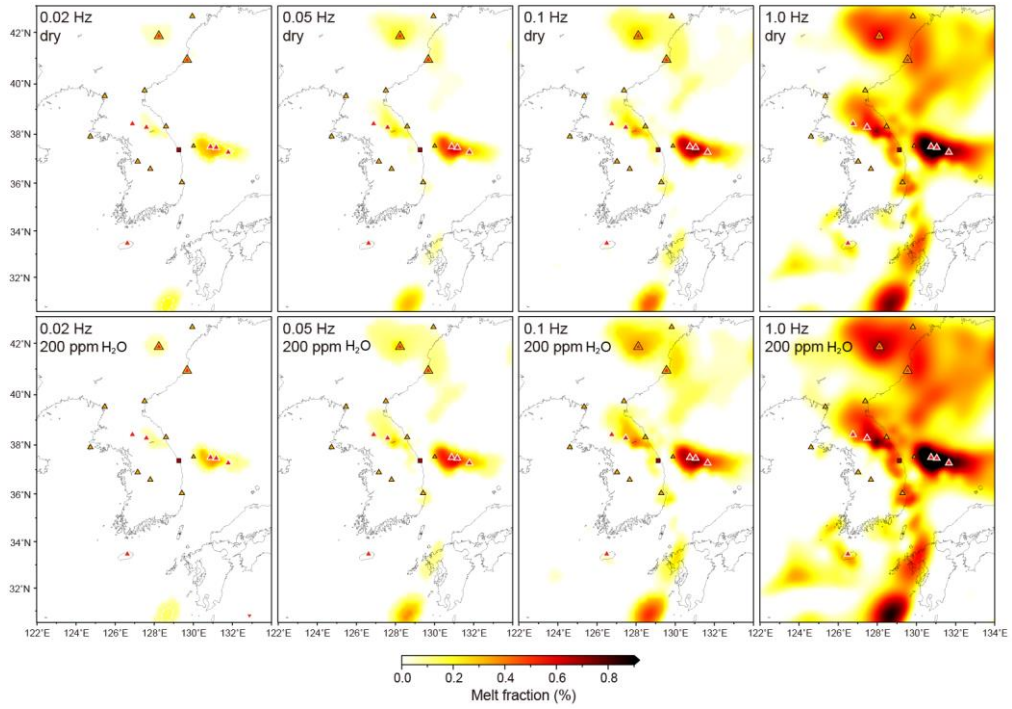
Figure 4.17 Calculated melt distribution at the upper mantle depth of 100 km predicted with different frequencies (0.02–1 Hz) and water concentrations.
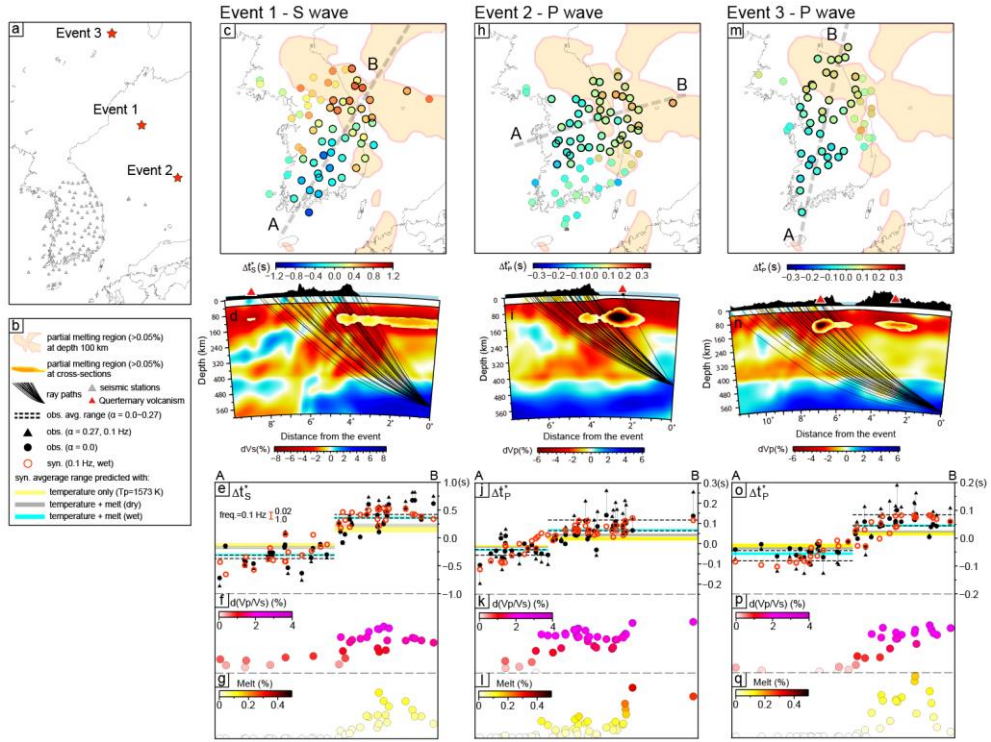
Figure 4.18 Attenuation of deep focus earthquakes and its relationship with velocity structures, d(Vp/Vs), and melt contents. (a) Distribution of seismic events and stations. (b) Figure legend. (c) S wave attenuation for Event 1 (PDE: 2017−07−12, 19:48:07.80, 40.8548°, 131.6565°, 545.0 km, Mw 5.9) plotted at the 100−km depth pierce points. The gray dashed line indicates the location of the profile shown in d. The orange shaded area indicates the inferred melt distribution at the corresponding depth. Example stations (d–g) are circled in bold. (d) Vertical cross section of velocity perturbations with ray geometries shown by black lines. The yellow patches indicate the inferred melt distribution with melt contents > 0.05%. (e) Comparison of the observed and synthetic attenuations. The black dashed lines indicate the average of observations (α = 0.0 and 0.27 (0.1 Hz)) for two different sections. Yellow, gray, and cyan bars indicate the average of synthetics (0.1−1.0 Hz) predicted with temperature effect only (the potential temperature (T_P) = 1573 K)

dry melt, and wet melt (C_{OH} = 200 wt ppm), respectively. (f) Average d(Vp/Vs) values of 80–120 km depths along the rays of each example data. Only positive d(Vp/Vs) values are shown. (g) Average melt contents of 80–120 km depths along the rays of each example data. (h–i) Same as (c–g) but for P wave attenuation of Event 2 (PDE: 2018−12−30, 14:26:35.11, 38.3792° , 133.8402° , 431.81 km, mb 4.7). (m–q) Same as (c–g) but for P wave attenuation of Event 3 (PDE: 2016−01−02, 04:22:19.57, 44.8069° , 129.9406° , 585.47 km, Mw 5.8).
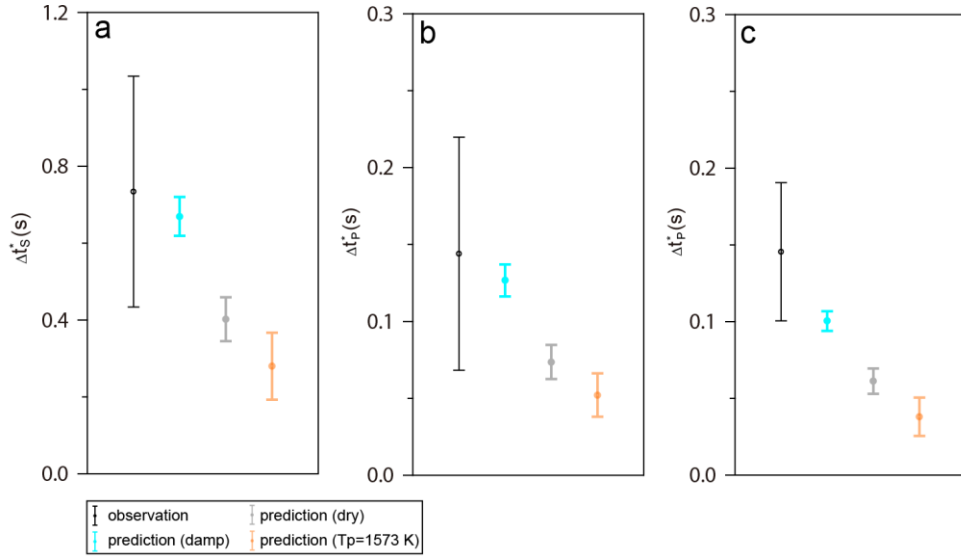
Figure 4.19 Comparison of observations and synthetic attenuations predicted with different conditions for (a) Event 1, (b) Event 2, and (c) Event 3. The uncertainty range of the observation reflects the results of $\alpha = 0.0$ to 0.27 (at 0.1 Hz) and variability in the determined corner frequency. The ranges of the synthetics reflect predictions at frequencies of $0.1{-}1.0$ Hz.
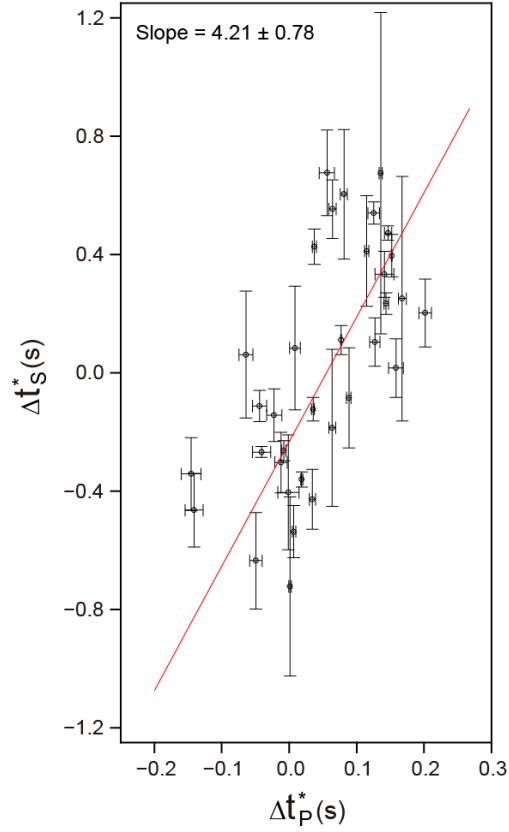
Figure 4.20 Plot of $\pmb{\Delta t_S^*}$ and $\pmb{\Delta t_P^*}$ for stations shown in Figure 4.18e of Event 1. The red line shows a linear regression for the dataset with the calculated slope and its $2\,\pmb{\sigma}$ uncertainty obtained by bootstrapping indicated in the upper left. The error bars for each plot indicate one standard deviation.

4.4. Discussions

4.4.1. Possible Other Effects

Compositional heterogeneities can change seismic velocity (Goes et al., 2000). We test for effects of different mantle compositions on seismic velocity (e.g., harzburgite, pyroxenite) (Figure 4.21). We observe only a limited velocity change (<0.5 %) for the harzburgite composition, which is significantly less than the variabilities among different attenuation models. This is consistent with previous studies suggesting that relatively minor influence of chemical composition of the upper mantle on seismic velocity than the temperature effect (e.g., Afonso et al., 2010; Cammarano et al., 2003). The presence of pyroxenite can arise a relatively large velocity variation (>2%) (Figure 4.21), however, it hardly affects seismic velocity of the peridotitic upper mantle due to its small proportion (e.g., Hirschmann & Stolper, 1996). It has been suggested that elastically accommodated grain boundary sliding (EAGBS) (Karato et al., 2015) leads to a sharp velocity reduction. This mechanism predicts a substantial velocity drop (~10%) at the mid−lithosphere discontinuity beneath continental lithosphere and lithosphere and asthenosphere boundary beneath oceanic plates with ages older than ~60 Ma (e.g., Olugboji et al., 2013; Selway et al., 2015). EAGBS activates at a characteristic frequency, which is determined by temperature, pressure, grain size, and water content (Karato et al. 2015). At a frequency range of the analyzed seismic velocity model of 0.05−0.1 Hz, EAGBS is expected to occur at 1000−1200 K at a 100 km depth. However, given that large velocity reductions (<−6%) are mostly found beneath recent volcanism (<1 Ma) accompanied with high surface heat flux (>70 mW/m^2), it is unlikely that EAGBS

operates at the corresponding depth due to high temperature (e.g., Cobden et al., 2018). A different choice of a seismic velocity model (e.g., Simutė et al., 2016) consistently showed slower velocities at the same locations where low velocities are observed, indicating that the observed low-velocity anomalies are robust (Figure 4.10).

Seismic attenuation can arise from extrinsic effects, such as scattering or frequency dependent focusing/defocusing. Most models of elastic scattering predicted strongly frequency dependent characteristics (α ~ 0.5) with Qp ~ Qs (e.g., Richards & Menke, 1983). However, this contradicts our results showing that optimum values of α determined to be between 0 and 0.2, and the measured Qp/Qs ~ 2.33, indicating that elastic scattering is unlikely a dominant mechanism for the observed attenuation. The relative excess of long-period energy compared to the short-period energy by focusing of the long-period wavefield can produce an apparently high attenuation (e.g., Allen et al., 1999). However, this mechanism is unlikely to be significant for t_P^* where high frequency energy (>1 Hz) is dominant (e.g., Bezada et al., 2017). We test for a long period focusing effect for S wave using 3-D seismic velocity structures. We find that there are no localized long-period focusing or systematic increases in wave amplitudes with increasing period beneath the major upper mantle low velocity zones (Figure 4.22). Based on these results, we conclude that the observed attenuation variations are robust and largely reflect intrinsic attenuation, i.e., anelasticity, of the upper mantle.
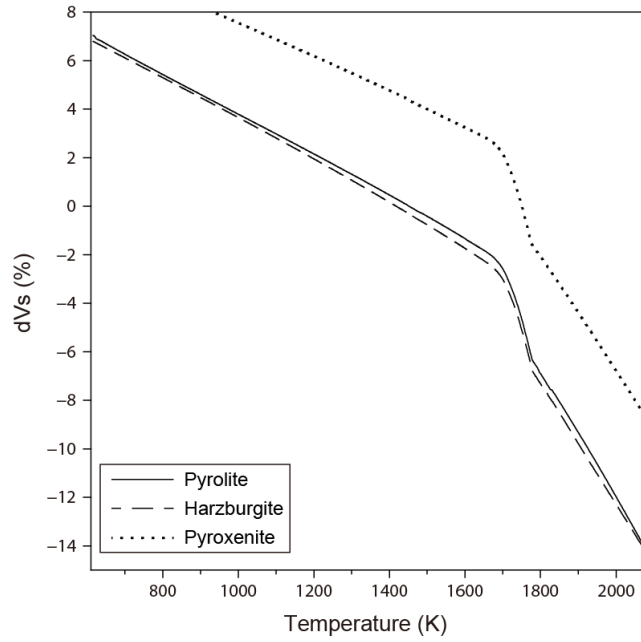
Figure 4.21 Comparison of the relationship between dVs and temperature for different compositions at a depth of 100 km calculated with the anelastic model of Yamauchi and Takei (2016). The velocity perturbations are shown with respect to ak135 global reference model (Kennett et al., 1995).
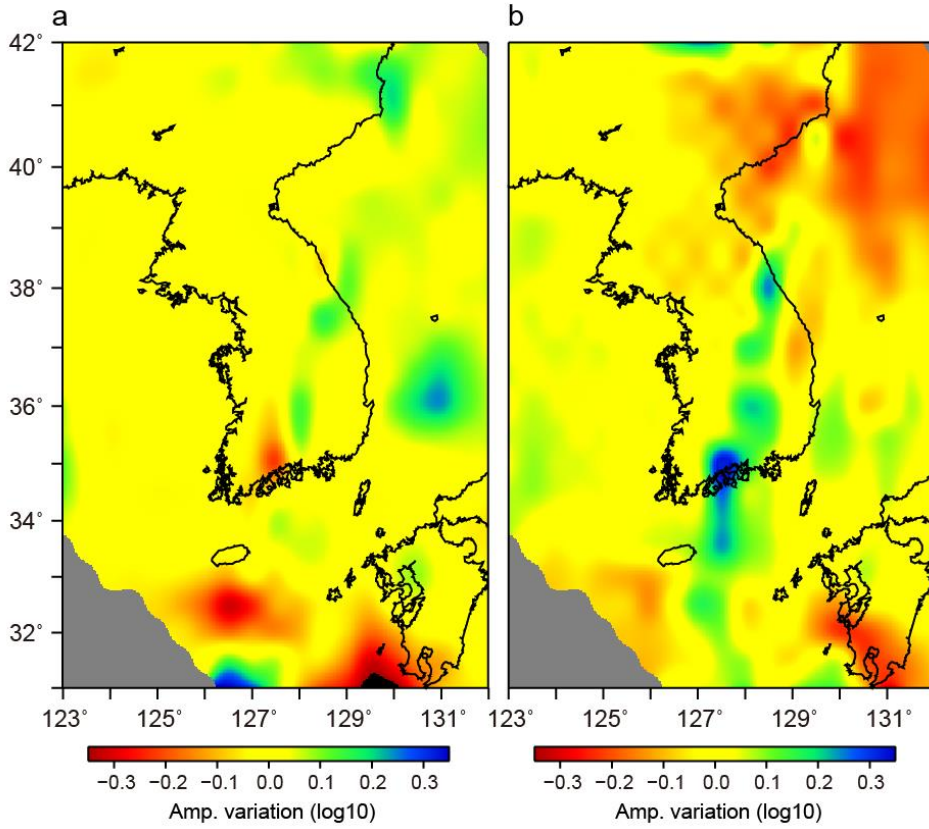
Figure 4.22 Frequency dependent amplitude variations of synthetic S wave wavefield of Event 1 (Figure 4.18a) calculated with 3−D velocity structures. (a) Amplitude difference between waveforms filtered in the frequency ranges of 0.1−0.2 Hz and 0.05−0.1 Hz. The positive (negative) values indicate larger (smaller) amplitudes at higher frequency. (b) Amplitude difference between waveforms filtered in the frequency ranges of 0.2−0.35 Hz and 0.1−0.2 Hz. The gray shaded regions indicate unsampled areas.

4.4.2. Physical Properties of the Upper Mantle

The temperature profiles based on seismic velocity without allowing the presence of melt show excessively high temperatures at the upper mantle depths ~90–150 km (Figure 4.23a). The profiles show a steep increase in temperature with increasing depths, which reaches >1800 K at ~80–120 km and gradually decreases and approaches the mantle adiabat with the potential temperature (T_P) of ~1573 ± 100 K at deeper depths. The temperatures at shallower depths (< 80 km) follow conductive continental geotherms with 65–75 mW/m^2, which is consistent with regional surface heat flux (Lee et al., 2009). The inferred T_P is broadly consistent with previous results of basalt geochemistry of ~1523–1673 K (Ball et al., 2021; Brenna et al., 2014; Choi, 2021; Kimura et al., 2018; Kuritani et al., 2019; Sakuyama et al., 2014), which are within the range of the normal upper mantle temperature (Lee et al., 2009). Pronounced temperature increases at 80–120 km are difficult to be reconciled with the adiabatic mantle temperature or the conductive geothermal gradient. Instead, our results predict the presence of a small fraction of melt (0.1–0.8%) at the corresponding depth range (Figure 4.23b).

Given that the T_P is within the range of ambient mantle potential temperature, localized excess heat, such as by hot mantle plume, is unlikely for generating partial melting. Also, decompressional melting under dry mantle condition with normal mantle temperature (T_P ~1573–1673 K) favors shallower melting (<65–85 km) (e.g, Rychert et al., 2012), which is inconsistent with the observed deeper melts (Figure 4.23c). Calculated mantle temperature and melt distribution suggest an upper mantle condition of average mantle temperature with reduced peridotite solidus. For T_P of ~1673 K, which is in the

middle of possible potential temperature range, the seismically derived geothermal profile shows crossover of the mantle peridotite solidus with C_{OH} = 450 wt ppm. The estimated water content is possible to be an upper bound to account for the observed depth extent of the melt considering that the presence of CO_2 as well as water can also reduce the solidus, which was not accounted for by our analysis (e.g., Dasgupta et al., 2013). The variations in the observed seismic attenuation and Vp/Vs show a better fit with predictions of a hydrated condition than those of a dry condition (Figure 4.18). Mantle condition inferred from joint interpretation of electrical conductivity and P wave velocity (Ichiki et al., 2006) suggests a wet (C_{OH} = 1000 ppm H/Si) pyrolytic upper mantle with moderate temperature (~1550 K) at shallower mantle depths (<200 km). In addition, water content of source mantle estimated from basalts in Baekdu (C_{OH} = 450 wt ppm, Kuritani et al., 2019) and Ulleung Island (C_{OH} = 600 wt ppm, Choi et al., 2021) indicate hydrated upper mantle conditions, which are in accord with our results.
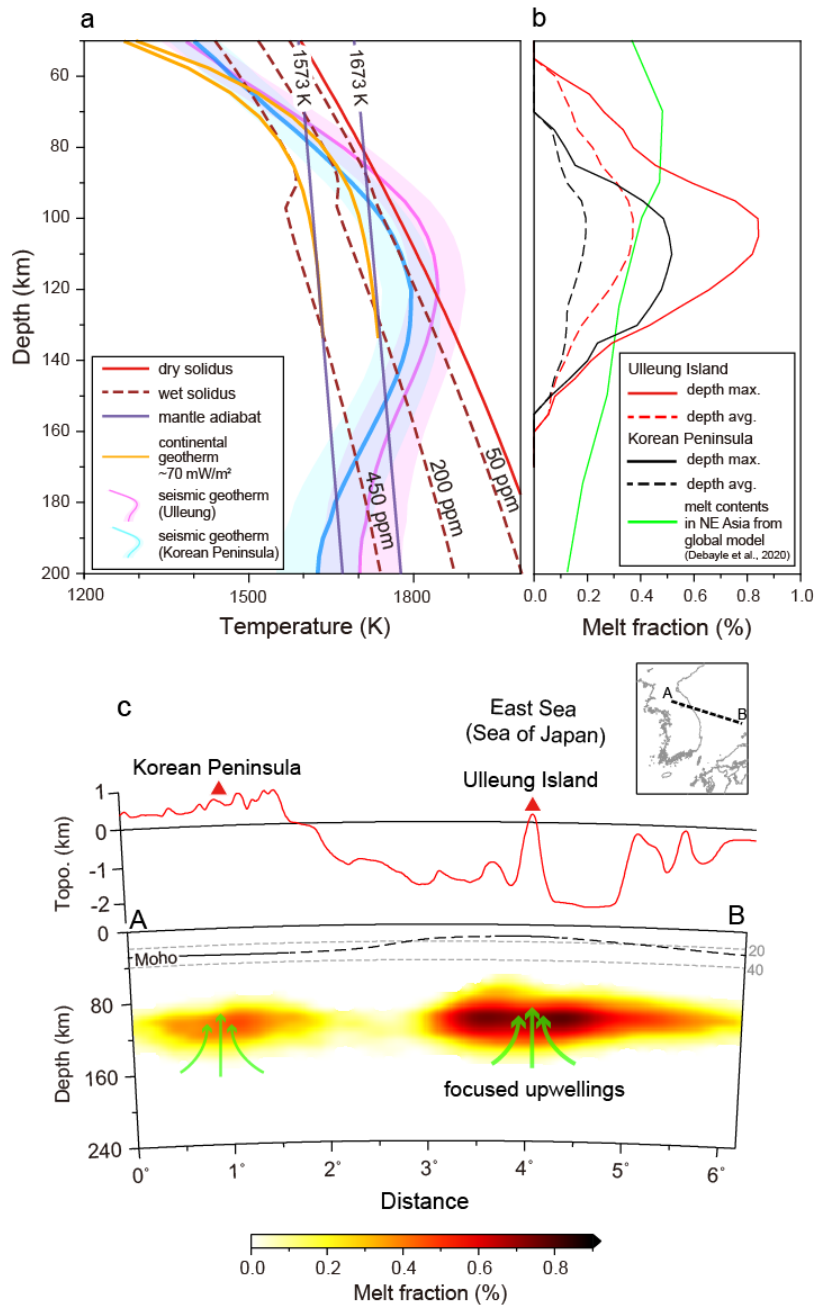
Figure 4.23 Possible mantle condition and melt distribution in northeast Asia margin. (a) Temperature profile from continental conductive geotherms and a seismic velocity model (this study). The red solid and brown dashed lines indicate mantle peridotite solidus for dry and damp conditions with different water contents. (b) Calculated melt contents with depth beneath major Quaternary

volcanic regions. The green line indicates the melt content in northeast Asia from global tomography (Debayle et al., 2020). (c) Illustration with mainly interpreted features. The inferred mantle upwellings are shown by curved green arrows. The curved black line represents Moho interfaces (solid: Chang & Baag, 2007, dashed: Laske et al., 2013). The red triangles on the surface indicate Quaternary volcanism, and the red line indicates surface topography. The location of the profile is shown in the inset map at the top right.

4.4.3. Active Upwelling and Melt Focusing Beneath Intraplate Volcanism in Northeast Asia

Our results show spatially separated and confined melt distributions (Figure 4.15). The global upper mantle melt model from seismic velocity and attenuation (Debayle et al., 2020) showed widespread shallow mantle melts (~0.2–0.4%) beneath the northeast Asia margin. Our attenuation results show distinct spatial variations that show contrasts between the inferred partial melting regions and the surrounding areas (Figures 4.18e, 4.18j, and 4.18o). This feature is difficult to reconcile with the widespread distribution of the upper mantle melt, since diffusion creep viscosity is expected to be sharply reduced at a small fraction of melt (<0.01%) (Holtzman, 2016; McCarthy & Takei, 2011), after which relatively moderate variation exists for higher melt concentrations (>0.1%) (Figures 4.8c and 4.8d). Therefore, the observed sharp lateral change in attenuation is more likely to occur by the contrast between the areas with and without melt, rather than local variations in melt concentrations within a widespread distribution. The discrepancy between the global and our model possibly results from different spatial resolutions owing to different seismic frequency ranges: the global model, using a dataset with a dominant period of ~100 s, reflects relatively long wavelength structures, which represents the spatially averaged characteristics of the upper mantle in our study area.

Major Quaternary volcanic activities (<0.5 Ma) (Figure 4.24) are located right above the potential melting regions (Figure 4.15), indicating that there are possible linkages between the two. The depth ranges of the melt zones identified in our model are comparable to the petrological constraints, which show melting depths extending to ~100 km beneath Ulleung Island (Chen et al., 2018), 75–90 km

beneath Hantangang River Volcanic Field (Sakuyama et al., 2014), 90–105 km for Baekdusan (Choi et al., 2020), and 75–105 km beneath Jeju Volcanic Island (Brenna et al., 2012). This coincidence indicates that the imaged melt zones are the possible magmatic source for volcanism.

The distribution of melt and its spatial coincidence of the Quaternary volcanism suggest localized decompressional melting at shallower mantle depths (<140 km) as a possible mechanism for the intraplate volcanoes (Figure 4.23c). Previous studies suggested mantle upwelling from deeper upper mantle mechanically or chemically instigated by the Pacific slab (Richard & Iwamori, 2010; Zhao et al., 2009; Tang et al., 2014; Yang & Faccenda, 2020). Although the subducting slab could facilitate mantle convection (e.g., Faccenna et al., 2010), a diapiric nature of deeper upper mantle melting makes it infeasible to be retained at shallower depths (e.g., Yang & Faccenda, 2020), indicating that other formational processes are needed to explain the imaged melt distributions. Convective upwelling can arise by thermal or structural heterogeneities in the upper mantle (e.g., King & Anderson, 1998; Conrad et al., 2010). Sharp variations in lithospheric thickness can derive localized shallow mantle convection beneath thinned lithosphere (Conrad et al., 2010). Heterogeneous lithospheric structures with a sharp transition have been imaged by seismic tomography adjacent to the Cenozoic volcanoes (e.g., S. Kim et al., 2016; Song et al., 2018), which have been suggested to be formed by lithospheric removal events (e.g., delamination) in recent geological period, the Quaternary, based on the spatial coincidence of recent volcanic regions in the eastern margin of the Korean Peninsula with higher topography, higher surface heat flux, and relatively low mantle velocity (Song et al.,

2020). The observed depth extent of melt is consistent with the results of geodynamic simulation that depicts mantle melting derived by edge-driven convection with hydrated upper mantle conditions (e.g., Kaislaniemi et al., 2014). The depth ranges of melt that extends to shallower depths (~65 km) with higher melt content (Figure 4.23c) are found beneath Ulleung Island, where continental lithosphere has been extended by the opening of the East Sea (Kim & Yoon, 2017). Relatively shallow depths of lithosphere-asthenosphere boundary could provide larger headspace beneath lithosphere for decompression melting, generating a larger melt content (e.g., Guo et al., 2020). A similar depth extent (~140 km) of the inferred melt distribution among different intraplate volcanoes possibly indicates a common mechanism under similar mantle condition operates for the intraplate volcanoes.

Depressed peridotite solidus by a mildly hydrated condition possibly facilitates the formation of buoyant shallow mantle melts through adiabatic upwelling. The presence of melt can lead to shear localization (Katz et al., 2006), which could promote melt segregation and active upwelling (Conrad et al., 2011) that further enhances and sustains the melt focusing beneath the Cenozoic volcanoes (e.g., Gallacher et al., 2017; Hirano et al., 2006). Concentrated low-velocity anomalies at shallow mantle depths (~80-120 km) are also observed beneath Cenozoic intraplate volcanism in the eastern China (e.g., Guo et al., 2016a,b; Rhie et al., 2018), suggesting that the process of small-scale convective upwelling and shallow decompressional melting is ubiquitous beneath intraplate volcanoes in northeast Asia. A similar process can be applied to intraplate volcanism in other areas where heterogeneous lithospheric structures have been observed to play a critical role in the upper

mantle convection (e.g., Kaviani et al., 2021), such as southern Australia (Davies & Rawlinson, 2014) or Middle East (Kaislaniemi et al., 2014).
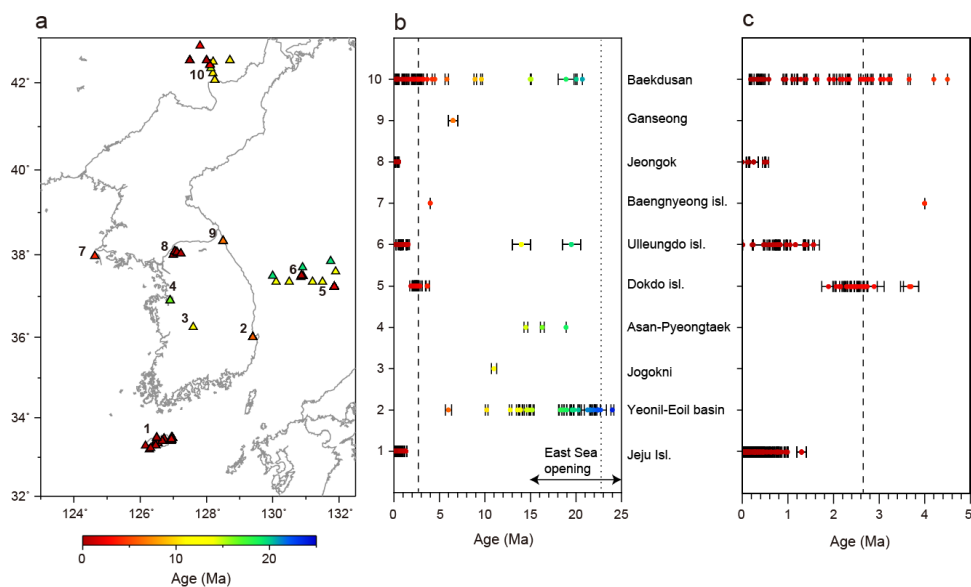
Figure 4.24 Distribution of Late Oligocene to recent (25–0 Ma) volcanic centers around the Korean Peninsula. (a) The volcanic centers investigated in this study are indicated by triangles colour–coded by time of eruption. (b) Eruption ages during 25–0 Ma for major Cenozoic volcanism. The numbers of list correspond to those in Figure 4.24a. The eruption events are indicated by circles colour–coded by eruption ages. The names of the volcanic regions are indicated in right. The horizontal error bars of each circle indicate age uncertainty. The dashed and dotted vertical lines represent the divisions between the Quaternary and Neogene, and the Neogene and Paleogene, respectively. References for Baekdusan: Choi et al. (2020), Wei et al. (2007), Ganseong: Choi et al. (2006), Jeongok: Choi et al. (2014), Kim et al. (2014), Baengnyeong island: Choi et al. (2006), Ulleungdo island: Brenna et al. (2014), Chen et al. (2017), Dokdo island: Chen et al. (2017), Asan–Pyeongtaek: Shin et al. (2006), Boeun; Arai et al. (2001), Yeonil–Eoil basin: Kim et al. (2005), Jeju island: Brenna et al. (2015a).

4.5. Conclusions

Pronounced volcanic activities found in intracontinental regions reflect intense mantle dynamics beneath plate interiors. Imaging of the distribution of mantle melting can provide direct evidence for understanding thermodynamic state of the upper mantle, which controls the emplacement of melt and surface volcanism. Northeast Asia margin, where there are active intraplate volcanoes isolated from tectonic boundaries or hot spots, is an ideal place for assessing the role of upper mantle dynamics on the intraplate volcanism, yet the physical mechanism controlling localized volcanism remains enigmatic. Here we show evidence of the presence of shallow upper mantle melts (~70–150 km) focused beneath the Quaternary intraplate volcanoes based on high–resolution seismic tomography, thermodynamic calculations, and seismic attenuation. Our results indicate mantle melting confined at shallow mantle depths without anomalously hot or wet plumes from deeper upper mantle as previously suggested. Instead, we propose that focused upper mantle upwellings of normal mantle temperature (T_P of ~1300 ° C) with mildly hydrated conditions (C_{OH} < 450 wt ppm) control localized, long–lived (>5 Ma) intraplate volcanism in northeast Asia.

Summary and Conclusions

Here, we have applied teleseismic body-wave traveltime tomography to image the detailed upper mantle structures in northeast Asia. We began in Chapter 1 by imaging Jeju Volcanic Island located off the southern Korean Peninsula based on the unique dataset from the temporary broadband array deployment. We imaged a strong low-velocity anomaly focused at sublithospheric depth (~60 km) beneath the central shield volcano and ramified low-velocity conduits connected from the deeper low-velocity anomaly to the surface volcanic field. We suggested the focused decompressional melting attributed to the transition of lithospheric thickness beneath the island as a possible mechanism for the volcanism. In Chapter 2, we constructed high-resolution crust and upper mantle 3-D P and S wave velocity models beneath the Archean-Proterozoic massifs in the southern Korean Peninsula by using datasets from local arrays consisting of permanent broadband, short period, and accelerometers for more than 5 years. We found the possible presence of a thick lithospheric root in the southwest with a sharp lateral decrease in lithospheric thickness in the northeast and along the eastern margin of the Korean Peninsula. Also, there are clear associations between high-temperature upper mantle and Cenozoic volcanism, high-heat flow, and high topography, which potentially indicates the ongoing modification of current continental margins. Based on our results, we suggested heterogeneous modification and ongoing reactivation of a craton lithosphere beneath the Korean Peninsula at the Sino-Korean craton margin in the eastern Eurasian plate. In Chapter 3, by including seismic data from southwestern Japan and using the data from the southern Korean Peninsula, we imaged the high-resolution stagnant

Pacific slab and the mantle transition zone structures beneath the northeast Asia margin. Based on comparisons with previous seismological studies, and together with a 3-D waveform simulation, we suggested the possible presence of a pronounced gap within the stagnant Pacific slab. In addition, we found a geographic correlation between the inferred slab gap area and the previously observed a melt layer atop the MTZ. We suggest that the observed correlation provides possible evidence of the dynamic interaction between the subducting slab and the surrounding upper mantle. In the last chapter, we conducted quantitative interpretation of the high-resolution upper mantle velocity model by applying thermodynamic calculations. We found focused shallow upper mantle melts beneath major Quaternary volcanoes at common depths between ~65 to 130 km. We verified the existence of shallow mantle melting by observing lateral variations in the attenuation of local deep earthquake signals that coincide with the imaged features. Based on our results, we concluded that intraplate volcanism in our study area formed by focused decompressional melting. Our model favored the melt generation at moderate temperature ($T_P \sim 1300\,^\circ$C) possibly with a mildly hydrated condition. We further propose that a similar process can be applied to other areas with localized and long-lasting intraplate volcanic activities when localized convective instability can derive in the upper mantle such as by heterogeneous lithospheric thickness or dynamic influences by subducting slab.

Seismic body-wave travel time provides profound information on the interior of the Earth. Extraction of the arrival times of the seismic body waves offers a unique opportunity to directly constrain the three-dimensional properties of the mantle at various depths. In order to constrain the detailed properties of the Earth's structure,

high-quality records of seismic rays are required. Currently, though there are many seismic arrays deployed around the globe, numerous uncertainties remain to be concerned in the seismically constrained structure, such as 1) data noise, 2) variable model parameterizations, 3) non-uniqueness of the solution model, and 4) variable spatial density of the sensitivities of seismic rays. We can present a better solution model by integrating more datasets and reducing the effects from data uncertainties, model non-uniqueness, and uneven data sensitivity. Deploying seismic stations can be one of the remedies to deal with the problem. However, with a limited number of seismic stations, it is necessary to extract as much information as possible from the currently collected data. We could use a variety of body-wave phases from a single seismic event, e.g., core phases, reflected phases. Since these phases have low signal-to-noise ratios due to extended ray trajectories, an improved technique for signal detection is needed. Indeed, recent studies have suggested various approaches for it, e.g., waveform stacking (Nelson & Grand, 2018) or array interferometry (Lin et al., 2013). Also, we could use different model parameterizations that correlate data sensitivity and uncertainties with velocity parameters, such as by statistical methods (e.g., Burdick & Lekić, 2017). As seismic travel times and waveforms are also sensitive to anisotropic properties as well as isotropic properties, one could better represent a seismic model by incorporating various elastic parameters (e.g., Wang et al., 2014). Accounting for a finite frequency effect of seismic phases (e.g., Dahlen et al., 2000; Hung et al., 2000; Montelli et al., 2004) could also improve data sensitivity compared to the ray-theoretical approach for a limited data set. Various characteristics of seismic body wave signals (e.g., amplitude,

waveform) as well as travel time can also be used to provide more information on the properties of the mantle structures.

The limitation of teleseismic travel time tomography majorly comes from its low vertical resolution owing to the near vertical (<25°) incidence angle of teleseismic rays. To alleviate this problem, we could use local earthquakes with high incident angles, surface waves, or ambient noise datasets to improve the resolution. The improved solution model will allow the observed structure to be quantitatively analyzed in a finer scale. Joint assessments of multiple datasets, e.g., by joint inversion, could complement the spatial resolution of different datasets. Pursuing a joint interpretation of the current data set with other seismological data sets, such as the receiver function, enables us to obtain a higher resolution throughout the upper mantle, possibly across the major discontinuities, such as interfaces between the crust to the upper mantle and the upper and lower mantle.

The current limitation in constraining the mechanism of intraplate volcanism in northeast Asia based on seismic tomography models is that the seismic models mainly reflect physical properties of the upper mantle, not chemical properties (e.g., volatiles, trace element contents), which are possibly have significant impact on mantle convection (e.g., Richard & Iwamori, 2010; Hier-Majumder & Tauzin, 2017). How much chemical heterogeneity in the upper mantle affects convective instability or emplacement of melt is an essential part to be constrained to comprehend the development of volcanism. Despite this limitation, it is evident that the seismic tomography has by far the highest resolution compared to other geophysical or geochemical methods. We further extend our study to investigate thermodynamic properties of the whole upper mantle, and constrain the physical (or

chemical) interaction between different parts of the upper mantle (e.g., lithosphere, asthenosphere, stagnant slab, mantle transition zone). Geodynamic simulation will be helpful for thorough understanding of the upper mantle convective system by providing a timescale for a change in the physical behavior of mantle convection and its thermodynamic evolution (e.g., Ballmer et al., 2011; Liu & Stegman, 2012). Joint interpretation with geochemical results is necessary to verify the proposed mechanisms from seismological methods.

Bibliography

Abers, G. A., Fischer, K. M., Hirth, G., Wiens, D. A., Plank, T., Holtzman, B. K., ... and Gazel, E. (2014). Reconciling mantle attenuation-temperature relationships from seismology, petrology, and laboratory measurements. *Geochem. Geophys. Geosyst*, *15*(9), 3521–3542. https://doi.org/10.1002/2014GC005444

Adenis, A., Debayle, E., and Ricard, Y. (2017). Attenuation tomography of the upper mantle. *Geophys. Res. Lett.* *44*(15), 7715–7724. https://doi.org/10.1002/2017GL073751

Afonso, J. C., Ranalli, G., Fernàndez, M., Griffin, W. L., O'Reilly, S. Y., and Faul, U. (2010). On the Vp/Vs–Mg# correlation in mantle peridotites: Implications for the identification of thermal and compositional anomalies in the upper mantle. *Earth Planet. Sci. Lett.*, *289*(3–4), 606–618. https://doi.org/10.1016/j.epsl.2009.12.005

Ahn, U. S. (2016). Study of the last volcanic activity on historical records on Jeju Island, Korea. *The J. Petrol. Soc. Korea*, *25*(1), 69–83. https://doi.org/10.7854/JPSK.2016.25.1.69

Ahn, U. S., and Hong, S. S. (2017). Volcanological history of the Baengnokdam summit crater area, Mt. Halla in Jeju Island, Korea. *J. Petrol. Soc. Korea*, *26*(3), 221–234. https://doi.org/10.7854/JPSK.2017.26.3.221

Aizawa, Y., Barnhoorn, A., Faul, U. H., Fitz Gerald, J. D., Jackson, I., and Kovács, I. (2008). Seismic properties of Anita Bay dunite: an exploratory study of the influence of water. *J. Petrol.*, *49*(4), 841–855. https://doi.org/10.1093/petrology/egn007

Aki, K., Christoffersson, A., and Husebye, E. S. (1977). Determination of the three–dimensional seismic structure of the lithosphere. *J. Geophys. Res. 82*(2), 277–296. https://doi.org/10.1029/JB082i002p00277

Allen, R. M., Nolet, G., Morgan, W. J., Vogfjörd, K., Bergsson, B. H., Erlendsson, P., ... and Stefánsson, R. (1999). The thin hot plume beneath Iceland. *Geophys. J. Int.*, *137*(1), 51–63. https://doi.org/10.1046/j.1365–246x.1999.00753.x

Amante, C., and B. W. Eakins (2009), ETOP01 1 arc-minute global relief model: Procedures, data sources and analysis, NOAA Tech. Memo. NESDIS NGDC-24, 19 pp.

An, M., Wiens, D. A., Zhao, Y., Feng, M., Nyblade, A., Kanao, M., ... and Lévêque, J. J. (2015). Temperature, lithosphere-asthenosphere boundary, and heat flux beneath the Antarctic Plate inferred from seismic velocities. *J. Geophys. Res., Solid Earth*, *120*(12), 8720–8742. https://doi.org/10.1002/2015JB011917

Anderson, D. L., Ben-Menahem, A., and Archambeau, C. B. (1965). Attenuation of seismic energy in the upper mantle. *J. Geophys. Res.*, *70*(6), 1441–1448. https://doi.org/10.1029/JZ070i006p01441

Arai, S., Kida, M., Abe, N., and Yurimoto, H. (2001). Petrology of peridotite xenoliths in alkali basalt (11 Ma) from Boun, Korea: an insight into the upper mantle beneath the East Asian continental margin. *J. Miner. Petrol. Sci.*, *96*(3), 89–99. https://doi.org/10.2465/jmps.96.89

Argnani, A., Cimini, G. B., Frugoni, F., Monna, S., and Montuori, C. (2016). The role of continental margins in the final stages of arc formation: Constraints from teleseismic tomography of the Gibraltar and Calabrian Arc (Western Mediterranean). *Tectonophysics*, *677−678*, 135–152. https://doi.org/10.1016/j.tecto.2016.03.037

Artemieva, I. M. (2006). Global 1° × 1° thermal model TC1 for the continental lithosphere: implications for lithosphere secular evolution. *Tectonophysics*, *416*(1-4), 245–277. https://doi.org/10.1016/j.tecto.2005.11.022

Artemieva, I. M., (2019). Lithosphere structure in Europe from thermal isostasy. *Earth Sci. Rev.*, *188*, 454–468. https://doi.org/10.1016/j.earscirev.2018.11.004

Artemieva, I. M., and Mooney, W.D. (2002). On the relations between cratonic lithosphere thickness, plate motions, and basal drag. *Tectonophysics*, *358*(1-4), 211–231. https://doi.org/10.1016/S0040−1951(02)00425−0

Asamori, K., and Zhao, D. (2015). Teleseismic shear wave tomography of

the Japan subduction zone, *Geophys. J. Int.*, *203*(3), 1752–1772, https://doi.org/10.1093/gji/ggv334

Baek, S., Choi, S. H., Lee, S. G., Lee, S. R., and Lee, H. M. (2014). Geochemistry of anorthositic xenolith and host tholeiite basalt from Jeju Island, South Korea. *Geosci. J.*, *18*(2), 125–135. https://doi.org/10.1007/s12303-013-0060-9

Ball, P. W., White, N. J., Maclennan, J., and Stephenson, S. N. (2021). Global influence of mantle temperature and plate thickness on intraplate volcanism. *Nat. Commun.*, *12*(1), 1–13.

Ballmer, M. D., Conrad, C. P., Smith, E. I., and Johnsen, R. (2015a). Intraplate volcanism at the edges of the Colorado Plateau sustained by a combination of triggered edge-driven convection and shear-driven upwelling. *Geochem. Geophys. Geosyst.*, *16*(2), 366–379. https://doi.org/10.1002/2014GC005641

Ballmer, M. D., Ito, G., Van Hunen, J., and Tackley, P. J. (2011). Spatial and temporal variability in Hawaiian hotspot volcanism induced by small-scale convection. *Nat Geosci.*, *4*(7), 457–460. https://doi.org/10.1038/ngeo1187

Ballmer, M. D., Schmerr, N.C., Nakagawa, T., and Ritsema, J. (2015b). Compositional mantle layering revealed by slab stagnation at ~1000-km depth. *Sci. Adv.*, *1*(11), e1500815. https://doi.org/10.1126/sciadv.1500815

Ballmer, M. D., Van Hunen, J., Ito, G., Tackley, P. J., and Bianco, T. A. (2007). Non-hotspot volcano chains originating from small-scale sublithospheric convection. *Geophys. Res. Lett.*, *34*(23). https://doi.org/10.1029/2007GL031636

Bao, X., Eaton, D.W., and Guest, B. (2014). Plateau uplift in western Canada caused by lithospheric delamination along a craton edge. *Nat. Geosci.*, *7*(11), 830. https://doi.org/10.1038/ngeo2270

Bastow, I. D. (2012). Relative arrival-time upper-mantle tomography and the elusive background mean. *Geophys. J. Int.*, *190*(2), 1271–1278. https://doi.org/10.1111/j.1365-246X.2012.05559.x

Bastow, I. D., Nyblade, A. A., Stuart, G. W., Rooney, T. O., and Benoit, M. H. (2008). Upper mantle seismic structure beneath the Ethiopian hot spot: Rifting at the edge of the African low-velocity anomaly, *Geochem. Geophys. Geosyst.*, *9*(12), 1–25. https://doi.org/10.1029/2008GC002107

Bastow, I. D., Stuart, G. W., Kendall, J. M., and Ebinger, C. J. (2005). Upper-mantle seismic structure in a region of incipient continental breakup: Northern Ethiopian rift. *Geophys. J. Int.*, *162*(2), 479–493. https://doi.org/10.1111/j.1365-246X.2005.02666.x

Behn, M. D., Hirth, G., and Elsenbeck II, J. R. (2009). Implications of grain size evolution on the seismic structure of the oceanic upper mantle. *Earth Planet. Sci. Lett.*, *282*(1–4), 178–189. https://doi.org/10.1016/j.epsl.2009.03.014

Benz, H. M., Chouet, B. A., Dawson, P. B., Lahr, J. C., Page, R. A., and Hole, J. A. (1996). Three-dimensional P and S wave velocity structure of Redoubt Volcano, Alaska. *J. Geophys. Res., Solid Earth*, *101*(B4), 8111–8128. https://doi.org/10.1029/95JB03046

Bercovici, D., and Karato, S. I. (2003). Whole-mantle convection and the transition-zone water filter. *Nature*, *425*(6953), 39–44. https://doi.org/10.1038/nature01918

Bezada, M. J. (2017). Insights into the lithospheric architecture of Iberia and Morocco from teleseismic body-wave attenuation. *Earth Planet. Sci. Lett.*, *478*, 14–26. http://doi.org/10.1016/j.epsl.2017.08.029

Bina, C.R., and Helffrich, G. (1994). Phase transition Clapeyron slopes and transition zone seismic discontinuity topography. *J. Geophys. Res., Solid Earth*, *99*(B8), 15853–15860. https://doi.org/10.1029/94JB00462

Bird, P. (2003). An updated digital model of plate boundaries. *Geochem. Geophys. Geosyst.*, *4*(3), 1–52. https://doi.org/10.1029/2001GC000252

Biryol, C. B., Beck, S. L., Zandt, G., and Özacar, A. A. (2011). Segmented African lithosphere beneath the Anatolian region inferred from teleseismic P wave tomography. *Geophys. J. Int.*, *184*(3), 1037–1057. https://doi.org/10.1111/j.1365-246X.2010.04910.x

Boore, D. M., and Boatwright, J. (1984). Average body-wave radiation

coefficients. *Bull. Seismol. Soc. Am*, *74*(5), 1615–1621

Boyce, A., Bastow, I.D., Golos, E.M., Rondenay, S., Burdick, S., and van der Hilst, R.D. (2019). Variable modification of continental lithosphere during the Proterozoic Grenville orogeny: Evidence from teleseismic P–wave tomography. *Earth Planet. Sci. Lett.*, *525*, 115763. https://doi.org/10.1016/j.epsl.2019.115763

Boyden, J. A., Müller, R. D., Gurnis, M., Torsvik, T. H., Clark, J. A., Turner, M., et al. (2011). Next–generation plate–tectonic reconstructions using GPlates. In G. R. Keller, and C. Baru (Eds.), Geoinformatics: Cyberinfrastructure for the solid Earth sciences (pp. 95–114). Cambridge: Cambridge University Press. https://doi.org/10.1017/CBO9780511976308.008

Brenna, M., Cronin, S. J., Kereszturi, G., Sohn, Y. K., Smith, I. E. M., and Wijbrans, J. (2015a). Intraplate volcanism influenced by distal subduction tectonics at Jeju Island, Republic of Korea. *Bull. Volcanol.*, *77*(1), 7. https://doi.org/10.1007/s00445–014–0896–5

Brenna, M., Cronin, S. J., Németh, K., Smith, I. E. M., and Sohn, Y. K. (2011). The influence of magma plumbing complexity on monogenetic eruptions, Jeju Island, Korea. *Terra Nova*, *23*(2), 70–75. https://doi.org/10.1111/j.1365–3121.2010.00985.x

Brenna, M., Cronin, S. J., Smith, I. E. M., Maas, R., and Sohn, Y. K. (2012a). How small–volume basaltic magmatic systems develop: A case study from the Jeju Island volcanic field, Korea. *J. Petrol.*, *53*(5), 985–1018. https://doi.org/10.1093/petrology/egs007

Brenna, M., Cronin, S. J., Smith, I. E. M., Sohn, Y. K., and Maas, R. (2012b). Spatio–temporal evolution of a dispersed magmatic system and its implications for volcano growth, Jeju Island Volcanic Field, Korea. *Lithos*, *148*, 337–352. https://doi.org/10.1016/j.lithos.2012.06.021

Brenna, M., Cronin, S. J., Smith, I. E. M., Sohn, Y. K., and Németh, K. (2010). Mechanisms driving polymagmatic activity at a monogenetic volcano, Udo, Jeju Island, South Korea. *Contrib. Mineral. Petrol.*, *160*(6), 931–950. https://doi.org/10.1007/s00410–010–0515–1

Brenna, M., Németh, K., Cronin, S. J., Sohn, Y. K., Smith, I. E., and Wijbrans, J. (2015b). Co-located monogenetic eruptions ~200 kyr apart driven by tapping vertically separated mantle source regions, Chagwido, Jeju Island, Republic of Korea. *Bull. Volcanol.*, *77*(5), 43. https://doi.org/10.1007/s00445-015-0928-9

Brenna, M., Price, R., Cronin, S. J., Smith, I. E., Sohn, Y. K., Kim, G. B., and Maas, R. (2014). Final magma storage depth modulation of explosivity and trachyte-phonolite genesis at an intraplate volcano: a case study from Ulleung Island, South Korea. *J. Petrol.*, *55*(4), 709-747. https://doi.org/10.1093/petrology/egu004

Buchen, J., Marquardt, H., Speziale, S., Kawazoe, T., Ballaran, T. B., and Kurnosov, A. (2018). High-pressure single-crystal elasticity of wadsleyite and the seismic signature of water in the shallow transition zone. *Earth Planet. Sci. Lett.*, 498, 77-87. https://doi.org/10.1016/j.epsl.2018.06.027

Burdick, S., and Lekić, V. (2017). Velocity variations and uncertainty from transdimensional P-wave tomography of North America. *Geophys. J. Int.*, *209*(2), 1337-1351. https://doi.org/10.1093/gji/ggx091

Cai, Y.C., Fan, H.R., Santosh, M., Hu, F.F., Yang, K.F., and Li, X.H. (2018). Decratonic gold mineralization: evidence from the Shangzhuang gold deposit, eastern North China Craton. *Gondwana Res.*, *54*, 1-22. https://doi.org/10.1016/j.gr.2017.09.009

Cammarano, F., Goes, S., Vacher, P., and Giardini, D. (2003). Inferring upper-mantle temperatures from seismic velocities. *Phys. Earth Planet. Inter.*, *138*(3-4), 197-222. https://doi.org/10.1016/S0031-9201(03)00156-0

Cammarano, F., and Romanowicz, B. (2007). Insights into the nature of the transition zone from physically constrained inversion of long-period seismic data. *Proc. Natl. Acad. Sci.*, *104*(22), 9139-9144. https://doi.org/10.1073/pnas.0608075104

Cañón-Tapia, E., and Walker, G. P. (2004). Global aspects of volcanism: The perspectives of "plate tectonics" and "volcanic systems." *Earth*

Sci.   Rev.,   66(1-2),   163-182.
https://doi.org/10.1016/j.earscirev.2003.11.001

Cantwell, P. R., Tang, M., Dillon, S. J., Luo, J., Rohrer, G. S., and Harmer, M.
P. (2014). Grain boundary complexions. *Acta Mater.*, *62*, 1-48.
https://doi.org/10.1016/j.actamat.2013.07.037

Chang, K. H., and Zhao, X. (2012). North and South China suturing in the
east end: What happened in Korean Peninsula?. *Gondwana Res.*, *22*(2),
493-506. https://doi.org/10.1016/j.gr.2011.12.010

Chang, S.J., and Baag, C.E. (2007). Moho depth and crustal Vp/Vs variation
in southern Korea from teleseismic receiver functions: implication for
tectonic affinity between the Korean Peninsula and China. *Bull. Seismol.
Soc. Am.*, *97*(5), 1621-1631. https://doi.org/10.1785/0120050264

Chang, S.J., Ferreira, A. M., and Faccenda, M. (2016). Upper-and mid-
mantle interaction between the Samoan plume and the Tonga-Kermadec
slabs. *Nat. Commun.*, *7*(1), 1-9. https://doi.org/10.1038/ncomms10799

Chang, S.J., Ferreira, A.M., Ritsema, J., van Heijst, H.J., and Woodhouse, J.H.
(2015). Joint inversion for global isotropic and radially anisotropic mantle
structure including crustal thickness perturbations. *J. Geophys. Res., Solid
Earth*, *120*(6), 4278-4300. https://doi.org/10.1002/2014JB011824

Chantel, J., Manthilake, G., Andrault, D., Novella, D., Yu, T., and Wang, Y.
(2016). Experimental evidence supports mantle partial melting in the
asthenosphere.   *Sci.   Adv.*,   *2*(5),   e1600246.   https://doi.org/
10.1126/sciadv.1600246

Chen, C., Zhao, D., Tian, Y., Wu, S., Hasegawa, A., Lei, J., et al. (2017).
Mantle transition zone, stagnant slab and intraplate volcanism in Northeast
Asia. *Geophys. J. Int.*, *209*(1), 68-85. https://doi.org/10.1093/gji/ggw491

Chen, L., (2010). Concordant structural variations from the surface to the
base of the upper mantle in the North China Craton and its tectonic
implications.   *Lithos*,   *120*(1-2),   96-115.
https://doi.org/10.1016/j.lithos.2009.12.007

Chen, L., Cheng, C., and Wei, Z. (2009). Seismic evidence for significant
lateral variations in lithospheric thickness beneath the central and western

North China Craton. *Earth Planet. Sci. Lett.*, *286*(1-2), 171-183. https://doi.org/10.1016/j.epsl.2009.06.022

Chen, L., Jiang, M., Yang, J., Wei, Z., Liu, C., and Ling, Y. (2014). Presence of an intralithospheric discontinuity in the central and western North China Craton: Implications for destruction of the craton. *Geology*, *42*(3), 223-226. https://doi.org/10.1130/G35010.1

Chen, S. S., Lee, S. G., Lee, T. J., Lee, Y. S., and Liu, J. Q. (2018). Multi-stage magmatic plumbing system of the volcano: A case study from Ulleung Island, South Korea. *Lithos*, *314*, 201-215. https://doi.org/10.1016/j.lithos.2018.05.028

Chen, Y. W., Wu, J., and Suppe, J. (2019). Southward propagation of Nazca subduction along the Andes. *Nature*, *565*(7740), 441-447. https://doi.org/10.1038/s41586-018-0860-1

Cheng, C., Chen, L., Yao, H., Jiang, M., and Wang, B. (2013). Distinct variations of crustal shear wave velocity structure and radial anisotropy beneath the North China Craton and tectonic implications. *Gondwana Res.*, *23*(1), 25-38. https://doi.org/10.1016/j.gr.2012.02.014

Cheong, A.C., Jo, H.J., Jeong, Y.J., and Li, X.H. (2018). Magmatic response to the interplay of collisional and accretionary orogenies in the Korean Peninsula: Geochronological, geochemical, and O-Hf isotopic perspectives from Triassic plutons. *Geol. Soc. Am. Bull.*, *131*(3-4), 609-634. https://doi.org/10.1130/B32021.1

Cho, H.M., Baag, C.E., Lee, J.M., Moon, W.M., Jung, H., Kim, K.Y., and Asudeh, I. (2006). Crustal velocity structure across the southern Korean Peninsula from seismic refraction survey. *Geophys. Res. Lett.*, *33*(6), L06307. https://doi.org/10.1029/2005GL025145

Cho, M., Kim, H., Lee, Y., Horie, K., and Hidaka, H. (2008). The oldest (ca. 2.51 Ga) rock in South Korea: U-Pb zircon age of a tonalitic migmatite, Daeijak Island, western Gyeonggi massif. *Geosci. J.*, *12*(1), 1-6. https://doi.org/10.1007/s12303-008-0001-1

Cho, M., Kim, T., Yang, S.Y., and Yi, K. (2017). Paleoproterozoic to Triassic crustal evolution of the Gyeonggi Massif, Korea: Tectonic correlation with

the North China craton. In: Richard, D.L., Thigpen, J.R., Merschat A.J. (Eds.), Linkages and Feedbacks in Orogenic Systems, *Geol. Soc. Am Mem.*, *213*, 165–197. Boulder, CO: Geological Society of America. https://doi.org/10.1130/MEM213

Choi, D.K. (2019). Evolution of the Taebaeksan Basin, Korea: II, late Paleozoic sedimentation in a retroarc foreland basin and assembly of the proto-Korean Peninsula. *Isl. Arc*, *28*(1), e12277. https://doi.org/10.1111/iar.12277

Choi, H.O., Choi, S.H., Lee, D.C., and Kang, H.C. (2013). Geochemical evolution of basaltic volcanism within the tertiary basins of southeastern Korea and the opening of the East Sea (Sea of Japan). *J. Volcanol. Geoth. Res.*, *249*, 109–122. https://doi.org/10.1016/j.jvolgeores.2012.09.007

Choi, H.O., Choi, S. H., Lee, Y. S., Ryu, J. S., Lee, D. C., Lee, S. G., ... and Liu, J. Q. (2020). Petrogenesis and mantle source characteristics of the late Cenozoic Baekdusan (Changbaishan) basalts, North China Craton. *Gondwana Res.*, *78*, 156–171. https://doi.org/10.1016/j.gr.2019.08.004

Choi, S.H. (2021). Geochemistry and petrogenesis of Quaternary volcanic rocks from Ulleung Island, South Korea. *Lithos*, 380, 105874. https://doi.org/10.1016/j.lithos.2020.105874

Choi, S.H., Mukasa, S.B., Kwon, S.-T., and Andronikov, A.V. (2006). Sr, Nd, Pb and Hf isotopic compositions of late Cenozoic alkali basalts in South Korea: Evidence for mixing between the two dominant asthenospheric mantle domains beneath East Asia. *Chem. Geol.*, *232*(3), 134–151. https://doi.org/10.1016/j.chemgeo.2006.02.014

Chough, S.K., Kwon, S. T., Ree, J. H., and Choi, D. K. (2000). Tectonic and sedimentary evolution of the Korean Peninsula: A review and new view. *Earth Sci. Rev.*, *52*(1–3), 175–235. https://doi.org/10.1016/S0012-8252(00)00029-5

Chough, S.K., Shinn, Y.J., and Yoon, S.H. (2018). Regional strike-slip and initial subsidence of Korea Plateau, East Sea: tectonic implications for the opening of back-arc basins. *Geosci. J.*, *22*(4), 533–547. http://dx.doi.org/10.1007/s12303-018-0017-0

Chough, S.K., and Sohn, Y.K. (2010). Tectonic and sedimentary evolution of a Cretaceous continental arc-backarc system in the Korean Peninsula: New view. *Earth Sci. Reviews*, *101*(3-4), 225-249. https://doi.org/10.1016/j.earscirev.2010.05.004

Chwae, U.C., Kim K.B., Hong. S.H., Lee, B.J., Hwang, J.H., Park, K.H., et al. (1995). Geological map of Korea scale 1:1,000,000, Korea Institute of Geoscience and Mineral Resources, Daejeon, South Korea

Cline, C. J. II, Faul, U. H., David, E. C., Berry, A. J. and Jackson, I. (2018). Redox-influenced seismic properties of upper-mantle olivine. *Nature*, *555*, 355-358. https://doi.org/10.1038/nature25764

Cobden, L., Trampert, J., and Fichtner, A. (2018). Insights on upper mantle melting, rheology, and anelastic behavior from seismic shear wave tomography. *Geochem., Geophys., Geosyst.*, 19(10), 3892-3916. https://doi.org/10.1029/2017GC007370

Connolly, J. A. (2005). Computation of phase equilibria by linear programming: a tool for geodynamic modeling and its application to subduction zone decarbonation. *Earth Planet. Sci. Lett.*, *236*(1-2), 524-541. https://doi.org/10.1016/j.epsl.2005.04.033

Connor, C.B., and Conway, F.M. (2000). Basaltic volcanic fields. In H. Sigurdsson (Ed.), *Encyclopedia of volcanoes* (pp. 331-343). San Diego, CA: Academic

Conrad, C.P., Bianco, T. A., Smith, E. I., and Wessel, P. (2011). Patterns of intraplate volcanism controlled by asthenospheric shear. *Nat. Geosci.*, *4*, 317-321. https://doi.org/10.1038/ngeo1111

Conrad, C. P., Wu, B., Smith, E. I., Bianco, T. A., and Tibbetts, A. (2010). Shear-driven upwelling induced by lateral viscosity variations and asthenospheric shear: A mechanism for intraplate volcanism. *Phys. Earth Planet. Inter.*, *178*(3), 162-175. https://doi.org/10.1016/j.pepi.2009.10.001

Currie, C. A., Huismans, R. S., and Beaumont, C. (2008). Thinning of continental backarc lithosphere by flow-induced gravitational instability. *Earth Planet. Sci. Lett.*, *269*(3-4), 436-447.

https://doi.org/10.1016/j.epsl.2008.02.037

Dahlen, F. A., Hung, S. H., and Nolet, G. (2000). Fréchet kernels for finite—frequency traveltimes—I. Theory. *Geophys. J. Int.*, *141*(1), 157–174. https://doi.org/10.1046/j.1365–246X.2000.00070.x

Dasgupta, R., Mallik, A., Tsuno, K., Withers, A. C., Hirth, G., and Hirschmann, M. M. (2013). Carbon—dioxide—rich silicate melt in the Earth's upper mantle. *Nature*, *493*(7431), 211–215. https://doi.org/10.1038/nature11731

Davies, D.R., and Rawlinson, N. (2014). On the origin of recent intraplate volcanism in Australia. *Geology*, *42*(12), 1031–1034. https://doi.org/10.1130/G36093.1

Davies, D. R., Rawlinson, N., Iaffaldano, G., and Campbell, I. H. (2015). Lithospheric controls on magma composition along Earth's longest continental hotspot track. *Nature*, *525*(7570), 511–514. https://doi.org/10.1038/nature14903

Debayle, E., Bodin, T., Durand, S., and Ricard, Y. (2020). Seismic evidence for partial melt below tectonic plates. *Nature*, *586*(7830), 555–559. https://doi.org/10.1038/s41586–020–2809–4

Debayle, E., Dubuffet, F., and Durand, S. (2016), An automatically updated S—wave model of the upper mantle and the depth extent of azimuthal anisotropy, *Geophys. Res. Lett*, *43*, 674–682, doi:10.1002/2015GL067329

Debayle, E., and Ricard, Y. (2012). A global shear velocity model of the upper mantle from fundamental and higher Rayleigh mode measurements. *J. Geophys. Res., Solid Earth*, *117*(B10). https://doi.org/10.1029/2012JB009288

Duggen, S., Hoernle, K.A., Hauff, F., Kluegel, A., Bouabdellah, M., and Thirlwall, M.F. (2009). Flow of Canary mantle plume material through a subcontinental lithospheric corridor beneath Africa to the Mediterranean. *Geology*, *37*(3), 283–286. https://doi.org/10.1130/G25426A.1

Durek, J. J., and Ekström, G. (1996). A radial model of anelasticity consistent with long—period surface—wave attenuation. *Bull. Seismol. Soc.*

Am., *86*(1A), 144–158

Dziewonski, A. M., and Anderson, D. L. (1981). Preliminary reference Earth model. *Phys. Earth Planet. Int.*, *25*(4), 297–356. https://doi.org/10.1016/0031-9201(81)90046-7

Eberhart-Phillips, D., and Chadwick, M. (2002). Three-dimensional attenuation model of the shallow Hikurangi subduction zone in the Raukumara Peninsula, New Zealand. *J. Geophys. Res., Solid Earth*, *107*(B2), ESE-3. https://doi.org/10.1029/2000JB000046

Eilon, Z. C., and Abers, G. A. (2017). High seismic attenuation at a mid-ocean ridge reveals the distribution of deep melt. *Sci. adv.*, *3*(5), e1602829. https://doi.org/10.1126/sciadv.1602829

Ekström, G., Nettles, M., and Dziewoński, A. M. (2012). The global CMT project 2004–2010: Centroid-moment tensors for 13,017 earthquakes. *Phys. Earth Planet. Int.*, *200*, 1–9. https://doi.org/10.1016/j.pepi.2012.04.002

Evanzia, D., Pulliam, J., Ainsworth, R., Gurrola, H., and Pratt, K. (2014). Seismic Vp & Vs tomography of Texas & Oklahoma with a focus on the Gulf Coast margin. *Earth Planet. Sci. Lett.*, *402*, 148–156. https://doi.org/10.1016/j.epsl.2013.12.027

Faccenna, C., Becker, T. W., Lallemand, S., Lagabrielle, Y., Funiciello, F., and Piromallo, C. (2010). Subduction-triggered magmatic pulses: A new class of plumes?, *Earth Planet. Sci. Lett.*, *299*(1), 54–68. https://doi.org/10.1016/j.epsl.2010.08.012

Faul, U. H., and Jackson, I. (2005). The seismological signature of temperature and grain size variations in the upper mantle. *Earth Planet. Sci. Lett.*, *234*(1–2), 119–134. https://doi.org/10.1016/j.epsl.2005.02.008

Fichtner, A., and Leeuwen, T. V. (2015). Resolution analysis by random probing. *J. Geophys. Res., Solid Earth*, *120*(8), 5549–5573. https://doi.org/10.1002/2015JB012106

Fichtner, A., and van Driel, M. (2014). Models and Fréchet kernels for frequency-(in) dependent Q. *Geophys. J. Int.*, *198*(3), 1878–1889. https://doi.org/10.1093/gji/ggu228

Foley, S.F. (2008). Rejuvenation and erosion of the cratonic lithosphere. *Nat. Geosci*, *1*(8), 503–510. https://doi.org/10.1038/ngeo261

Fukao, Y., and Obayashi, M. (2013). Subducted slabs stagnant above, penetrating through, and trapped below the 660 km discontinuity. *J. Geophys. Res., Solid Earth*, *118*(11), 5920–5938. https://doi.org/10.1002/2013JB010466

Gao, S., Rudnick, R.L., Yuan, H.L., Liu, X.M., Liu, Y.S., Xu, W.L., et al., (2004). Recycling lower continental crust in the North China craton. *Nature*, *432*(7019), 892–897. https://doi.org/10.1038/nature03162

Gao, W., Grand, S. P., Baldridge, W. S., Wilson, D., West, M., Ni, J. F., and Aster, R. (2004). Upper mantle convection beneath the central Rio Grande rift imaged by *P* and *S* wave tomography. *J. Geophys. Res., Solid Earth*, *109*(B3), 11539–11169. https://doi.org/10.1029/2003JB002743

Gallacher, R. J., Keir, D., Harmon, N., Stuart, G., Leroy, S., Hammond, J. O., ... and Ahmed, A. (2016). The initiation of segmented buoyancy－driven melting during continental breakup. *Nat. Commun.*, *7*(1), 1–9. https://doi.org/10.1038/ncomms13110

Garapić, G., Faul, U. H., and Brisson, E. (2013). High-resolution imaging of the melt distribution in partially molten upper mantle rocks: evidence for wetted two-grain boundaries. *Geochem., Geophys., Geosyst.*, *14*(3), 556–566. https://doi.org/10.1029/2012GC004547

Giacomuzzi, G., Civalleri, M., De Gori, P., and Chiarabba, C. (2012). A 3D Vs model of the upper mantle beneath Italy: Insight on the geodynamics of central Mediterranean. *Earth Planet. Sci. Lett.*, *335*, 105–120. https://doi.org/10.1016/j.epsl.2012.05.004

Goes, S., Govers, R., and Vacher, P. (2000). Shallow mantle temperatures under Europe from *P* and *S* wave tomography. *J. Geophys. Res., Solid Earth*, *105*(B5), 11153–11169. https://doi.org/10.1029/1999JB900300

Govers, R., and Fichtner, A. (2016). Signature of slab fragmentation beneath Anatolia from full－waveform tomography. *Earth Planet. Sci. Lett.*, *450*, 10–19. https://doi.org/10.1016/j.epsl.2016.06.014

Griffin, W.L., Andi, Z., O'Reilly, S.Y., and Ryan, C.G., (1998). Phanerozoic

evolution of the lithosphere beneath the Sino−Korean craton. In: Flower, M.F.J., Chung, S−.L., Lo, C.−H., Lee, T.−Y. (Eds.), Mantle dynamics and plate interactions in east Asia, 107−126. Washington, D. C.: Am. Geophys. Union. https://doi.org/10.1029/GD027p0107

Guo, P., Niu, Y., Sun, P., Gong, H., and Wang, X. (2020). Lithosphere thickness controls continental basalt compositions: An illustration using Cenozoic basalts from eastern China. *Geology*, *48*(2), 128−133. https://doi.org/10.1130/G46710.1

Guo, Z., Afonso, J. C., Qashqai, M. T., Yang, Y., and Chen, Y. J. (2016a). Thermochemical structure of the North China Craton from multi− observable probabilistic inversion: Extent and causes of cratonic lithosphere modification. *Gondwana Res.*, 37, 252−265. https://doi.org/10.1016/j.gr.2016.07.002

Guo, Z., Chen, Y. J., Ning, J., Yang, Y., Afonso, J. C., and Tang, Y. (2016b). Seismic evidence of on−going sublithosphere upper mantle convection for intraplate volcanism in Northeast China. *Earth Planet. Sci. Lett., 433*, 31− 43. https://doi.org/10.1016/j.epsl.2015.09.035

Guo, Z., Wang, K., Yang, Y., Tang, Y., John Chen, Y., and Hung, S. H. (2018). The origin and mantle dynamics of Quaternary intraplate volcanism in Northeast China from joint inversion of surface wave and body wave. *J. Geophys. Res., Solid Earth*, *123*(3), 2410−2425. https://doi.org/10.1002/2017JB014948

Hammond, W. C., and Humphreys, E. D. (2000). Upper mantle seismic wave velocity: Effects of realistic partial melt geometries. *J. Geophys. Res., Solid Earth*, *105*(B5), 10975−10986. https://doi.org/10.1029/2000JB900041

Han, G., Li, J., Guo, G., Mooney, W. D., Karato, S. I., and Yuen, D. A. (2021). Pervasive low−velocity layer atop the 410−km discontinuity beneath the northwest Pacific subduction zone: Implications for rheology and geodynamics. *Earth Planet. Sci. Lett.*, *554*, 116642. https://doi.org/10.1016/j.epsl.2020.116642

Havlin, C., Holtzman, B. K., and Hopper, E. (2021). Inference of

thermodynamic state in the asthenosphere from anelastic properties, with applications to North American upper mantle. *Phys. Earth Planet. Inter.*, *314*, 106639

Hawley, W. B., and Allen, R. M. (2019). The fragmented death of the Farallon plate. *Geophys. Res. Lett.*, *46*, 7386–7394. https://doi.org/10.1029/2019GL083437

Hayes, G.P., Moore, G.L., Portner, D.E., Hearne, M., Flamme, H., Furtney, M., and Smoczyk, G.M. (2018). Slab2, a comprehensive subduction zone geometry model. *Science*, *362*(6410), 58–61. https://doi.org/10.1126/science.aat4723

He, C., and Zheng, Y.F. (2018). Seismic evidence for the absence of deeply subducted continental slabs in the lower lithosphere beneath the Central Orogenic Belt of China. *Tectonophysics*, *723*, 178–189. https://doi.org/10.1016/j.tecto.2017.12.018

Hernlund, J. W., Tackley, P. J., and Stevenson, D. J. (2008). Buoyant melting instabilities beneath extending lithosphere: 1. Numerical models. *J. Geophys. Res., Solid Earth*, *113*(B4). https://doi.org/10.1029/2006JB004862

Hier-Majumder, S., and Tauzin, B. (2017). Pervasive upper mantle melting beneath the western US. *Earth Planet. Sci. Lett.*, *463*, 25–35. https://doi.org/10.1016/j.epsl.2016.12.041

Hirano, N., Takahashi, E., Yamamoto, J., Abe, N., Ingle, S. P., Kaneoka, I., ... and Suyehiro, K. (2006). Volcanism in response to plate flexure. *Science*, *313*(5792), 1426–1428. https://doi.org/10.1126/science.1128235

Hirschmann, M. M. (2000). Mantle solidus: Experimental constraints and the effects of peridotite composition. *Geochem., Geophys., Geosyst.*, 1(10). https://doi.org/10.1029/2000GC000070

Hirschmann, M. M., and Stolper, E. M. (1996). A possible role for garnet pyroxenite in the origin of the "garnet signature" in MORB. *Contrib. Mineral. Petrol.*, *124*(2), 185–208. https://doi.org/10.1007/s004100050184

Hirschmann, M. M., Tenner, T., Aubaud, C., and Withers, A. C. (2009).

Dehydration melting of nominally anhydrous mantle: The primacy of partitioning. *Phys. Earth Planet. Inter.,* *176*(1–2), 54–68. https://doi.org/10.1016/j.pepi.2009.04.001

Hirth, G., and Kohlstedt, D. L. (1996). Water in the oceanic upper mantle: implications for rheology, melt extraction and the evolution of the lithosphere. *Earth Planet. Sci. Lett.,* *144*(1–2), 93–108. https://doi.org/10.1016/0012−821X(96)00154−9

Hirth, G., and Kohlstedt, D. L (2003). Rheology of the upper mantle and the mantle wedge: A view from the experimentalists. *Geophys. Monogr.,* *138*, 83–106. https://doi.org/10.1029/138GM06

Hoernle, K., White, J. D. L., Van den Bogaard, P., Hauff, F., Coombs, D. S., Werner, R., et al. (2006). Cenozoic intraplate volcanism on New Zealand: Upwelling induced by lithospheric removal. *Earth Planet. Sci. Lett., 248*(1–2), 350–367. https://doi.org/10.1016/j.epsl.2006.06.001

Hoke, L., and Lamb, S. (2007). Cenozoic behind−arc volcanism in the Bolivian Andes, South America: Implications for mantle melt generation and lithospheric structure. *J. Geol. Soc.,* *164*(4), 795–814. https://doi.org/10.1144/0016−76492006−092

Holford, S. P., Hillis, R. R., Hand, M., and Sandiford, M. (2011). Thermal weakening localizes intraplate deformation along the southern Australian continental margin. *Earth Planet. Sci. Lett.,* *305*(1−2), 207−214. https://doi.org/10.1016/j.epsl.2011.02.056

Holtzman, B. K. (2016). Questions on the existence, persistence, and mechanical effects of a very small melt fraction in the asthenosphere. *Geochem., Geophys., Geosyst.,* *17*(2), 470−484. https://doi.org/10.1002/2015GC006102

Hu, J., L. Liu, M. Faccenda, Q. Zhou, K.M. Fischer, S. Marshak, and C. Lundstrom (2018). Modification of the Western Gondwana craton by plume−lithosphere interaction. *Nat. Geosci.,* *11*(3), 203−210. https://doi.org/10.1038/s41561−018−0064−1

Huang, H.−H., Lin, F.−C., Schmandt, B., Farrell, J., Smith, R. B., and Tsai, V. C. (2015). The Yellowstone magmatic system from the mantle plume

to the upper crust. *Science*, *348*(6236), 773–776. https://doi.org/10.1126/science.aaa5648

Huang, J., and Zhao, D. (2006). High-resolution mantle tomography of China and surrounding regions. *J. Geophys. Res., Solid Earth*, *111*, B09305. https://doi.org/10.1029/2005JB004066

Huang, Z., Li, H., Zheng, Y., and Peng, Y. (2009). The lithosphere of North China Craton from surface wave tomography. *Earth Planet. Sci. Lett.*, *288*(1–2), 164–173. https://doi.org/10.1016/j.epsl.2009.09.019

Huang, Z., Peng, Y., Luo, Y., Zheng, Y., and Su, W. (2004). Azimuthal anisotropy of Rayleigh waves in East Asia. *Geophys. Res. Lett.*, *31*(15), L15617. https://doi.org/10.1029/2004GL020399

Huang, Z., Zhao, D., Hasegawa, A., Umino, N., Park, J. H., and Kang, I. B. (2013). Aseismic deep subduction of the Philippine Sea plate and slab window. *J. Asian Earth Sci.*, *75*, 82–94. https://doi.org/10.1016/j.jseaes.2013.07.002

Hung, S.-H., Dahlen, F. A., and Nolet, G. (2000). Fréchet kernels for finite-frequency traveltimes-II. Examples. *Geophys. J. Int.*, *141*(1), 175–203. https://doi.org/10.1046/j.1365-246X.2000.00072.x

Hyndman, R.D. (2019). Mountain Building Orogeny in Precollision Hot Backarcs: North American Cordillera, India-Tibet, and Grenville Province. *J. Geophys. Res., Solid Earth*, *124*(2), 2057–2079. https://doi.org/10.1029/2018JB016697

Ichiki, M., Baba, K., Obayashi, M., and Utada, H. (2006). Water content and geotherm in the upper mantle above the stagnant slab: Interpretation of electrical conductivity and seismic P-wave velocity models. *Phys. Earth Planet. Int.*, *155*(1–2), 1–15. https://doi.org/10.1016/j.pepi.2005.09.010

Irifune, T., Higo, Y., Inoue, T., Kono, Y., Ohfuji, H., and Funakoshi, K. (2008). Sound velocities of majorite garnet and the composition of the mantle transition region. *Nature*, *451*(7180), 814–817. https://doi.org/10.1038/nature06551

Ito, E., and Takahashi, E. (1989). Postspinel transformations in the system Mg2SiO4-Fe2SiO4 and some geophysical implications. *J. Geophys. Res.*,

Solid Earth, *94*(B8), 10637–10646. https://doi.org/10.1029/JB094iB08p10637

Iwasaki, T., Sato, H., Ishiyama, T., Shinohara, M., and Hashima, A. (2015, December). Fundamental structure model of island arcs and subducted plates in and around Japan. In *AGU Fall Meeting Abstracts* (Vol. 2015, pp. T31B–2878).

Jackson, I., and Faul, U. H. (2010). Grainsize–sensitive viscoelastic relaxation in olivine: Towards a robust laboratory–based model for seismological application. *Phys. Earth Planet. Inter.*, *183*(1–2), 151–163. https://doi.org/10.1016/j.pepi.2010.09.005

Jacobsen, S. D., Jiang, F., Mao, Z., Duffy, T.S., Smyth, J.R., Holl, C.M., and Frost, D.J. (2008), Effects of hydration on the elastic properties of olivine, *Geophys. Res. Lett.*, *35*, L14303. https://doi.org/10.1029/2008GL034398

Jacobsen, S.D., and Smyth, J.R. (2006). Effect of water on the sound velocities of ringwoodite in the transition zone. *Geophys. Monogr.—*Am. Geophys. Union 168, 131.

Jacobsen, S.D., Smyth, J.R., Spetzler, H., Holl, C.M., and Frost, D.J. (2004). Sound velocities and elastic constants of iron–bearing hydrous ringwoodite. *Phys. Earth Planet. Inter. 143–144*, 47–56. https://doi.org/10.1016/j.pepi.2003.07.019

James, D. E., Fouch, M. J., Carlson, R. W., and Roth, J. B. (2011). Slab fragmentation, edge flow and the origin of the Yellowstone hotspot track. *Earth Planet. Sci. Lett.*, *311*(1–2), 124–135. https://doi.org/10.1016/j.epsl.2011.09.007

Jiang, M., Ai, Y., Chen, L., and Yang, Y. (2013). Local modification of the lithosphere beneath the central and western North China Craton: 3–D constraints from Rayleigh wave tomography. *Gondwana Res. 24*(3–4), 849–864. https://doi.org/10.1016/j.gr.2012.06.018

Kaban, M.K., Stolk, W., Tesauro, M., El Khrepy, S., Al-Arifi, N., Beekman, F., et al. (2016). 3D density model of the upper mantle of Asia based on inversion of gravity and seismic tomography data. *Geochem. Geophys. Geosyst*, *17*(11), 4457–4477. https://doi.org/10.1002/2016GC006458

Kaislaniemi, L., and Van Hunen, J. (2014). Dynamics of lithospheric thinning and mantle melting by edge-driven convection: Application to Moroccan Atlas mountains. *Geochem. Geophys. Geosyst*, *15*(8), 3175–3189. https://doi.org/10.1002/2014GC005414

Kameyama, M., and Nishioka, R. (2012). Generation of ascending flows in the big mantle wedge (BMW) beneath northeast Asia induced by retreat and stagnation of subducted slab. *Geophys. Res. Lett.*, *39*(10), 1–6. https://doi.org/10.1029/2012GL051678

Kanamori, H., and Stewart, G. S. (1976). Mode of the strain release along the Gibbs fracture zone, Mid-Atlantic Ridge. *Phys. Earth Planet. Inter.*, *11*(4), 312–332. https://doi.org/10.1016/0031-9201(76)90018-2

Kang, T.-S., and Shin, J.S. (2006). Surface-wave tomography from ambient seismic noise of accelerograph networks in southern Korea. *Geophys. Res. Lett., 33*(17), L17303. https://doi.org/10.1029/2006GL027044

Kang, T.-S., and Shin, J. S. (2009). Shear-wave splitting beneath southern Korea and its tectonic implication. *Tectonophysics*, *471*(3), 232–239. https://doi.org/10.1016/j.tecto.2009.02.021

Karato, S.I. (1993). Importance of anelasticity in the interpretation of seismic tomography. *Geophys. Res. Lett.*, *20*(15), 1623–1626. https://doi.org/10.1029/93GL01767

Karato, S. I. (2011). Water distribution across the mantle transition zone and its implications for global material circulation. *Earth Planet. Sci. Lett.*, *301*(3–4), 413–423. https://doi.org/10.1016/j.epsl.2010.11.038

Karato, S. I., and Jung, H. (1998). Water, partial melting and the origin of the seismic low velocity and high attenuation zone in the upper mantle. *Earth Planet. Sci. Lett.*, *157*(3–4), 193–207. https://doi.org/10.1016/S0012-821X(98)00034-X

Karato, S. I., Olugboji, T., and Park, J. (2015). Mechanisms and geologic significance of the mid-lithosphere discontinuity in the continents. *Nat. Geosci.*, *8*(7), 509–514. https://doi.org/10.1038/ngeo2462

Karlstrom, K.E., Coblentz, D., Dueker, K., Ouimet, W., Kirby, E., Van Wijk, J., et al. (2012). Mantle-driven dynamic uplift of the Rocky Mountains

and Colorado Plateau and its surface response: Toward a unified hypothesis. *Lithosphere*, *4*(1), 3–22. https://doi.org/10.1130/L150.1

Katz, R. F., Spiegelman, M., and Holtzman, B. (2006). The dynamics of melt and shear localization in partially molten aggregates. *Nature*, *442*(7103), 676–679. https://doi.org/10.1038/nature05039

Kaviani, A., Mahmoodabadi, M., Rümpker, G., Pilia, S., Tatar, M., Nilfouroushan, F., ... and Ali, M. Y. (2021). Mantle−flow diversion beneath the Iranian plateau induced by Zagros' lithospheric keel. *Sci. Rep.*, *11*(1), 1–12. https://doi.org/10.1038/s41598−021−81541−9

Kennett, B. L. N. (1991). The removal of free surface interactions from three−component seismograms. *Geophys. J. Int.*, *104*(1), 153–163. https://doi.org/10.1111/j.1365−246X.1991.tb02501.x

Kennett, B. L. N., Engdahl, E. R., and Buland, R. (1995). Constraints on seismic velocities in the Earth from traveltimes. *Geophys. J. Int.*, *122*(1), 108–124. https://doi.org/10.1111/j.1365−246X.1995.tb03540.x

Kennett, B. L. N., Sambridge, M. S., and Williamson, P. R. (1988). Subspace methods for large inverse problems with multiple parameter classes. *Geophys. J. Int.*, *94*(2), 237–247. https://doi.org/10.1111/j.1365−246X.1988.tb05898.x

Kim, D.E., Seong, Y.B., Byun, J., Weber, J., and Min, K. (2016). Geomorphic disequilibrium in the Eastern Korean Peninsula: Possible evidence for reactivation of a rift−flank margin. *Geomorphology*, *254*, 130–145. https://doi.org/10.1016/j.geomorph.2015.11.022.

Kim, G. B., and Yoon, S. H. (2017). An insight into asymmetric back−arc extension: Tecto−magmatic evidences from the Ulleung Basin, the East Sea (Sea of Japan). *Tectonophysics*, *717*, 182–192. https://doi.org/10.1016/j.tecto.2017.07.016

Kim, J.−S., Son, M., Kim, J.−S., and Kim, J. (2005). 40Ar/39Ar Ages of the Tertiary Dike Swarm and Volcanic Rocks, SE Korea. *J. Petrol. Soc. Korea*, 6, 93–107.

Kim, K. H., Tanaka, T., Suzuki, K., Nagao, K., and Park, E. J. (2002). Evidences of the presence of old continental basement in Cheju volcanic

Island, South Korea, revealed by radiometric ages and Nd−Sr isotopes of granitic rocks. *Geochem. J.*, *36*(5), 421–441. https://doi.org/10.2343/geochemj.36.421

Kim, S., Rhie, J., and Kim, G. (2011). Forward waveform modelling procedure for 1−D crustal velocity structure and its application to the southern Korean Peninsula. *Geophys. J. Int.*, *185*(1), 453–468. https://doi.org/10.1111/j.1365−246X.2011.04949.x

Kim, S., Tkalčić, H., and Rhie, J. (2017). Seismic constraints on magma evolution beneath Mount Baekdu (Changbai) volcano from transdimensional Bayesian inversion of ambient noise data. *J. Geophys. Res., Solid Earth*, *122*(7), 5452–5473. https://doi.org/10.1002/2017JB014105

Kim, S., Tkalčić, H., Rhie, J., and Chen, Y. (2016). Intraplate volcanism controlled by back−arc and continental structures in NE Asia inferred from transdimensional Bayesian ambient noise tomography. *Geophys. Res. Lett.*, *43*(16), 8390–8398. https://doi.org/10.1002/2016GL069483

Kim, S.W., Cho, D.L., Lee, S.B., Kwon, S., Park, S.I., Santosh, M., and Kee, W.S. (2018). Mesoproterozoic magmatic suites from the central−western Korean Peninsula: Imprints of Columbia disruption in East Asia. *Precamb. Res.*, *306*, 155–173. https://doi.org/10.1016/j.precamres.2017.12.038

Kim, S.W., Kee, W.S., Lee, S.R., Santosh, M., and Kwon, S. (2013). Neoproterozoic plutonic rocks from the western Gyeonggi massif, South Korea: implications for the amalgamation and break−up of the Rodinia supercontinent. *Precamb. Res.*, *227*, 349–367. https://doi.org/10.1016/j.precamres.2012.01.014

Kim, S.W., Kwon, S., Koh, H.J., Yi, K., Jeong, Y.J., and Santosh, M. (2011). Geotectonic framework of Permo−Triassic magmatism within the Korean Peninsula. *Gondwana Res.*, *20*(4), 865–889. https://doi.org/10.1016/j.gr.2011.05.005

Kim, S.W., Kwon, S., Park, S.I., Lee, C., Cho, D.L., Lee, H.J., et al. (2016). SHRIMP U−Pb dating and geochemistry of the Cretaceous plutonic rocks in the Korean Peninsula: a new tectonic model of the Cretaceous Korean

Peninsula. *Lithos*, *262*, 88–106. https://doi.org/10.1016/j.lithos.2016.06.027

Kim, S.W., Kwon, S., Santosh, M., Cho, D.L., Kee, W.S., Lee, S.B., and Jeong, Y.J. (2019). Detrital zircon U—Pb and Hf isotope characteristics of the Early Neoproterozoic successions in the central—western Korean Peninsula: Implication for the Precambrian tectonic history of East Asia. *Precamb. Res.*, *322*, 24–41. https://doi.org/10.1016/j.precamres.2018.12.008

Kim, S.W., Kwon, S., Yi, K., and Santosh, M. (2014). Arc magmatism in the Yeongnam massif, Korean Peninsula: Imprints of Columbia and Rodinia supercontinents. *Gondwana Res.*, *26*(3–4), 1009–1027. https://doi.org/10.1016/j.gr.2013.08.020

Kim, S.W., Park, S.I., Jang, Y., Kwon, S., Kim, S.J., and Santosh, M. (2017). Tracking Paleozoic evolution of the South Korean Peninsula from detrital zircon records: implications for the tectonic history of East Asia. *Gondwana Res.*, *50*, 195–215. https://doi.org/10.1016/j.gr.2017.05.009

Kim, Y., Lee, C., and Kim, S.S. (2015). Tectonics and volcanism in East Asia: Insights from geophysical observations. *J. Asian Earth Sci.*, *113*, 842–856. https://doi.org/10.1016/j.jseaes.2015.07.032

Kimura, J.—I., Sakuyama, T., Miyazaki, T., Vaglarov, B.S., Fukao, Y., and Stern, R.J. (2018). Plume—stagnant slab—lithosphere interactions: Origin of the late Cenozoic intra—plate basalts on the East Eurasia margin. *Lithos*. *300*, 227–249. https://doi.org/10.1016/j.lithos.2017.12.003

King, S. D. (2011). Eruptions above mantle shear. *Nat. Geosci.*, *4*, 279–280. https://doi.org/10.1038/ngeo1135

King, S. D., and Anderson, D. L. (1998). Edge—driven convection. *Earth Planet. Sci. Lett.*, *160*(3), 289–296. https://doi.org/10.1016/S0012—821X(98)00089—2

King, S. D., and Ritsema, J. (2000). African hot spot volcanism: Small—scale convection in the upper mantle beneath cratons. *Science*, *290*(5494), 1137–1140. https://doi.org/10.1126/science.290.5494.1137

Knopoff, L. (1964), Q, *Rev. Geophys.*, *2*(4), 625–660.

https://doi.org/10.1029/RG002i004p00625

Ko, B. K., and Yun, S. H. (2016). A preliminary study on calculating eruption volumes of monogenetic volcanoes and volcanic hazard evaluation in Jeju Island. *J. Petrol. Soc. Korea*, *25*(2), 143–149. https://doi.org/10.7854/JPSK.2016.25.2.143

Koh, G. W., Park, J. B., Kang, B.-R., Kim, G.-P., and Moon, D. C. (2013). Volcanism in Jeju Island. *J. Geol. Soc. Korea*, *49*(2), 209–230. https://doi.org/10.14770/jgsk.2013.49.2.209

Koh, J. S., Yun, S. H., and Kang, S. S. (2003). Petrology of the volcanic rocks in the Paekrogdam crater area, Mt. Halla, Jeju Island. *J. Geol, Soc, Korea*, *12*(1), 1–15

Komatitsch, D., and Tromp, J. (1999). Introduction to the spectral element method for three-dimensional seismic wave propagation. *Geophys. J. Int.*, *39*(3), 806–822. https://doi.org/10.1046/j.1365-246x.1999.00967.x

Kuritani, T., Ohtani, E., and Kimura, J. I. (2011). Intensive hydration of the mantle transition zone beneath China caused by ancient slab stagnation. *Nat. Geosci.*, *4*(10), 713–716. https://doi.org/10.1038/ngeo1250

Kuritani, T., Xia, Q. K., Kimura, J. I., Liu, J., Shimizu, K., Ushikubo, T., ... and Yoshimura, S. (2019). Buoyant hydrous mantle plume from the mantle transition zone. *Sci. Rep.*, *9*(1), 1–7. https://doi.org/10.1038/s41598-019-43103-y

Kusky, T.M., Windley, B.F., Wang, L., Wang, Z., Li, X., and Zhu, P. (2014). Flat slab subduction, trench suction, and craton destruction: comparison of the North China, Wyoming, and Brazilian cratons. *Tectonophysics*, *630*, 208–221. https://doi.org/10.1016/j.tecto.2014.05.028

Kwon, S., Sajeev, K., Mitra, G., Park, Y., Kim, S. W., and Ryu, I. C. (2009). Evidence for Permo-Triassic collision in far east Asia: the Korean collisional orogen. *Earth Planet. Sci. Lett.*, *279*(3–4), 340–349. https://doi.org/10.1016/j.epsl.2009.01.016

Lai, Y., Chen, L., Wang, T., and Zhan, Z. (2019). Mantle transition zone structure beneath Northeast Asia from 2-D triplicated waveform modeling: Implication for a segmented stagnant slab. *J. Geophys. Res., Solid Earth*,

124(2), 1871–1888. https://doi.org/10.1029/2018JB016642

Laske, G., Masters, G., Ma, Z., and Pasyanos, M. (2013), April. Update on CRUST1.0—A 1–degree global model of Earth's crust. In: Geophysical Research Abstract 15, 2658. Vienna, Austria: EGU General Assembly

Le Corvec, N., Spörli, K. B., Rowland, J., and Lindsay, J. (2013). Spatial distribution and alignments of volcanic centers: Clues to the formation of monogenetic volcanic fields. *Earth Sci. Rev., 124*, 96–114. https://doi.org/10.1016/j.earscirev.2013.05.005

Lee, B.C., Oh, C.W., Cho, D.L., and Yi, K. (2019). Paleoproterozoic (2.0–1.97 Ga) subduction–related magmatism on the north–central margin of the Yeongnam Massif, Korean Peninsula, and its tectonic implications for reconstruction of the Columbia supercontinent. *Gondwana Res., 72*, 34–53. https://doi.org/10.1016/j.gr.2019.02.002

Lee, C., and Lim, C. (2014). Short–term and localized plume–slab interaction explains the genesis of Abukuma adakite in northeastern Japan. *Earth Planet. Sci. Lett., 396*, 116–124. https://doi.org/10.1016/j.epsl.2014.04.009

Lee, C. T. A., Luffi, P., and Chin, E. J. (2011). Building and destroying continental mantle. *Annu. Rev. Earth. Pl. Sc., 39*, 59–90. https://doi.org/10.1146/annurev–earth–040610–133505

Lee, M. W. (1982). Petrology and geochemistry of Jeju volcanic island, Korea. *Sci. Rep. Tohoku Univ., Sendai, 15*(2), 177–256

Lee, S.H., Rhie, J., Park, Y., and Kim, K. H. (2014). Topography of the 410 and 660 km discontinuities beneath the Korean Peninsula and southwestern Japan using teleseismic receiver functions. *J. Geophys. Res., Solid Earth, 119*(9), 7245–7257. https://doi.org/10.1002/2014JB011149

Lee, S.R., and Walker, R.J. (2006). Re–Os isotope systematics of mantle xenoliths from South Korea: evidence for complex growth and loss of lithospheric mantle beneath East Asia. *Chem. Geol., 231*(1–2), 90–101. https://doi.org/10.1016/j.chemgeo.2006.01.003

Lee, Y., Park, S., Kim, J., Kim, H.C., and Koo, M.H. (2010). Geothermal

resource assessment in Korea. *Renew. Sust. Energ. Rev.*, 2392–2400. https://doi.org/10.1016/j.rser.2010.05.003

Legendre, C. P., Zhao, L., and Chen, Q. F. (2015). Upper-mantle shear-wave structure under East and Southeast Asia from automated multimode inversion of waveforms. *Geophys. J. Int.*, *203*(1), 707–719. https://doi.org/10.1093/gji/ggv322

Lei, J., and Zhao, D. (2005). P wave tomography and origin of the Changbai intraplate volcano in Northeast Asia. *Tectonophysics*, *397*(3–4), 281–295. https://doi.org/10.1016/j.tecto.2004.12.009

Levander, A., Bezada, M.J., Niu, F., Humphreys, E.D., Palomeras, I., Thurner, S.M., et al. (2014). Subduction-driven recycling of continental margin lithosphere. *Nature*, *515*(7526), 253–256. https://doi.org/10.1038/nature13878a

Levander, A., Schmandt, B., Miller, M.S., Liu, K., Karlstrom, K.E., Crow, R.S., et al. (2011). Continuing Colorado plateau uplift by delamination-style convective lithospheric downwelling. *Nature* *472*(7344), 461. https://doi.org/10.1038/nature10001

Lévêque, J.-J., and Masson, F. (1999). From ACH tomographic models to absolute velocity models. *Geophys. J. Int.*, *137*(3), 621–629. https://doi.org/10.1046/j.1365-246x.1999.00808.x

Li, C., and van der Hilst, R. D. (2010). Structure of the upper mantle and transition zone beneath Southeast Asia from traveltime tomography. *J. Geophys. Res., Solid Earth*, *115*(B7), B07308. https://doi.org/10.1029/2009JB006882

Li, J., and Song, X. (2018). Tearing of Indian mantle lithosphere from high-resolution seismic images and its implications for lithosphere coupling in southern Tibet. *P. Natl. A. Sci.*, *115*(33), 8296–8300. https://doi.org/10.1073/pnas.1717258115

Li, J., Wang, X., Wang, X., and Yuen, D. A. (2013). P and SH velocity structure in the upper mantle beneath Northeast China: Evidence for a stagnant slab in hydrous mantle transition zone. *Earth Planet. Sci. Lett.*, *367*, 71–81. https://doi.org/10.1016/j.epsl.2013.02.026

Li, J., Zheng, Y., Thomsen, L., Lapen, T. J., and Fang, X. (2018). Deep earthquakes in subducting slabs hosted in highly anisotropic rock fabric. *Nat. Geosci.*, *11*(9), 696–700. https://doi.org/10.1038/s41561-018-0188-3

Li, M., Zhang, S., and Wu, T. (2018). Fine crustal and uppermost mantle *S* wave velocity structure beneath the Tengchong volcanic area inferred from receiver function and surface-wave dispersion: Constraints on magma chamber distribution. *Bull. Volcanol.*, *80*, 25. https://doi.org/10.1007/s00445-018-1197-1

Li, S., Suo, Y., Li, X., Zhou, J., Santosh, M., Wang, P., et al. (2019). Mesozoic tectono-magmatic response in the East Asian ocean-continent connection zone to subduction of the Paleo-Pacific Plate. *Earth Sci. Rev.*, 192, 91–137. https://10.1016/j.earscirev.2019.03.003

Li, S.R., and Santosh, M. (2014). Metallogeny and craton destruction: records from the North China Craton. *Ore Geol. Rev. 56*, 376–414. https://doi.org/10.1016/j.oregeorev.2013.03.002.

Li, S.R., and Santosh, M., (2017). Geodynamics of heterogeneous gold mineralization in the North China Craton and its relationship to lithospheric destruction. *Gondwana Res.*, *50*, 267–292. https://doi.org/10.1016/j.gr.2017.05.007

Liang, X., Shen, Y., Chen, Y.J., Ren, Y., 2011. Crustal and mantle velocity models of southern Tibet from finite frequency tomography. *J. Geophys. Res.*, *116*, B02408, http://dx.doi.org/10.1029/2009/2009JB007159.

Lin, F. C., Tsai, V. C., Schmandt, B., Duputel, Z., and Zhan, Z. (2013). Extracting seismic core phases with array interferometry. *Geophys. Res. Lett.,* *40*(6), 1049–1053. https://doi.org/10.1002/grl.50237

Liu, J., Li, J., Hrubiak, R., and Smith, J. S. (2016). Origins of ultralow velocity zones through slab-derived metallic melt. *P. Natl. A. Sci.*, *113*(20), 5547–5551. https://doi.org/10.1073/pnas.1519540113

Liu, L., Morgan, J.P., Xu, Y., and Menzies, M. (2018a). Craton Destruction 1: Cratonic Keel Delamination Along a Weak Midlithospheric Discontinuity Layer. *J. Geophys. Res., Solid Earth*, *123*(11), 10040–10068.

https://doi.org/10.1029/2017JB015372

Liu, L., Morgan, J.P., Xu, Y., and Menzies, M., (2018b). Craton Destruction 2: Evolution of Cratonic Lithosphere After a Rapid Keel Delamination Event. *J. Geophys. Res., Solid Earth*, *123*(11), 10069–10090. https://doi.org/10.1029/2017JB015374

Liu, L., and Stegman, D. R. (2012). Origin of Columbia River flood basalt controlled by propagating rupture of the Farallon slab. *Nature*, *482*(7385), 386–389. https://doi.org/10.1038/nature10749

Liu, S., Gurnis, M., Ma, P., and Zhang, B. (2017). Reconstruction of northeast Asian deformation integrated with western Pacific plate subduction since 200 Ma. *Earth Sci. Rev.*, *175*, 114–142. https://doi.org/10.1016/j.earscirev.2017.10.012

Liu, S., Suardi, I., Yang, D., Wei, S., and Tong, P. (2018). Teleseismic traveltime tomography of northern Sumatra. *Geophys. Res. Lett.*, *45*(24), 13,231–13,239. https://doi.org/10.1029/2018GL078610

Liu, Z., Park, J., and Karato, S. I. (2016). Seismological detection of low-velocity anomalies surrounding the mantle transition zone in Japan subduction zone. *Geophys. Res. Lett.*, *43*(6), 2480–2487. https://doi.org/10.1002/2015GL067097

Liu, Z., Park, J., and Karato, S. I. (2018). Seismic evidence for water transport out of the mantle transition zone beneath the European Alps. *Earth Planet. Sci. Lett.*, *482*, 93–104. https://doi.org/10.1016/j.epsl.2017.10.054

Lu, C., Grand, S. P., Lai, H., and Garnero, E. J. (2019). TX2019slab: A new P and S tomography model incorporating subducting slabs. *J. Geophys. Res., Solid Earth*, 124(11), 11549–11567. https://doi.org/10.1029/2019JB017448

Lu, G., Kaus, B.J., and Zhao, L. (2011). Thermal localization as a potential mechanism to rift cratons. *Phys. Earth Planet. Inter.*, *186*(3–4), 125–137. https://doi.org/10.1016/j.pepi.2011.04.006

Ma, J., Tian, Y., Liu, C., Zhao, D., Feng, X., and Zhu, H. (2018). *P* wave tomography of Northeast Asia: Constraints on the western Pacific plate

subduction and mantle dynamics. *Phys. Earth Planet. Inter.*, *274*, 105–126. https://doi.org/10.1016/j.pepi.2017.11.003

Ma, P., Liu, S., Gurnis, M., and Zhang, B. (2019). Slab horizontal subduction and slab tearing beneath East Asia. *Geophys. Res. Lett.*, *46*. https://doi.org/10.1029/2018GL081703

Maccaferri, F., Bonafede, M., and Rivalta, E. (2010). A numerical model of dyke propagation in layered elastic media. *Geophys. J. Int.*, *180*(3), 1107–1123. https://doi.org/10.1111/j.1365–246X.2009.04495.x

Mao, Z., Jacobsen, S. D., Jiang, F., Smyth, J. R., Holl, C. M., and Duffy, T. S. (2008). Elasticity of hydrous wadsleyite to 12 GPa: implications for Earth's transition zone. *Geophys. Res. Lett.*, *35*(21). https://doi.org/10.1029/2008GL035618

Martí, J., López, C., Bartolini, S., Becerril, L., and Geyer, A. (2016). Stress controls of monogenetic volcanism: A review. *Front. Earth Sci.*, *4*, 106. https://doi.org/10.3389/feart.2016.00106

Martí, J., Villaseñor, A., Geyer, A., López, C., and Tryggvason, A. (2017). Stress barriers controlling lateral migration of magma revealed by seismic tomography. *Sci. Rep.*, *7*, 40757. https://doi.org/10.1038/srep40757

Mavko, G. M. (1980). Velocity and attenuation in partially molten rocks. *J. Geophys. Res., Solid Earth*, *85*(B10), 5173–5189. https://doi.org/10.1029/JB085iB10p05173

McCarthy, C., and Takei, Y. (2011). Anelasticity and viscosity of partially molten rock analogue: Toward seismic detection of small quantities of melt. *Geophys. Res. Lett.*, *38*(18). https://doi.org/10.1029/2011GL048776

McCarthy, C., Takei, Y., and Hiraga, T. (2011). Experimental study of attenuation and dispersion over a broad frequency range: 2. The universal scaling of polycrystalline materials. *J. Geophys. Res., Solid Earth*, *116*(B9). https://doi.org/10.1029/2011JB008384

McLean, D., Albert, P. G., Suzuki, T., Nakagawa, T., Kimura, J. I., Chang, Q., ... and Members, S. P. (2020). Refining the eruptive history of Ulleungdo and Changbaishan volcanoes (East Asia) over the last 86 kyrs using distal sedimentary records. *J. Volcanol. Geoth. Res*, *389*, 106669.

https://doi.org/10.1016/j.jvolgeores.2019.106669

Mégnin, C., and Romanowicz, B. (2000). The three-dimensional shear velocity structure of the mantle from the inversion of body, surface and higher-mode waveforms. *Geophys. J. Int.*, *143*(3), 709–728. https://doi.org/10.1046/j.1365−246X.2000.00298.x

Mei, S., Bai, W., Hiraga, T., and Kohlstedt, D. L. (2002). Influence of melt on the creep behavior of olivine-basalt aggregates under hydrous conditions. *Earth Planet. Sci. Lett*, *201*(3−4), 491–507. https://doi.org/10.1016/S0012−821X(02)00745−8

Menzies, M.A., Fan, W., and Zhang, M. (1993). Palaeozoic and Cenozoic lithoprobes and the loss of > 120 km of Archaean lithosphere, Sino−Korean craton, China. *Geol. Soc. Spec. Publ,* 76(1), 71–81. https://doi.org/10.1144/GSL.SP.1993.076.01.04

Miller, D. S., and Smith, R. B. (1999). *P* and *S* velocity structure of the Yellowstone volcanic field from local earthquake and controlled−source tomography. *J. Geophys. Res., Solid Earth*, *104*(B7), 15105–15121. https://doi.org/10.1029/1998JB900095

Missenard, Y., and Cadoux, A. (2012). Can Moroccan Atlas lithospheric thinning and volcanism be induced by edge−driven convection? *Terra Nova*, *24*(1), 27–33. https://doi.org/10.1111/j.1365−3121.2011.01033.x

Montelli, R., Nolet, G., Dahlen, F. A., Masters, G., Engdahl, E. R., and Hung, S. H. (2004). Finite−frequency tomography reveals a variety of plumes in the mantle. *Science*, *303*(5656), 338–343. https://doi.org/10.1126/science.1092485

Moresi, L., Betts, P.G., Miller, M.S., and Cayley, R.A. (2014). Dynamics of continental accretion. *Nature*, *508*(7495), 245. https://doi.org/10.1038/nature13033

Morgan, W. J. (1971). Convection plumes in the lower mantle. *Nature*, *230*(5288), 42–43. https://doi.org/10.1038/230042a0

Motoki, M. H., and Ballmer, M. D. (2015). Intraplate volcanism due to convective instability of stagnant slabs in the mantle transition zone. *Geochem. Geophys. Geosyst.*, *16*(2), 538–551.

https://doi.org/10.1002/2014GC005608

Müller, R. D., Cannon, J., Qin, X., Watson, R. J., Gurnis, M., Williams, S., et al. (2018). GPlates: Building a virtual Earth through deep time. *Geochem. Geophys. Geosyst.*, *19*. https://doi.org/10.1029/2018GC007584

Müller, R. D., Sdrolias, M., Gaina, C., and Roest, W. R. (2008). Age, spreading rates, and spreading asymmetry of the world's ocean crust. *Geochem, Geophys, Geosyst*, *9*(4). https://doi.org/10.1029/2007GC001743

Nakagawa, T., Tackley, P.J., Deschamps, F., and Connolly, J.A. (2010). The influence of MORB and harzburgite composition on thermo-chemical mantle convection in a 3-D spherical shell with self-consistently calculated mineral physics. *Earth Planet. Sci. Lett.*, *296*(3), 403–412. https://doi.org/10.1016/j.epsl.2010.05.026

Nakajima, J., Hirose, F., and Hasegawa, A. (2009). Seismotectonics beneath the Tokyo metropolitan area, Japan: Effect of slab-slab contact and overlap on seismicity. *J. Geophys. Res., Solid Earth*, *114*(B8). https://doi.org/10.1029/2008JB006101

Nakamura, E., Campbell, I. H., McCulloch, M. T., and Sun, S. S. (1989). Chemical geodynamics in a back arc region around the Sea of Japan: Implications for the genesis of alkaline basalts in Japan, Korea, and China. *J. Geophys. Res., Solid Earth*, *94*(B4), 4634–4654. https://doi.org/10.1029/JB094iB04p04634

Nakamura, E., McCulloch, M. T., and Campbell, I. H. (1990). Chemical geodynamics in the back-arc region of Japan based on the trace element and Sr-Nd isotopic compositions. *Tectonophysics*, *174*(3), 207–233. https://doi.org/10.1016/0040-1951(90)90323-Z

Nelson, P. L., and Grand, S. P. (2018). Lower-mantle plume beneath the Yellowstone hotspot revealed by core waves. *Nat. Geosci.*, *11*(4), 280–284. https://doi.org/10.1038/s41561-018-0075-y

Németh, K. (2010). Monogenetic volcanic fields: Origin, sedimentary record, and relationship with polygenetic volcanism. In E. Cañón-Tapia and A. Szakács (Eds.), *What is a volcano?* (pp. 43–66). Boulder, CO: Geological Society of America. https://doi.org/10.1130/2010.2470(04)

Németh, K., and Kereszturi, G. (2015). Monogenetic volcanism: Personal views and discussion. *Int. J. Earth Sci.*, *104*(8), 2131–2146. https://doi.org/10.1007/s00531-015-1243-6

Nishiyama, N., Kato, T., Irifune, T., and Wada, K. (2009). Phase relations in harzburgite: Stagnation of harzburgite at the lower part of the mantle transition zone and interpretation of seismic discontinuity at 600 km depth. *EOS, 90*, DI11A-07.

Obayashi, M., Yoshimitsu, J., and Fukao, Y. (2009). Tearing of stagnant slab. *Science*, *324*(5931), 1173–1175. https://doi.org/10.1126/science.1172496

Oh, C.W. and Kusky, T. (2007). The Late Permian to Triassic Hongseong-Odesan collision belt in South Korea, and its tectonic correlation with China and Japan. *Int. Geol. Rev.*, *49*(7), 636–657. https://doi.org/10.2747/0020-6814.49.7.636

Oh, C.W., Lee, B.C., Yi, S.B. and Ryu, H.I. (2019). Correlation of Paleoproterozoic igneous and metamorphic events of the Korean Peninsula and China; Its implication to the tectonics of Northeast Asia. *Precamb. Res.*, *326*, 334–362, https://doi.org/10.1016/j.precamres.2018.03.010

Olugboji, T. M., Karato, S. I., and Park, J. (2013). Structures of the oceanic lithosphere-asthenosphere boundary: Mineral-physics modeling and seismological signatures. *Geochem., Geophys., Geosyst.*, *14*(4), 880–901. https://doi.org/10.1002/ggge.20086

Otofuji, Y.-I., Matsuda, T., and Nohda, S. (1985). Opening mode of the Japan Sea inferred from the palaeomagnetism of the Japan Arc. *Nature*, *317*, 603–604. https://doi.org/10.1038/317603a0

Pandey, S., Yuan, X., Debayle, E., Priestley, K., Kind, R., Tilmann, F., and Li, X. (2014). A 3D shear-wave velocity model of the upper mantle beneath China and the surrounding areas. *Tectonophysics*, *633*, 193–210. https://doi.org/10.1016/j.tecto.2014.07.011

Papaleo, E., Cornwell, D., and Rawlinson, N. (2018). Constraints on North Anatolian Fault Zone width in the crust and upper mantle from S wave

teleseismic tomography. *J. Geophys. Res., Solid Earth*, *123*(4), 2908–2922. https://doi.org/10.1002/2017JB015386

Park, K. H., Park, J. B., Cheong, C. S., and Oh, C. W. (2005). Sr, Nd and Pb isotopic systematics of the Cenozoic basalts of the Korean Peninsula and their implications for the Permo−Triassic continental collision boundary. *Gondwana Res.*, *8*(4), 529–538. https://doi.org/10.1016/S1342−937X(05)71153−9

Pasyanos, M. E., Masters, T. G., Laske, G., and Ma, Z. (2014). LITHO1.0: An updated crust and lithospheric model of the Earth. *J. Geophys. Res., Solid Earth*, *119*(3), 2153–2173. https://doi.org/10.1002/2013JB010626

Piromallo, C., Becker, T. W., Funiciello, F., and Faccenna, C. (2006). Three-dimensional instantaneous mantle flow induced by subduction. *Geophys. Res. Lett.*, *33*(8), 1–4. https://doi.org10.1029/2005GL025390

Podolefsky, N. S., Zhong, S., and McNamara, A. K. (2004). The anisotropic and rheological structure of the oceanic upper mantle from a simple model of plate shear. *Geophys. J. Int.*, *158*(1), 287–296. https://doi.org/10.1111/j.1365−246X.2004.02250.x

Portner, D. E., Beck, S., Zandt, G., and Scire, A. (2017), The nature of subslab slow velocity anomalies beneath South America, *Geophys. Res. Lett.*, *44*, https://doi.org/10.1002/2017GL073106.

Portner, D. E., Delph, J. R., Biryol, C. B., Beck, S. L., Zandt, G., Özacar, A. A., et al. (2018). Subduction termination through progressive slab deformation across Eastern Mediterranean subduction zones from updated P−wave tomography beneath Anatolia. *Geosphere*, *14*(3), 907–925. https://doi.org/10.1130/GES01617.1

Pozgay, S. H., Wiens, D. A., Conder, J. A., Shiobara, H., and Sugioka, H. (2009). Seismic attenuation tomography of the Mariana subduction system: Implications for thermal structure, volatile distribution, and slow spreading dynamics. *Geochem., Geophys., Geosyst.*, *10*(4). https://doi.org/10.1029/2008GC002313

Priestley, K., Debayle, E., McKenzie, D., and Pilidou, S. (2006). Upper mantle structure of eastern Asia from multimode surface waveform

tomography. *J. Geophys. Res., Solid Earth*, *111*(B10), B10304. https://doi.org/10.1029/2005JB004082

Prieto, G. A., Parker, R. L., and Vernon Iii, F. L. (2009). A Fortran 90 library for multitaper spectrum analysis. *Comput. Geosci.*, *35*(8), 1701–1710. https://doi.org/10.1016/j.cageo.2008.06.007

Rawlinson, N., Davies, D.R., and Pilia, S. (2017). The mechanisms underpinning Cenozoic intraplate volcanism in eastern Australia: Insights from seismic tomography and geodynamic modeling. *Geophys. Res. Lett.*, *44*(19), 9681–9690. https://doi.org/10.1002/2017GL074911

Rawlinson, N., de Kool, M., and Sambridge, M. (2006a). Seismic wavefront tracking in 3D heterogeneous media: applications with multiple data classes. *Explor. Geophy.*, *37*(4), 322–330. https://doi.org/10.1071/EG06322

Rawlinson, N., and Kennett, B. L. N. (2004). Rapid estimation of relative and absolute delay times across a network by adaptive stacking. *Geophys. J. Int.*, *157*(1), 332–340. https://doi.org/10.1111/j.1365-246X.2004.02188.x

Rawlinson, N., and Kennett, B. L. N. (2008). Teleseismic tomography of the upper mantle beneath the southern Lachlan Orogen, Australia. *Phys. Earth Planet. Inter.*, *167*(1–2), 84–97. https://doi.org/10.1016/j.pepi.2008.02.007

Rawlinson, N., Reading, A. M., and Kennett, B. L. N. (2006b). Lithospheric structure of Tasmania from a novel form of teleseismic tomography. *J. Geophys. Res., Solid Earth*, *111*(B2), B02301. https://doi.org/10.1029/2005JB003803

Rawlinson, N., Salmon, M., and Kennett, B.L.N. (2014). Transportable seismic array tomography in southeast Australia: Illuminating the transition from Proterozoic to Phanerozoic lithosphere. *Lithos, 189*, 65–76. https://doi.org/10.1016/j.lithos.2013.06.001

Rawlinson, N., and Sambridge, M. (2003). Seismic traveltime tomography of the crust and lithosphere. *Adv. Geophys.*, *46*, 81–199.

Rawlinson, N., and Sambridge, M. (2004). Wave front evolution in strongly

heterogeneous layered media using the fast marching method. *Geophys. J. Int.*, *156*(3), 631–647. https://doi.org/10.1111/j.1365−246X.2004.02153.x

Ren, J., Tamaki, K., Li, S., and Junxia, Z. (2002). Late Mesozoic and Cenozoic rifting and its dynamic setting in Eastern China and adjacent areas. *Tectonophysics*, *344*(3–4), 175–205. https://doi.org/10.1016/S0040−1951(01)00271−2

Rhie, J., Kim, S., Woo, J. U., and Song, J. H. (2016, December). Three−dimensional velocity model of crustal structure in the southern Korean Peninsula and its full−waveform validations. *In AGU Fall Meeting Abstracts* (Vol. 2016, pp. S43B−2861).

Rhie, J., Lee, S. J., and Kim, S. (2018, December). Radial anisotropy of the upper mantle beneath the northeast Asia from Bayesian inversions of ambient noise data. *In AGU Fall Meeting Abstracts* (Vol. 2018, pp. DI13B−0042).

Richard, G. C., and Iwamori, H. (2010). Stagnant slab, wet plumes and Cenozoic volcanism in East Asia. *Phys. Earth Planet. Inter.*, *183*(1), 280–287. https://doi.org/10.1016/j.pepi.2010.02.009

Richards, P. G., and Menke, W. (1983). The apparent attenuation of a scattering medium. *Bull. Seismol. Soc. Am.*, *73*(4), 1005–1021.

Ringwood, A.E., and Irifune, T. (1988). Nature of the 650−km seismic discontinuity: implications for mantle dynamics and differentiation. *Nature*, *331*, 131–136. https://doi.org/10.1038/331131a0

Ritsema, J., Deuss, A., Van Heijst, H. J., and Woodhouse, J. H. (2011). S40RTS: A degree−40 shear−velocity model for the mantle from new Rayleigh wave dispersion, teleseismic traveltime and normal−mode splitting function measurements. *Geophys. J. Int.*, *184*(3), 1223–1236. https://doi.org/10.1111/j.1365−246X.2010.04884.x

Rychert, C. A., Hammond, J. O., Harmon, N., Kendall, J. M., Keir, D., Ebinger, C., ... and Stuart, G. (2012). Volcanism in the Afar Rift sustained by decompression melting with minimal plume influence. *Nat. Geosci.*, *5*(6), 406–409. https://doi.org/10.1038/ngeo1455

Sadeghi, H., Suzuki, S., and Takenaka, H. (2000). Tomographic low-velocity anomalies in the uppermost mantle around the northeastern edge of Okinawa trough, the backarc of Kyushu. *Geophys. Res. Lett.*, *27*(2), 277–280. https://doi.org/10.1029/1999GL008385

Sager, W. W., Handschumacher, D. W., Hilde, T. W., and Bracey, D. R. (1988). Tectonic evolution of the northern Pacific plate and Pacific-Farallon Izanagi triple junction in the Late Jurassic and Early Cretaceous (M21-M10). *Tectonophysics*, *155*(1-4), 345–364. https://doi.org/10.1016/0040-1951(88)90274-0

Sakuyama, T., Nagaoka, S., Miyazaki, T., Chang, Q., Takahashi, T., Hirahara, Y., et al. (2014). Melting of the uppermost metasomatized asthenosphere triggered by fluid fluxing from ancient subducted sediment: constraints from the Quaternary basalt lavas at Chugaryeong volcano, Korea. *J. Petrol.*, *55*(3), 499–528. https://doi.org/10.1093/petrology/egt074

Sakuyama, T., Tian, W., Kimura, J. I., Fukao, Y., Hirahara, Y., Takahashi, T., et al. (2013). Melting of dehydrated oceanic crust from the stagnant slab and of the hydrated mantle transition zone: Constraints from Cenozoic alkaline basalts in eastern China. *Chem. Geol.*, *359*, 32–48. http://doi.org/10.1016/j.chemgeo.2013.09.012

Sandwell, D. T., Winterer, E. L., Mammerickx, J., Duncan, R. A., Lynch, M. A., Levitt, D. A., and Johnson, C. L. (1995). Evidence for diffuse extension of the Pacific plate from Pukapuka ridges and cross-grain gravity lineations. *J. Geophys. Res., Solid Earth*, *100*(B8), 15087–15099. https://doi.org/10.1029/95JB00156

Santosh, M. (2010). Assembling North China Craton within the Columbia supercontinent: the role of double-sided subduction. *Precamb. Res.*, *178*(1-4), 149–167. https://doi.org/10.1016/j.precamres.2010.02.003

Savage, B., Covellone, B.M., and Shen, Y. (2017). Wave speed structure of the eastern North American margin. *Earth Planet. Sci. Lett.*, *459*, 394–405. https://doi.org/10.1016/j.epsl.2016.11.028

Schellart, W. P. (2004). Kinematics of subduction and subduction-induced flow in the upper mantle. *J. Geophys. Res., Solid Earth*, *109*(B7), B07401.

https://doi.org/10.1029/2004JB002970

Schlömer, A., Geissler, W. H., Jokat, W., and Jegen, M. (2017). Hunting for the Tristan mantle plume-An upper mantle tomography around the volcanic island of Tristan da Cunha. *Earth Planet. Sci. Lett.*, *462*, 122–131. https://doi.org/10.1016/j.epsl.2016.12.028

Schmandt, B., Dueker, K. G., Hansen, S. M., Jasbinsek, J. J., and Zhang, Z. (2011). A sporadic low-velocity layer atop the western US mantle transition zone and short-wavelength variations in transition zone discontinuities. *Geochem. Geophys. Geosyst.*, 12(8). https://doi.org/10.1029/2011GC003668

Schmandt, B., and Humphreys, E. (2010a), Seismic heterogeneity and small-scale convection in the southern California upper mantle, *Geochem. Geophys. Geosyst.*, *11*, Q05004, https://doi.org/10.1029/2010GC003042

Schmandt, B., and Humphreys, E. (2010b). Complex subduction and small-scale convection revealed by body-wave tomography of the western United States upper mantle. *Earth Planet. Sci. Lett.*, *297*(3-4), 435–445. https://doi.org/10.1016/j.epsl.2010.06.047

Schmandt, B., Jacobsen, S.D., Becker, T.W., Liu, Z., and Dueker, K.G. (2014), Dehydration melting at the top of the lower mantle, *Science*, *344*(6189), 1265–1268. https://doi.org/ 10.1126/science.1253358

Schmandt, B., and Lin, F.-C. (2014). *P* and *S* wave tomography of the mantle beneath the United States. *Geophys. Res. Lett.*, *41*(18), 6342–6349. https://doi.org/10.1002/2014GL061231

Schulze, K., Marquardt, H., Kawazoe, T., Ballaran, T. B., McCammon, C., Koch-Müller, M., ... and Marquardt, K. (2018). Seismically invisible water in Earth's transition zone?. *Earth Planet. Sci. Lett*, 498, 9–16. https://doi.org/10.1016/j.epsl.2018.06.021

Selway, K., Ford, H., and Kelemen, P. (2015). The seismic mid-lithosphere discontinuity. *Earth Planet. Sci. Lett.*, *414*, 45–57. https://doi.org/10.1016/j.epsl.2014.12.029

Sethian, J. A., and Popovici, A. M. (1999). 3-D traveltime computation using the fast marching method. *Geophysics*, *64*(2), 516–523.

https://doi.org/10.1190/1.1444558

Shen, W., Wiens, D.A., Stern, T., Anandakrishnan, S., Aster, R.C., Dalziel, I., et al. (2018). Seismic evidence for lithospheric foundering beneath the southern Transantarctic Mountains, Antarctica. *Geology*, *46*(1), 71–74. https://doi.org/10.1130/G39555.1

Shen, Y., and Blum, J. (2003). Seismic evidence for accumulated oceanic crust above the 660-km discontinuity beneath southern Africa. *Geophys. Res. Lett.*, *30*(18). https://doi.org/10.1029/2003GL017991

Shin, H. J., Kil, Y. W., Jin, M. S., and Lee, S. H. (2006). Petrological study on upper mantle xenoliths from Asan and Pyeongtaek area. *J. Geol. Soc. Korea*, 42(1), 95–113.

Shin, Y. H., Choi, K. S., Koh, J.-S., Yun, S.-H., Nakamura, E., and Na, S.-H. (2012). Lithospheric-folding-based understanding on the origin of the back-arc basaltic magmatism beneath Jeju volcanic island. *Tectonics*, *31*(4), TC4005. https://doi.org/10.1029/2011TC003092

Sigloch, K., McQuarrie, N., and Nolet, G. (2008). Two-stage subduction history under North America inferred from multiple-frequency tomography. *Nat. Geosci.*, *1*(7), 458–462. https://doi.org/10.1038/ngeo231

Sigloch, K., and Mihalynuk, M. G. (2013). Intra-oceanic subduction shaped the assembly of Cordilleran North America. *Nature*, *496*(7443), 50–56. https://doi.org/10.1038/nature12019

Sigurdsson, H., Houghton, B., McNutt, S., Rymer, H., and Stix, J. (Eds.). (2015). The encyclopedia of volcanoes. Elsevier.

Simmons, N. A., Forte, A. M., Boschi, L., and Grand, S. P. (2010). GyPSuM: A joint tomographic model of mantle density and seismic wave speeds. *J. Geophys. Res., Solid Earth*, *115*(B12). https://doi.org/10.1029/2010JB007631

Simutė, S., Steptoe, H., Cobden, L., Gokhberg, A., and Fichtner, A. (2016). Full-waveform inversion of the Japanese Islands region. *J. Geophys. Res., Solid Earth*, *121*(5), 3722–3741. https://doi.org/10.1002/2016JB012802

Sinogeikin, S.V., Bass, J.D., and Katsura, T. (2001). Single-crystal

elasticity of g−(Mg0.91Fe0.09)2SiO4 to high pressures and to high temperatures. *Geophys. Res. Lett.*, *28*, 4335–4338. https://doi.org/10.1029/2001GL013843

Smith, I. E. M., and Németh, K. (2017). Source to surface model of monogenetic volcanism: A critical review. *Geol. Soc. Spec. Publ.*, *446*(1), 1–28. https://doi.org/10.1144/sp446.14

Sobolev, S. V., Zeyen, H., Stoll, G., Werling, F., Altherr, R., and Fuchs, K. (1996). Upper mantle temperatures from teleseismic tomography of French Massif Central including effects of composition, mineral reactions, anharmonicity, anelasticity, and partial melt. *Earth Planet. Sci. Lett.*, *139*(1–2), 147–163. https://doi.org/10.1016/0012−821X(95)00238−8

Sohn, Y. K., Cronin, S. J., Brenna, M., Smith, I. E. M., Németh, K., White, J. D. L., et al. (2012). Ilchulbong tuff cone, Jeju Island, Korea, revisited: A compound monogenetic volcano involving multiple magma pulses, shifting vents, and discrete eruptive phases. *Geol. Soc. Am. Bull.*, *124*(3–4), 259–274. https://doi.org/10.1130/B30447.1

Sohn, Y. K., and Park, K. H. (2004). Early−stage volcanism and sedimentation of Jeju Island revealed by the Sagye borehole, SW Jeju Island, Korea. *Geosci. J.*, *8*(1), 73. https://doi.org/10.1007/bf02910280

Sohn, Y. K., and Park, K. H. (2005). Composite tuff ring/cone complexes in Jeju Island, Korea: Possible consequences of substrate collapse and vent migration. *J. Volcanol. Geoth. Res.*, *141*(1–2), 157–175. https://doi.org/10.1016/j.jvolgeores.2004.10.003

Sohn, Y. K., Park, K. H., and Yoon, S.−H. (2008). Primary versus secondary and subaerial versus submarine hydrovolcanic deposits in the subsurface of Jeju Island, Korea. *Sedimentology*, *55*(4), 899–924. https://doi.org/10.1111/j.1365−3091.2007.00927.x

Sohn, Y. K., Yoon, W. S., Ahn, U. S., Kim, G. B., Lee, J. H., Ryu, C. K., et al. (2015). Stratigraphy and age of the human footprints−bearing strata in Jeju Island, Korea: Controversies and new findings. *J. Archaeol. Sci.: Reports*, *4*, 264–275. https://doi.org/10.1016/j.jasrep.2015.09.014

Song, J.−H., Kim, S., and Rhie, J. (2020). Heterogeneous modification and

reactivation of a craton margin beneath the Korean Peninsula from teleseismic travel time tomography. *Gondwana Res., 81*, 475–489. https://doi.org/10.1016/j.gr.2019.11.016

Song, J.-H., Kim, S., Rhie, J., Lee, S.-H., Kim, Y., and Kang, T.-S. (2018). Imaging of lithospheric structure beneath Jeju Volcanic Island by teleseismic travel time tomography. *J. Geophys. Res., Solid Earth*, *123*(8), 6784–6801. https://doi.org/10.1029/2018JB015979

Steinberger, B., Bredow, E., Lebedev, S., Schaeffer, A., and Torsvik, T.H. (2019). Widespread volcanism in the Greenland-North Atlantic region explained by the Iceland plume. *Nat. Geosci.*, *12*(1), 61. https://doi.org/10.1038/s41561-018-0251-0

Sun, M., Gao, S. S., Liu, K. H., and Fu, X. (2020). Upper mantle and mantle transition zone thermal and water content anomalies beneath NE Asia: Constraints from receiver function imaging of the 410 and 660 km discontinuities. *Earth Planet. Sci. Lett.*, *532*, 116040. https://doi.org/10.1016/j.epsl.2019.116040

Takada, A. (1989). Magma transport and reservoir formation by a system of propagating cracks. *Bull. Volcanol.*, *52*(2), 118–126. https://doi.org/10.1007/BF00301551

Takei, Y. (2002). Effect of pore geometry on VP/VS: From equilibrium geometry to crack. *J. Geophys. Res., Solid Earth*, *107*(B2). https://doi.org/10.1029/2001JB000522

Takei, Y. (2017). Effects of partial melting on seismic velocity and attenuation: A new insight from experiments. *Annu. Rev. Earth. Pl. Sc.*, *45*, 447–470. https://doi.org/10.1146/annurev-earth-063016-015820

Tang, J., Xu, W., Wang, F., and Ge, W. (2018). Subduction history of the Paleo-Pacific slab beneath Eurasian continent: Mesozoic-Paleogene magmatic records in Northeast Asia. *Sci. China Earth Sci. 61*(5), 527–559. https://doi.org/10.1007/s11430-017-9174-1

Tang, Y., Obayashi, M., Niu, F., Grand, S. P., Chen, Y. J., Kawakatsu, H., et al. (2014). Changbaishan volcanism in northeast China linked to subduction-induced mantle upwelling. *Nat. Geosci.*, *7*, 470–475.

https://doi.org/10.1038/ngeo2166

Tao, K., Grand, S.P., and Niu, F. (2018). Seismic structure of the upper mantle beneath Eastern Asia from full waveform seismic tomography. *Geochem. Geophys. Geosyst.*, *19*(8), 2732–2763. https://doi.org/10.1029/2018GC007460

Tatsumi, Y., Shukuno, H., Yoshikawa, M., Chang, Q., Sato, K., and Lee, M. W. (2005). The petrology and geochemistry of volcanic rocks on Jeju Island: Plume magmatism along the Asian continental margin. *J. Petrol.*, *46*(3), 523–553. https://doi.org/10.1093/petrology/egh087

Tauzin, B., Debayle, E., and Wittlinger, G. (2010). Seismic evidence for a global low–velocity layer within the Earth's upper mantle. *Nat. Geosci.*, *3*(10), 718–721. https://doi.org/10.1038/ngeo969

Tauzin, B., Kim, S., and Afonso, J. C. (2018). Multiple phase changes in the mantle transition zone beneath northeast Asia: Constraints from teleseismic reflected and converted body waves. *J. Geophys. Res., Solid Earth*, *123*(8), 6636–6657. https://doi.org/10.1029/2017JB015238

Tauzin, B., Kim, S., and Kennett, B.L.N. (2017). Pervasive seismic low–velocity zones within stagnant plates in the mantle transition zone: Thermal or compositional origin?. *Earth Planet. Sci. Lett.*, *477*, 1–13. https://doi.org/10.1016/j.epsl.2017.08.006

Thomas, W.A., 2006. Tectonic inheritance at a continental margin. *Geol. Soc. Am. today*, *16*(2), 4–11. https://doi.org/10.1130/1052–5173(2006)016<4:TIAACM>2.0.CO;2

Thomson, A. R., Walter, M. J., Kohn, S. C., and Brooker, R. A. (2016). Slab melting as a barrier to deep carbon subduction. *Nature*, *529*(7584), 76–79. https://doi.org/10.1038/nature16174

Thurber, C. H. (2003). Seismic tomography of the lithosphere with body waves. *Pure Appl. Geophys.*, *160*(3–4), 717–737. https://doi.org/10.1007/PL00012555

Thybo, H., and Artemieva, I. M. (2013). Moho and magmatic underplating in continental lithosphere. *Tectonophysics*, *609*, 605–619. https://doi.org/10.1016/j.tecto.2013.05.032

Valentine, G. A., and Perry, F. V. (2007). Tectonically controlled, time-predictable basaltic volcanism from a lithospheric mantle source (central Basin and Range Province, USA). *Earth Planet. Sci. Lett.*, *261*(1), 201–216. https://doi.org/10.1016/j.epsl.2007.06.029

Van Decar, J. C., and Crosson, R. S. (1990). Determination of teleseismic relative phase arrival times using multi-channel cross-correlation and least squares. *Bull. Seismol. Soc. Am.*, *80*(1), 150–169.

Van Wijk, J. W., Baldridge, W. S., Van Hunen, J., Goes, S., Aster, R., Coblentz, D. D., et al. (2010). Small-scale convection at the edge of the Colorado Plateau: Implications for topography, magmatism, and evolution of Proterozoic lithosphere. *Geology*, *38*(7), 611–614. https://doi.org/10.1130/G31031.1

Van Wijk, J., Van Hunen, J., and Goes, S. (2008). Small-scale convection during continental rifting: Evidence from the Rio Grande rift. *Geology*, *36*(7), 575–578. https://doi.org/10.1130/G24691A.1

Walter, M. J., Kohn, S. C., Araujo, D., Bulanova, G. P., Smith, C. B., Gaillou, E., et al. (2011). Deep mantle cycling of oceanic crust: evidence from diamonds and their mineral inclusions. *Science*, *334*(6052), 54–57. https://doi.org/10.1126/science.1209300

Wang, J., Wu, H., and Zhao, D. (2014). P wave radial anisotropy tomography of the upper mantle beneath the North China Craton. *Geochem. Geophys. Geosyst.*, *15*(6), 2195–2210. https://doi.org/10.1002/2014GC005279

Wang, K., Zhao, L., Xu, X., and Yang, J. (2018). Heterogeneous destruction of the North China Craton: Coupled constraints from seismology and geodynamic numerical modeling. *Sci. China Earth Sci.*, *61*(5), 515–526. https://doi.org/10.1111/j.1365-246X.2010.04901.x

Wang, K.L., O'Reilly, S.Y., Griffin, W.L., Chung, S.L., and Pearson, N.J. (2003). Proterozoic mantle lithosphere beneath the extended margin of the South China block: In situ Re-Os evidence. *Geology 31*(8), 709–712. https://doi.org/10.1130/G19619.1

Wang, X. C., Wilde, S. A., Li, Q. L., and Yang, Y. N. (2015). Continental flood basalts derived from the hydrous mantle transition zone. *Nat. Commun.*, *6*,

7700. https://doi.org/10.1038/ncomms8700

Wang, Y., He, Y., Lu, G., and Wen, L. (2020). Seismic, thermal and compositional structures of the stagnant slab in the mantle transition zone beneath southeastern China. *Tectonophysics*, *775*, 228208. https://doi.org/10.1016/j.tecto.2019.228208

Wang, Z., and Kusky, T.M. (2019). The importance of a weak mid‒lithospheric layer on the evolution of the cratonic lithosphere. *Earth Sci. Rev.*, *190*, 557‒569. https://doi.org/10.1016/j.earscirev.2019.02.010.

Wei, H., Wang, Y., Jin, J., Gao, L., Yun, S. H., and Jin, B. (2007). Timescale and evolution of the intracontinental Tianchi volcanic shield and ignimbrite‒forming eruption, Changbaishan, Northeast China. *Lithos*, *96*(1‒2), 315‒324. https://doi.org/10.1016/j.lithos.2006.10.004

Wei, S. S., Wiens, D. A., Zha, Y., Plank, T., Webb, S. C., Blackman, D. K., Dunn, R. A., and Conder, J. A. (2015). Seismic evidence of effects of water on melt transport in the Lau back‒arc mantle. *Nature*, *518*(7539), 395‒398. https://doi.org/10.1038/nature14113

Wei, W., Xu, J., Zhao, D., and Shi, Y. (2012). East Asia mantle tomography: New insight into plate subduction and intraplate volcanism. *J. Asian Earth Sci., 60*, 88‒103. https://doi.org/10.1016/j.jseaes.2012.08.001

Wei, W., Zhao, D., Xu, J., Zhou, B., and Shi, Y. (2016). Depth variations of *P* wave azimuthal anisotropy beneath Mainland China. *Sci. Rep.*, *6*, 29614. https://doi.org/10.1038/srep29614

Wessel, P., Smith, W. H., Scharroo, R., Luis, J., and Wobbe, F. (2013). Generic mapping tools: Improved version released. *Eos*, *94*(45), 409‒410. https://doi.org/10.1002/2013EO450001

West, J. D., Fouch, M. J., Roth, J. B., and Elkins‒Tanton, L. T. (2009). Vertical mantle flow associated with a lithospheric drip beneath the Great Basin. *Nat. Geosci.*, *2*(6), 439‒444. https://doi.org/10.1038/ngeo526

Won, C.K., Lee, M.W., Noh, J.H., and Lee, H.K. (1994). Cretaceous volcanic activity in Tongri basin. *J. Geol. Soc. Korea*, *30*(6), 542‒562

Woo, Y., Yang, K., Kil, Y., Yun, S. H., and Arai, S. (2014). Silica‒and LREE‒enriched spinel peridotite xenoliths from the Quaternary intraplate alkali

basalt, Jeju Island, South Korea: Old subarc fragments? *Lithos*, *208–209*, 312–323. https://doi.org/10.1016/j.lithos.2014.09.003

Wu, F.-Y., Yang, J.H., Xu, Y.G., Wilde, S.A., and Walker, R.J. (2019). Destruction of the North China Craton in the Mesozoic. *Annu. Rev. Earth. Pl. Sc.*, *47*, 173–195. https://doi.org/10.1146/annurev-earth-053018-060342

Wu, J., Suppe, J., Lu, R., and Kanda, R. (2016). Philippine Sea and East Asian plate tectonics since 52 Ma constrained by new subducted slab reconstruction methods. *J. Geophys. Res., Solid Earth*, *121*(6), 4670–4741. https://doi.org/10.1002/2016JB012923

Wu, W., Ni, S., and Irving, J. C. (2019). Inferring Earth's discontinuous chemical layering from the 660-kilometer boundary topography. *Science*, *363*(6428), 736–740. https://doi.org/10.1126/science.aav0822

Xu, W., Lithgow-Bertelloni, C., Stixrude, L., and Ritsema, J. (2008). The effect of bulk composition and temperature on mantle seismic structure. *Earth Planet. Sci. Lett.*, *275*(1–2), 70–79. https://doi.org/10.1016/j.epsl.2008.08.012

Xu, X., Zhao, L., Wang, K., and Yang, J. (2018). Indication from finite-frequency tomography beneath the North China Craton: The heterogeneity of craton destruction. *Sci. China Earth Sci. 61*(9), 1238–1260. https://doi.org/10.1007/s11430-017-9201-y

Yamauchi, H., and Takei, Y. (2016). Polycrystal anelasticity at near-solidus temperatures. *J. Geophys. Res., Solid Earth*, *121*(11), 7790–7820. https://doi.org/10.1002/2016JB013316

Yang, J., and Faccenda, M. (2020). Intraplate volcanism originating from upwelling hydrous mantle transition zone. *Nature*, *579*(7797), 88–91. https://doi.org/10.1038/s41586-020-2045-y

Yang, J.H., O'Reilly, S.Y., Walker, R.J., Griffin, W., Wu, F.Y., Zhang, M., et al., (2010). Diachronous decratonization of the Sino-Korean craton: Geochemistry of mantle xenoliths from North Korea. *Geology*, *38*(9), 799–802. https://doi.org/10.1130/G30944.1

Yang, K., Hidas, K., Falus, G., Szabó, C., Nam, B., Kovács, I., and Hwang, B.

(2010). Relation between mantle shear zone deformation and metasomatism in spinel peridotite xenoliths of Jeju Island (South Korea): Evidence from olivine CPO and trace elements. *J. Geodyn.*, *50*(5), 424–440. https://doi.org/10.1016/j.jog.2010.05.005

Yang, K., Szabó, C., Arai, S., Yu, J. E., and Jung, H. (2012). Silica enrichment of Group II xenoliths by evolved alkali basalt from Jeju Island, South Korea: Implication for modification of intraplate deep-seated rocks. *Miner. Petrol.*, *106*(1-2), 107–130. https://doi.org/10.1007/s00710-012-0222-x

Yang, T., Moresi, L., Zhao, D., Sandiford, D., and Whittaker, J. (2019). Cenozoic lithospheric deformation in Northeast Asia and the rapidly-aging Pacific Plate. *Earth Planet. Sci. Lett.*, *492*, 1–11. https://doi.org/10.1016/j.epsl.2018.03.057

Yang, X. and Gao, H. (2018). Full-wave seismic tomography in the northeastern United States: New insights into the uplift mechanism of the Adirondack Mountains. *Geophys. Res. Lett.*, *45*, 5992–6000. https://doi.org/10.1029/2018GL078438

Ye, L., Lay, T., Kanamori, H., Zhan, Z., and Duputel, Z. (2016). Diverse rupture processes in the 2015 Peru deep earthquake doublet. *Sci. Adv.*, *2*(6), e1600581. https://doi.org/10.1126/sciadv.1600581

Yoo, H. J., Herrmann, R. B., Cho, K. H., and Lee, K. (2007). Imaging the three-dimensional crust of the Korean Peninsula by joint inversion of surface-wave dispersion and teleseismic receiver functions. *Bull. Seismol. Soc. Am.*, *97*(3), 1002–1011. https://doi.org/10.1785/0120060134

Youssof, M., Thybo, H., Artemieva, I.M., and Levander, A. (2015). Upper mantle structure beneath southern African cratons from seismic finite-frequency *P* and *S* body wave tomography. *Earth Planet. Sci. Lett., 420*, 174–186. https://doi.org/10.1016/j.epsl.2015.01.034

Zhai, M., Guo, J., Li, Z., Chen, D., Peng, P., Li, T., ... and Fan, Q. (2007). Linking the Sulu UHP belt to the Korean Peninsula: Evidence from eclogite, Precambrian basement, and Paleozoic sedimentary basins. *Gondwana Res.*, *12*(4), 388–403.

https://doi.org/10.1016/j.gr.2007.02.003

Zhang, B. H., and Xia, Q. K. (2021). Influence of water on the physical properties of olivine, wadsleyite, and ringwoodite. *Eur. J. Mineral.*, 33(1), 39–75. https://doi.org/10.5194/ejm−33−39−2021

Zhang, H.F. (2005). Transformation of lithospheric mantle through peridotite−melt reaction: a case of Sino−Korean craton. *Earth Planet. Sci. Lett.*, *237*(3–4), 768–780. https://doi.org/10.1016/j.epsl.2005.06.041

Zhang, M., Guo, Z., Cheng, Z., Zhang, L., and Liu, J. (2014). Late Cenozoic intraplate volcanism in Changbai volcanic field on the border of China and North Korea: Insights into deep subduction of the Pacific slab and intraplate volcanism. *J. Geol. Soc.*, *172*(5), 648–663. https://doi.org/10.1144/jgs2014−080

Zhao, D., Tian, Y., Lei, J., Liu, L., and Zheng, S. (2009). Seismic image and origin of the Changbai intraplate volcano in East Asia: Role of big mantle wedge above the stagnant Pacific slab. *Phys. Earth Planet. Inter.*, *173*(3), 197–206. https://doi.org/10.1016/j.pepi.2008.11.009

Zhao, D., Yamamoto, Y., and Yanada, T. (2013). Global mantle heterogeneity and its influence on teleseismic regional tomography. *Gondwana Res.*, *23*(2), 595–616. https://doi.org/10.1016/j.gr.2012.08.004

Zhao, L., Allen, R. M., Zheng, T., and Zhu, R. (2012). High-resolution body wave tomography models of the upper mantle beneath eastern China and the adjacent areas. *Geochem. Geophys. Geosyst.*, 13(6). https://doi.org/10.1029/2012GC004119

Zheng, J., O'Reilly, S.Y., Griffin, W.L., Lu, F., Zhang, M., and Pearson, N.J. (2001). Relict refractory mantle beneath the eastern North China block: significance for lithosphere evolution. *Lithos,* *57*(1), 43–66. https://doi.org/10.1016/S0024−4937(00)00073−6

Zheng, J.P., Lee, C.T., Lu, J.G., Zhao, J.H., Wu, Y.B., Xia, B., et al. (2015). Refertilization−driven destabilization of subcontinental mantle and the importance of initial lithospheric thickness for the fate of continents. *Earth Planet. Sci. Lett.*, *409*, 225–231. https://doi.org/10.1016/j.epsl.2014.10.042

Zheng, Y., Shen, W., Zhou, L., Yang, Y., Xie, Z., and Ritzwoller, M. H. (2011). Crust and uppermost mantle beneath the North China Craton, northeastern China, and the Sea of Japan from ambient noise tomography. *J. Geophys. Res., Solid Earth*, *116*(B12), B12312. https://doi.org/10.1029/2011JB008637

Zhou, Y. (2018). Anomalous mantle transition zone beneath the Yellowstone hotspot track. *Nat. Geosci*, *11*(6), 449–453. https://doi.org/10.1038/s41561−018−0126−4

Zhu, H., Bozdağ, E., Peter, D., and Tromp, J. (2012). Structure of the European upper mantle revealed by adjoint tomography. *Nat. Geosci.*, 5(7), 493–498. https://doi.org/10.1038/ngeo1501

Abstract in Korean (국문 초록)

화산 활동과 판구조 운동(예, 판의 섭입)은 지구 내부의 활발한 맨틀 대류를 입증하며, 지구 내부 열역학적 상태를 이해하는데 중요한 연구 대상이다. 지진파는 지각과 맨틀을 통과하면서 이들의 물리적인 상태를 반영하며, 이를 분석하여 지구 내부의 열적 및 성분적 특성에 대해 연구할 수 있다. 본 논문에서는 다양한 지진학적 방법을 활용하여 판 내 화산활동과 판의 섭입이 활발히 일어나고 있는 동북 아시아 상부 맨틀 구조를 연구한다. 구체적으로, 원거리 지진 주시 토모그래피를 사용하여 판 내 화산으로 알려진 제주도 하부 암석권 및 연약권의 구조(제 1장), 한반도 하부의 암석권 및 연약권 구조(제 2장), 동북아시아 지역의 상부 맨틀 전이대와 정체된 슬랩(제 3장), 한반도 주변 제 4기 화산체 하부의 얕은 연약권(제 4장)의 3차원 구조를 영상화하고 분석한다. 연구 자료로 원거리 지진의 실체파 신호(P, S파)를 이용하여 연구 지역에 조밀하게 설치된 지진계 간의 파형 유사성을 기반한 방법으로 정밀하게 측정된 상대 주시 잔차를 사용하며, 해당 잔차를 최소화할 수 있는 최적의 3차원 속도 구조 모델을 비선형 반복 역산 방법을 통해 구한다. 제 1장에서는, 서울대학교 지진학 연구실에서 제주도에 약 2년간 설치한 임시 지진 관측망 자료를 사용하였으며, 제주도 하부 상승하는 마그마와 대륙 암석권 간의 상호작용으로 발달한 복잡한 형태의 마그마 시스템을 영상화 하였다. 제 2장에서는 한반도의 시생대 및 원생대 대륙암권 하부의 상부 맨틀을 영상화하며, 그 결과 동북 아시아 대륙 연변부에서 불균질한 수정 및 재활성화를 겪은 오래되고 두꺼운 암석권 구조를 확인하였다. 제 3장에서는 한반도와 일본 남서부의 관측망 자료를 사용하여 한반도를 포함한 동북아시아 하부의 깊은 상부 맨틀 구조를 영상화 하였다. 그 결과 유라시아판 하부에 정체된 태평양 슬랩의 불균질한 분포를 확인하였고, 기존 연구에서 해상도 한계로 보이지 않았던 한반도 하부의 슬랩 간극의 존재를 새롭게 밝혀낸다. 또한 한반도에 기록된 원거리 지진의 S파를 분석하여 슬랩 간극에 의한 파면 왜곡을 관측하였고 이를 3차원 파형 시

뮬레이션을 통해 모사하였다. 마지막으로 제 4장에서는 기존에 얻어진 고해상도 속도 구조 모델을 바탕으로 동북 아시아 상부 맨틀의 열적 및 성분적 특성을 열역학적 계산 및 지진파 감쇠 특성을 고려하여 정량적으로 추정한다. 그 결과 한반도 주변 제 4기 화산 지역(예, 울릉도, 독도, 백두산, 제주도, 한탄강 유역)의 국지적이고 지속적인 마그마 발달에 기여하였을 것으로 생각되는 집중된 얕은 연약권 맨틀의 부분 용융을 확인하였다. 전 장을 통틀어, 상부 맨틀 구조들의 기원, 진화, 그리고 상호 관계에 대해 지질학적, 지구조적, 그리고 지구동역학적인 관점에서 해석하고 논의한다.

주요어: 상부 맨틀, 원거리 지진 주시 토모그래피, 판 내 화산, 맨틀 전이대, 파형 모델링, 지진파 감쇠

학번: 2016-20419